A N N U A L R E P O R T

2016

and list of publications

Bayerisches Forschungsinstitut
für Experimentelle Geochemie und Geophysik
Universität Bayreuth

Bayerisches Geoinstitut
Universität Bayreuth
D-95440 Bayreuth
Germany

Telephone: +49-(0)921-55-3700
Telefax: +49-(0)921-55-3769
e-mail: bayerisches.geoinstitut@uni-bayreuth.de
www: http://www.bgi.uni-bayreuth.de

Editorial compilation by: Stefan Keyssner and Petra Buchert
Section editors: Andreas Audétat, Tiziana Boffa Ballaran, Leonid Dubrovinsky, Dan Frost, Gregor Golabek, Tomoo Katsura, Takaaki Kawazoe, Hans Keppler, Hauke Marquardt, Katharina Marquardt, Catherine McCammon, Nobuyoshi Miyajima, Dave Rubie, Gerd Steinle-Neumann

Staff and guests of the Bayerisches Geoinstitut in **July 2016**:

Die Mitarbeiter und Gäste des Bayerischen Geoinstituts im **Juli 2016**:

First row, from left (1. Reihe, v. links) Robert Arato, Daria Simonova, Katherine Armstrong, Eleanor Jennings, Ahmed El Goresy, Ulrike Trenz, Leyla Ismailova, Andrea Adams, Nicki Siersch, Caterina Melai, Stella Chariton

Second row, from left (2. Reihe, v. links) Joanna Emilien, Catherine McCammon, Tiziana Boffa Ballaran, Dorothea Wiesner, Sourav Kumar Misra, Yangting Lin, Dmitry Druzhbin, Fabian Wagle, Heinz Fischer, Ananya Mallik, Rong Huang

Third row, from left (3. Reihe, v. links) Stefan Keyssner, Alireza Zarei, Petra Buchert, Vera Laurenz, Nobuyoshi Miyajima, Tomoo Katsura, Zhaodong Liu, Hongzhan Fei, Florian Heidelbach, Tariq Ejaz, Daohan Zhang

Fourth row, from left (4. Reihe, v. links) Thomas Meier, Dan Frost, Svyatoslav Shcheka, Takaaki Kawazoe, Robert Farla, Raphael Njul, Andreas Audétat, Leonid Dubrovinsky, Georgios Aprilis, Johannes Buchen, Marcel Thielmann

Fifth row, from left (5. Reihe, v. links) Baptiste Journaux, Sylvain Petitgirard, Matteo Masotta, Sumith Abeykoon, Gerd Steinle-Neumann, Alexander Kurnosov, Ulrich Böhm, Takahiro Yoshioka, Lin Wang, Yang Li, Haihao Guo, Gregor Golabek, Steffen Klumbach

Absent (Es fehlten) Caroline Bollinger, Alok Chaudari, Irina Chuvashova, Pierre Condamine, Nicole Fischer, Julia Immoor, Takayuki Ishii, Hans Keppler, Lydia Kison-Herzing, Kurt Klasinski, Detlef Krauße, Holger Kriegl, Sven Linhardt, Hauke Marquardt, Katharina Marquardt, Sergey Ovsyannikov, Joana Polednia, Esther Posner, Anke Potzel, Gerd Ramming, Oliver Rausch, Dave Rubie, Romina Scharfenberg, Hubert Schulze, Kirsten Schulze, Stefan Übelhack

Contents

Foreword

In 2016 we celebrated the 30th anniversary of the foundation of the Bayerisches Geoinstitut. As part of the three day festivities a number of institute alumni presented some of their recent findings together with recollections of their time spent at BGI. We were particularly pleased to also welcome our founding director Fritz Seifert who gave an intriguing insight into the events that led to the foundation of the BGI and described the early challenges faced by the fledgling institute. One of the most effective founding policies at BGI was to have a strong focus on the support of early career post-doctoral researchers, which allowed the institute to capitalize on new ideas and perspectives, as it continues to do today. This and an emphasis on advances in new experimental design and remarkable technical support were critical components in the rapid development of the institute's reputation. A measure of the success of these policies could be obtained during the 30th anniversary festivities while listening to the presentations of our alumni, who now fill many senior academic positions at universities all over the world.

2016 also marked the start of our DFG funded International Research and Training Group on Deep Earth Volatile Cycles, which is a collaboration with the Department of Earth Sciences at Tohoku University in Sendai, Japan. Twelve PhD positions are funded in this programme over the next 4.5 years and we were pleased to admit the first PhD students in 2016. By exchanging researchers with Tohoku University diverse aspects of the cycling of volatiles within the Earth's interior will be studied in a collaboration that takes explicit advantage of the complementary expertise of scientists at the two institutions. We held our first joint workshop in Tohoku University in Sendai at the start of July, which was attended by over 20 scientists from the BGI, and over the course of 2016 we were also very pleased to welcome more than 20 researchers from Tohoku at the BGI. I would like to express my appreciation to my Japanese counterpart in the IRTG, Prof. Michihiko Nakamura, for his readiness to enthusiastically pursue this collaboration.

In addition to the fact that the yearbook is now in colour, two further highlights, within this year's reports can be found in section 3.5 that have implications for the way that volatile elements may be stored in the Earth's silicate mantle. For many years it has been recognized that H_2O can substitute into the crystal structure of mantle minerals in the form of OH defects and thus the solid mantle is able to absorb an important compliment of water. However, the reported new measurements find that when minerals are in equilibrium with oxygen poor fluids they can also incorporate molecular hydrogen (H_2) into their crystal structures. Such oxygen poor conditions likely prevailed as planets were formed, and although hydrogen would have been present, it was thought that in the absence of oxygen to form water, silicate minerals would have been left hydrogen free. These results imply that a small but significant proportion of hydrogen could have indeed been trapped in silicate minerals as the terrestrial planets formed. The second highlight concerns experiments to study the solubility of nitrogen in mantle minerals. Experiments show that minerals, particularly in the Earth's transition

zone, between approximately 410 and 660 km depth, are able to host significant levels of nitrogen. Previously it was considered that the Earth's atmosphere was by far the main reservoir for nitrogen on Earth. These results call this perception into question and raise the possibility that nitrogen could have been variably partitioned between the mantle and atmosphere over geological time.

On the behalf of my colleagues, I would like to thank the *Free State of Bavaria* as represented by the *Bavarian State Ministry of Science, Research and Art* as well as the *Advisory Board for High-Pressure Research in Geoscience* for their continuing support and strong commitment to the Bayerisches Geoinstitut. I would further like to thank the *President and Leadership of the University of Bayreuth* for their high regard of the profile field "High Pressure and High Temperature Research". We also gratefully acknowledge generous support from external funding agencies, in particular the *Alexander von Humboldt Foundation*, the *European Union*, the *German Science Foundation,* and the *Federal Ministry of Education and Research*, which continue to contribute greatly to the further development and success of the Geoinstitut.

Bayreuth, March 2017 Dan Frost

Vorwort

Im Jahr 2016 feierten wir das 30-jährige Jubiläum der Gründung des Bayerischen Geoinstituts. Im Rahmen der dreitägigen Feierlichkeiten präsentierten eine Reihe von ehemaligen Institutsmitgliedern ihre neuesten Forschungsergebnisse zusammen mit Erinnerungen an ihre Zeit am BGI. Wir waren ganz besonders erfreut über den Vortrag unseres Gründungsdirektors Fritz Seifert, der einen faszinierenden Einblick in die Ereignisse gab, die zur Entstehung des BGI führten und der die ersten Herausforderungen für das junge Institut beschrieb. Eine der effektivsten Gründungsstrategien des BGI war es, einen starken Fokus auf die Unterstützung von jungen Nachwuchswissenschaftlern zu setzen, die es dem Institut ermöglichten, innovative Ideen und Perspektiven zu nutzen und zu entwickeln, so wie wir es bis heute noch fortführen. Dies und der Schwerpunkt auf der Entwicklung neuer experimenteller Apparaturen, sowie die ausgezeichnete technische Unterstützung, waren entscheidende Komponenten in der raschen Entwicklung der Reputation des Instituts. Einen Eindruck des Erfolgs dieser Strategie konnte man aus den Vorträgen unserer ehemaligen Mitarbeiter während der Feierlichkeiten gewinnen, von denen jetzt viele leitende akademische Positionen an Universitäten auf der ganzen Welt innehaben.

2016 war auch der Beginn unseres DFG-geförderten Internationalen Forschungs- und Ausbildungskollegs (IRTG) ‚Deep Earth Volatile Cycles', in enger Zusammenarbeit mit dem *Department of Earth Sciences* der Tohoku Universität in Sendai, Japan. Zwölf Promotionsstellen werden in diesem Programm in den nächsten 4,5 Jahren finanziert und wir freuen uns, dass die ersten Doktoranden im Jahr 2016 ihre Arbeit aufgenommen haben. Durch den Austausch von Wissenschaftlern mit der Tohoku Universität können verschiedene Aspekte des Kreislaufs von volatilen Elementen im Inneren der Erde untersucht werden, wodurch das komplementäre Fachwissen der Wissenschaftler an beiden Institutionen optimal ausgeschöpft wird. Anfang Juli 2017 organisierten wir unseren ersten gemeinsamen Workshop an der Tohoku Universität in Sendai, an dem über 20 Wissenschaftler aus dem BGI teilnahmen und waren darüber hinaus sehr erfreut, im Laufe des Jahres 2016 ebenfalls mehr als 20 Forscher aus Tohoku am BGI empfangen zu dürfen. Ich möchte Prof. Michihiko Nakamura, Sprecher für den japanischen Teil des IRTG, daher ausdrücklich für sein enthusiastisches Engagement in diesem Vorhaben danken.

Neben der Tatsache, dass in diesem Jahr der Jahresbericht in Farbe vorliegt, möchte ich insbesondere zwei wissenschaftliche Beiträge explizit hervorheben, die in Abschnitt 3.5 vorgestellt werden. Sie behandeln die Mechanismen, durch die flüchtige Elemente im silikatischen Erdmantel gespeichert werden können. Seit einigen Jahren ist bekannt, dass H2O in die Kristallstruktur von Mantelmineralen in Form von OH-Defekten eingebaut werden kann und somit der feste Mantel ein potentiell wichtiges Reservoir für Wasser in der Erde darstellt. Allerdings zeigen neue Messungen, dass Minerale, wenn sie sich im Gleichgewicht mit sauerstoffarmen Flüssigkeiten befinden, auch molekularen Wasserstoff (H2) in ihren Kristallstrukturen aufnehmen können. Solche sauerstoffarmen Bedingungen herrschten

wahrscheinlich zur Zeit der frühen Planetenbildung. Und obwohl damals molekularer Wasserstoff vorhanden war, wurde angenommen, dass selbst bei Abwesenheit von Sauerstoff zur Bildung von Wasser, Silikatminerale frei von Wasserstoff geblieben wären. Die hier präsentierten Ergebnisse zeigen, dass ein kleiner, aber signifikanter Anteil an Wasserstoff tatsächlich in Silikatmineralen gespeichert werden konnte, als die terrestrischen Planeten entstanden. Der zweite bahnbrechende Beitrag betrifft Experimente zur Untersuchung der Löslichkeit von Stickstoff in Mantelmineralen. Diese zeigen, dass Minerale, vor allem in der Übergangszone der Erde zwischen etwa 410 und 660 km Tiefe, in der Lage sind, signifikante Mengen an Stickstoff aufzunehmen. Bisher wurde davon ausgegangen, dass die Erdatmosphäre das bei weitem größte Reservoir für Stickstoff auf der Erde darstellt. Die vorliegenden Ergebnisse stellen nun diese Auffassung in Frage und eröffnen die Möglichkeit, dass die Verteilung des Stickstoffs zwischen Erdmantel und Atmosphäre über geologische Zeiträume hinweg stark variiert haben könnte.

Meine Kollegen und ich möchten dem *Freistaat Bayern*, vertreten durch das *Bayerische Staatsministerium für Wissenschaft, Forschung und Kunst*, und dem *Beirat für Geowissenschaftliche Hochdruckforschung der Bayerischen Akademie der Wissenschaften* unseren Dank für ihre fortwährende Unterstützung des Bayerischen Geoinstituts aussprechen. Darüberhinaus möchten wir dem Präsidenten und der Hochschulleitung der Universität Bayreuth ausdrücklich für ihre zuverlässige und kontinuierliche Unterstützung des Profilfeldes ‚Hochdruck- und Hochtemperaturforschung' danken. Wir sind auch für die großzügige Förderung durch externe Geldgeber dankbar, insbesondere der *Alexander-von-Humboldt-Stiftung*, der *Europäischen Union,* der *Deutschen Forschungsgemeinschaft* und dem *Bundesministerium für Bildung und Forschung*, die ebenfalls wesentlich zur Entwicklung und zum Erfolg des Bayerischen Geoinstituts beigetragen haben.

Bayreuth, im März 2017 Dan Frost

1. Advisory Board and Directorship

1.1 Advisory Board

The *Beirat für Geowissenschaftliche Hochdruckforschung der Bayerischen Akademie der Wissenschaften* advises on the organisation and scientific activities of the institute. Members of this board are:

Prof. Dr. G. BREY	Institut für Geowissenschaften der Johann Wolfgang Goethe-Universität, Frankfurt am Main
Prof. Dr. U. CHRISTENSEN	Max-Planck-Institut für Sonnensystemforschung, Katlenburg-Lindau
Prof. Dr. R. GROSS (Vice Chairman)	Walther-Meißner-Institut für Tieftemperatur-forschung (WMI), Garching
Prof. Dr. R. KNIEP	Emeritus, Max-Planck-Institut für Chemische Physik fester Stoffe, Dresden
Prof. Dr. H. PALME	Emeritus, Institut für Mineralogie und Geochemie der Universität zu Köln – Senckenberg Forschungsinstitut und Naturmuseum Frankfurt/M.
Prof. Dr. M. RIEDERER (Chairman)	Julius-von-Sachs-Institut für Biowissenschaften, Würzburg
Prof. Dr. E. SALJE, FRS, FRSA	Department of Earth Sciences, University of Cambridge
Prof. Dr. H. SOFFEL	Emeritus, Institut für Allgemeine und Angewandte Geophysik der Universität München

The Advisory Board held a meeting in Bayreuth (29.04.2016).

1.2 Leadership

Prof. Dr. Dan FROST (Director)
Prof. Dr. Tomoo KATSURA (Deputy Director)
Prof. Dr. Hans KEPPLER

2. Staff, Funding and Facilities

2.1 Staff

At the end of 2016 the following staff positions existed in the Institute:

- Scientific staff: **13**
- Technical staff: **14**
- Administrative staff: **3**
- Administrative officer: **1**

During 2016, 47 scientific positions (392 months) were funded by grants raised externally by staff members of the institute. In addition 4 long-term scientific positions (43 months) were funded by the resources of the BGI Visiting Scientists' Programme (see Sect. 7) which also supported short-term visits for discussing future projects or presenting research results (see Sect. 5). 12 student assistants (89 months) were funded by externally raised grants. 10 scientists (81 months) were supported by personal grants (stipends).

2.2 Funding

In 2016, the following financial resources were available from the Free State of Bavaria:

- Visiting Scientists' Programme: 216.000 €
- Consumables: 559.000 €
- Investment funding: 40.000 €
- Special funding (Free State of Bavaria/University of Bayreuth 152.000 €

The total amount of national/international external funding (*"Drittmittel"*) used for ongoing research projects in 2016 was 3.037.000 € (Positions: 1.866.000 €; equipment, consumables and travel grants: 1.171.000 €).

	positions	**equipment, consumables, travel grants**	**total**
• AvH	86.000 €	45.000 €	131.000 €
• BMBF	97.000 €	234.000 €	331.000 €
• DFG	1.334.000 €	643.000 €	1.977.000 €
• EU	245.000 €	93.000 €	338.000 €
• Others	104.000 €	156.000 €	260.000 €
			3.037.000€

(AvH = Alexander von Humboldt Foundation; BMBF = Federal Ministry of Education and Research; DFG = German Science Foundation; EU = European Union; Others: DAAD, Chinese Science Council, Japanese Society for the Promotion of Science, German-Israeli Foundation for Scientific Research and Development)

In the following list only the BGI components of the funding is listed in cases where joint projects involved other research institutions. Principal investigators and the duration of the grants are listed in brackets. Total project funding refers to the funding over the entire duration of this project.

Funding institution	Project, Funding	Total Project Funding
BAdW	Bavarian Academy of Sciences research project (H. Marquardt)	36.000 €
BMBF	056K13WC4 (L.S. Dubrovinsky – 7.13-6.16) "NANORES: Nanofokussierende Röntgenoptiken und Probenumgebungen für die resonante Kernstreuung zum Studium von schnellen Prozessen in Chemie, Biologie und in Materie unter extremen Bedingungen" Total funding:	475.300 €
BMBF	KEI0500009612 (T. Katsura – 7.13-6.16) "Aufbau einer experimentellen Station mit einer großvolumigen Hochdruckapparatur an der Damping-Wiggler-Beamline des Deutschen Elektronen Synchrotron (DESY)" Total funding:	1.186.000 €
BMBF	05K16WC2 (T. Katsura – 7.16-6.19) "Erweiterung der Druckbereiche der In-Situ-Röntgen-beobachtung mit der Großvolumen-Hochdruckapparatur an der PETRA-III-Extension des Deutschen Elektronen-Synchrotrons DESY" Total funding:	543.478 €
BMBF	05K13WC1 (H. Keppler – 7.13-6.16) "Aufbau einer Hochdruckpresse vom Multi-Anvil-Typ an der Forschungs-Neutronenquelle FRM II in Garching" Total funding:	3.499.590 €
BMBF	05K16WCA (H. Keppler – 7.16-6.19) "Aufbau einer Hochdruckpresse vom Multi-Anvil-Typ an der Forschungs-Neutronenquelle FRM II in Garching" Total funding:	410.278 €
DFG	AU 314/5-1 (A. Audétat – 10.14-9.17) "Development of new oxybarometers for silicic magmas" Position: E13/2, 36 months 90.900 € student assistant 5.000 € Consumables: 35.000 € Overhead: 26.100 €	157.000 €
DFG	BO 2550/7-1 (T. Boffa Ballaran, A. Woodland – 8.13-7.16) "Crystal chemistry of ferric iron in the deep upper mantle and transition zone" Position: student assistant 5.000 € Consumables and travel funding: 9.500 € Overhead: 2.900 €	17.400 €

DFG	BO 2550/8-1 (T. Boffa Ballaran – 9.14-8.16) DFG SPP 1385 'The first 10 Million Years of the Solar System – a Planetary Materials Approach' "Der Einfluss von Mantel Rheologie auf die frühe Differenzierung eisiger Satelliten" Positions: E 13, 24 months 127.200 € student assistant 10.000 € Consumables: 12.285 € Equipment: 27.216 € Overhead: 35.300 €	212.001 €
DFG	DU 393/9-1 (L.S. Dubrovinsky – 1.15-12.17) DFG TP 7 'Chemische Reaktionen zwischen Karbonaten und pyrolitischem Erdmantel und Entstehung ultratiefer Diamanten' "Structures, properties and reactions of carbonates at high temperatures and pressures" Position: E 13 (66 %), 36 months 120.600 € Consumables: 32.250 € Overhead: 30.600 €	183.450 €
DFG	DU 393/10-1 (L.S. Dubrovinsky, C.A. McCammon – 8.15-7.17) DFG SPP 1833 'Building a Habitable Earth' "Leichte Elemente im Kern einer bewohnbaren Erde" Position: E 13, 36 months 206.700 € Consumables: 20.250 € Overhead: 45.400 €	272.350 €
DFG	FR 1555/9-1 (D.J. Frost – 2.15-1.16) "Die Phasenbeziehungen mafischer Gesteine im Erdmantel und Geo-Barometer für Eklogit und Pyroxenit bis zu den Bedingungen der Mantel-Übergangszone" Position: E 13 (75 %), 12 months 44.500 € Overhead: 8.900 €	53.400 €
DFG	FR 1555/10-1 (D.J. Frost – 8.15-7.18) DFG SPP 1833 'Building a Habitable Earth' "Die Ermittlung des Mechanismus der frühzeitigen Oxidation des Erdinneren" Position: E 13 (75 %), 36 months 143.600 € Consumables: 22.250 € Overhead: 33.200 €	199.050 €
DFG	FR 1555/11-1 (D.J. Frost – 3.16-2.23) Gottfried Wilhelm Leibniz-Preis 2016	2.500.000 €
DFG	GRK 2156/1 (D.J. Frost, et al. – 4.16-10.20) Internationales Graduiertenkolleg "Deep Earth Volatile Cycles"	3.257.358 €
DFG	HE 3285/2-1 (F. Heidelbach – 4.13-3.16) "Reaction kinetics and plastic deformation in mantle rocks" 1 position: 36 months 188.900 € Consumables and travel funding: 21.500 € Overhead: 42.100 €	252.500 €

DFG	KA 3434/3 (T. Katsura – 4.13-3.16) "Dislocation recovery experiment of hydrous olivine as a function of water content and crystallographic orientation" 1 position: E 13, 36 months 196.200 € Consumables and travel funding: 20.000 € Overhead: 43.000 €	249.300 €
DFG	KA 3434/7-1 (T. Katsura – 6.14-5.17) "Messung der Korngrenzendiffusion von Forsterit in Abhängigkeit des Wassergehalts" 1 position: E 13, 36 months 196.200 € student assistant 5.000 € Consumables and travel funding: 20.388 € Overhead: 31.700 €	253.288 €
DFG	KA 3434/8-1 (T. Katsura – 4.15-3.18) "Bestimmung des Drei-Phasen-Stabiliätsfelds des Post-spinell-Übergangs in $(Mg,Fe)_2SiO_4$: Erörterung der extremen Schärfe der 660-km-Diskontinuität und deren Bedeutung für die chemische Struktur und die Dynamik des tiefen Erd-mantels" 1 position: E 13, 36 months 196.200 € student assistant 5.000 € Consumables and travel funding: 16.000 € Overhead: 43.300 €	260.500 €
DFG	KA 3434/9-1 (T. Katsura – 9.15-8.18) "Messung von Si-Selbstdiffusionskoeffizienten in Wadsleyit als Funktion des Wassergehaltes" 1 position: E 13, 36 months 196.200 € student assistant 5.000 € Consumables and travel funding: 45.750 € Overhead: 49.500 €	296.450 €
DFG	KE 501/10-1 (H. Keppler – 7.13-6.16) "DFG Core Facility: High-pressure laboratories of Bayerisches Geoinstitut" Total funding:	544.600 €
DFG	KE 501/11-1 (H. Keppler – 2013-2017) "Electrical conductivity and dissociation of fluids in crust and mantle" Total funding:	267.800 €
DFG	KE 501/8-2 (H. Keppler – 2014-2017) "In-situ observation of the crystallization kinetics and texture evolution of basalts" Total funding:	174.000 €
DFG	KE 501/13-1 (H. Keppler – 2016-2018) "Nitrogen in the deep mantle" Total funding:	214.669 €
DFG	KO 3958/2-1 (N. de Koker, G. Steinle-Neumann – 2.11-3.16) DFG SPP 1488 (PlanetMag) "Thermal and electrical conductivity of iron at planetary core conditions from ab initio computations" Positions: E 13, 36 months 186.300 € student assistant (79 h/month) 12 months 7.965 € Consumables and travel funding: 9.000 € Publication costs: 2.250 € Overhead: 41.100 €	246.615 €

DFG	MA 4534/4-1 (H. Marquardt – 9.15-8.18) "Deformationsexperimente an (Mg,Fe)O Ferroperiklas bei hohen Drücken und gleichzeitig hohen Temperaturen" Positions: E13 2/3, 36 months: 123.000 € Consumables: 33.850 € Overhead: 31.400 €	188.250 €
DFG	MA 6287/2-1 (K. Marquardt – 11.14-7.16) "Korngrenzcharakterverteilung in Olivin" Travel funding: 7.800 € Overhead: 1.600 €	9.400 €
DFG	MA 6287/3-1 (K. Marquardt, R. Dohmen – 9.15-8.18) "Elementverteilung in Geomaterial-Korngrenzen unter Berücksichtigung ihrer Geometrie" Positions: E13 2/3, 36 months: 123.000 € student assistant 2.500 € Consumables: 26.445 € Overhead: 30.400 €	182.345 €
DFG	MA 6287/5-1 (S. Chakraborty, K. Marquardt, T. Fockenberg – 10.16-9.19) "Experimentelle Kalibrierung von Granat-Pyroxen Diffusionschronometrie für Anwendungen in terrestrische und planetare Proben" Positions: student assistant 5.000 € Consumables: 5.000 € Overhead: 2.200 €	12.200 €
DFG	MA 6287/6-1 (K. Marquardt – 11.16-10.19) "Änderungen der Korngrenzcharakterverteilung in Olivin-dominierten Gesteinen als Funktion des Chemismus" Positions: E13 75 %, 36 months: 147.000 € student assistant 5.000 € Consumables, global funding: 45.030 € Overhead: 43.300 €	240.330 €
DFG	MC 3/18-1 (C.A. McCammon, L.S. Dubrovinsky, D.J. Frost – 7.13-6.17) "The effect of pressure, temperature and oxygen fugacity on the stability of subducted carbonates and implications for the deep carbon cycle" Positions: E 13/2, 36 months 88.000 € student assistant 5.000 € Equipment, consumables and travel funding: 31.650 € Overhead: 24.900 €	149.550 €
DFG	MC 3/19-2 (C.A. McCammon, S. Gilder – 9.13-8.17) DFG SPP 1488 (PlanetMag) "How pressure influences the magnetic properties of titanomagnetite and iron with implications for magnetic anomalies and core fields" Equipment, consumables and travel funding: 6.400 € Overhead: 1.300 €	7.700 €

DFG	MC 3/20-1 (C.A. McCammon – 10.15-9.18) DFG FOR 2125 (CarboPaT) "Elastic properties of carbonates at high pressure and high temperature" Positions: E13 2/3, 36 months: 123.000 € Equipment, consumables and travel funding: 32.250 € Overhead: 30.600 €	185.850 €
DFG	OV 110/1-3 (S.V. Ovsyannikov – 9.15-8.17) "Structural and electronic properties of sesquioxides at high pressures and temperatures: new forms, new insights and new possible applications" Positions: E 13, 24 months 136.600 € Consumables and travel funding: 20.000 € Overhead: 31.300 €	187.900 €
DFG	PE 2334/1-1 (S. Petitgirard – 10.15-9.17) DFG SPP 1833 'Building a Habitable Earth' "Dichte und Verbleib von Silikatschmelzen im frühen Erdmantel" Positions: E 13, 36 months 206.700 € student assistant 5.000 € Consumables: 42.750 € Overhead: 50.900 €	305.350 €
DFG	RU 1323/2-2 (D.C. Rubie, D.J. Frost, H. Palme – 6.12-5.16) DFG SPP 1385 'The first 10 Million Years of the Solar System – a Planetary Materials Approach' "Conditions, timescales and cosmochemical evolution during the early accretion of terrestrial planets" Positions: E 13/2, 24 months 56.500 € Consumables and travel funding: 40.000 € Publication costs: 1.500 € Overhead: 19.600 €	117.600 €
DFG	RU 1323/9-1 (D.C. Rubie – 3.14-2.16) DFG SPP 1385 'The first 10 Million Years of the Solar System – a Planetary Materials Approach' "Chemische Entwicklung der Metallkerne von Kleinplaneten in der Frühgeschichte des Sonnensystems" Positions: E 13 (75 %), 24 months 88.000 € student assistant 10.000 € Consumables and travel funding: 20.572 € Overhead: 23.700 €	142.272 €
DFG	STE 1105/10-1 (G. Steinle-Neumann – 4.14-3.17) DFG SPP 1488 (PlanetMag) "Structure and electronic transport properties of metallic liquids at conditions of planetary cores" Positions: E 13, 24 months 125.500 € student assistant 18.798 € Consumables: 9.820 € Overhead: 30.800 €	184.918 €

DFG	STE 1105/12-1 (G. Steinle-Neumann, N. Tosi – 4.16-3.19) DFG SPP 1833 'Building a Habitable Earth' "Kristallisation des irdischen Magmaozeans: Thermo- und Geodynamik" Positions: E13 (75%), 36 months 143.600 € student assistant 5.000 € Consumables: 8.250 € Overhead: 31.400 €	188.250 €
DFG	Emmy Noether-Programm (H. Marquardt – 2014-2019) "Structure and Elasticity of GeoMaterials at Extreme Conditions (GeoMaX)" Positions: group leader, E14/E15, 60 months: 375.400 € post doc, E13, 60 months: 317.200 € 2 PhD students, 2/3 E13, 36 months: 264.400 € student assistant: 11.904 € Consumables, travel funding: 222.550 € Investments: 127.714 € Overhead: 184.400 €	1.503.568 €
EU	European Research Council (ERC) Advanced Grant No. 290568 (D.C. Rubie – 5.12-4.17) "Accretion and Early Differentiation of the Earth and Terrestrial Planets" ("ACCRETE") Positions, consumables and travel funding:	1.826.200 €
Minerva Foun-dation	Minerva Followship for completion of Ph.D. work with Prof. Daer at the Hebrew University of Jerusalem, Israel (V. Vlček – 1.16-6.16) Budget:	9.000 €

2.3 Laboratory and office facilities

The institute occupies an area of

ca. 1350 m^2 laboratory space
ca. 480 m^2 infrastructural areas (machine shops, computer facilities, seminar room, library)
ca. 460 m^2 office space
in a building which was completed in 1994.

2.4 Experimental and analytical equipment

The following major equipment is available at the Bayerisches Geoinstitut:

I. High-pressure apparatus
- 15 MN/1500 tonne Kawai-type multianvil high-pressure apparatus (40 GPa, 2000 K)
- 6 x 8 MN/6x800 tonne independently acting-anvil press (25 GPa, 3000 K)
- 50 MN/5000 tonne multianvil press (25 GPa, 3000 K)
- 12 MN/1200 tonne multianvil press (25 GPa, 3000 K)
- 10 MN/1000 tonne multianvil press (25 GPa, 3000 K)
- 5 MN/500 tonne multianvil press (20 GPa, 3000 K)
- 5 MN/500 tonne press with a deformation DIA apparatus
- 4 piston-cylinder presses (4 GPa, 2100 K)
- Cold-seal vessels (700 MPa, 1100 K, H_2O), TZM vessels (300 MPa, 1400 K, gas), rapid-quench device
- Internally-heated autoclave (1 GPa, 1600 K)
- High-pressure gas loading apparatus for DAC

II. Structural and chemical analysis
- 1 X-ray powder diffractometer
- 1 X-ray powder micro-diffractometer
- 1 X-ray powder diffractometer with furnace and cryostat
- 2 automated single-crystal X-ray diffractometers
- High-brilliance X-ray system
- Single crystal X-ray diffraction with super-bright source
- 1 Mössbauer spectrometer (1.5 - 1300 K)
- 3 Mössbauer microspectrometers
- 2 FTIR spectrometers with IR microscope
- FEG transmission electron microscope (TEM), 200 kV analytical, with EDS and PEELS
- FEG scanning TEM, 80-200 kV analytical, with 4-SDDs EDS and post-column energy filter (EFTEM/EELS)
- FEG scanning electron microscope (SEM) with BSE detector, EDS, EBSD and CL
- Dual beam device, focused ion beam (FIB) and FEG SEM. In situ easy-lift manipulator, STEM and EDS detector, and beam deceleration option
- 3 Micro-Raman spectrometers with ultraviolet and visible lasers
- Tandem-multipass Fabry-Perot interferometer for Brillouin scattering spectroscopy
- JEOL JXA-8200 electron microprobe; fully-automated with 14 crystals, 5 spectrometer configuration, EDX, capability for light elements
- 193 nm Excimer Laser-Ablation ICP-MS
- ICP-AES sequential spectrometer
- Water content determination by Karl-Fischer titration
- GC/MS-MS for organic analyses
- Confocal 3D surface measurement system

III. *In situ* determination of properties

Diamond anvil cells for powder and single crystal X-ray diffraction, Mössbauer, IR, Raman, optical spectroscopy, electrical resistivity measurements up to at least 100 GPa

Facility for in situ hydrothermal studies in DAC

Externally heated DACs for in situ studies at pressures to 100 GPa and 1200 K

1-atm furnaces to 1950 K, gas mixing to 1600 K, zirconia fO_2 probes

1-atm high-temperature creep apparatus

Gigahertz ultrasonic interferometer with interface to resistance-heated diamond-anvil cells

Heating stage for fluid inclusion studies

Impedance/gain-phase analyser for electrical conductivity studies

Apparatus for in situ measurements of thermal diffusivity at high P and T

Laser-heating facility for DAC

Portable laser heating system for DAC

The Geoinstitut is provided with well equipped machine shops, an electronic workshop and sample preparation laboratories. It has also access to the university computer centre.

3. Forschungsprojekte

3.1 Struktur und Dynamik der Erde und Planeten

Die terrestrischen Planeten im Sonnensystem bildeten sich über einen Zeitraum von etwa 100 Millionen Jahren. Zuerst kollidierten sogenannte Planetesimale untereinander, in späteren Stadien der Akkretion kam es zu Zusammenstößen von mehrere tausend Kilometer messenden planetaren Embryos mit verbleibenden Planetesimalen und untereinander. Durch die Freisetzung kinetischer Energie und den Zerfall kurzlebiger radioaktiver Isotope wurden die wachsenden Körper zumindest teilweise aufgeschmolzen, was zur Bildung eines Magmaozeans führte und die Entstehung eines dichten Eisenkerns erleichterte. Bei der letzten großen Kollision der Proto-Erde mit einem etwa Mars-großen Körper formte sich eine heiße Scheibe, aus welcher der anfangs aufgeschmolzene Erdmond hervorging.

Der erste Beitrag beschäftigt sich mit Planetesimalen, den ersten Bausteinen der Planeten, die in der protoplanetaren Scheibe entstanden sind. Moderne astrophysikalische Modelle deuten darauf hin, dass diese wenige Dutzend bis Hundert Kilometer großen Körper innerhalb kurzer Zeit durch Gravitationskollaps in der aus Mikro- bis Millimeter großen Partikeln bestehenden Scheibe entstanden. Die Studie beschäftigt sich mit der frühen Entwicklung eines dieser Körper, nämlich dem Ursprungskörper der seltenen Meteoritengruppe der Angriten. Geochemische Studien zeigten, dass trotz einer Magmaozeanphase zu Beginn der Entwicklung dieses Körpers, die zu sehr effizienter Durchmischung führte, dennoch frühzeitig geochemische Reservoire entstanden sind. Mittels 2D und 3D-Modellen wurde untersucht, unter welchen Bedingungen sich im Inneren des Körpers dennoch geochemische Reservoire bilden konnten. Die numerischen Resultate zeigen, dass die Reservoire während der finalen Kristallisation des Magmaozeans in einem genügend kleinen Ursprungskörper gebildet werden konnten und langfristig stabil sind.

Die zweite Studie widmet sich der Phase der Planetenentstehung, in der planetare Embryos miteinander kollidierten, um größere Körper zu bilden. Hierfür wurden dreidimensionale SPH-Modelle (SPH = *smoothed particle hydrodynamics*) mit geodynamischen 3D-Modellen kombiniert, um sowohl die Kollision als auch die längerfristige Entwicklung des Zielkörpers zu modellieren. Dies bietet die Möglichkeit, die Einschränkungen sowohl der SPH-Modelle, nämlich, dass nur wenige Tage nach der Kollision modelliert werden können, als auch die geodynamischer Modelle, dass nur vertikale Einschläge mittels Parametrisierung simuliert werden können, zu beseitigen. Zu diesem Zweck wird das Endresultat einer spezifischen SPH-Simulation als Anfangsbedingung für das geodynamische Modell genutzt. In ausführlichen Berechnungen wurde ermittelt, wann nach der Kollision der Datentransfer durchgeführt werden kann, ohne dass mit der Zeit weiterhin zurückfallendes Auswurfmaterial die längerfristige thermomechanische Entwicklung des Körpers beeinflusst.

Wie bereits erwähnt, war das Innere des Mondes zu Beginn aufgeschmolzen. Die dritte Studie beschäftigt sich mit der möglichen Existenz einer heutzutage geschmolzenen Schicht im

untersten Mondmantel, deren Existenz nach der Neuauswertung von seismischen Daten vor einigen Jahren vorgeschlagen wurde. Basierend auf Kristallisationsmodellen für den lunaren Magmaozean wurde Eisen- und Titan-reiches Material angenommen, das nach seiner späten Kristallisation zur Kern-Mantel-Grenze absank und dort wieder aufgeheizt wurde. In dieser Studie soll geklärt werden, ob unter den heutigen Druck- und Temperaturbedingungen im untersten Mondmantel dieses Material sowohl geschmolzen als auch dichter sein kann als der restliche Mantel, um seine Stabilität an der Kern-Mantel-Grenze zu erklären.

Die vierte Studie beschäftigt sich mit der inneren Struktur des Mondes der Erde. Hierfür wurde ein 1D Modell des Mondinneren entwickelt, welches geophysikalische, geochemische und mineralogische Daten kombiniert. Unter Annahme verschiedener Temperaturprofile und wahlweise eines homogenen oder geschichteten Mondmantels wurde mittels der Modelle ein großer Parameterraum abgedeckt, in dem verschiedene Parameter, wie zum Beispiel die Schichtdicken, variiert wurden. Es zeigte sich, dass dieses kombinierte Modell es ermöglicht, den Radius des Mondkerns, der bislang nur ungenau bekannt war, deutlich einzugrenzen.

Im heutigen Asteroidengürtel und in irdischen Meteoritensammlungen ist Olivin-reiches Material, verglichen mit der Anzahl an metallischen Asteroiden und Eisenmeteoriten, sehr selten. Im fünften Beitrag wird diskutiert, ob es sich bei Olivin-reichen Asteroiden, statt um Überbleibsel zerstörter Körper, um Material von den terrestrischen Planeten handeln kann. Wie bereits erwähnt, kam es während der späteren Phase der Akkretion terrestrischer Planeten zu massiven Kollisionen. Die Kollisionen produzierten für gewöhnlich erhebliche Mengen an Auswurfmaterial, das nicht akkretiert wurde und in einigen Fällen durch Störungen auf eine neue heliozentrische Bahn umgelenkt wurde. Die vorliegende Studie zeigt, dass das Volumenverhältnis zwischen Eisen-, Mantel- und Krustenmaterial, das im heutigen Asteroidengürtel beobachtet werden kann, deutlich besser mit den Verhältnissen in der Erde oder dem Mars übereinstimmt, als mit Ergebnissen von intakten differenzierten Objekten im Asteroidengürtel, wie dem Asteroiden Vesta.

Nach dem Ende der Akkretion kühlten die terrestrischen Planeten ab und entwickelten an ihrer Oberfläche eine thermische Grenzschicht, genannt Lithosphäre. Wegen der niedrigen Temperatur an der heutigen Erdoberfläche wird erwartet, dass in der Lithosphäre Elastizität ein wichtiger Parameter ist und zusammen mit der Topographie den Spannungszustand in dieser Schicht merklich beeinflusst. Während die Bedeutung der Topographie in den letzten Jahren erkannt wurde und mittels einer weichen Oberflächenschicht, der sogenannten „*sticky air*“ mit berücksichtigt wird, wird Elastizität bislang in den meisten Modellen zur Mantelkonvektion ignoriert. In der vorliegenden Studie wurden nun sowohl Topographie als auch Elastizität mit berücksichtigt. Hierbei wurden ein Finite-Element-Code mit freier Oberfläche und ein Finite-Differenzen-Code mit einer weichen Oberflächenschicht („*sticky air*“) gegeneinander getestet. Die gute Übereinstimmung der Resultate zeigt, dass die „*sticky air*“-Methode mit der Berücksichtigung der Elastizität kompatibel ist.

Die Lokalisierung von Deformationsprozessen in der Lithosphäre ist von großer Bedeutung für die Zuordnung geologischer Prozesse auf der Erde, wie der Entstehung neuer Plattengrenzen. Frühere Studien unter Verwendung vereinfachter Rheologie zeigten, dass das Wechselspiel von Korngrößenreduzierung und Reibungshitze die notwendige Spannung verringert, um thermisches Durchgehen („*thermal runaway*“) zu ermöglichen. Der abschließende Beitrag dieses Kapitels zeigt auf, dass der Einfluss weiterer Deformationsarten, wie der des Peierls-Mechanismus, ebenfalls mit berücksichtigt werden muss, da dieser die Effizienz von Reibungshitze reduziert und es somit erschwert, thermisches Durchgehen zu erreichen.

3.2 Geochemie

Die in diesem Kapitel beschriebenen Forschungsprojekte umfassen Themen von der Kern-Mantel-Differenzierung bis zu magmatischen und hydrothermalen Prozessen nahe der Erdoberfläche. Eines der gemeinsamen Themen in den Untersuchungen über Prozesse in der tiefen Erde ist das Element Eisen. Eisen führte nicht nur zur geochemischen Differenzierung von Planeten und Planetesimalen im Verlauf der Kernbildung, sondern es kontrolliert auch den Oxidationszustand des Erdmantels durch seine Wertigkeit in Mineralen und möglicherweise in Schmelzen. Die Mehrzahl der übrigen Untersuchungen ist überwiegend Erzlagerstätten gewidmet – einerseits durch direkte Untersuchungen über das Verhalten von Metallen, andererseits durch Methodenentwicklung zur Bestimmung von Druck, Temperatur oder Bedingungen der Sauerstofffugazität (fO_2) bei der Magmenkristallisation.

Die ersten fünf Beiträge des Kapitels beschreiben Phasenbeziehungen und Elementdiffusion in Fe-reichen Flüssigkeiten sowie Elementverteilungen zwischen Fe-reichen Lösungen und Silikatschmelzen. Zwei Beiträge befassen sich thematisch mit der Erde, zwei mit kleineren terrestrischen Planeten, ein Betrag mit beiden Bereichen. Jennings *et al.* untersuchen das Verhalten von Si, O, Mg, W und Mo bei der Metall-Silikat-Verteilung unter extremen Bedingungen, um die Natur und Häufigkeit leichter Elemente im Erdkern einzugrenzen und die Ursache des W-Defizits im Erdmantel zu identifizieren. Es wird bestätigt, dass Si und O in angemessener Weise in die Eisenschmelze abwandern, so dass beide Elemente wahrscheinlich im Erdkern präsent sind. Die verfügbaren W-Verteilungskoeffizienten wurden ebenfalls umfassend zusammengestellt, um den Einfluss von P, T und fO_2 enger einzugrenzen. Die Untersuchungen von Laurenz *et al.* konzentrieren sich auf das Verhalten sehr siderophiler Elemente bei der Abtrennung junger Sulfidschmelzen in den Erdkern. Die Ergebnisse lassen vermuten, dass die Sulfidabscheidung, gefolgt von der sogenannten ´Late Veneer` Akkretion , mit den globalen chondritischen Re-Os-Verhältnissen im Erdmantel kompatibel ist. Die Beiträge von Rubie *et al.* und Pommier *et al.* handeln beide von Prozessen, die in terrestischen Planeten ablaufen, die kleiner als die Erde sind. Rubie *et al.* fanden heraus, dass der extrem niedrige Si-Gehalt in Eisenmeteoriten durch kleiner werdende Verteilungskoeffizienten für Si-Metall/Silikatschmelze bei zunehmenden oxidierenden

Bedingungen, wie sie in den äußeren Regionen des Sonnensystems vorherrschen, erklärt werden kann. Pommier *et al.* belegen Phasenbeziehungen in Systemen unter Bedingungen, wie sie in kleineren terrestrischen Planeten herrschen, um das mögliche Vorhandensein leichter Elemente in ihren Kernen zu untersuchen und herauszufinden, wie diese die Dynamik der Planeten beeinflussen könnten. Sie entdeckten, dass sich eventuell eine stabile Schicht aus FeO in einigen dieser Planetesimale gebildet hat. Posner *et al.* entwickelten ein Modell für die Si-, O- und Cr-Diffusion in Eisenschmelzen, mit dem Ziel, geodynamische Modelle planetarer Differenzierung zu verfeinern. Sie fanden heraus, dass Diffusionskoeffizienten als Maßstab für Schmelztemperaturen herangezogen werden können; daraus können genauere Zeit-integrierte Modelle zur planetaren Akkretion und Differenzierung erstellt werden.

Die folgenden vier Artikel betreffen die Stabilität Fe-haltiger Phasen und davon abhängiger Eisen-Wertigkeiten in den silikatischen Anteilen der Erde. Auf der Basis einer Reihe von fO_2-gepufferten Multianvil-Experimenten entdeckten Armstrong *et al.,* dass oberhalb von Drücken von ca. 15 GPa das $Fe^{3+}/\Sigma Fe$-Verhältnis in andesitischen Schmelzen mit zunehmendem Druck drastisch steigt. Das bedeutet, dass der gegenwärtige Gradient in der Sauerstofffugazität zwischen dem tiefen und dem flacheren Erdmantel schon in einem frühen Magmaozean bestanden haben muss. Woodland *et al.* fanden heraus, dass oberhalb eines Druckes von 10 GPa verschiedene Eisenverbindungen mit einer Stöchiometrie zwischen der von Fe_xO und Fe_3O_4 stabil sind und zwar Fe_5O_6 und $Ca_2Fe_2O_7$. Diese Phasen vergrößern die Komplexität bei der Kontrolle der Sauerstofffugazität im Erdmantel. In der nachfolgenden Untersuchung schlagen Siersch *et al.* vor, dreiwertiges Eisen einzubeziehen, um bei Bedingungen, die denen an der Basis der Übergangszone in ungefähr 600 km Tiefe entsprechen, das Stabilitätsfeld von Majorit-Granat auf Kosten von Akimotoit auszudehnen. Dies könnte allerdings in erster Linie ein experimentelles Phänomen sein, da typischerweise der Anteil an Eisen (III) im Erdmantel niedriger ist als in den Experimenten und sich daher dieser Effekt im Erdmantel nicht einstellt. Eisenverbindungen können möglicherweise auch eine Rolle im Kohlenstoff-Kreislauf in der tieferen Erde spielen. Auf den Ergebnissen von laserbeheizten Diamantstempel-Experimenten basierend argumentieren Serovaysky *et al.,* dass erhebliche Anteile an Kohlenstoff in den tiefen Erdmantel zurückgeführt werden können, indem in subduzierten Sedimenten eingeschlossene Kohlenstoffwasserstoffe mit Fe-führenden Gesteinen des Erdmantels zu Eisenkarbid reagieren.

Zwei folgende Artikel widmen sich Phänomenen der Diffusion. Polednia *et al.* quantifizieren Korngrenzen-Diffusion von Fe und La in Yttrium-Aluminium-Granat (YAG). Die Ergebnisse dienen in erster Linie dazu, die Fertigung und Leistungsfähigkeit polykristalliner YAG-Laser zu verbessern. Sie können auch für geowissenschaftliche Fragestellungen herangezogen werden, so zum Beispiel nach der Ursache der rätselhaften Metasomatose in Mantelgesteinen oder nach dem Einfluss von Korngrenzfilmen auf das Deformationsverhalten der Minerale. Audétat und Zhang fanden heraus, dass Kupfer extrem schnell durch gewöhnliche gesteinsbildende Minerale wie Plagioklas, Amphibol, Olivin, Klino- und Orthopyroxen und Apatit diffundieren kann, woraus sich Zweifel an dem Cu-Gehalt ergeben, der für Einschlüsse in Silikatschmelzen und ihren Wirtsmineralen genannt wird.

Die Thermobarometrie von felsischen Magmen der oberen Erdkruste ist Thema der folgenden zwei Beiträge. Arató und Audétat testeten ein neu entwickeltes Oxybarometer, das auf der Verteilung von Vanadium zwischen Magnetit und Silikatschmelze basiert. Dazu wurde eine große Anzahl natürlicher silikareicher Magmen einbezogen; die Ergebnisse stimmen gut mit denen überein, die aus der Fe-Ti-Oxid-Oxybarometrie gewonnen wurden. Zarei und Audétat führten ein Langzeit-Projekt zur Eichung eines Thermobarometers auf der Basis der Elementverteilung von Ge und Al zwischen Quarz und Silikatschmelze fort, um das bestehende Titan-in-Quarz-Thermobarometer zu verfeinern.

Guo und Audétat untersuchten die Goldlöslichkeit in oxidierten, schwefelführenden Fluiden. Sie erkannten, dass vorhandener, oxidierter Schwefel die Löslichkeit von Gold nicht fördert, dass aber die Goldextraktion durch magmatische Fluide unter oxidierenden Bedingungen, die typisch sind für das Milieu von porphyrischem Kupfer, recht effizient gewesen sein mag. Nicht zuletzt führten Zhang und Audétat detaillierte petrographische und mikroanalytische Untersuchungen an zwei porphyrischen Mo-Lagerstätten in den USA durch. Aus den Ergebnissen schlossen sie, dass die erzbringenden Magmen nicht besonders Mo-reich waren, dass aber die Metallextraktion und -anreicherung aufgrund niedriger Schmelzviskositäten ungewöhnlich effizient waren.

3.3 Mineralogie, Kristallchemie und Phasenübergänge

Mineralogische Untersuchungen an den wesentlichen Bausteinen der Erde spielen weiterhin eine große Rolle in unserem Bestreben, das Erdinnere und seine dynamischen Phänomene besser zu verstehen. Ein experimenteller Ansatz ist bei den Untersuchungen zur Kristallchemie des Mineralbestands sowie seiner Phasenstabilitäten und -übergänge unverzichtbar. Experimente sind dazu geeignet, Beziehungen zwischen den mikroskopischen Eigenschaften des untersuchten Materials und den makroskopischen Beobachtungen des Erdinneren herzustellen. In diesem Kapitel werden einige der neuesten Ergebnisse aus experimentellen Ansätzen dargestellt. Die Untersuchungen beinhalten Anwendungen und Entwicklungen der Hochdruck-Technologie und sehr genauer Messmethoden wie zum Beispiel Röntgenbeugung an Einkristallen, Brillouin-Streuung und Infrarot-Spektroskopie unter extremen Bedingungen, in Kombination mit modernster chemischer (*post mortem*) Analyse.

Eisen, der Hauptbestandteil des flüssigen äußeren und des festen inneren Erdkerns, ist weiterhin im Fokus der Forschung. Der martensitische Übergang des Eisens von der α-Phase zur ε-Phase wurde bei hohem Druck mit Hilfe der Einkristall-Röntgenbeugung untersucht. Weiterhin sind Effekte auf die elastischen Eigenschaften des Eisens in der Phase vor der Aufschmelzung von Bedeutung; man untersucht sie durch eine kombinierte Studie von Brillouin-Streuung und Röntgenbeugung an Argon als ein *fcc* Analogmaterial. Die elastischen Eigenschaften von Bridgmanit und Akimotoit, die zum Mineralbestand des unteren Mantels,

beziehungsweise der Übergangszone gehören, stehen ebenfalls im Rampenlicht der Forschung. $Mg_3Al_2Si_3O_{12}$ konnte als metastabiles Produkt in der Struktur des $LiNbO_3$-Typs verfeinert werden, das sich bei der retrograden Umwandlung aus der Perowskitstruktur bildete. Die Synthesen von qualitativ hochwertigen großen Einkristallen von OH-führenden Phasen lieferten Informationen über ihre Kristallchemie und ihr Kompressionsverhalten. Entdeckungen neuer Phasen von Eisenoxid und Mn-Karbonat offenbarten ein potentielles neues Wirtsmineral für dreiwertiges Eisen im Erdmantel sowie das Vorliegen von tetraedrischem Kohlenstoff im Karbonatgefüge.

Phasenstabilitäten von im unteren Erdmantel vorhandenen Mineralen und Mineralgesellschaften ermöglichen, Eigenschaften im mikroskopischen Bereich mit makroskopischen Beobachtungen zu verknüpfen und so die Deutung seismischer Diskontinuitäten im Bezug auf tiefreichende Kreisläufe volatiler Elemente einzugrenzen. Die Mächtigkeit der 660 Km-Diskontinuität steht in Beziehung zur Ausdehnung des Drei-Phasen-Feldes Ringwoodit + Bridgmanit + Ferroperiklas; ein neu entwickelter Aufbau einer Hochdruckzelle für *in situ* Röntgenbeugung verspricht deutlich präzisere Bestimmungen dieses Stabilitätsfeldes. Die Al_2O_3-Löslichkeit in Bridgmanit als Funktion des Drucks und der Temperatur ermöglicht eine genauere Eingrenzung der Subduktion von MORB (Mid Ocean Ridge Basalt) in den unteren Mantel. Ergebnisse einer Studie über Einkristalle aus Klinoferrosilit können mit metastabilem Pyroxen in „kalten“ Erdkrustenplatten in Zusammenhang gebracht werden. Ferroperiklas-Einschlüsse in Diamant können möglicherweise als ein Geobarometer für Diamanten aus großer Tiefe dienen und Phasenübergänge eisenführender Karbonate helfen bei der Bestimmung des Kohlenstoff-Kreislaufs im tiefen Erdinneren. In ähnlicher Weise liefern Kristallstrukturmessungen und spektroskopische Bestimmungen der Phase E sowie von OH in Rutil Informationen über den tiefen Wasser-Kreislauf.

3.4 Physikalische Eigenschaften von Mineralen

Durch die systematische Verbesserung unseres Kenntnisstandes über die physikalischen Eigenschaften von Mineralen und Gesteinen unter Druck- und Temperaturbedingungen, die im tiefen Erdinneren herrschen, gelingt es uns immer besser, geophysikalische Messgrößen wie zum Beispiel Geschwindigkeiten seismischer Wellen oder elektrische Leitfähigkeiten mit der Struktur und Zusammensetzung der Erde in Beziehung zu setzen. Dieses quantitative Verständnis ist auch ein Schlüssel für die Verfeinerung großmaßstäblicher Modellierungen, die darauf zielen, die dynamische Entwicklung unseres Planeten zu simulieren.

Der erste Beitrag dieses Kapitels zielt darauf, die Ursache hoher elektrischer Leitfähigkeit in 70-120 km Tiefe unter jungen ozeanischen Platten zu identifizieren, die durch magneto-tellurische Messungen gefunden wird. Die gemessene Leitfähigkeit ist größer als man für wasserfreien Olivin erwarten würde und kann auch nicht mit Protonenmigration in

wasserhaltigem Olivin erklärt werden. In dieser Studie wurde die Diffusionsrate von Mg (D_{Mg}), die ein Maß für die erwartete elektrische Leitfähigkeit darstellt, in Abhängigkeit von Druck, Temperatur und Wassergehalt bestimmt. Die Ergebnisse deuten darauf hin, dass die unter jungen Ozeanplatten beobachtete hohe Leitfähigkeit mit einem durch Wasser begünstigten Ionen-Leitvermögen erklärt werden kann, das auf der Migration von Mg-Leerstellen beruht.

Im zweiten Beitrag wird dargestellt, wie zwei Wadsleyit-Kristalle mit unterschiedlicher kristallographischer Orientierung zusammen in eine Diamantstempelzelle geladen wurden, um den möglichen Effekt einer ungleichförmigen Spannung auf ihr Kompressionsverhalten zu bestimmen. Beide Kristalle zeigen bis zu dem in dieser Studie erreichten Maximaldruck eine identische Kompressibilität. Daraus ist zu schließen, dass sie in der Diamantstempelzelle einem einheitlichen Stressfeld ausgesetzt waren.

Die folgenden fünf Artikel sind auf die Bestimmung der elastischen Wellengeschwindigkeiten verschiedener Minerale des Erdmantels ausgerichtet, um seismologische Messergebnisse für den Mantel zu interpretieren. Die ersten drei dieser Beiträge zeigen, wie das gleichzeitige Laden einer DAC mit mehreren Kristallen unterschiedlicher kristallographischer Orientierungen ein wertvolles Hilfsmittel für die Eingrenzung des Effekts des Kationenaustauschs auf die elastischen Eigenschaften der Endglieder einer Mineralreihe ist. Die orientierten Proben wurden mit Hilfe eines fokussierten Ionenstrahls (FIB) präpariert. Der Vorteil dieser Methode liegt darin, dass Messergebnisse aus der Brillouin-Spektroskopie und Röntgenbeugung an allen Proben unter exakt den gleichen Druck- und Temperatur- Bedingungen gewonnen werden können. Auf diese Weise kann der elastische Tensor von niedrigsymmetrischen Materialien mit hoher Präzision, wie im Fall Wadsleyit und Bridgmanit (dritter und vierter Beitrag), bestimmt werden. Für diese beiden Minerale wurde der Effekt des Fe-Einbaus und der gekoppelten Fe/Al-Substitution sehr genau bestimmt. Der fünfte Beitrag beschreibt, wie die gleichzeitige Messung an vier Kristallen dazu dient, kleine Elastizitäts-Veränderungen durch den Einbau von „Wasser“ und Eisen in Ringwoodit zu bestimmen.

Im Fall von undurchsichtigen Proben können Schallwellengeschwindigkeiten mit der Methode der inelastischen Kernstreuung bestimmt werden. Der sechste Beitrag dieses Kapitels beschreibt den Einsatz dieser Technik, um den Einfluss der Skiagit-Komponente ($Fe^{2+}_3Fe^{3+}_2Si_4O_{12}$) auf die Wellengeschwindigkeiten von Granat zu bestimmen. Diese Messungen sind von Bedeutung, weil Granate in Diamanteinschlüssen hohe Fe^{3+}-Gehalte aufweisen, wie vorherige Studien gezeigt haben. Dieselbe Methode wurde im siebten Beitrag benutzt, um zu zeigen, dass die Substitution von Fe in Magnesit die seismischen Wellengeschwindigkeiten dieses Karbonatminerals verringert, obwohl dieser Effekt bei hohen Drücken, wo Fe im niedrigem Spin-Zustand vorliegt, weniger ausgeprägt ist.

Elastizitätsmessungen unter Bedingungen des unteren Erdmantels sind immer noch eine Herausforderung, aber die Verknüpfung theoretischer Berechnungen mit Experimenten kann

zu belastbareren Ergebnissen führen und kann weiterhin experimentelle Unzulänglichkeiten identifizieren. Das wird sehr gut in dem achten Beitrag demonstriert, in dem Berechnungen nach der Dichtefunktionaltheorie verwendet wurden, um aktuelle Ergebnisse der inelastischen Kernstreuung in eisenreichem Post-Perowskit nachvollziehen zu können. Die Berechnungen deuten darauf hin, dass die in der Literatur angegebenen Geschwindigkeitsergebnisse aufgrund von experimentellen Artefakten zu niedrig sind.

Gläser werden oft als Ersatz herangezogen, um das Verhalten von Schmelzen, die im Erdmantel vorhanden sein können, zu beschreiben. Die Dichte von SiO_2-Glas ist bis zu einem Druck von 90 GPa mit der Röntgenabsorptionsmethode in der Diamantstempelzelle bestimmt worden. Der neunte Artikel präsentiert Ergebnisse, aus denen hervorgeht, dass die Dichten von SiO_2 und $MgSiO_3$ bei hohen Drücken bei Raumtemperatur identisch sind und entlang einer 4000 K-Isotherme um weniger als 1 % differieren. Daher spielt der Kieselsäuregehalt einer Schmelze für die Beurteilung ihrer Auftriebskräfte unter Bedingungen des untersten Erdmantels lediglich eine sekundäre Rolle.

Zum Abschluss werden in diesem Kapitel Resultate aus Härte-Bestimmungen an verschiedenen Granat-Kristallen diskutiert. Proben von polykristallinem Granat in Edelsteinqualität wurden bei 18 GPa und 2100 K entlang der Majorit-Pyrop-Mischkristallreihe synthetisiert und mit Hilfe der Pulver-Röntgendiffraktometrie charakterisiert. Die Vickers-Härte wurde mit Eindrücktests bestimmt; sie scheint mit wachsendem Pyrop-Anteil zuzunehmen.

3.5 Fluide, Schmelzen und ihre Wechselwirkung mit Mineralen

Das wichtigste flüchtige Element im Erdinnern ist wohl Wasserstoff, vor allem wegen seiner starken Auswirkungen auf Schmelztemperaturen und auf physikalische Eigenschaften, wie elektrische Leitfähigkeiten und Deformationsmechanismen. Normalerweise nimmt man an, dass Wasserstoff im Erdinnern in oxidierter Form vorliegt, als H_2O-Moleküle oder OH-Gruppen, gespeichert als Defekte in Mantelmineralen, als freies Fluid oder als Bestandteil von Silikatschmelzen. Unter den stark reduzierenden Bedingungen im tiefen Mantel (sowie im ganzen Mantel zu Beginn der Erdgeschichte) überwiegt aber wahrscheinlich molekularer Wasserstoff (H_2). Bis vor kurzem war völlig unklar, ob und in welchem Umfang molekulares H_2 in Mineralen gelöst werden kann. Der erste Beitrag in diesem Kapitel löst dieses Problem. Minerale des oberen Mantels (Olivin, Granat und Pyroxene) wurden in Piston-Cylinder-Experimenten mit Wasserstoff gesättigt und die H_2-Konzentrationen wurden anschließend mit Hilfe von Infrarot-Spektroskopie bestimmt. Durch die Wechselwirkung mit der umgebenden Silikatmatrix wird im H_2 ein Dipolmoment induziert, so dass das Molekül infrarotaktiv wird. Die Daten zeigen eine kleine, aber signifikante Löslichkeit. Dies bedeutet, dass bei der Akkretion der Erde aus dem Sonnennebel möglicherweise molekularer Wasserstoff direkt in Mineralen gelöst wurde. In einem weiteren Projekt wurde die Löslichkeit von H_2 in Silikatschmelzen als Funktion von Druck, Temperatur und Schmelzzusammensetzung

systematisch untersucht. Der dritte Beitrag in diesem Kapitel beschäftigt sich mit dem Einfluss des Redoxzustandes auf die Löslichkeit von OH in den Mineralen Wadsleyit und Ringwoodit in der Übergangszone des Mantels. Wenn OH und H_2O zu H_2 reduziert werden, muss die Menge an gelöstem OH in diesen Mineralen abnehmen, was in den Experimenten auch beobachtet wurde. Insgesamt werden diese drei Studien zu einem besseren Verständnis des Ursprungs und der Verteilung des Wassers in der Erde führen. Ein weiterer Beitrag in diesem Abschnitt des Jahresberichts beschreibt ein laufendes Projekt über die Rolle von H_2O und CO_2 bei der Schmelzbildung im Mantel.

Experimentelle Untersuchungen über die Speicherung von Stickstoff im Mantel sind vor allem am Bayerischen Geoinstitut vorangetrieben worden. Ein Beitrag in diesem Kapitel enthält die ersten Daten zur Löslichkeit von Stickstoff in den Mineralen der Übergangszone und des unteren Mantels. Wadsleyit und Ringwoodit können etwa 50-200 ppm Stickstoff aufnehmen, die Löslichkeit in den Mineralen des unteren Mantels ist dagegen geringer. Insgesamt zeigen diese Daten, dass etwa 40 Atmosphärenmassen von Stickstoff im tiefen Mantel gespeichert werden könnten. Ein weiterer Beitrag untersucht die Rolle von Silikatschmelzen beim Transport von Stickstoff in Subduktionszonen.

Die letzten beiden Projekte in diesem Kapitel des Jahresberichtes beschäftigen sich mit den Eigenschaften von wässrigen Fluiden in der Kruste und im oberen Mantel. Ein neues Modell für die elektrische Leitfähigkeit von NaCl-haltigen Fluiden wird vorgestellt, basierend auf Messungen am Bayerischen Geoinstitut. Dieses Modell erlaubt eine bessere Interpretation von magnetotellurischen Daten; es hilft insbesondere dabei, in Bereichen hoher Leitfähigkeit in Kruste und Mantel Silikatschmelzen von wässrigen Fluiden zu unterscheiden. Der letzte Beitrag in diesem Kapitel enthält neue Daten über die Löslichkeit von Gold in wässrigen Fluiden, die wichtig sind, um den Ursprung hydrothermaler Goldlagerstätten zu verstehen. Es wird gezeigt, dass unter relativ oxidierenden Bedingungen und bei hohen Salinitäten erstaunlich hohe Gold-Löslichkeiten bis in den Bereich von Gewichtsprozent erreicht werden können.

3.6 Rheologie und Metamorphose

Die dynamischen Bewegungsabläufe im Erdinneren sind die Antriebskräfte für globale tektonische Ereignisse und den Materialaustausch zwischen der Oberfläche und den Tiefen unseres Planeten. Sie sind Ursache katastrophaler Erdbeben oder explosionsartiger Vulkanausbrüche und fördern den Wärmefluss, der wiederum den thermischen Zustand des Erdinneren beeinflusst. Für das Verständnis dynamischer Abläufe im Erdinneren ist die genaue quantitative Bestimmung der rheologischen Eigenschaften des Materialbestandes im Erdmantel sowie der Verformungsmechanismen unerlässlich.

Einen entscheidenden Schritt in global betrachteter Tektonik stellt das Einsetzen örtlich begrenzter Verformung bei beginnender Subduktion dar. Der erste Beitrag dieses Kapitels

widmet sich der Boudinage-Bildung, die ein Beispiel für Spannungsansammlungen in einer bestimmten Geometrie ist. Das Vorhandensein von frühen Störungen entlang einer lagenförmigen Ausgangsgeometrie scheint ein Schlüsselaspekt für die Boudinage-Bildung und die assoziierte Spannungslokalisierung zu sein. Eklogitlagen, an der Basis von Gebirgszügen und auf subduzierten Platten aufliegend, spielen Schlüsselrollen in der Plattentektonik. In der zweiten Studie des Kapitels wird untersucht warum bi-mineralischer Eklogit um zwei Größenordnungen schwächer ist als reiner Granat. Es scheint, dass eine Schwächung von Klinopyroxen durch ein verändertes Deformationsverhalten von (100)-Zwillingsbildung bei niedriger Temperatur zu Verformung durch die Aktivierung von Vielfach-Gleitsystemen nach {110}[001] und {110} ½ <110 > bei hohen Temperaturen stattfindet. Der dritte Beitrag dieses Kapitels beschreibt Keimbildung und Wachstum von Granat unter deviatorischer Spannung, welcher für die Bestimmung der Druckbedingungen von Eklogit und Peridotit von großer Bedeutung ist. Das Gefüge von metamorph gebildetem Granat scheint nicht nur durch den Chemismus sondern auch durch Korngefüge und Verformungsmechanismen, insbesondere durch Korngrenzengleiten beeinflusst zu sein.

Plastische Verformung von Mineralen durch Versetzungskriechen resultiert in einer bevorzugt dem Kristallgitter folgenden Ordnung (*lattice-preferred orientation - LPO*), die Ursache seismischer Anisotropie sein kann. Im vierten Beitrag werden Untersuchungen aktiver Gleitsysteme in Periklas, dem zweithäufigsten Mineral im unteren Erdmantel, beschrieben. Dazu werden Ergebnisse aus Verformungsexperimenten und numerischen Untersuchungen (*Elasto-ViscoPlastic Self Consistent (EVPSC) modeling*) verglichen. Der fünfte Beitrag erläutert Verformungsexperimente an kubischem $CaSiO_3$-Perowskit, einem bedeutenden Mineral in der Übergangszone und im unteren Mantel. Perowskit wurde aus pulverförmigem Wollastonit synthetisiert und in einer Diamantstempelzelle mit Widerstandsheizung deformiert. Auch diese Ergebnisse wurden mit denen aus EVPSC-Simulationen verglichen, um die aktivierten Gleitsysteme zu erkennen. In der sechsten Studie wird über Ergebnisse von Verformungsexperimenten mit Ferroperiklas bei hohen Temperaturen und Druckbedingungen des unteren Erdmantels berichtet. Die schon früher festgestellte Zunahme der Periklasfestigkeit bei Raumtemperatur wird auch bei hohen Temperaturen beobachtet, jedoch ist die Rate des Anstiegs kleiner.

Das dominierende Mineral im oberen Mantel ist Olivin, dessen mechanische Eigenschaften von zahlreichen Forschern untersucht wurden. Der siebte Beitrag beschreibt die Entwicklung einer neuen Methode zur Untersuchung des Einflusses von deviatorischer Spannung auf die Migration von Forsterit-Aggregaten entlang von Korngrenzen bei hohen Temperaturen und Drücken; die Rolle, die Korngrenzen bei der Verformung polykristalliner Proben spielen, ist bisher kaum verstanden. Der achte Artikel stellt Diffusionsuntersuchungen an Korngrenzen von Forsterit durch molekular-dynamische Simulationen vor. Es konnte eine systematische Beziehung zwischen dem Exzess-Volumen an Korngrenzen, das durch die weniger definierte Struktur der Korngrenze entsteht und dem Diffusionskoeffizienten beobachtet werden; dagegen zeigt eine Misorientierung benachbarter Kristalle weder einen systematischen Einfluss auf Diffusionskoeffizienten noch auf das Exzess-Volumen der Korngrenzen.

Die im neunten Beitrag vorgestellten Untersuchungen widmen sich der Eigendiffusion von Silizium im Wadsleyitgitter als einer Funktion des Wassergehalts. Hier wird versucht, eine Methode zur Gewinnung verlässlicher Diffusionsprofile einzuführen. Dafür werden Einkristalle mit einem Forsteritfilm überzogen, der mit stabilen Isotopen angereichert ist. Der letzte Beitrag dieses Kapitels berichtet über eine negative Korrelation zwischen Wassergehalt und Versetzungsmobilität im Olivin-Gleitsystem [001](100). Diese Beziehung wurde an einfach gescherten Olivin-Einkristallen mit unterschiedlichen Wassergehalten festgestellt. Die Versetzungsmobilität wird in Ausheilexperimenten bestimmt. Es wird ermittelt wie schnell die Versetzungsdichte, die durch Oxidationsexperimente ermittelbar wird, sinkt. Das Ergebnis lässt annehmen, dass sich die Kernstruktur der Versetzung bei der Aufnahme von Wasser ändern kann.

3.7 Materialwissenschaften

Hochdruck-Materialwissenschaft teilt mit der Mineralphysik und Petrologie nicht nur die Methodik der Synthese, sondern auch theoretische Werkzeuge und Analysemethoden für Untersuchungen unter hohem Druck und hoher Temperatur, d.h. *in situ*. Am Bayerischen Geoinstitut sind zahlreiche Wissenschaftler in beiden Feldern tätig; aufgrund ihrer Erfahrung und Kompetenzen in der Mineralphysik bearbeiten sie auch an der Spitze der Materialwissenschaften wichtige Fragestellungen in der Festkörperphysik und -chemie, bei hohen Drücken.

Das Synthese von Fe_4O_5 unter hohem Druck ist ein Beispiel, bei dem eine Entdeckung in der Mineralphysik zu einem wichtigen Eckpfeiler der Hochdruck-Materialwissenschaften wurde. Nach Magnetit (Fe_3O_4) war Fe_4O_5 das erste Eisenoxid, in dem Eisen in gemischten Valenzzuständen vorkam. Seine Entdeckung führte zur Synthese zahlreicher weiterer Eisenoxide mit gemischter Valenz. Gleichzeitig bleibt Fe_4O_5 selbst ein interessantes Forschungsobjekt: Röntgenbeugung sowie Messungen von elektrischem Widerstand und magnetischer Suszeptibilität haben zur Entdeckung einer neuer Art von Ladungsordnung bei Temperaturen unter 150 K geführt. Auf dem Eisengitter, das sich kanalartig durch die Struktur zieht, ordnen sich die Eisenatome in Dimere und Trimere, was wiederum zu einer Störung des Kristallgitters führt.

Die Systeme Bor-Kohlenstoff (B-C) sowie P_3N_5-P_2O_3 bilden ähnlich komplexe Lösungen, und sind aufgrund ihres Potentials als ultraharte Materialien beziehungsweise wegen ihrer extremen chemischen Stabilität von Interesse. Für $B_{13}C_2$ sowie PON werden hier *in situ*-Untersuchungen in der Diamantstempelzelle vorgestellt. Die Struktur und Stabilität von $B_{13}C_2$ wird mit Hilfe von Einkristall-Röntgenbeugung sowie optischer Spektroskopie untersucht, und entgegen theoretischer Vorhersagen durchläuft dieses Borcarbid bis zu 70 GPa keinen Phasenübergang. Wie für $B_{13}C_2$ wird auch die Stabilität von PON mittels Einkristall-Röntgenbeugung untersucht, und eine komplexe Serie von Kompressionsmechanismen der Tetraeder überführt PON von einer losen Gerüststruktur in ein dicht gepacktes Gitter.

Ebenso in der Diamantstempelzelle wurden zwei organische Verbindungen untersucht: das *einfache* C_3H_8-Propan, ein wichtiger Bestandteil von Erdgas und zwei *komplexe* Metall-organische Gerüste (*metal-organic framework*, MOF). Propan wird in der festen Phase – unter kryogenen Temperaturen – bis 40 GPa mit Hilfe von Raman-Spektroskopie untersucht, wobei drei Phasenübergänge entdeckt werden: Diese können mit C-C und CH_2-CH_3-Dehnungen des Gerüsts, sowie mit CH_3-Verformungen assoziiert werden.

Metall-organische Gerüste zeigen ein großes Potential als multiferroische Materialien, die in Mehrstufen-Schaltelementen angewandt werden können. Durch die große Flexibilität des organischen Gerüsts können unterschiedliche Metall-Ionen in MOF eingebaut werden, um physikalische Eigenschaften gezielt abzustimmen. Struktur-Eigenschaft-Beziehungen von MOF sind jedoch nicht ausreichend bekannt, deswegen können Hochdruck-Experimente einen Beitrag zu deren Verständnis leisten. Durch eine Kombination von Röntgenbeugung, Mössbauer- und Ramanspektroskopie kann die Polarität der Metallionen in den Verbindungen bestimmt werden. Eine solche Charakterisierung unter hohem Druck kann bei der Synthese von dichten MOF gezielt eingesetzt werden, sowohl bei Normal- als auch bei Hochdruck.

Die letzten beiden Beiträge dieses Abschnitts untersuchen das Hochdruck-Verhalten einer anderen Klasse von Materialien, Metallen. In beiden Projekten werden theoretische Methoden verwendet, um Eigenschaften von Eisen zu untersuchen. Da frühe Methoden in der Dichtefunktionaltheorie nicht in der Lage waren, grundlegende Eigenschaften von Eisen vorherzusagen – z. B. die stabile Phase von Eisen bei Normaldruck oder die Zustandsgleichung der Hochdruckphase in der hexagonal dichtest gepackten Struktur (*hexagonal close packed*, hcp) –, hat sich Eisen als wichtiger Referenzpunkt für neu-entwickelte Dichtefunktionale etabliert. Hier wird eine neu-etablierte Methode auf hcp Fe angewendet, die den Elektronen-Austausch korrekt beschreibt, um zu sehen, ob diese Methode die Defizite anderer Näherungen überwinden kann. Diese Methode ist jedoch nicht in der Lage, die Zustandsgleichung von hcp Fe hinreichend gut zu beschreiben. Dies legt die Vermutung nahe, dass Elektronen-Korrelation oder Magnetismus eine wichtige Rolle im Kompressionsverhalten von hcp Fe spielen, trotz ambivalenter experimenteller Hinweise. Im letzten Beitrag dieses Abschnitts werden Molekulardynamik-Simulationen verwendet, um die Struktur von flüssigem Eisen zu beschreiben. Die vorgestellten Ergebnisse ebnen den Weg zu einer verbesserten Charakterisierung seines Kompressionsverhaltens bei hohem Druck.

3.8 Methodische Entwicklungen

Die Verfeinerung experimenteller Methoden und die Entwicklung neuer Forschungsansätze ist und bleibt ein beständiges und wichtiges Ziel in den Erd- und Materialwissenschaften. Derartige Entwicklungen sind zum Beispiel dazu geeignet, mit Experimenten in höhere Druck- und Temperaturbereiche vorzustoßen und so unsere Kenntnisse über das tiefe Erdinnere zu verbessern, oder um zu neuartigen Bestimmungen von physikalischen und

chemischen Materie-Eigenschaften zu kommen. Sie können auch neue Erkenntnisse zur chemischen Zusammensetzung und zu Kristallfehlern von natürlichen und experimentell synthetisierten Proben liefern. Die Artikel dieses Kapitels behandeln daher zahlreiche Aspekte methodischer Entwicklungen.

Methodische Weiterentwicklungen der Multianvil-Technik sind auch für detaillierte Analysen von gewonnenen Proben von Vorteil, da Multianvil-Experimente relativ große Probenvolumen produzieren sowie ein stabileres Heizverhalten mit kleineren Temperaturgradienten entlang der Probe, im Vergleich mit Proben in der Diamantstempelzelle (DAC), aufweisen. Der erste Beitrag dieses Kapitels berichtet von neuen technischen Errungenschaften bei dem Einsatz einer Vielstempelapparatur mit neu-entwickelten härteren Wolframkarbid-Würfeln. Diese Würfel ermöglichen Hochdruckexperimente bis 63 GPa bei Raumtemperatur und bis 45 GPa bei 2000 K. Im zweiten Artikel wird das schnelle Abschrecken einer Probe mit über 6000 K/s in einer neuartigen Probenumgebung in einer Multianvil-Presse beschrieben. Dadurch wird es möglich, einige bisher nicht abschreckbare Phasen bei Raumbedingungen zu gewinnen und diese mit verschiedenen analytischen Methoden zu charakterisieren.

In vier folgenden Beiträgen werden methodische Weiterentwicklungen für DACs vorgestellt. Im ersten wird über ein tragbares CO_2-Laserheizsystem berichtet, mit dem Probleme überwunden werden, die bisher beim Beheizen mit Glasfaser-Lasern entstanden. Des Weiteren könnte der Einsatz gepulster Laser (an Stelle von Dauerstrich-Lasern) chemische Reaktionen zwischen Probe und Diamantstempeln in der DAC verhindern, die z.B. zu fehlerhaften Messwerten der Schmelztemperatur von Eisen bei hohem Druck führen. Der vierte Artikel beschreibt chemische Reaktionen zwischen einer Eisenprobe und den Diamantstempeln bei der gleichzeitigen Aufheizung einer Probe mit einem gepulsten und einem kontinuierlichen Laserstrahl in derselben DAC-Probenkammer. Der sich anschließende Beitrag stellt Neuentwicklungen für einen Aufbau zur Sauerstoffbefüllung einer DAC-Probenkammer und dessen Leistungsfähigkeit vor. Des Weiteren beschreibt die sechste Studie eine resonante Mikrospule für kernmagnetische Resonanzmessungen in der DAC zur Untersuchung von Viskosität und Polymerisationsgrad von Silikatgläsern sowie magnetischer und elektronischer Eigenschaften von Feststoffen bei hohem Druck.

Die drei letzten Beiträge dieses Kapitels präsentieren Fortschritte in der Probenanalytik. Die Identifizierung und Beschreibung von Versetzungen und Stapelfehlern in Kristallen ist bei Untersuchungen der rheologischen Eigenschaften, die durch Versetzungsbewegung kontrolliert werden, von Bedeutung. Beitrag sieben und acht behandeln den Einsatz der *Electron Channeling Contrast Imaging*-Methode (ECCI) im Rasterelektronenmikroskop (REM) als neues Verfahren in den Geowissenschaften. Diese Methode ermöglicht die Erkennung und quantitative Bestimmung von Versetzungen und insbesondere Stapelfehlern in Mineralen. Der das Kapitel abschließende Beitrag berichtet über die Verlässlichkeit und Leistungsfähigkeit eines Lexikonansatzes zur quantitativen Interpretation von rückgestrahlten Elektronenbeugungsbildern (EBSD) von Mineralen im REM.

3. Research Projects

3.1 Earth and Planetary Structure and Dynamics

The terrestrial planets formed within roughly 100 million years after the start of the solar system. In the beginning collisions involved planetesimals; during the later stages of accretion planetary embryos collided with remaining planetesimals and with other embryos. Due to the release of kinetic energy and the decay of short-lived radioactive isotopes magma oceans formed on the growing planetary bodies, allowing for effective core segregation. The last giant impact involving proto-Earth and a Mars-sized impactor body led to the formation of a hot disk from which the initially molten Moon accreted.

The first contribution in this section deals with planetesimals, small building blocks of terrestrial planets, formed in the protoplanetary disc. Modern astrophysical theories indicate that these objects with a size of a dozen to hundreds of kilometers formed within a short time from micro- to millimeter-sized particles. One of these planetesimals was the parent body of the rare angrite meteorite group. Geochemical studies have shown that despite experiencing a magma ocean stage that caused efficient remixing, geochemical reservoirs were formed early on. The study used 2D and 3D numerical models to determine conditions under which geochemical reservoirs could have emerged. The results indicate that on sufficiently small objects such reservoirs could have formed during the final stages of magma ocean crystallization and remained stable ever since.

The second contribution discusses the phase of planet formation when planetary embryos collided among each other to form larger terrestrial objects. For this purpose a 3D SPH (=*smoothed particle hydrodynamics*) model was serially coupled with a 3D geodynamical model to study both the impact process and the longer-term evolution of the target body. This method allows the limitations of both SPH models and geodynamical models to be overcome. Namely, SPH models describe only a short time period after the impact process. On the other hand impacts can be only prescribed in a simplified way in geodynamical models. Therefore the final state of each SPH simulation can serve as input data for a geodynamical model. Since ejecta material falling back onto the target body can affect the thermomechanical evolution, detailed tests were performed to assess the sensitivity of the handoff time between both models.

As mentioned previously, the lunar interior was initially molten. The third study in this section discusses the potential existence of a present-day molten layer in the lowermost lunar mantle as suggested by a reanalysis of seismic data a few years ago. Based on crystallization models it has been suggested that iron and titanium-rich material solidified late and sank down to the core-mantle boundary, where the material was reheated. The study aims at determining whether this material could still be molten at the present-day pressure and temperature conditions in the lowermost lunar mantle and whether this material would also be negatively buoyant compared to ambient mantle material, thus explaining its stability at the core-mantle boundary.

The fourth study discusses the lunar interior structure. For this purpose a 1D model was developed that utilizes geophysical, geochemical and mineralogical data to improve our understanding of the lunar interior. Using different temperature profiles and either a homogeneous or a differentiated lunar mantle, a large parameter space was covered by varying parameters, such as layer thicknesses. The results show that this combined model allows for an improved determination of the lunar core radius, which was previously not well known.

In the present-day asteroid belt and in meteorite collections, olivine-rich material is very rare compared to metallic asteroids and iron meteorites. The fifth contribution in this section discusses whether this material could come from the terrestrial planets rather than being leftover material from asteroid breakup processes. As mentioned above, massive collisions occurred during the later stages of terrestrial planet accretion. Usually these collisions produced significant amounts of escaping ejecta material, and it is viable that part of this material was perturbed into new heliocentric orbits. The study shows that the volume ratios between crustal, mantle and core material as observed in the asteroid belt is closer to those ratios for planets like Mars or Earth than those for intact differentiated asteroids like Vesta.

After the end of accretion the terrestrial planets started to cool down and developed a thermal boundary layer at their surfaces known as the lithosphere. Due to Earth's low surface temperature it can be expected that elasticity is important in the lithosphere and, together with topography, it will have an important effect on the stress state in the lithosphere. While the importance of topography was recognized several years ago and is nowadays accounted for by introducing a low viscosity surface layer called "sticky air", most mantle convection simulations neglect elasticity. The present study considers both topography and elasticity. The study compared the results of a finite-element code with a true free surface with those obtained by a finite-difference code employing the "sticky air" method. The good agreement among the codes shows that the "sticky air" method is compatible with the application of elasticity.

Localization of deformation processes in the lithosphere is important for geological processes on Earth like the formation of new plate boundaries. Previous studies using simplified rheology indicated that the interaction between grain size reduction and shear heating can lower the stress necessary to achieve thermal runaway. This last contribution shows that the consideration of additional deformation mechanisms like the Peierls mechanism is important since it reduces the efficiency of shear heating and therefore makes it more difficult to achieve thermal runaway.

a. *Post-magma ocean mixing of reservoirs inside the angrite parent body (G.J. Golabek, B. Bourdon/Lyon, A.B. Rozel and T.V. Gerya/Zurich)*

Angrite meteorites are a rare group being part of the achondrite class. Geochemical evidence indicates the presence of a magma ocean during the early evolution of their parent body.

Nevertheless Hf-W data indicate the presence of at least two distinct mantle reservoirs. Here, using available theoretical models we show that reservoir preservation during the magma ocean stage is unlikely. We test the scenario that impact contamination caused the mantle reservoir formation during the post magma ocean stage. For this purpose we use 2D and 3D finite-difference numerical models to study reservoir mixing during the post-magma ocean stage (Fig. 3.1-1) and derive semi-analytical models for the mixing evolution. Finally, we apply available constraints derived from geochronological, thermal and remanent magnetization data to our numerical results to estimate the radius of the angrite parent body. The best fit to the data can be obtained for a small angrite parent body with less than 100 km radius.

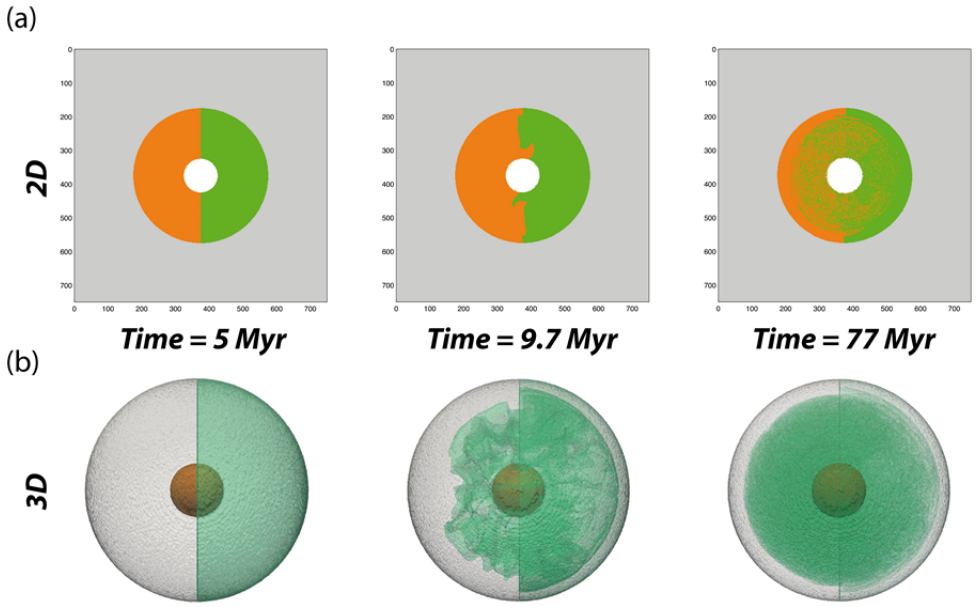

Fig. 3.1-1: Reservoir mixing for a planetesimal with R_P = 200 km and core radius R_C = 50 km in (a) 2D and (b) 3D calculation shown for comparable times. In the 2D calculation the two initially hemispherical reservoirs are plotted in green and orange. For visualization purposes the 3D model shows only one of the reservoirs and the subfigures are magnified compared to the 2D models.

b. *Coupling collision and geodynamical models (G.J. Golabek, M. Jutzi and A. Emsenhuber/ Bern, T.V. Gerya/Zurich)*

The crustal dichotomy is the dominant geological feature on planet Mars. The exogenic approach to the origin of the crustal dichotomy assumes that the northern lowlands correspond to a giant impact basin formed after primordial crust formation. However these simulations only consider the impact phase without studying the long-term repercussions of such a collision.

The endogenic approach, suggesting a degree-1 mantle upwelling underneath the southern highlands, relies on a high Rayleigh number and a particular viscosity profile to form a low

degree convective pattern within the geological constraints for the dichotomy formation. Such vigorous convection, however, results in continuous magmatic resurfacing, destroying the initially dichotomous crustal structure in the long-term.

A further option is a hybrid exogenic-endogenic approach, which proposes an impact-induced magma ocean and subsequent superplume in the southern hemisphere. However these models rely on simple scaling laws to impose the thermal effects of the collision.

Here we use impact simulations performed with a SPH code serially coupled with geodynamical computations performed using the code I3VIS to improve the latter approach and test it against observations. We are exploring collisions varying the impactor velocities, impact angles and target body properties, and are gauging the sensitivity to the handoff from SPH to I3VIS.

As expected, our first results indicate the formation of a transient hemispherical magma ocean in the impacted hemisphere, and the merging of the cores (Fig. 3.1-2).

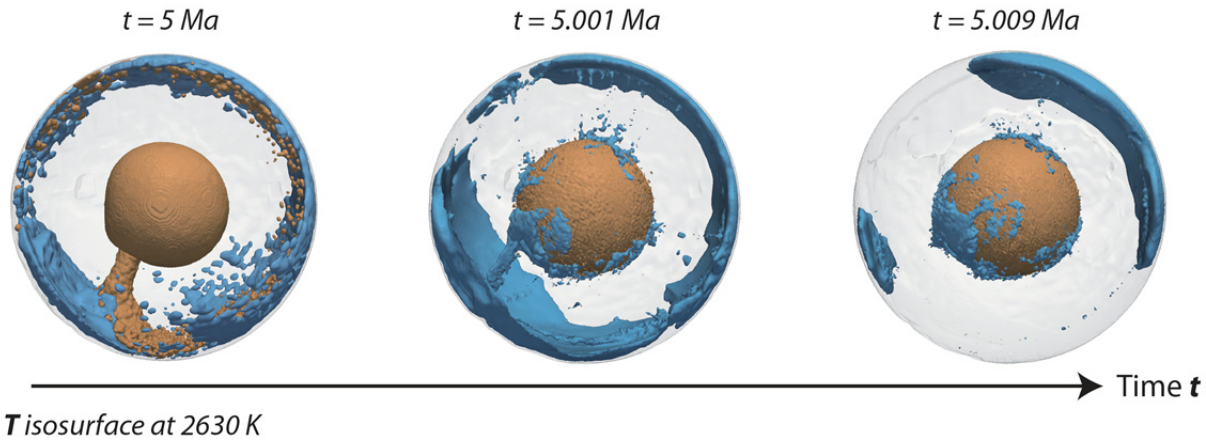

Fig. 3.1-2: I3ELVIS result for the evolution of a Mars-sized planet after a grazing collision with a 1000 km radius impactor. Temperature isosurface at 2630 K, corresponding to the liquidus of peridotite at martian CMB pressure.

We also find that impact angle and velocity have a strong effect on the post-impact temperature field and on the timescale and nature of core merger.

c. *Understanding the evolution of the interior of the Moon by in situ density determination of deep lunar melts (A. Mallik, T. Ejaz/Kharagpur, S. Petitgirard, S. Shcheka, W. Malfait/Zurich, M. Wilke/Potsdam and G. Garapic/New Paltz)*

11 of the 25 varieties of pristine, near-primary lunar glasses from Apollo missions 11 to 17, have FeO concentrations > 6 wt. % and TiO_2 concentrations > 16 wt. %. Experiments on

these pristine lunar glasses source their depths in the lunar mantle between 275-690 km from the surface. How is it possible to obtain Fe-Ti-rich sources in the lunar mantle at such depths, which is contrary to the expected sequence of crystallization of the lunar magma ocean? Perhaps the most appealing way to do so is by overturn of the lunar mantle. The last 95 % of the lunar magma ocean during crystallization produced a dense, radioactive element-rich (KREEP), ilmenite (Fe-Ti)-rich layer below the floatation crust of plagioclase, which could sink through the mantle due to its density. If the Moon does have a Fe-rich core, this layer could have sunk until the CMB (core mantle boundary) where it can undergo heating by radioactive decay and rise as an upwelling once it achieves thermal buoyancy. The upwelling can provide heat for partial melting to produce mare basalts in the lunar interior. Inefficient overturn, convective mixing and/or upwelling can create Fe-Ti-rich zones in the lunar mantle that can be probable sources of Fe-Ti-rich mare basalts. On the other hand, a partially molten layer near the CMB of the present-day Moon has been proposed based on the absence of observed deep far-side quakes, reflected phases from deep moonquakes as well as tidal energy dissipation in the lunar interior. The most likely source for the partial melt would be the Fe-Ti-rich layer that is the product of the overturn episode and the melt will be stable at the CMB only if it is denser than the overlying mantle. So far, based on published estimates, lunar basalts that likely contain contributions from this overturned Fe-Ti-rich layer are less dense than the overlying mantle at *P-T* conditions of their generation, hence, they will rise and not sink. The phase equilibria and melt compositions will be highly dependent on the proportion of mixing between this Fe-Ti-rich layer and the surrounding ambient mantle.

We have undertaken an experimental study to investigate the phase equilibria of the Fe-Ti-rich layer and the ambient mantle (mixed in different proportions) at pressures ranging from 2 to 4.8 GPa, covering the depths from sources of Fe-Ti-rich basalts (obtained from previous studies) to the lunar CMB. Preliminary results show that the overturned Fe-Ti rich layer will undergo complete melting at *P-T* conditions relevant for generation of Fe-Ti rich mare basalts. This implies that a melt of the same composition as the Fe-Ti rich layer will sink to the CMB and remain stable until present day, only if it is denser than the surrounding mantle. Density estimates of the molten Fe-Ti layer obtained using the current range of published values of isothermal bulk moduli and their pressure-temperature derivatives do not help conclude the fate of such melt because the densities encompass values that are both higher and lower than that of the lunar mantle (Fig. 3.1-3). Hence, we have proposed to measure the density of Fe-Ti enriched lunar melts *in situ* at the relevant *P-T* conditions using the X-ray absorption technique in a Paris-Edinburgh press at ESRF. The depth of density crossover between these melts and the ambient lunar mantle will determine whether: (a) the melts will sink and settle at the lunar core-mantle boundary (CMB), forming the partial melt layer suspected at the present CMB based on seismic studies; or, (b) the melts will rise, undergo reactive flow with the surrounding lunar mantle, and likely erupt as mare basalts that have been sampled by Apollo and Luna missions.

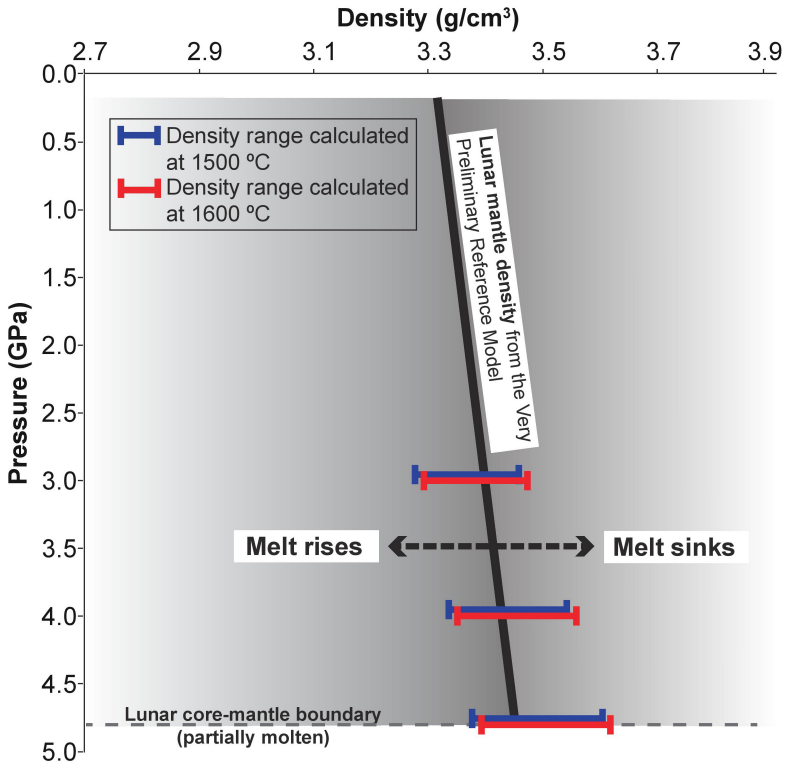

Fig. 3.1-3: Calculated density ranges of Fe-Ti-rich lunar melt using published values of isothermal bulk moduli and their pressure-temperature derivatives from previous studies.

d. *Constraints on lunar structure from combined geochemical, mineralogical, and geophysical modeling (A. Mallik, in collaboration with H. Fuqua/Berkeley, P. Bremner/Gainesville, M.R. Diamond/Berkeley, S.J. Lock/Cambridge, S. Panovska/Potsdam, Y. Nishikawa/Paris, H.J. Perez/Paris, A. Shahar/Washington DC, W.R. Panero/Columbus, P.H. Lognonne/Paris and U. Faul/Cambridge)*

The internal structure of the Moon is poorly constrained. In this study, we use a multidisciplinary approach to attempt to constrain key parameters of the lunar structure. We use 1-D lunar compositional models with chemically and mineralogically distinct layers, and forward calculated physical parameters, in order to constrain the internal structure. We consider both a chemically well-mixed model with uniform bulk composition, and a chemically stratified model that includes a mantle with preserved mineralogical stratigraphy from magma ocean crystallization. Additionally, we use four different lunar temperature profiles that span the range of proposed selenotherms, giving eight separate sets of lunar models. In each set, we employed a grid search and a differential evolution genetic search algorithm to extensively explore model space, where the thickness of individual compositional layers was varied. In total, we forward calculated over one hundred thousand lunar models.

It has been proposed that a dense, partially molten layer exists at the CMB to explain the lack of observed far-side deep moonquakes, the observation of reflected seismic phases from deep

moonquakes, and enhanced tidal dissipation. However, subsequent models have proposed that these observables can be explained in other ways. In this study, using a variety of modeling techniques, we find that such a layer may have been formed by overturn of an ilmenite-rich layer, formed after the crystallization of a magma ocean. We therefore include a denser layer (modeled as an ilmenite-rich layer) at both the top and bottom of the lunar mantle in our models.

From our preliminary results, we find models that explain the observed lunar mass and moment of inertia and estimated bulk silicate lunar composition from previous studies. We find that only a narrow range of core radii are consistent with these constraints. Furthermore, in the chemically well-mixed models, we find that a dense layer is required in the upper mantle to meet the moment of inertia requirement. In no set of models is the mass of the lower dense layer well constrained. For the models that fit the observed mass and moment of inertia, we calculated 1-D seismic velocity profiles, most of which compare well with those determined by inverting the Apollo seismic data from previous studies.

e. *Olivine in the asteroid belt comes from the terrestrial planets (S.A. Jacobson, D.C. Rubie and D.J. Frost, in collaboration with A. Morbidelli/Nice and F. DeMeo/Cambridge)*

The low relative abundance of olivine-rich meteorites, presumably mantle material, compared to iron meteorites, presumably core material, and the low relative abundance of A-type asteroids, again presumably mantle material, compared to M-type asteroids, again presumably core material, has been referred to as the "missing mantle" problem. The "battered to bits" solution proposes that since silicates are significantly weaker than metals, mantle material is ground to dust whereas core material survives.

Using the Sloan Digitial Sky Survey (SDSS) moving object color survey with high spectral resolution follow-up and as well as earlier surveys, the total volume of not-Vestoid V-type and A-type asteroids is estimated to be 1.1×10^5 and 2.2×10^6 km^3, respectively. The total estimated volume of M-type asteroids is estimated to be 2.5×10^7 km^3, but only approximately 38 % of M-types are consistent with a metal-rich surface from radar albedo measurements. Withholding a discussion of the uncertainties until the next paragraphs and making conservative assumptions relative to our conclusions, the volume ratio of crust, mantle, and core material in the asteroid belt is $1: 20: 88$.

The 1.1×10^5 km^3 estimate of not-Vestoid V-type material is a conservative upper limit of the total volume of crust material, because it undoubtedly includes a significant number of Vestoid family members even after we remove identified family members from hierarchical clustering methods. We exclude Vesta and its family members, because Vesta is an intact planetesimal, so it did not contribute mantle or core material to the asteroid belt. The middle and outer regions of the asteroid belt are likely devoid of Vestoid contamination, and these regions contain only about 3.6×10^4 km^3 of V-type material. Using this lower bound the volume ratios of crust, mantle, and core material in the asteroid belt are $1: 61: 265$.

The 2.2×10^6 km^3 estimate of A-type material has an uncertainty of approximately 40 % mostly from the volume uncertainties of the largest members. Indeed, 354 Eleonora contains about 88 % of the total volume, the other 12 % is pre-dominantly spread amongst six other asteroids. However, the total volume of A-type material is a likely lower bound on the total volume of mantle material in the asteroid belt, since Sa-type asteroids may be altered A-type asteroids. The other differentiated asteroid types such as R- and O- contain very little volume and so do not affect the results of this analysis.

The 9.6×10^6 km^3 estimate of metal-rich M-type asteroids is still a conservative upper limit of the total volume of core material [7], because about 64 % of these radar metal-rich M-type asteroids display a hydrated mineral spectral feature, which could be a secondary feature from subsequent implantation of carbonaceous material or indicative of the bulk composition. If hydration features are indicative of bulk composition, then the total volume ratios of crust, mantle, and core material in the asteroid belt are $1: 20: 32$. From this assessment, the nominal volume ratio of crust, mantle, and core material in the asteroid belt may be $1: 20: 88$, but the expected range of possible volume ratios are about $1: 8 - 85: 32 - 265$.

The "battered to bits" hypothesis posits that these differentiated materials are the direct consequence of disrupted differentiated planetesimals (Ceres- and Vesta-sized or smaller). Differentiation models based on the assumption of different pure chondrite parent bodies predict volume ratios of crust, mantle, and core material to be 1:0.78:0.27 for H chondrite models, 1:1.1:0.27 for L chondrite models, 1:1.2:0.14 for LL chondrite models, and 1:4.0:0.40 for CO/CV chondrite models. Considering only the crust to mantle ratios, the best fit to the observed V- and A-type asteroids appears to be a CO/CV chondrite parent body, especially when the largest, 354 Eleonora, is ignored. However, the only preserved differentiated planetesimal, Vesta, appears to differ significantly from these estimates, when different investigators have tried to explain both bulk properties of the body and the HED meteorite evidence, they have calculated volume ratios of crust, mantle, and core material from 1:0.11:0.05 to 1:0.99:0.26. It has been hypothesized that Vesta may not be an intact planetesimal, but in order to match the nominal volume ratio of crust, mantle, and core material in the asteroid belt of $1: 20: 88$, and incredible volume equal to many times the mass of Vesta must have been lost even in the most favorable cases. Unlike small planetesimals, larger planets have much more mantle and core material relative to crust material with volume ratios of crust, mantle, and core material of 1:9.1:1.6 for Mars, 1:44:8.8 for the early Earth, and 1:88:17 for Earth today. The crust to mantle ratio for differentiated planets is much more similar to the ratios observed in the asteroid belt. Indeed, the best estimate for the asteroid belt would seem to match a planet somewhat larger than Mars.

The 'Giant Impact' phase of terrestrial planet formation has long been identified in both numerical simulations. Furthermore, the giant impact hypothesis is the leading model for the formation of the Moon. These giant impacts likely produce impact ejecta that escape into heliocentric orbit. Indeed, hit'n'run impacts can produce significant masses of debris even projectile core material.

A large variety of different ejecta outcomes can occur given the specifics of each giant impact event. In low impact angle but high impact energy events, large amounts of crust and mantle material may be ejected. The ratio of crust to mantle material has not been reported but likely spans from crustal dominance for small impacts that do not excavate deeply, but the volume ratio of ejected materials will approach the crust to mantle ratio of the entire planet as impacts grow in size. Since the largest impacts create the most debris, the crust to mantle ratios set by these impacts dominate the final ratio amongst all of the ejecta.

Unlike low impact angle impacts, high angle hit'n'run impacts generate most of their debris from the projectile. In this case, core material may not just be present but in much higher relative abundance relative to crust and mantle material than in the planetary parent body, since a large fraction of the silicate material may be sheared away and accreted by the target body while the remaining crust, mantle and core material is tidally ripped into a 'string of pearls' configuration of smaller bodies.

These giant impacts are unlikely to have occurred locally in the asteroid belt since that would require a comminution of a half-Earth sized body (roughly the right crust to mantle ratio) by a factor of 3×10^{-6}. Instead, we propose that this ejecta is transported, albeit inefficiently, from the terrestrial planet forming region into the asteroid belt via scattering events with the planetary embryos present in the terrestrial disk. In the terrestrial planet forming regions large quantities of debris should be generated, but only this small portion needs to be transported to match the observed quantities of differentiated asteroids.

The not Vestoid V- and A-type asteroids likely originate from the growing planets including Earth as indicated by (1) their relative abundances, which are consistent with the interiors of differentiated terrestrial planets, (2) their very low absolute abundances, which are consistent with inefficient dynamical transport, and (3) their absence in known disrupted planetesimals (*i.e.*, asteroid families) with the exception of the Vestoids.

f. *The influence of viscoelasticity on the stress state of the lithosphere: A comparison between a sticky air and real free surface approaches (M. Thielmann, in collaboration with V. Patocka/Prague)*

Numerical models of mantle convection typically employ a temperature- or pressure-dependent viscous or viscoplastic rheology and elasticity is ignored. This might be a good approximation for modelling the Earth's mantle where large temperatures result in low viscosities. However, with decreasing temperature, the viscosity of the rock increases, which might induce a change from viscous to elastic behaviour. Additionally, most mantle convection models employ a free slip boundary condition, whereas the Earth's surface is more accurately described by a free surface boundary condition. In finite element mantle

convection models, the implementation of such a boundary condition is straightforward whereas in finite difference/finite volume mantle convection models, it is commonly approximated by adding a low viscosity layer on top of the model domain (also called the "sticky air" approach).

Previous work has shown that the stress state of the lithosphere is significantly altered when a viscoelastic rheology is considered. Additionally, it has been shown that topography values estimated from models which employ a free slip boundary condition severely overestimate the maximum topography.

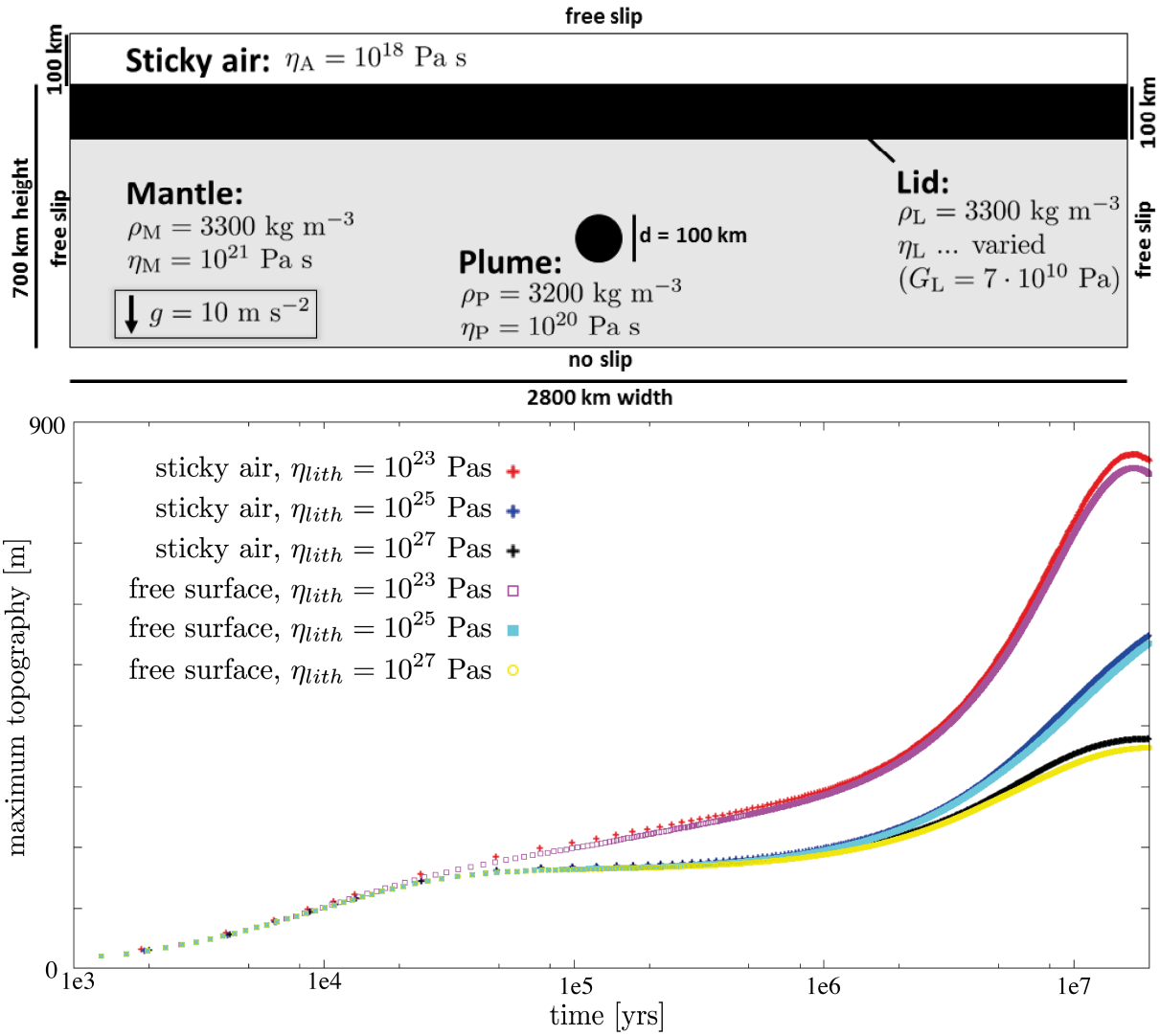

Fig. 3.1-4: (top row) Model setup. A circular plume is inserted in a viscous mantle which is overlain by a viscoelastic lithosphere. Due to its buoyancy, the plume rises, which results in a surface uplift above the plume. (bottom row) Time series of the maximum amplitude for several models. Results for both the true free surface and the sticky air approach yield very similar results.

In this project we investigate the impact of both numerical approaches on the topography and stress state of the lithosphere using a simplified model of a plume rising beneath a viscoelastic lithosphere (see Fig. 3.1-4). First simulations show good agreement between the maximum topography and the average stress computed in both models. This highlights the applicability of the sticky air approach which is easy to implement in models employing Eulerian meshes. Future work will include plastic yielding in the lithosphere, as this will reduce the effective viscosity in the uppermost lithospheric layers and thus also the stress state.

g. *Grain size assisted thermal runaway in mantle rocks: Impact of complex rheologies (M. Thielmann)*

The process of ductile strain localization in the lithosphere is one of the major processes shaping the Earth, as it controls the formation of shear zones and thus plate boundaries. Furthermore, depending on the speed of strain localization, this process might even result in earthquake-like events at depths where brittle failure is unlikely. Recent work has shown that the interplay between grain size reduction and shear heating significantly reduces the stress needed for thermal runaway (compared to models where only shear heating is considered). However, only dislocation and diffusion creep were considered in those models whereas mantle rocks exhibit even more complex rheologies where additionally Peierls creep and dislocation accommodated grain boundary sliding (disGBS) might also play a role.

In this study, I use numerical models of a slab in simple shear to investigate the impact of each single deformation mechanism on the critical stress needed for thermal runaway. Results indicate that while diffusion creep significantly reduces the critical stress, Peierls creep and disGBS limit the efficiency of shear heating and thus prevent thermal runaway (see Fig. 3.1.-5).

The reason for this inhibition lies in the fact that additional deformation mechanisms, in particular Peierls creep, limit the maximal stresses that can be reached for a given background temperature and strain rate and thus also limit the amount of heat that is produced during deformation.

Additionally, results indicate that the effect of disGBS is secondary to the effect of Peierls creep, which is mostly dominant at stresses where thermal runaway occurs. Given that the rheological parameters for Peierls creep are still highly unconstrained, the numerical results highlight the necessity to further investigate this mechanism.

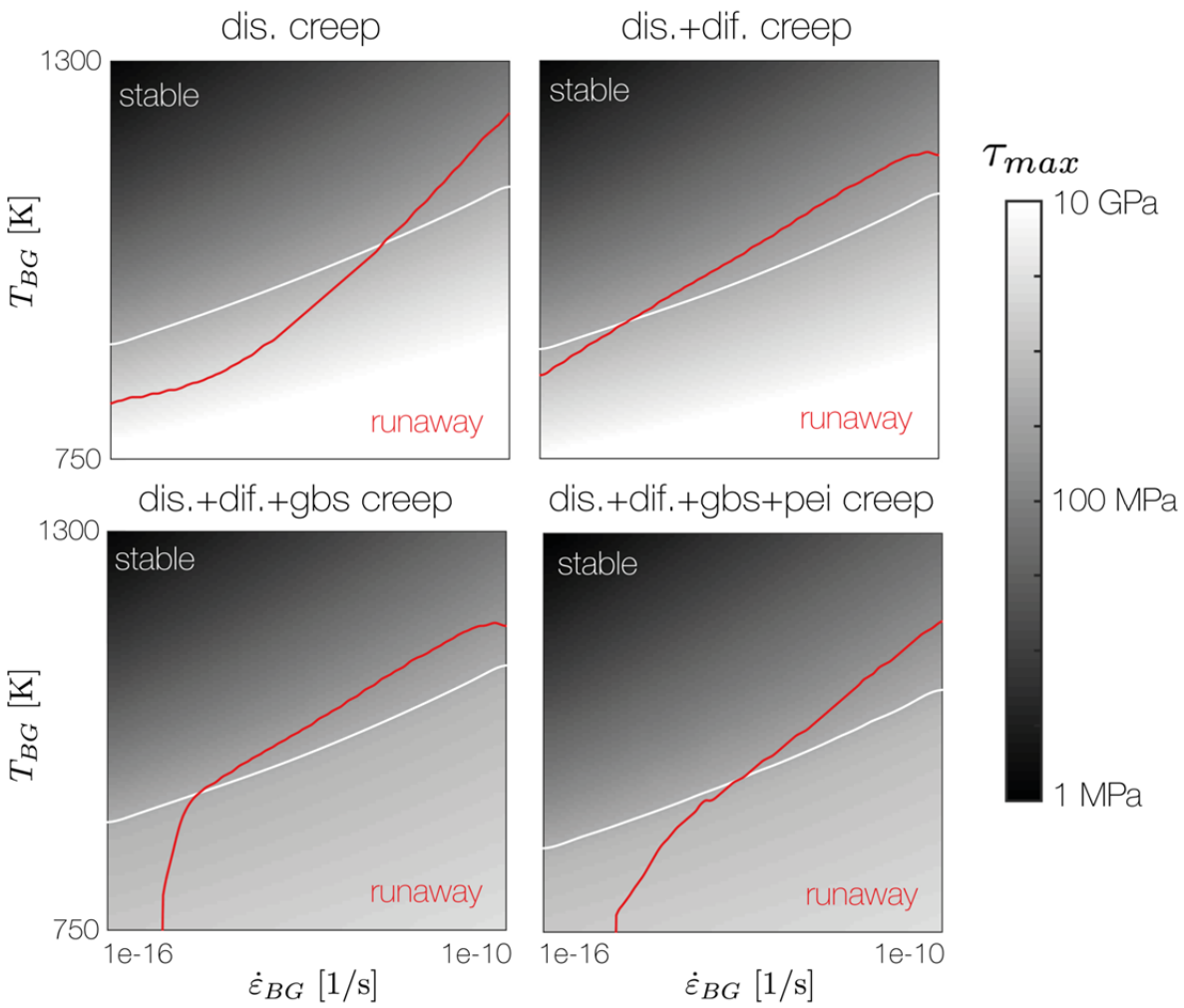

Fig. 3.1-5: Maximum stress and occurrence of thermal runaway for different background strain rates and temperatures. Grey colours indicate the maximum stress reached in each simulation, with the white line being the 500 MPa isoline. The red line indicates the regime boundary between stable simulations and simulations exhibiting thermal runaway. Each subplot shows simulation results for different combinations of deformation mechanisms.

3.2 Geochemistry

The studies presented in this section cover issues ranging from core–mantle differentiation to magmatic and hydrothermal processes operating close to the Earth's surface. A common theme of the studies dealing with deep processes is iron, which caused not only geochemical differentiation of planets and planetesimals during core formation, but also controls the oxidation state of the mantle via the valence state of Fe in minerals and potentially melts. Most of the remaining studies are broadly linked to ore deposits - either via direct investigations of the behaviour of metals, or via development of methods that allow the pressure, temperature or oxygen fugacity (fO_2) conditions of magma crystallization to be determined.

The first five contributions deal with phase relations and element diffusion within Fe-rich liquids and element partitioning between Fe-rich liquids and silicate melt. Two of these focus on Earth, two on smaller terrestrial planets, and one can be applied to both. Jennings *et al.* investigate the behaviour of Si, O, Mg, W and Mo during metal–silicate partitioning at extreme conditions to constrain the nature and abundance of light elements within the Earth's core and to identify the reason for the W deficiency in the mantle. They confirm that Si and O partition suitably into liquid iron such that they are both likely present in the Earth's core. The available partition coefficients of W were also comprehensively compiled in order to better constrain the effects of P, T and fO_2. The study of Laurenz *et al.* focuses on the behaviour of highly siderophile elements during segregation of late sulphide melts into the Earth's core. The results suggest that sulphide segregation followed by the accretion of a Late Veneer is consistent with the overall chondritic Re-Os ratios of the Earth's mantle. The contributions of Rubie *et al.* and Pommier *et al.* both deal with processes operating in terrestrial planets that are smaller than the Earth. Rubie *et al.* found that the extremely low Si content of iron meteorites can be explained by decreasing Si metal–silicate melt partition coefficients with increasingly oxidized conditions prevailing in the outer regions of the solar system. Pommier *et al.* constrained phase relations in the systems Fe-S and Fe-S-O at conditions relevant to small terrestrial planets to investigate the potential presence of light elements in their cores and how this could affect their dynamics. They found that a solid layer of FeO may have formed in some of these planetesimals. Posner *et al.* developed a model for Si, O and Cr diffusion in liquid iron with the aim of refining geodynamic models of planetary differentiation. They found that the diffusion coefficients can be scaled to the melting temperature, which can be used to constrain time-integrated models for planetary accretion and differentiation.

The next four contributions concern the stability of iron-bearing phases and corresponding iron valence states in the silicate portion of the Earth. Based on a series of fO_2-buffered multianvil experiments Armstrong *et al.* discovered that above a pressure of ca. 15 GPa the $Fe^{3+}/\Sigma Fe$ ratio in andesitic melt increases dramatically with pressure, which means that the

apparent gradient in oxygen fugacity between the deeper and shallower mantle would have already been established in an early magma ocean. Woodland *et al.* found that above a pressure of ca. 10 GPa several iron compounds with stoichiometries between those of Fe_xO and Fe_3O_4 are stable, namely Fe_5O_6 and $Ca_2Fe_2O_7$. These phases add further complexities to the control on oxygen fugacity in the Earth's mantle. In the following study by Siersch *et al.* the presence of ferric iron is proposed to expand the stability field of majoritic garnet at the expense of akimotoite at conditions comparable with the base of the transition zone at ~600 km. This may be more of an experimental problem, however, as typical mantle ferric iron contents are probably lower than those in the experiments and may not have this effect. Iron compounds could potentially play a role also in the deep carbon cycle. Based on laser-heated diamond anvil cell experiments Serovaiskii *et al.* argue that significant amounts of carbon may be recycled into the deep mantle by means of hydrocarbon liquids trapped in subducted sediments, which react with Fe-bearing mantle rocks to form iron carbide.

The following two studies deal with diffusion phenomena. Polednia *et al.* quantify grain boundary diffusion of Fe and La in yttrium-aluminium-garnet (YAG). The results are primarily used to optimize the manufacture and performance of polycrystalline YAG lasers, but they can also be applied to geological questions such as the origin of cryptic metasomatism in mantle rocks or the effect of grain boundary films on their deformation behaviour. Audétat and Zhang found that copper can diffuse extremely rapidly through common rock-forming minerals such as plagioclase, amphibole, olivine, clinopyroxene, orthopyroxene and apatite, raising doubts as to whether Cu contents recorded in silicate melt inclusions and their host minerals are trustworthy.

Thermobarometry of felsic upper crustal magmas is the topic of the next two contributions. Arató and Audétat tested a newly developed oxybarometer based on the partitioning of vanadium between magnetite and silicate melt on a large number of natural, silicic magmas and found that the results agree well with those obtained via Fe-Ti-oxide oxybarometry. Zarei and Audétat continued a long-term project to calibrate a thermobarometer based on the partitioning of Ge and Al between quartz and silicate melt and to refine the already existing Titanium-in-quartz thermobarometer.

Guo and Audétat investigated the solubility of gold in oxidized, sulfur-bearing fluids. They found that the presence of oxidized sulfur does not enhance Au solubility, but that Au extraction by magmatic fluids may have been particularly efficient at the oxidized conditions typical of a porphyry Cu environment. Last but not least, Zhang and Audétat performed a detailed petrographic and microanalytical study on two porphyry Mo deposits in the United States, from which they concluded that the mineralizing magmas were not particularly Mo-rich, but that metal extraction and focusing may have been unusually efficient due to low melt viscosities.

a. *Partitioning of light elements and siderophile elements into the core: An experimental and database approach (E.S. Jennings, D.C. Rubie, D.J. Frost, S. Petigirard, V. Laurenz, N. Miyajima and O. Lord/Bristol)*

The Earth's core is thought to have formed by the segregation of Fe-rich metallic liquid from one or more silicate magma oceans early in Earth's history. Its density deficit could be explained if it consists of around 10 % of a light element, with Si and O being two strong candidates. In addition, the low concentration of siderophile elements in the Earth's mantle relative to chondrites are likely explained by their fractionation into the core. However, the feasibility of these hypotheses depends upon the geochemical behaviour of the elements involved at the high pressure and temperature conditions of core formation, *i.e.*, how they partitioned between the liquid metal of the core and liquid silicate of one or more magma oceans during core segregation. In this ongoing study, we perform new metal-silicate partitioning experiments and create an extensive database of previously published experiments to interrogate a) the partitioning of light elements (Si, O +/- Mg) into the core and b) reassess the *P*, *T* and compositional dependencies of W and Mo partitioning, in order to better understand the apparent W deficiency in the present-day bulk silicate Earth.

We perform laser-heated diamond anvil cell (DAC) and multianvil (MA) experiments in the simple Mg-Si-Fe-O system to examine light element partitioning between silicate melt and liquid metal without the complicating effect of other species being present. MA experiments (BGI) are run in single-crystal MgO capsules with mixed powdered starting materials, where the metal contains some Si in order to reduce the fO_2. DAC experiments are run in Re gaskets with single crystal MgO disk insulators and either metal foil or powder within a glassy silicate powder. Pressure is estimated from ruby fluorescence and diamond Raman shifts; temperatures are estimated spectroscopically in 1D and 2D. Compositionally simple system experiments are well suited for thermodynamic analysis. DAC run products are prepared as lamella by focussed ion beam milling and analysed by TEM; we are also developing a technique to analyse thicker slices of DAC experiments by EPMA with the hope to increase analytical precision and to decrease fluorescence in order to be able to achieve lower detection limits (*e.g.*, for Mg in metal; see below). Preliminary results along with published data indicate that Si and O are able to coexist within liquid metal at high *PT* conditions and that partitioning is predominantly a function of temperature and fO_2, confirming the feasibility of these elements being present in the core.

EPMA is advantageous over analytical TEM for quantitative chemical analysis because it is convenient to use, provides data of better precision, is less affected by fluorescence, and requires less time-intensive sample preparation. However, thin samples (< 3 microns) and small analytical areas (< 10 microns) present unique analytical challenges: samples that are too thin to give low totals, with different elements being affected to different extents, and secondary fluorescence caused by nearby grain boundaries is known to contaminate trace element analyses. We are performing various test analyses on 1-3 micron thick samples by

EPMA in order to assess the effects of thickness and geometry on data quality, and supplement the obtained results with Monte-Carlo simulations (using the software pyPENEPMA) to investigate the consequences with regard to quantitative analysis of DAC samples.

We have compiled a database of over 700 published and unpublished (from studies conducted at BGI) metal-silicate partitioning experiments in order to statistically interrogate the effects of pressure, temperature, oxygen fugacity and melt compositions on partitioning behaviour. The use of a larger dataset leads to more widely applicable partition coefficients. In particular, we focus on W, which is depleted in the present-day mantle relative to what is expected from current estimates of bulk Earth concentration and partition coefficient. We use the newly fitted partition coefficients for accretion models in which the silicate and metal compositions vary more widely than the variations typically seen in single experimental studies.

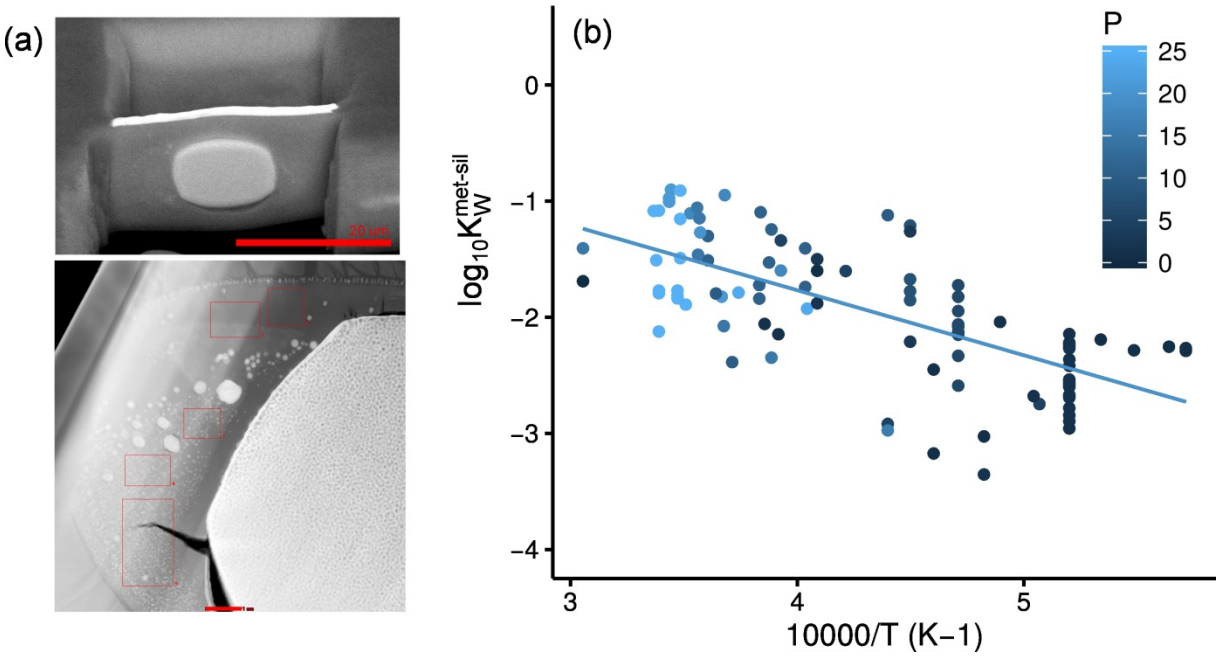

Fig. 3.2-1: a) top: image of a DAC experiment being prepared for TEM analysis by FIB (red bar is 20 µm); bottom: TEM image of fine-scale structures of a DAC experiment showing quenched metal, silicate and quench features (red bar is 1 µm). b) Experimental W partitioning data ($K = D_W/D_{Fe}$, activity-corrected) as a function of temperature and pressure from the compiled dataset, plus corresponding fitting curve. There is a high degree of covariance between pressure and temperature in the dataset.

b. *Sulphide-silicate partitioning of Re and Os at high pressures and temperatures (V. Laurenz, D.C. Rubie and D.J. Frost)*

The origin of highly siderophile element (HSE; Re, Os, Ir, Ru, Pt, Pd, Rh, Au) abundances in the Earth's mantle is generally explained by the so-called Late-Veneer hypothesis. This

proposes segregation of Fe-rich metal to form the Earth's core, during which the mantle became strongly depleted in HSEs. Abundances of the HSEs were then raised to their current values by the addition of chondritic material to the mantle after core formation ceased. It has been proposed that sulphide melt was also sequestered to the core. Our recent experimental results have shown that sulphide segregation could explain suprachondritic Pd/Ir and Ru/Ir ratios observed for the Earth's mantle, because Ru and Pd are less chalcophile than Ir and Pt under high *P-T* conditions.

One of the most powerful constraints for HSE geochemistry in the Earth's mantle is its Os-isotope composition. ^{187}Re undergoes β-decay to ^{187}Os with a half-life of 41.6 Ga. ^{187}Os/^{188}Os ratios of the mantle can therefore be utilized as a monitor of its time-integrated Re/Os ratio. The Earth's mantle shows an overall enstatite chondrite-like Os-isotope composition, indicating that the Earth's mantle evolved with a long-term chondritic Re/Os ratio. In contrast, Os is much more chalcophile than Re at low *P-T* conditions (1200-1400 °C and 1 bar) so that Re and Os become fractionated by sulphide-silicate equilibration during MORB genesis. However, to assess whether sulphide segregation is consistent with the chondritic Re-Os signature of the mantle requires information on the sulphide-silicate partitioning of Re and Os at appropriate conditions.

We, therefore, experimentally investigated the sulphide-silicate partitioning of Re and Os at high pressures and temperatures. A molten peridotite composition was equilibrated with FeS melt doped with Re and Os (~ 10 wt. % each). Experiments were performed at temperatures of 2100-2400 °C and pressures of 7-21 GPa. All experiments were run in a multianvil-apparatus using single-crystal MgO capsules. Major element compositions of quenched silicate and sulphide melts were determined by electron microprobe, whereas Re and Os concentrations in the silicate melt were analysed using LA-ICPMS.

Experimental results indicate that both Re and Os behave as chalcophile elements under high *P-T* conditions. Overall, $K_D^{\text{sulphide-silicate}}$ (Os) is ~ 1.5-2 orders of magnitude higher than $K_D^{\text{sulphide-silicate}}$ (Re) (Fig. 3.2-2). $K_D^{\text{sulphide-silicate}}$ for Re increases with increasing temperature, while the effect of *T* on Os sulphide-silicate partitioning is less clear. This is most likely due to the extremely low Os concentrations in the quenched silicate melt, which are challenging to analyse by LA-ICPMS. We have used the results of Re sulphide-silicate partitioning in a simple core formation model to constrain the behaviour of Re and other HSEs (Pt, Pd, Ru, Ir) during core formation. The behaviour of Os could not be modelled because the metal-silicate partitioning of Os at high *P-T* is not well known. The results reveal that mantle abundances of Re and the other HSEs are well reproduced. If Ir is used as a proxy for the behaviour of Os the model suggests that sulphide segregation may be consistent with the chondritic Re-Os ratio of Earth's mantle. Once data on the metal-silicate partitioning of Os are available, the results of this study will be incorporated into a combined accretion and core-formation model in order to test whether the segregation of a sulphide melt to the core is consistent with the chondritic Re-Os ratio of Earth's mantle.

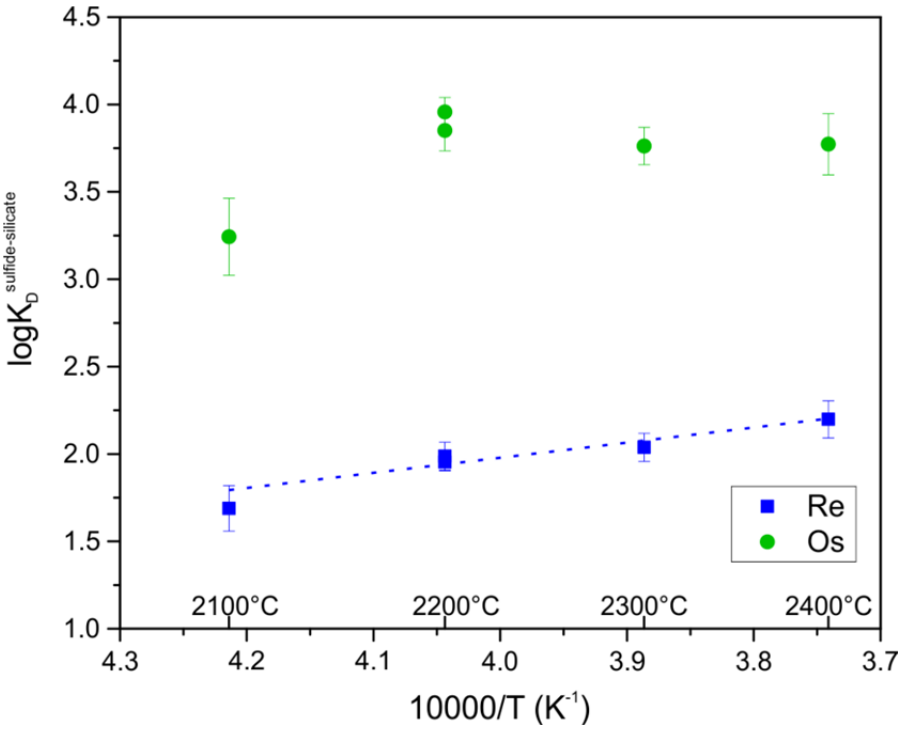

Fig. 3.2-2: Partitioning of Re and Os between sulphide melt and peridotite liquid. Logarithmic values of the exchange coefficient $K_D^{\text{sulfide-silicate}}$ of Re and Os are plotted as a function of inverse temperature. $K_D^{\text{sulfide-silicate}}$ (Os) is about 2 orders of magnitude higher than that of Re.

c. *Conditions of core-mantle differentiation of planetesimals constrained by silicon concentrations in iron meteorites (D.C. Rubie, E.S. Posner, E.S. Jennings and H. Palme/Frankfurt)*

Most groups of iron meteorites are considered to have originated as planetesimal cores because of their trace element systematics. For example, the concentrations of elements such as Ni, Au, Ir and Os can be explained by the fractional crystallization of liquid Fe-Ni metal that contains some S, C and P. Core formation in early-formed planetesimals would not only segregate highly siderophile elements into planetary cores, but also weakly-siderophile elements such as Si, Cr, V and Mn. However, the concentrations of Si and Cr in iron meteorites are so low that it has been concluded that they cannot have been established by metal-silicate equilibration at high temperatures. Concentrations of Si in iron meteorites are below 1 ppm in most cases and it has been concluded previously that this is at least 100 times lower than expected at magmatic temperatures.

We have shown previously that the compositions of bodies that formed early in the Solar System were determined by an oxidation gradient in the protoplanetary disc (Fig. 3.2-3). Bodies that formed close to the Sun, *e.g.*, at heliocentric distances < 1 astronomical units (AU) were highly reduced such that all Fe was present as metal which also had a significant

Si content. With increasing heliocentric distance, bodies were increasingly oxidized along the gradient such that the ratio of FeO in silicate to Fe in metal increased. We have modelled core-mantle differentiation of planetesimals over this range of oxidation states based on mass balance combined with metal-silicate element partitioning at different differentiation temperatures. We assumed that bulk compositions are defined by solar (CI) element ratios with oxygen content being the only compositional variable. At differentiation temperatures below the peridotite liquidus (~ 2045 K at low pressure), the presence of olivine and orthopyroxene in the partial molten silicate is taken into account.

Results are shown in Fig. 3.2-4 for planetesimals with a radius of ~ 250 km and differentiation temperatures of 2000 K and 1600 K. At both differentiation temperatures, the calculated concentrations of silicon in planetesimal cores decrease strongly with increasing heliocentric distance as the oxidation state (oxygen content) increases. At the higher temperature of 2000 K, the lowest Si concentration is higher than values analysed in iron meteorites by a factor of 10. At 1600 K however, calculated values are consistent with analysed values in all bodies that originated at heliocentric distances > 1.7 AU because of a lower silicon partition coefficient.

There are two possible conclusions based on these results. (1) Planetesimals underwent core-mantle differentiation at temperatures significantly below that of the peridotite liquidus, at oxidation states that resulted in very low Si concentrations in the cores. (2) Differentiation temperatures were high and resulted in high concentrations of Si in the core. During planetesimal cooling, the core and mantle equilibrated partially thus reducing the Si concentrations to the observed values. We are currently developing a model of core-mantle interaction during planetesimal cooling that will enable the second possibility to be evaluated.

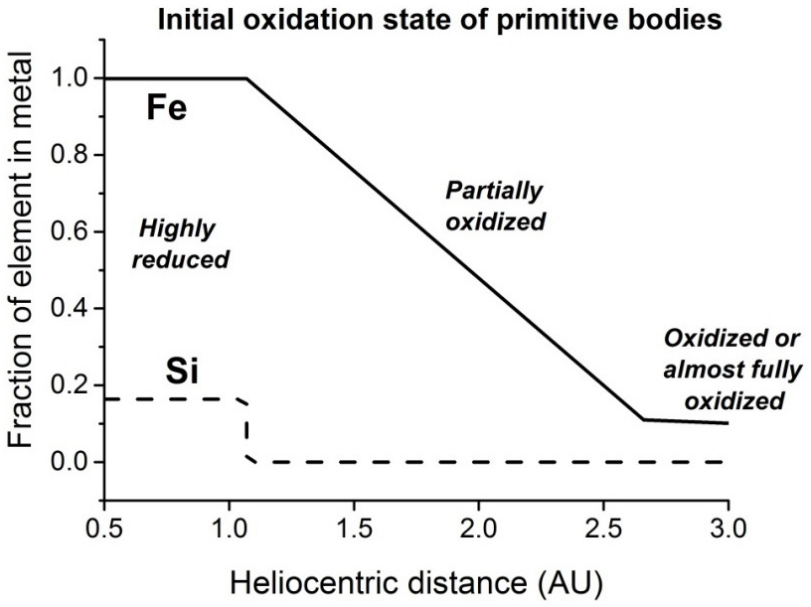

Fig. 3.2-3: Oxidation gradient in the protoplanetary disc defined by the fractions of bulk Fe and Si that are present as metal.

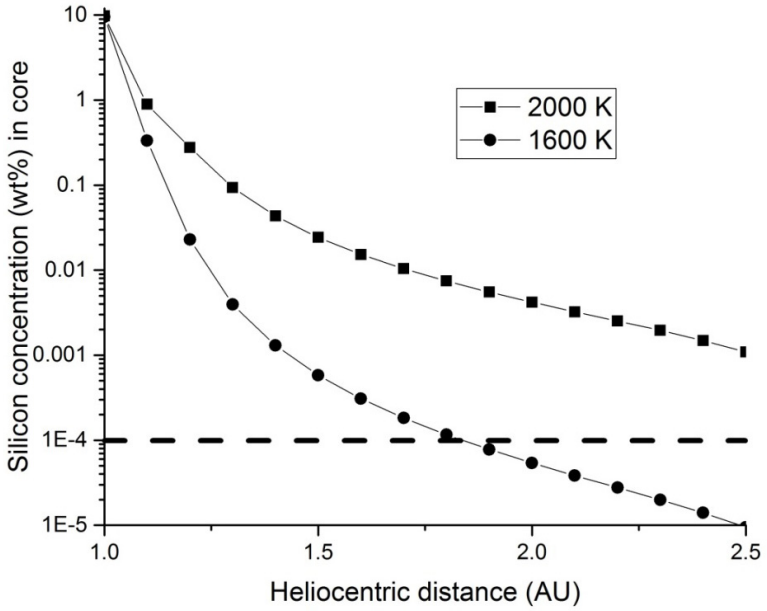

Fig. 3.2-4: Silicon content of planetesimal cores after core-mantle differentiation as a function of heliocentric distance for planetesimals with a radius of 250 km. Results are shown for differentiation temperatures of 2000 K and 1600 K. The horizontal dashed line shows the upper limit of Si concentrations that have been reported previously in iron meteorites.

d. *Melting phase relations in the Fe-S and Fe-S-O systems at core conditions in small terrestrial bodies (A. Pommier/San Diego, V. Laurenz, C.J. Davies/San Diego and D.J. Frost)*

A combination of several wt. % of light elements (*e.g.*, sulphur, oxygen, hydrogen, nitrogen, carbon, silicon) could have been added to the metallic core of terrestrial planets during differentiation processes. Sulphur is thought to be a major light element in such cores due to its high solubility in liquid iron and due to the possible segregation of liquid FeS into the core. Another major candidate is oxygen because of its high abundance in the bulk Earth, its partitioning behaviour into metal at core pressure and temperature, and because thermodynamic calculations and high-pressure experiments showed a high solubility of S and O in liquid iron. Because high solubilities of S and O in liquid Fe are observed also at shallower pressure than Earth's core pressure, it is possible that the metallic cores of terrestrial planetary bodies smaller than the Earth, such as Mars, Mercury, and Ganymede, also contain these two light elements in significant amounts.

We report an experimental investigation of the phase equilibria in the Fe-S and Fe-S-O systems at high temperatures (1400-1850 °C) and high pressure (15 and 21 GPa) using a multianvil apparatus. The results of this study are used to understand the effect of oxygen on core dynamics of small terrestrial planets, such as Mars, Mercury, and Ganymede. Our experiments show that oxygen has little effect on the liquidus temperature and that the formation of FeO occurs in the form of a solid layer at the Fe-S liquid – Fe solid interface at high temperature (> 1400 °C at 21 GPa).

Oxygen fugacities calculated for each O-bearing sample show that redox conditions vary from ΔIW=-0.65 to 0. Considering the relative density of each phase and existing evolutionary models of terrestrial cores, we apply our experimental results to the cores of Mars, Mercury, and Ganymede. We show that the presence of FeO in small terrestrial planets tends to contribute to compositional stratification within the core due to density contrasts. Depending on the redox and thermal history of the planet, FeO may also help to form a transitional redox zone at the core-mantle boundary.

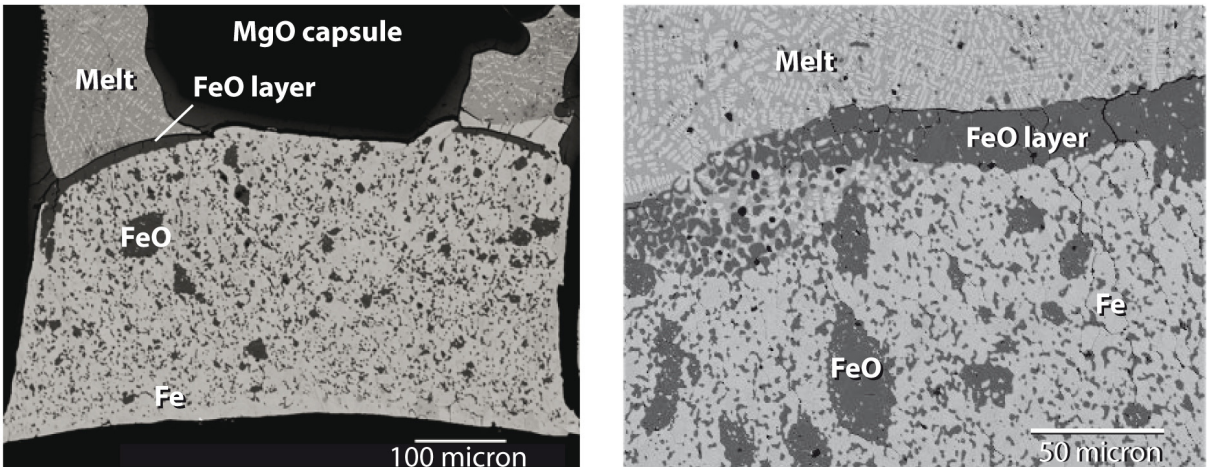

Fig. 3.2-5: Back-scattered electron images of run products in the Fe-S-O system. Left: FeO layer (grey) in a sample containing 3 wt. % O from 15 GPa, 1500 °C. Note the slightly lighter colour of the MgO capsule in the vicinity of the sample, which stems from the formation of ferropericlase and can be used to estimate fO_2. Right: Sample containing 3 wt. % O equilibrated at 1400 °C and 15 GPa, showing the presence of a continuous FeO layer at the liquid/solid interface

e. *Experimental and theoretical determination of Si, O, Cr diffusion in liquid iron at high P-T (E.S. Posner, D.C. Rubie, D.J. Frost, V. Vlček and G. Steinle-Neumann)*

Diffusion transport properties of molten iron and iron alloys at high pressures and temperatures are important for understanding large-scale geodynamic processes and thermochemical evolution of planetary interiors, such as the time and length scales of metal-silicate equilibration during core formation and chemical exchange across core-mantle boundaries during cooling. The chemical diffusivity of light and siderophile elements in liquid iron under *P-T* conditions of the Earth's core and during its formation are also required to constrain the composition and potential chemical stratification of planetary cores, in addition to the kinetics of chemical buoyancy from inner core crystallization that partially drives planetary geodynamos. In order to better understand the effects of pressure and temperature on Si, O, and Cr diffusion in liquid iron, we have conducted (1) chemical diffusion-couple experiments combined with numerical modelling of diffusion profiles to

account for non-isothermal annealing, and (2) first principles molecular dynamic (FP-MD) calculations from ambient pressure to 330 GPa and 2200-5500 K. This is the first study to jointly use and compare experimental and theoretical results, conducted under similar conditions, to measure the effect of pressure on diffusion in liquid iron and iron alloys.

One important result from this study is that diffusion coefficients in liquid iron can be scaled to melting temperature (Fig. 3.2-6), a finding that simplifies the modelling of chemical diffusion length and timescales that occur over a wide range of pressure conditions (*i.e.*, descending metal droplets during core formation, or chemical evolution of planetary bodies of different radii) (Fig. 3.2-7). A homologous temperature relation for diffusion in liquid metals was predicted from theory but had not been previously verified by experiments. Additionally, the wide range of *P-T* conditions afforded by FP-MD simulations provides new insight into the chemical systematics of liquid iron alloys in terms of their compression mechanisms (*e.g.*, trends of interatomic distances and coordination numbers with increasing liquid density), as well as a connection between transport and structural properties, which may be used as a proxy to estimate the solubility and/or solid-liquid partition coefficients of relevant solute species.

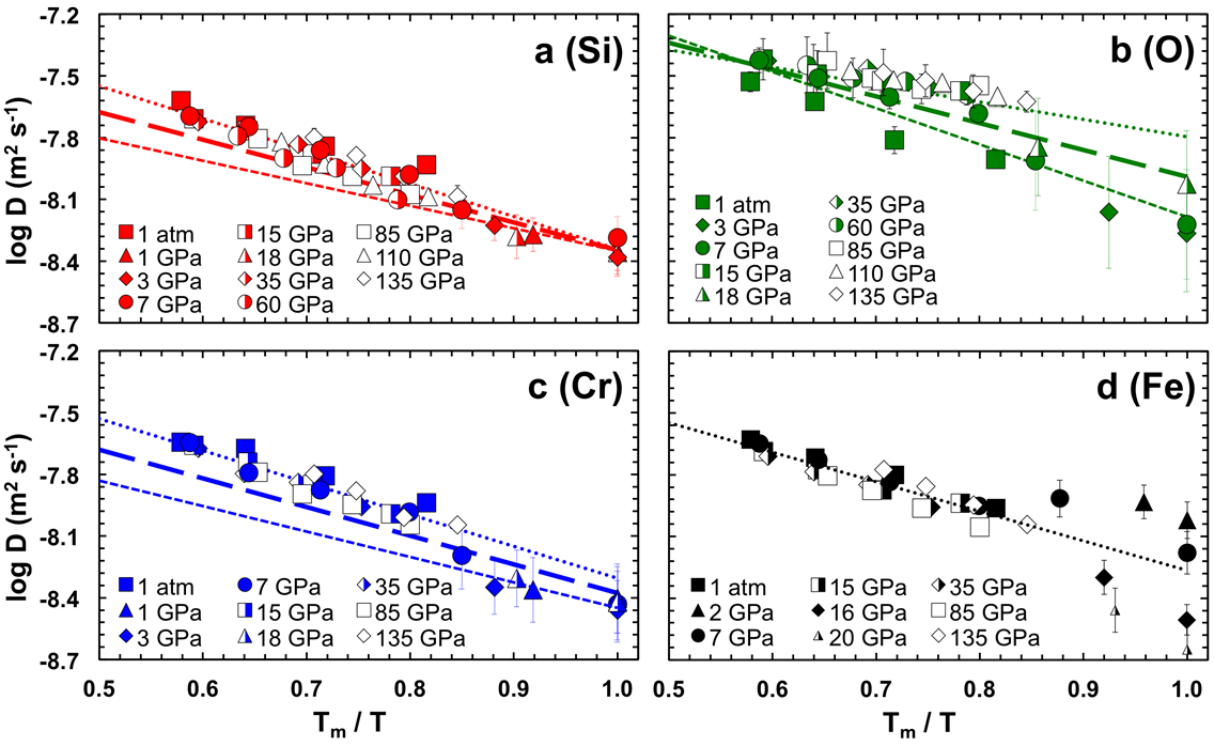

Fig. 3.2-6: Diffusion coefficients determined from experiments performed at up to 18 GPa and calculations performed at up to 135 GPa are shown as a function of T_m / T for (a) Si, (b) O, (c) Cr, and (d) Fe. Experimental Fe self-diffusion data are from (Dobson, 2002, *PEPI* 130:271). Linear fits to the experimental data (short-dashed lines) and FP-MD results (dotted lines) are shown. Averaged linear fits to both experiments and calculations are shown as long-dashed lines for Si, O, Cr.

Diffusion coefficients calculated from FP-MD simulations are in excellent agreement with experimental results. Arrhenian activation terms of Si, O, and Cr chemical diffusion obtained by both methods are appreciably smaller and more consistent with empirical and theoretical data than previously reported experimental values for Fe and alloying element self-diffusion in liquid iron and iron alloys derived from much smaller data sets. Our findings corroborate theoretical estimates that diffusion coefficients are scalable to homologous temperature (T_m/T), where T_m is the melting temperature, yielding constant Si and Cr diffusivities of approximately 5×10^{-9} m^2 s^{-1} along the melting curve from ambient to core pressures. Oxygen diffusion is 2-3 times faster than that of Si and Fe, in agreement with previous theoretical studies. The homologous temperature activation term determined from FP-MD calculations for Si diffusion is larger by a factor of 1.3 than the value determined from experiments but diffusion coefficients at T_m are identical within error for both two methods. Verification of a homologous temperature relation for chemical diffusion in liquid iron implies that low-pressure experiments can be used as accurate analogues of mass transport properties of the Earth's outer core.

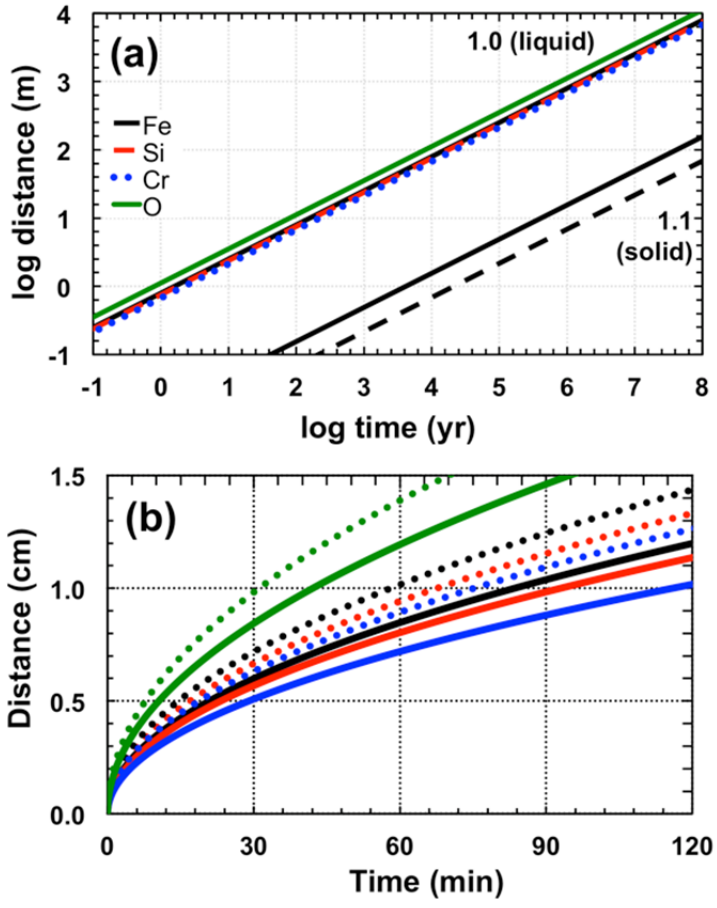

Fig. 3.2-7: Characteristic diffusion distances are shown as a function of time for Fe (black curves), Si (red), O (green), and Cr (blue) at liquidus temperatures ($T_h = T_m/T = 1$). For comparison, Fe-Ni interdiffusion in solid iron ($T_h = 1.1$) is shown in panel (a) following Reaman *et al.* (2012, *EPSL* 349-350:8) (black curve) and Yunker and Van Orman (2007, *EPSL* 254:203) (dashed curve). Centimeter-scale diffusion times in liquid iron and its alloys for $T_h = 1$ and $T_h = 0.9$ (dotted curves) are shown in panel (b).

Chemical equilibration timescales, t_{eq}, of liquid metal droplets sinking in a magma ocean during accretion are largely controlled by the droplet size (*i.e.*, diffusion distance). In order to estimate maximum timescales for chemical equilibration within sinking metallic bodies, we use a simple model for diffusion in a sphere of radius *a* based on the chemical potential alone using diffusion coefficients calculated for a range of T_m/T values. We show our results in Fig. 3.2-7. Chemical equilibration in emulsified metal-silicate mixtures ($r << 1$ mm) is nearly instantaneous ($t_{eq} << 1$ min), while metallic droplets of $r \sim 0.5$ cm would require several tens of minutes. Impactor cores of 500 m radius, on the other hand, even if completely molten during descent, would not equilibrate on realistic timescales of core formation, requiring 10^4-10^5 years for diffusive equilibration. This finding implies that large impactor cores can maintain chemical disequilibrium with the surrounding silicate liquid during rapid gravitational descent through a magma ocean. The effects of turbulent mixing in the liquid sphere interior could significantly reduce t_{eq} and should be investigated in future studies to yield "realistic timescales" that incorporate additional mixing processes.

f. *The effect of pressure on the ferric/ferrous ratio of silicate melts: Implications for the redox profile of a terrestrial magma ocean (K. Armstrong, D.J. Frost, D.C. Rubie, C.A. McCammon and T. Boffa Ballaran)*

During core formation, mantle silicates were in chemical equilibrium with iron metal. Oxybarometry of mantle xenoliths and mid-ocean ridge basalts, however, indicate that today the upper mantle is uniformly 4-5 orders of magnitude more oxidised than the level imposed by metallic iron. Studies of ancient rocks suggest that this more oxidised state was attained by at least 3.9 Ga, so oxidation occurred very rapidly after core formation ceased. One proposed oxidation process is based on the observation that the high-pressure phase bridgmanite can contain large amounts of ferric iron, even when coexisting with iron metal. This stability of ferric iron may force the disproportionation of FeO into Fe_2O_3 and metallic iron. Subsequent removal of some of this precipitated metallic iron to the core would result in raising the bulk oxygen content of the mantle.

It is possible that silicate melts may mirror this behaviour and that an analogous process could occur at depth within a global magma ocean. During the later stages of accretion, the Earth almost certainly experienced at least one giant impact that was energetic enough to have melted a significant fraction of the mantle. Metallic iron would fall through the molten silicate, ultimately setting the $Fe^{3+}/\sum Fe$ ratio of the magma ocean at the high pressure and temperature conditions of its base. If pressure stabilises ferric iron in silicate melts, this $Fe^{3+}/\sum Fe$ ratio may be relatively high. This would establish a redox gradient in the magma ocean similar to that in the Earth's mantle today, where for the same $Fe^{3+}/\sum Fe$ ratio, the melt would be in equilibrium with metallic iron at its base but with an oxygen fugacity several log units higher at the surface.

To test this hypothesis, silicate melt was equilibrated at variable pressures at a constant fO_2, defined by the reaction Ru + O_2 = RuO_2, extending the work of O'Neill *et al.* (Am Min. 91, 404; 2006). A starting material with an andesitic bulk composition (in wt. %: SiO_2 – 57.3, TiO_2 – 3.0, Al_2O_3 – 14.8, Fe_2O_3 – 9.4, MgO – 2.1, CaO – 7.4, Na_2O – 4.4, and K_2O – 1.1.) was sealed in welded Pt capsules and equilibrated at high pressures and superliquidus temperatures in a multianvil press. Recovered samples were sliced to a thickness of 500 µm for transmission Mössbauer spectroscopy, with one side polished for SEM, X-ray diffraction, and electron microprobe analyses. Transmission Mössbauer spectra were collected over a 500 µm diameter spot in the centre of selected samples that were parallel ground to a thickness of 500 µm, giving an effective Mössbauer thickness of roughly 10 mg Fe/cm^2.

In all experiments, the sample melted completely but crystallised on quenching. Backscattered electron images, XRD, and EMPA indicate all samples comprise homogeneous clinopyroxene, coesite or stishovite, and the pure buffer phases Ru and RuO_2.

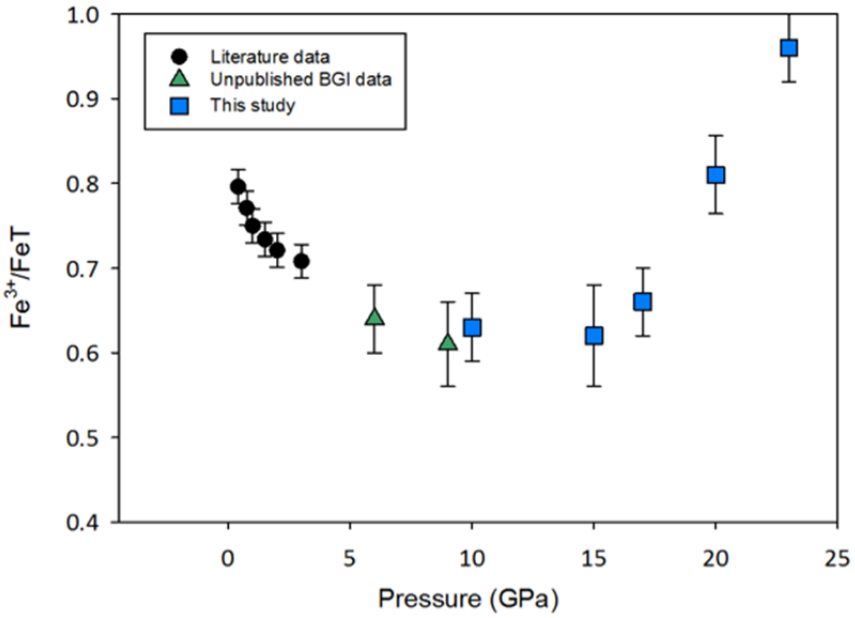

Fig. 3.2-8: $Fe^{3+}/\sum Fe$ ratio, as measured by transmission Mössbauer spectroscopy, of an andesitic melt at the Ru/RuO_2 oxygen fugacity buffer as a function of pressure. The increase in ferric iron that begins above 15 GPa potentially indicates that Fe^{3+} is being stabilised with pressure. If this is the case, the reaction 3FeO = Fe^0 + Fe_2O_3 may proceed to the right at depth in a magma ocean, precipitating metallic iron. The removal of some of this iron to the core would result in a net oxidation of the silicate mantle.

Figure 3.2-8 summarises the results obtained from this study, along with previous work perfromed with the same composition at the Ru/RuO_2 fO_2 buffer. At lower pressures, the ferric iron content decreases with pressure, which has been attributed to a positive volume change of the reaction FeO + ¼ O_2 = $FeO_{1.5}$. However, at higher pressures this trend has reversed and the ferric iron content begins to increase. If this increase is a result of pressure,

then the ferric iron content of a chemically homogeneous magma ocean, which is set at high pressure, would be relatively high. Such a magma ocean would have an oxygen fugacity gradient with depth; metal saturated at its base, but in equilibrium with more oxidised volatile species, such as H_2O and CO_2, at the surface.

g. *Fe_5O_6 and related Fe-oxides (A.B. Woodland and L. Uenver-Thiele/Frankfurt, T. Boffa Ballaran and D.J. Frost)*

Iron is a major constituent of the Earth and its ability to adopt different valence states (Fe°, Fe^{2+}, Fe^{3+}) makes the simple Fe-O system fundamental for understanding many geochemical processes. Until recently, it was generally accepted that wustite (Fe_xO), magnetite (Fe_3O_4) and hematite (Fe_2O_3) are the stable phases in this system. However, the discovery of Fe_4O_5 as a breakdown product of magnetite at high pressures and temperatures changes the phase relations relevant for deep mantle conditions. The more recent discovery of Fe_5O_6 adds even more complexity to the high-pressure, high-temperature phase relations in the Fe-O system. With a $Fe^{3+}/\sum Fe = 0.4$, Fe_5O_6 is expected to be stable under more reducing conditions than Fe_4O_5, which has $Fe^{3+}/\sum Fe = 0.5$. Experiments were performed to determine the P-T stability of Fe_5O_6 in order to assess the potential for this phase to occur in the deep upper mantle or transition zone (*i.e.*, 8-23 GPa and 1000-1600 °C). The low-P phase boundary lies at around 9 GPa, with magnetite + wustite being the stable low-P assemblage. Fe_5O_6 has a large stability field, up to at least 23 GPa over a wide range in temperature. Its crystal structure was confirmed by single-crystal diffraction measurements to belong to the *Cmcm* space group. Depending on the bulk oxidation state, Fe_5O_6 can coexist with either wustite or Fe_4O_5. However, in several experiments another phase appeared in the run products. Analysis of powder X-ray diffraction patterns revealed this phase to be consistent the crystal structure of $Ca_2Fe_7O_{11}$, which implies a stoichiometry of $Fe^{2+}{}_5Fe^{3+}{}_4O_{11}$. This phase represents an intermediate stacking sequence and composition between Fe_5O_6 and Fe_4O_5, which leads to a reduction in symmetry to a monoclinic unit cell. The stability range of this phase remains to be determined, but it indicates that a significant number of Fe-oxide phases with different stoichiometries become stable at pressures of ~ 10 GPa and above.

h. *Phase relations at the base of the transition zone (N.C. Siersch, T. Boffa Ballaran and D.J. Frost)*

Seismic wave velocities at the base of the transition zone, determined from 1 D reference models, are significantly faster than mineral physics based models for the expected velocities if the mantle is composed of either a peridotite or basaltic bulk composition. It has, consequently, been suggested that this may result from temperature anomalies associated with stagnant slabs at the base of the transition zone. Such lower temperatures relative to the

mantle geotherm, however, will stabilize the mineral akimotoite at the expense of majoritic garnet. Very little is known about the composition of akimotoite in mantle compositions and in particular about its Fe and Al content when akimotoite is present in equilibrium with ringwoodite. This is hence the aim of this study.

Five experiments were performed in a multianvil apparatus using a KLB-1 peridotite starting composition in a Re foil capsule. These runs were conducted at pressures between 22 and 23 GPa and heated at temperatures between 1300 and 1600 °C for 10 to 21 hours. After recovery, the samples were embedded in hardened epoxy and polished on one side such that X-ray diffraction phase identification measurements and electron microprobe analyses could be performed. The run-products were found to consist exclusively of ringwoodite and majoritic garnet, a result which is in clear conflict with the synthesis conditions of akimotoite previously reported. The major element compositions of several crystals of ringwoodite and majoritic garnets in each sample were measured using the electron microprobe.

The compositions of the ringwoodite and majoritic garnet crystals do not differ significantly among the different experimental runs. Ringwoodite was found to contain 1.5(7) wt. % of Al_2O_3 in its structure and iron oxide contents were 14(2) wt. % in ringwoodite and 12(1) wt. % in majorite. This implies a surprisingly high Fe-Mg garnet-ringwoodite exchange coefficient compared to previous results. It is possible that this results from high levels of ferric iron in majorite that may cause an expansion of the garnet stability field at the expense of akimotoite. More synthesis experiments need to be performed at different P-T and fO_2 conditions to explore the stability field of akimotoite within a mantle bulk composition.

i. *Iron hydride formation from hydrocarbons and iron-bearing rocks at upper mantle conditions (A. Serovaiskii, E. Mukhina and A. Kolesnikov/Moscow; C.A. McCammon, G. Aprillis and L.S. Dubrovinsky; V. Kutcherov/Stockholm)*

Subduction plays a key role in mass transfer between the Earth's crust and mantle. During subduction crustal components including O, Si, Fe and C submerge into the mantle. It is generally believed that carbon in subducting slabs is present mainly in the form of carbonates and crystalline graphite. However, giant petroleum deposits exist in sediments above subduction zones, thus it seems justified to consider also petroleum in the global carbon cycle. During subduction petroleum hydrocarbons may transform and react with surrounding minerals (primarily iron-bearing minerals) during increasing pressure and temperature. Therefore, we decided to investigate the possible chemical interaction between hydrocarbons and iron-bearing rocks at mantle conditions (1000-2000 K, 2.5-10 GPa).

Experiments were conducted in laser-heated diamond anvil cells (DACs) with a culet size of 250 μm and equipped with rhenium gaskets. Powdered ^{57}Fe-enriched pyroxene-like glass $(Mg_{0.91}Fe_{0.09})(Si_{0.91}Al_{0.09})O_3$, ferropericlase with compositions $(Mg_{0.8}Fe_{0.2})O$ and

$(Mg_{0.75}Fe_{0.25})O$, and wustite $Fe_{0.94}O$ were used in different experiments as iron-bearing compounds. As a source of hydrocarbons we chose natural Astrakhan's crude oil and synthetic paraffin oil (n-alkanes C_{15}-C_{40}). The cell's chamber was first filled with powder of the iron-bearing substance and then soaked with liquid hydrocarbons which also served as a pressure medium in the cell. Mössbauer spectroscopy analyses were performed before and after each heating.

The experimental results demonstrate that iron hydride FeH_x formed at temperatures ≥1350 K over the whole pressure range of 2.5-10 GPa (corresponding to the depth of 80-300 km) and independent of the chosen source of hydrocarbons and iron-bearing compounds. At pressures ≥7.4 GPa iron carbide Fe_3C formed in addition to iron hydride. Mössbauer spectra of starting mixtures and experimental products are presented in Fig. 3.2-9.

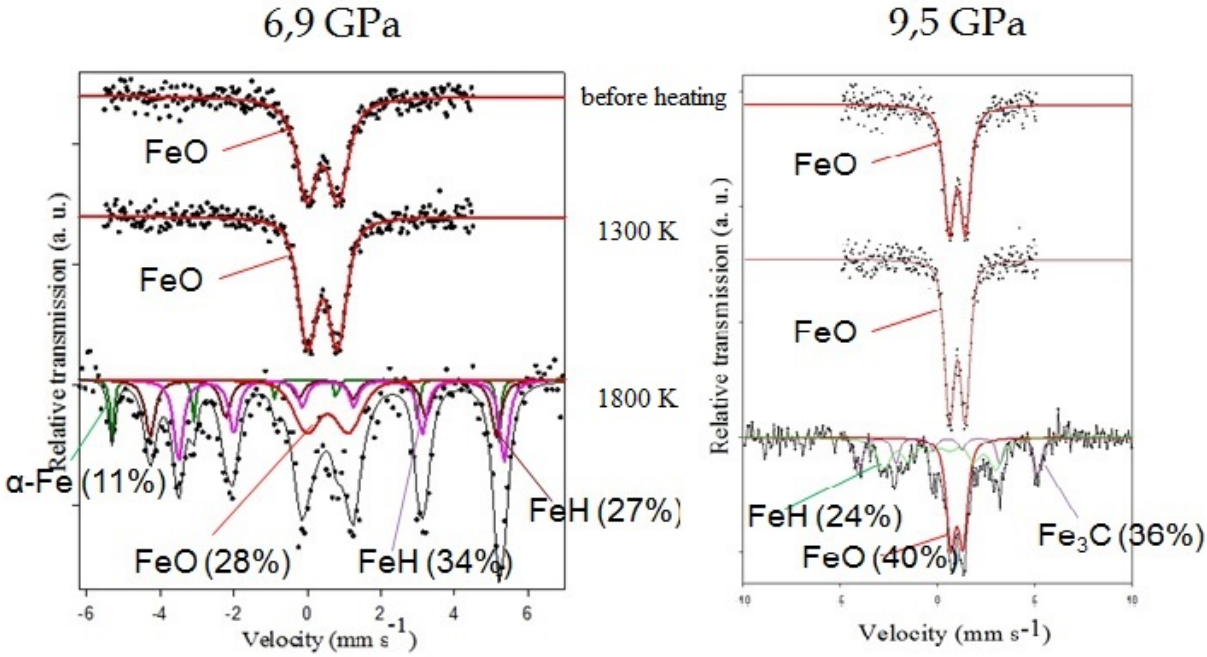

Fig. 3.2-9: Mössbauer spectra of two samples at 6.9 GPa and 9.5 GPa before heating (top), after heating to 1300 K (middle), and after heating to 1800 K (bottom).

Iron hydride has a rather low melting temperature but high density compared to the surrounding silicate rocks (~ 7.3-7.5 g/cm^3 of FeH_x vs 3.3 g/cm^3 for silicates, according to PREM). Therefore, iron hydride may form a negatively buoyant "hydride magma" that would tend to sink into the deep mantle and may be the deep source of hydrogen and reduced iron. A crude estimate suggests that $7.4 \cdot 10^{16}$ tons of iron hydride could have formed in the asthenosphere over the last 500 million years via chemical reaction between subducted hydrocarbons and iron-bearing rocks. This amount of iron hydrides is at least twice as high as the total mass of flood basalts present on Earth.

j. *Grain boundary diffusion and its relation to grain boundary segregation of multiple elements in garnet – an experimental study using the bicrystal setup, TEM and numerical modeling (J. Polednia and K. Marquardt, in collaboration with R. Dohmen/Bochum)*

The solubilities and diffusion rates of various rare earth elements in yttrium aluminium garnet (YAG) polycrystals are important for solid state laser technology because YAG is one of the most extensively used laser media for high power lasers. Polycrystalline ceramic lasers can be produced at low costs and their efficiency can be optimized by achieving high doping concentrations along grain boundaries. Lanthanum is a candidate element to improve the optical properties of YAG lasers and to act as a sintering aid. The presence of unwanted trace elements (*e.g.*, Fe^{3+}) in YAG can quench the laser emission. These trace elements may enter the YAG-ceramic by diffusion. Therefore, we studied the diffusion behaviour of La and Fe^{3+}. Besides industrial importance, grain boundary diffusion governs numerous geological phenomena, such as Coble creep deformation and recrystallization, which affect large-scale geodynamics although occurring on the nm scale.

We used the direct wafer bonding method to produce a synthetic bicrystal. A lanthanum-, iron-, and magnesium-containing thin-film, deposited by pulsed laser deposition (PLD) perpendicular to the grain boundary, serves as diffusant source. The diffusion experiments were carried out in a gas mixing furnace at 1000 °C and 1450 °C and ambient atmosphere (air), for durations of 24.1 h and 0.5 h for each temperature. We investigated the grain boundary structure prior to and after annealing on the atomic scale using high-resolution TEM (HRTEM) and mapped the concentration distribution of the elements of interest by energy dispersive X-ray spectroscopy in scanning (S)TEM mode (Fig. 3.2-10a).

Diffusion coefficients were determined from element distribution maps by fitting numerical diffusion profiles in two dimensions (diffusion map) to the measurements. (Fig. 3.2-10b). In the numerical model lattice diffusion is simply governed by the 2D version of Fick's second law, whereas grain boundary diffusion is affected by the segregation factor s as well as the effective grain boundary width δ. Diffusive flux normal to the boundary, anisotropic lattice diffusion (parallel and normal to the grain boundary), and surface diffusion are included in the model.

Grain boundary diffusion of La, Fe, and Mg at 1450 °C are fitted to be at least 9×10^{-11} m^2/s. This minimal value is a result of the limited extension of the profile measured. One sample contains additionally Ti, which leads to a significant decrease of La concentration in the grain boundary. The mechanism has yet to be understood. We find that grain boundary diffusion for all observed elements is at least 8 orders of magnitude faster than volume diffusion (D_{Fe3+}^{vol} $=8\times10^{-19}$ m^2/s, $D_{Mg2+}^{vol} = 3\times10^{-20}$ m^2/s). La is highly incompatible due to its large ionic size and does not diffuse into the crystal lattice at STEM resolution but preferentially segregates into the grain boundary. From the same experiment, we determined the product of segregation coefficient and effective grain boundary width ($\delta\times s$) and find that $\delta\times s$ of Fe^{3+} is 1.7 and of

Mg 1.8, whereas $\delta \times s$ for La is > 10. Due to the lack of volume diffusion, $\delta \times s$ for La can only be defined as a minimal value. The effective grain boundary width is less than 4 nm, limited by the analytical conditions chosen.

High dopant levels of La in YAG polycrystals are easy to obtain when grain sizes are small, whereas homogeneous doping of La on the scale of individual grains is more difficult. This study shows how incompatible elements can diffuse extremely effectively along grain boundaries - a process that plays an important role also in crustal and upper mantle rocks as it enables fast transport rates of incompatible elements. It is believed that generation of melts and metasomatic fluids that are highly enriched in incompatible elements is determined by grain boundary segregation characteristics.

The present experimental and analytical setup as well as the numerical code will be used in future work to study REE diffusion along variously oriented forsterite grain boundaries.

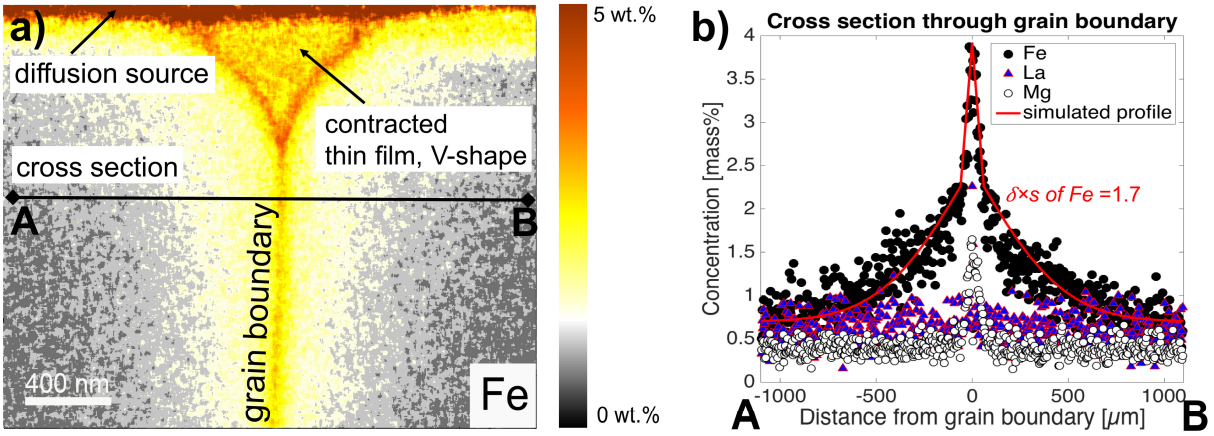

Fig. 3.2-10: a) Element distribution map of Fe after a bicrystal diffusion experiment, acquired by energy dispersive X-ray spectroscopy in STEM mode and corrected using the Cliff-Lorimer method. The investigated grain boundary is a near Σ5 (021)/[100] boundary. The concentration of Fe in the grain boundary after annealing is 4.0 wt. %, the respective concentrations of La and Mg are 2.3 wt. % and 1.7 wt. %. b) Measured diffusion profile (coloured dots) and simulated diffusion profile (green solid line). The grain boundary cross profile is at 200 nm distance from the source.

k. *Copper diffusion in minerals and its effect on melt inclusions (A. Audétat, in collaboration with L. Zhang/Hefei)*

Melt inclusions in natural assemblages of coexisting plagioclase, clinopyroxene, orthopyroxene and olivine commonly have contrasting Cu contents, which raises doubts as to whether they remained closed systems. A systematic investigation of Cu diffusion in magmatic minerals was thus conducted.

Two different types of experiments were performed: (1) Re-equilibration experiments on natural melt inclusions hosted in plagioclase, orthopyroxene and clinopyroxene. (2) Copper diffusion experiments on gem-quality crystals of plagioclase, orthopyroxene, clinopyroxene, olivine, apatite and amphibole. For the first type of experiments, several melt inclusions in selected phenocrysts (*e.g.*, orthopyroxene; Fig. 3.2-11a) were first analysed by LA-ICP-MS. Each phenocryst was then filled together with Cs-spiked trachyandesite powder ($\pm H_2O$) into an Au capsule and equilibrated for 3 days at 950 °C / 1 kbar in a cold-seal pressure vessel. After analysing several more melt inclusions in the same phenocryst, it was filled along with trachyandesite powder into a $Au_{95}Cu_{05}$ capsule and run at 930 °C / 1 kbar for another three days. Finally, some of the remaining melt inclusions were analysed (always with LA-ICP-MS).

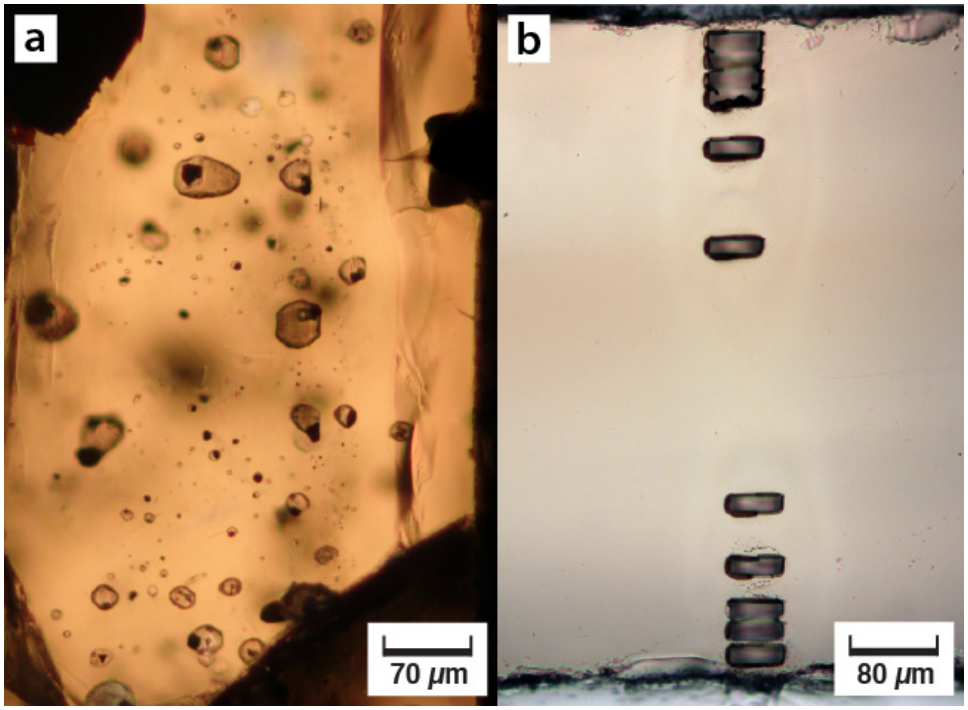

Fig. 3.2-11: (a) partly crystallized melt inclusions within an ortho- pyroxene phenocryst. (b) LA-ICP-MS profile across a gem-quality olivine.

For the second type of experiments, gem-quality mineral fragments of ~ 3x5x(0.5-1.5) mm size were filled together with Co-(±Li, Cu)-spiked trachyandesite powder into Cu foils and then equilibrated in the gas mixing furnace at 1050 °C, FMQ-0.7 for 2 hrs to 8 days. After quenching, the recovered crystals were cut longitudinally and transversely, and diffusion profiles were measured by LA-ICP-MS in three perpendicular directions (Fig. 3.2-11b).

The results of the re-equilibration experiments demonstrate that Cu contents of plagioclase-hosted melt inclusions can fully re-equilibrate within a few days at 930-950 °C. Copper contents decreased from 830±20 ppm to < 3 ppm in the first experiment, and then increased

back to 480±10 ppm in the second experiment. Interestingly, the external melt of the latter experiment contained only 77±8 ppm Cu, which suggests that Cu diffusion did not just follow a concentration gradient but was affected by additional factors. No significant Cu-loss or Cu-gain was observed for melt inclusions hosted in clinopyroxene and orthopyroxene.

The diffusion experiments performed at 1050 °C on gem-quality minerals produced systematic concentration profiles of Cu (±Li) after 8 days in the case of olivine (Fig. 3.2-12a), orthopyroxene, clinopyroxene and apatite, and after only 2 hrs in the case of plagioclase and amphibole. Calculated diffusion coefficients are high in all investigated minerals (Fig. 3.2-12b), with the highest values being observed for plagioclase and amphibole. Quantitative modelling based on these diffusion coefficients suggests that a melt inclusion of 50 µm size, enclosed within a crystal of 1 mm diameter, can diffusively reach equilibrium with the surrounding melt within only 2 hours in the case of plagioclase, within 2 days in the case of amphibole, and within 2-3 years in the case of olivine and apatite (Fig. 3.2-13). These results suggest that Cu concentrations in melt inclusions need to be treated with caution even in refractory minerals such as olivine.

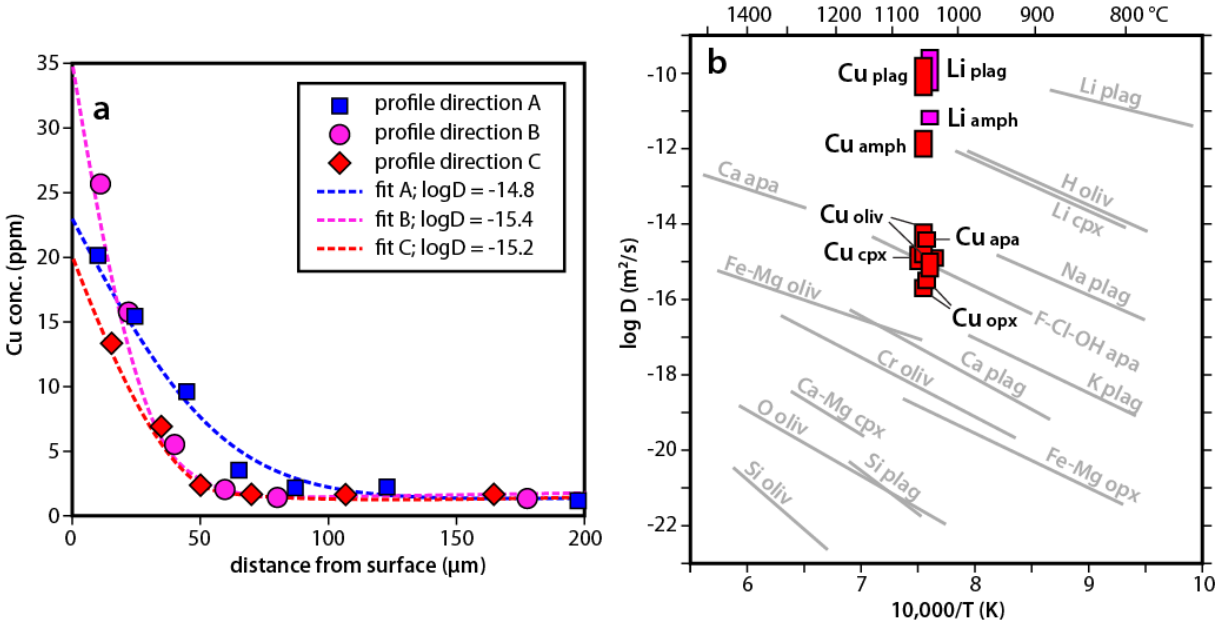

Fig. 3.2-12: (a) Cu diffusion profiles and corresponding fits along three crystallographic orientations in olivine1. (b) Cu and Li diffusion coefficients obtained in this study compared with literature data.

Unusually high and poorly reproducible Cu concentrations in natural, plagioclase- and orthopyroxene-hosted melt inclusions appear to result from post-entrapment Cu gain due to precipitation of a sulphide phase within the evolving melt inclusions. In the samples investigated in this study the sulphide phase is sulphide liquid containing 30-40 wt. % Cu, hence attainment of sulphide saturation leads to strong Cu-depletion in the residual melt,

which in turn causes Cu to diffuse from the external melt into the melt inclusion. In orthopyroxene-hosted melt inclusions, sulphide saturation appears to have been caused by Fe-loss due to sidewall crystallization, similar to the process leading to sulphide precipitation in olivine-hosted melt inclusions. In plagioclase-hosted melt inclusions, sulfide saturation appears to have been caused by H_2O loss after magma emplacement.

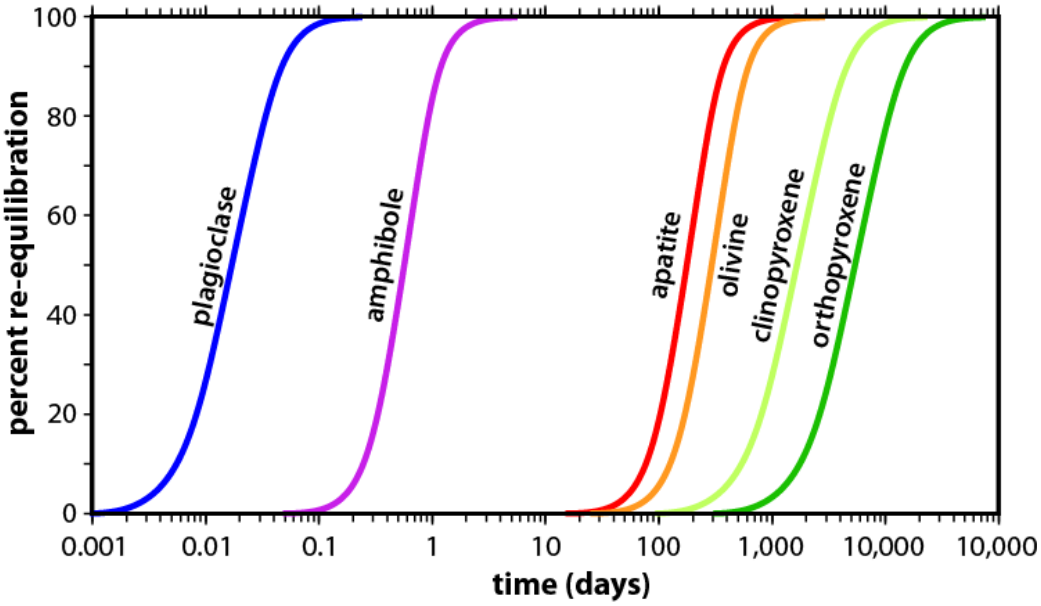

Fig. 3.2-13: Time required to diffusively equilibrate Cu concentrations in melt inclusions hosted in various minerals with Cu concentrations in an external melt. Calculations were performed for an inclusion-to-crystal size ratio of 0.05 and a temperature of 1050 °C, using the diffusion coefficients shown in Fig. 3.2-12b.

I. *Ge, Al and Ti partitioning between quartz and rhyolite melt, and its potential use for thermobarometry (A. Zarei and A. Audétat)*

Due to large disagreements between existing models of the titanium-in-quartz (TitaniQ) thermobarometer, experiments were performed to investigate the effect of temperature, pressure and melt alumina saturation index (ASI; molar ratio $Al_2O_3/ (Na_2O + K_2O + CaO)$ on the partitioning of germanium, aluminium and titanium between quartz and coexisting rhyolite melt. For this purpose, Ge- and Ti-bearing starting glasses were filled with aqueous solution into beakers manufactured out of single, synthetic quartz crystals, which were then welded into Au capsules and equilibrated at 730-1000 °C and 0.5-10 kbar in cold-seal pressure vessels and piston cylinder presses for durations of 5-7 days. Due to small temperature gradients (< 5 °C) along the quartz beaker during the experiments, quartz dissolved in the upper parts of the quartz beaker and precipitated in its lower part next to the pool of silicate melt. Recovered samples were analysed by laser-ablation ICP-MS. A representative example of an experimental run product is shown in Fig. 3.2-14, which depicts the lower part of the originally fluid-filled quartz beaker, tilted into horizontal position.

Melting of the Ge-bearing glass pieces in the bottom of the quartz beaker led to the formation of a pool of silicate melt, whereas SiO_2 re-distribution via the fluid phase resulted in the formation of a thin overgrowth of new quartz in the bottom part of the quartz capsule. Elemental concentrations were measured in profiles across the quenched melt, and both across and along the layer of newly precipitated quartz. Quartz–silicate melt distribution coefficients ($D^{qtz/melt}$) were calculated based on the composition of the silica melt at its surface and the composition of the latest-grown quartz.

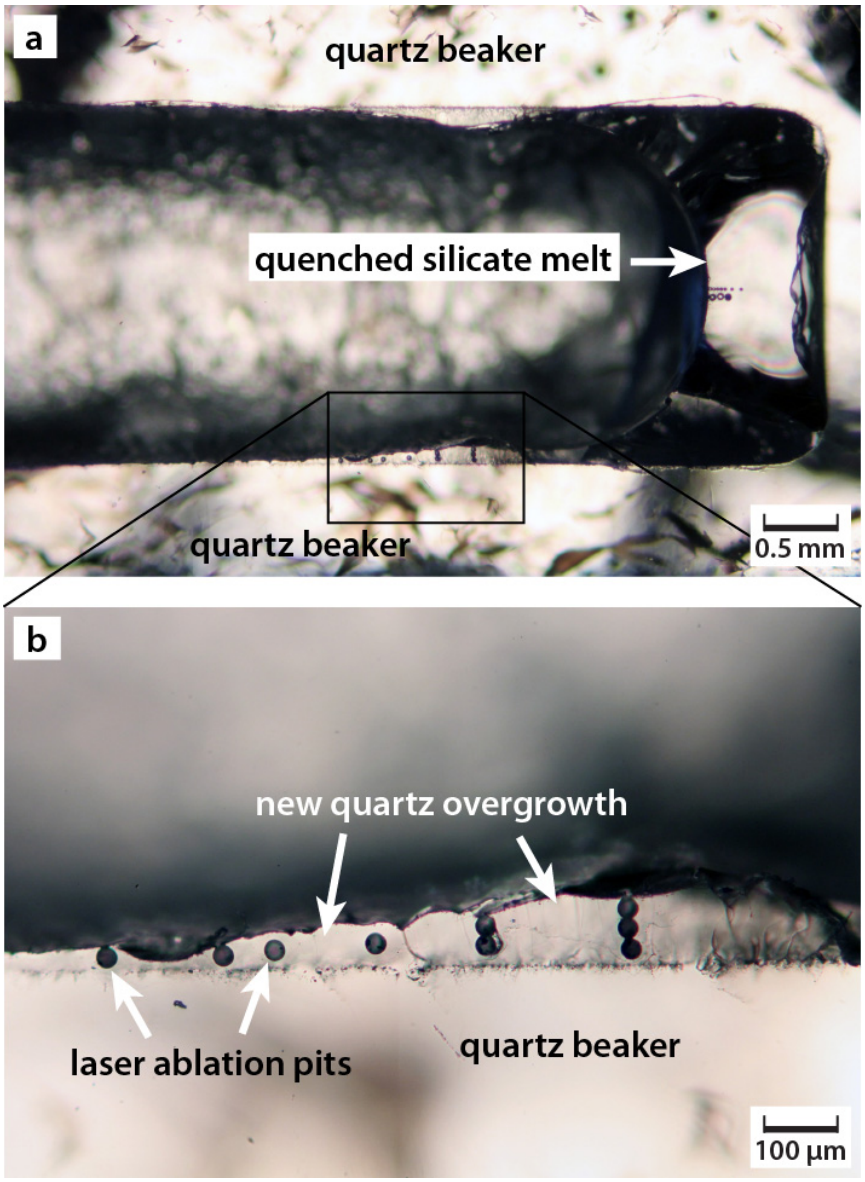

Fig. 3.2-14: Transmitted-light images of an experimental run product (800 °C, 2 kbar, 7 days). (a) overview image showing the quenched melt pool in the bottom of the quartz beaker (right side), and overgrowths of new quartz next to the melt pool. (b) close-up view of one of the new quartz overgrowths. Notice the LA-ICP-MS pits in the new quartz overgrowth (30 µm pit size) and in two profiles perpendicular to the surface of the silicate melt (one profile measured with 20 µm pit size, one with 40 µm pit size).

In contrast to previous quartz dissolution and reprecipitation experiments performed in melt-free, rutile-saturated systems the trace element content of newly formed quartz is independent of the thickness of new quartz overgrowth, suggesting that growth rate did not have any significant effect in the current experiments. The results suggest that $D_{Ge}^{qtz/melt}$ is relatively insensitive to ASI and temperature, whereas pressure may have a considerable effect at pressures ≤4 kbar. $D_{Ti}^{qtz/melt}$ depends strongly on all parameters investigated in this study, *i.e.*, on P, T and ASI, in agreement with current models of Ti solubility in quartz and silicate melts. The $D_{Ti}^{qtz/melt}$ values determined in the present study agree with the TitaniQ model of Huang and Audétat (2012) and disagree with the one of Thomas *et al.* (2010). $D_{Al}^{qtz/melt}$ depends on ASI, temperature, and potentially on pressure at pressures > 2 kbar. More experiments are needed at > 2 kbar to reliably assess the effects of pressure on Ti, Ge and Al partitioning between quartz and silicate melt.

m. *Vanadium magnetite–melt oxybarometry of natural, silicic magmas: A comparison between different oxybarometers and thermometers (R. Arató and A. Audétat)*

In order to test a newly developed oxybarometer for silicic magmas based on the partitioning of vanadium between magnetite and silicate melt, a comprehensive thermometry and oxybarometry study on 21 natural rhyolites to dacites was conducted. Utilized methods include Fe-Ti-oxide thermometry and -oxybarometry, zircon saturation thermometry, two-feldspar thermometry, and vanadium magnetite–melt oxybarometry. These methods were applied to (i) crystal-bearing obsidians (vitrophyres), because they commonly contain fresh Fe-Ti-oxides, and because magnetite–melt partition coefficients of vanadium ($D_V^{mgt/melt}$) can easily be obtained by analyzing magnetite phenocrysts and the surrounding, glassy matrix; as well as to (ii) devitrified/crystallized samples containing well-preserved inclusions of silicate melt and Fe-Ti-oxides within quartz and feldspar phenocrysts. The investigated rocks cover a wide range of oxygen fugacities and temperatures, and represent different melt compositions and geological settings.

Doubly-polished thick sections of approximately 300-400 µm thickness were prepared from each sample. These were carefully investigated under the petrographic microscope to search for Fe-Ti oxide-, feldspar- and melt inclusions preserved within quartz and feldspar phenocrysts, as well as for fresh Fe-Ti oxide- and feldspar phenocrysts/microphenocrysts. Special attention was paid to signs of magma mixing and other characteristics that could reflect non-equilibrium conditions, such as resorption- or alteration features, or multiple generations of individual mineral phases. Samples that showed any of these features were treated with special caution and were marked as “medium reliable” or “least reliable”, depending on the severity of the signs. All measurements were carried out by LA-ICP-MS. Traditionally, Fe-Ti oxide pairs are measured by electron microprobe. However, we performed comparative tests on microphenocrysts and found that LA-ICP-MS returns the same element concentrations within error. Apart from its higher sensitivity, a major advantage

of LA-ICP-MS is that it allows to analyze entire inclusions enclosed within other phenocrysts and to reconstitute their original composition by integrating the signal, which was essential for this study and would not have been possible by using the electron microprobe.

The results suggest that the newly developed vanadium magnetite–melt oxybarometer returns realistic fO_2 values independent of whether magnetite was measured as microphenocrysts or as inclusions within minerals, and whether melt was measured in the form of melt inclusion or as glassy matrix (Fig. 3.2-15). The new method thus allows fO_2 to be constrained also for slowly-cooled rocks such as granites, which contain Fe-Ti oxides that went through various stages of subsolidus re-equilibration, or to samples in which ilmenite is missing. However, our results also demonstrate that magma mixing is a very common and easily unnoticed phenomenon in silicic rocks, requiring special precautions in the application and interpretation of thermometers and oxybarometers in general. We also found that temperatures obtained via zircon saturation thermometry and two-feldspar thermometry in oxidized, metaluminous to peraluminous rhyolites are generally more reliable than the ones obtained via Fe-Ti-oxide thermometry.

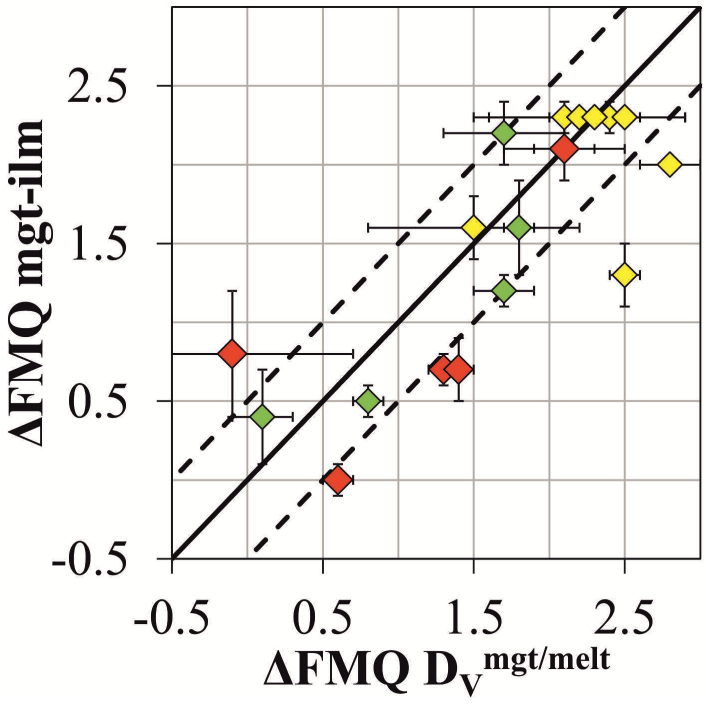

Fig. 3.2-15: Comparison of fO_2 values constrained via vanadium magnetite–melt partitioning, versus ones constrained via Fe-Ti oxide oxybarometry (Ghiorso & Evans, Am. J. Sci. 308, 957, 2008). Green diamonds represent the most reliable samples, whereas yellow and red diamonds refer to medium reliable and least reliable samples, respectively. The fO_2 values are presented in log units as relative to the fayalite-magnetite-quartz (FMQ) buffer. The dashed lines represent 0.5 log unit deviation from the 1:1 correspondence (solid line). Error bars indicate the standard deviation of the ΔFMQ values, calculated from magnetite-ilmenite and magnetite-melt pairs, respectively.

n. *Solubility of gold in oxidized, sulfur-bearing fluids at 500-850 °C and 200-230 MPa: a synthetic fluid inclusion study (H. Guo and A. Audétat)*

Gold is one of the most noble of all metals, existing dominantly as a native metal in the solid state and dissolving only scarcely into liquids or gases. Magmatic-hydrothermal fluids are an important transport agent for Au enrichment in the Earth's crust, being responsible for the formation of many types of Au ore deposits. Therefore, data on Au solubility in such fluids are essential for understanding the ore-forming processes. Previous studies on gold solubility in hydrothermal fluids focused either on relatively low temperatures representative of epithermal environments, on sulfur-free fluid systems, or on fluids containing reduced sulfur species. We thus studied Au solubility in fluids containing variable amounts of sulfate, chlorine and alkalies, at 500-850 °C, 200-230 MPa and oxygen fugacities ranging from log fO_2 = FMQ+1 to ~ FMQ+6 (FMQ: fayalite-magnetite-quartz buffer), with the aim to constrain Au dissolution mechanisms in sulfur-bearing aqueous fluids similar to those responsible for porphyry Cu-Au (±Mo) deposits.

We used synthetic fluid inclusions to trap fluids at high temperature and pressure, and subsequently analyzed their composition by LA-ICP-MS. Aqueous solutions containing various amounts of HCl, H_2SO_4, Na_2SO_4, LiCl, KCl, CsCl and $MnCl_2$ were prepared from analytical-grade chemicals and deionized water. Sodium chloride, and in a few runs elemental sulfur, were added as solids. Fluid inclusions were synthesized by either growing new quartz on etched quartz substrates in single Au capsules without oxygen buffers (Fig. 3.2-16), or by re-opening previously synthesized fluid inclusions through *in situ* cracking in double-capsules (AuPd/Au-Au) at controlled oxygen fugacity. The speciation of sulfur and gold was investigated *in situ* by Raman spectroscopy on fluid inclusions heated in a modified hydrothermal diamond anvil cell.

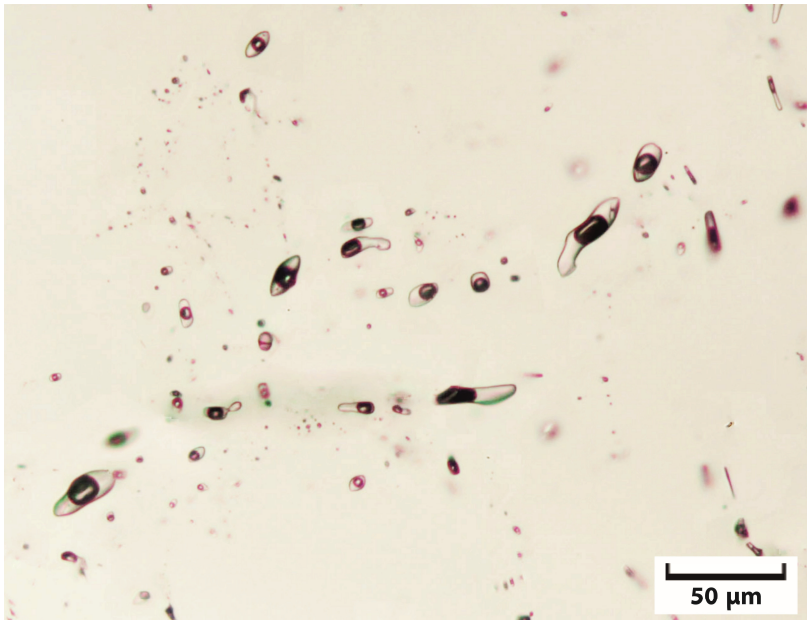

Fig. 3.2-16: Transmitted-light photomicrograph of fluid inclusions in quartz, synthesized at 800 °C and 2 kbar by growth of new quartz over an etched quartz substrate. The trapped fluid contains 20 wt. % NaCl, 3.5 wt. % HCl and 0.40±0.19 wt. % Au.

Gold solubility in fluids was found to increase with temperature, starting sulfate concentration, HCl-content, fluid salinity and oxygen fugacity (Fig. 3.2-17). Weight-percent level Au solubilities were observed in fO_2-unbuffered fluids containing sulfate and chlorine,

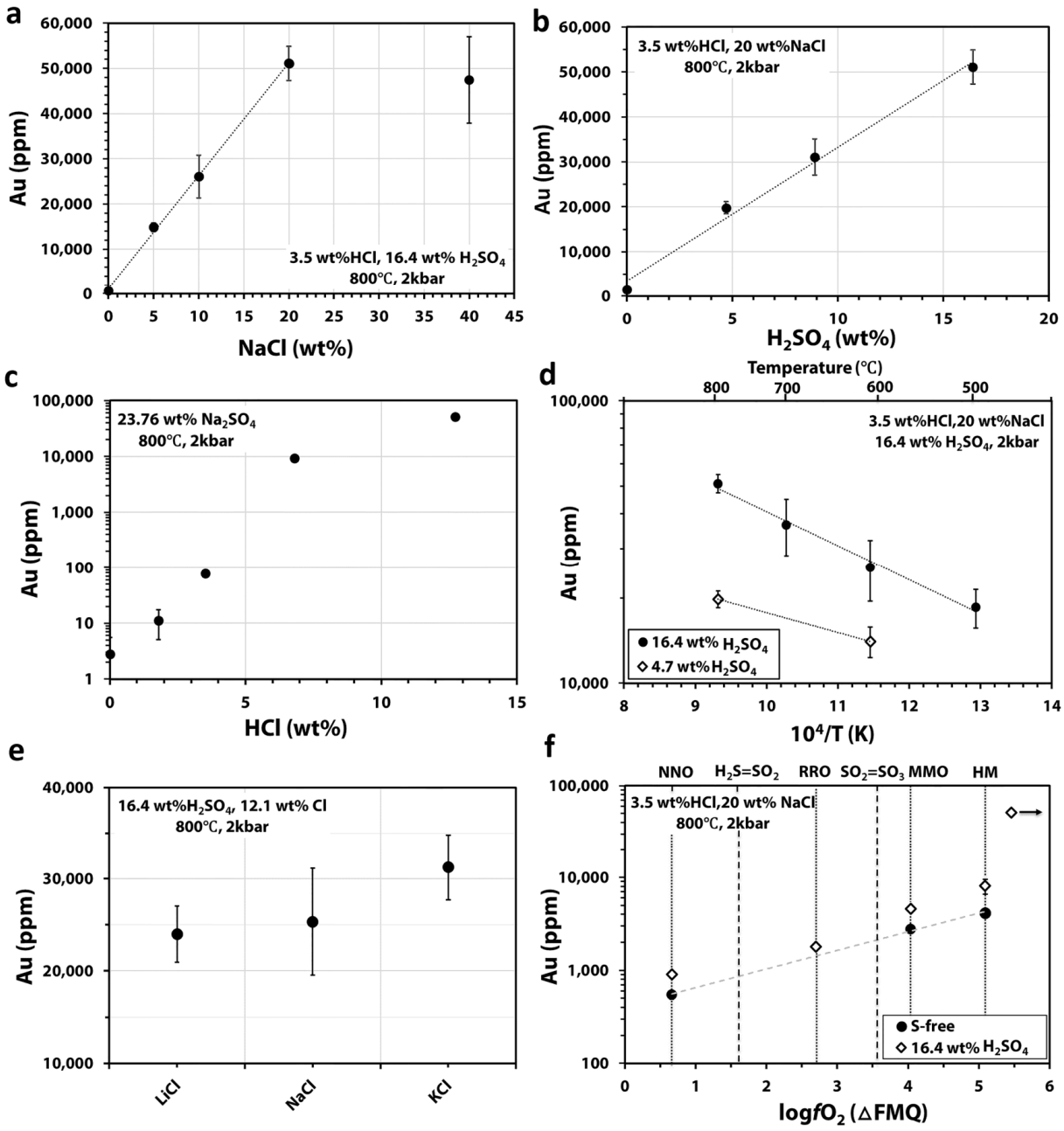

Fig. 3.2-17: Gold solubility in aqueous fluids at 500-800 °C and 2 kbar as a function of: (a) NaCl concentration in the starting fluid, (b) H_2SO_4 concentration in the starting fluid, (c) HCl concentration in the starting fluid, (d) temperature, (e) type of alkali ion and (f) oxygen fugacity. NNO: Ni-NiO buffer; RRO: Re-ReO_2 buffer; MMO: MnO-Mn_3O_4 buffer; HM: hematite-magnetite buffer; FMQ: fayalite-magnetite-quartz buffer.

which appears to be due to the formation of $NaAuCl_2$ complexes via the reaction:

$$Au + 1/2H_2SO_4 + HCl + NaCl = NaAuCl_2 + 1/2SO_2 + H_2O \qquad (1)$$

Fluids in porphyry Cu-Au (±Mo) ore forming environments (containing 7 wt. % NaCl, 1.0 wt. % S and 1.1 wt. % HCl; fO_2 buffered by hematite-magnetite at 600 °C, 2 kbar) may dissolve ~ 600 ppm Au, which is about two orders of magnitude higher than actual Au contents in natural magmatic-hydrothermal brines in porphyry Cu-Au (±Mo) deposits. Therefore, Au precipitation in porphyry Cu-Au (±Mo) deposits is not controlled via Au solubility in the fluid, but rather via the precipitation of Cu-Fe sulfides that incorporate Au as a minor or trace constituent and then exsolve native Au during cooling. However, fluid composition and fO_2 may control the Au mineralization potential at the stage at which aqueous fluids exsolve from the crystallizing magma.

o. *Chemistry, mineralogy and crystallization conditions of porphyry Mo-forming magmas at Urad–Henderson and Silver Creek, Colorado, USA (D.H. Zhang and A. Audétat)*

Porphyry Mo deposits, together with porphyry Cu-Mo (±Au) deposits, are our main source of molybdenum. High-grade, rift-related porphyry Mo deposits, which are associated with fluorine-rich, highly evolved rhyolitic magmas, have been studied extensively due to their high ore grade and the peculiar geochemical characteristics of the ore-forming magmas. Some researchers proposed that the ore-forming magmas were extremely Mo-rich, whereas others argued that they were not necessarily metal-rich, but that metal was extracted from unusually large volumes of magma. Recent findings of very high fluorine contents in melt inclusions at Climax indicated that melt extraction may have been promoted by fluorine via its effect on lowering melt viscosities. We have conducted a detailed mineralogical and melt inclusion study on two other Climax-type porphyry Mo deposits, Urad–Henderson and Silver Creek, both situated in the Colorado Mineral Belt, USA, with the aim to constrain the metal- and fluorine-content of the ore-forming magmas.

Inter-mineralization rhyolite melts at Urad-Henderson were highly evolved (four times more fractionated than average granite in the continental crust), contained 10-15 ppm Mo (Fig. 3.2-18), 6-7 wt. % H_2O and 0.5-0.7 wt. % F, and record crystallization conditions of 730-770 °C, 1-3 kbar and oxygen fugacities ca. two log units above the fayalite-magnetite-quartz buffer (log fO_2 ~ FMQ+2). Melts from two presumably syn-mineralization rhyolite dikes at Silver Creek were slightly less evolved and contained 3-5 ppm Mo (Fig. 3.2-18), 7-8 wt. % H_2O, ~ 0.3 wt. % F, and record crystallization conditions of 780-800 °C, 2-5 kbar.

Combined with published melt inclusion data from another Climax-type porphyry Mo deposit (Pine Grove, USA), it is striking that all these melts are characterized by distinctly lower fluorine contents but higher temperatures or/and higher water contents than those reported from Climax. Corresponding magma viscosities (log η = 3.5-4.9 Pa s) are lower than the viscosity of average granitic melts at the same temperature in all cases (Fig. 3.2-19), which may have facilitated crystal–melt segregation and accumulation of large volumes fractionated, crystal-poor melts in shallow magma chambers. The latter process appears to be critical for the formation of Climax-type porphyry Mo deposit.

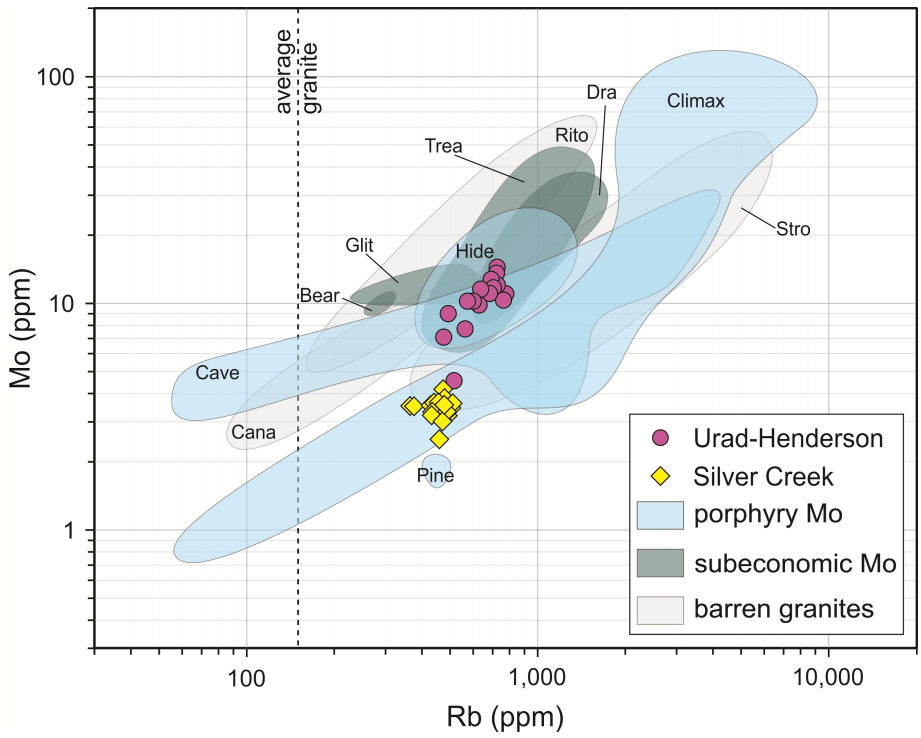

Fig. 3.2-18: Rb versus Mo diagram showing compositional trends of melt inclusions analyzed from porphyry Mo-mineralized, sub-economically Mo-mineralized, and barren magmas.

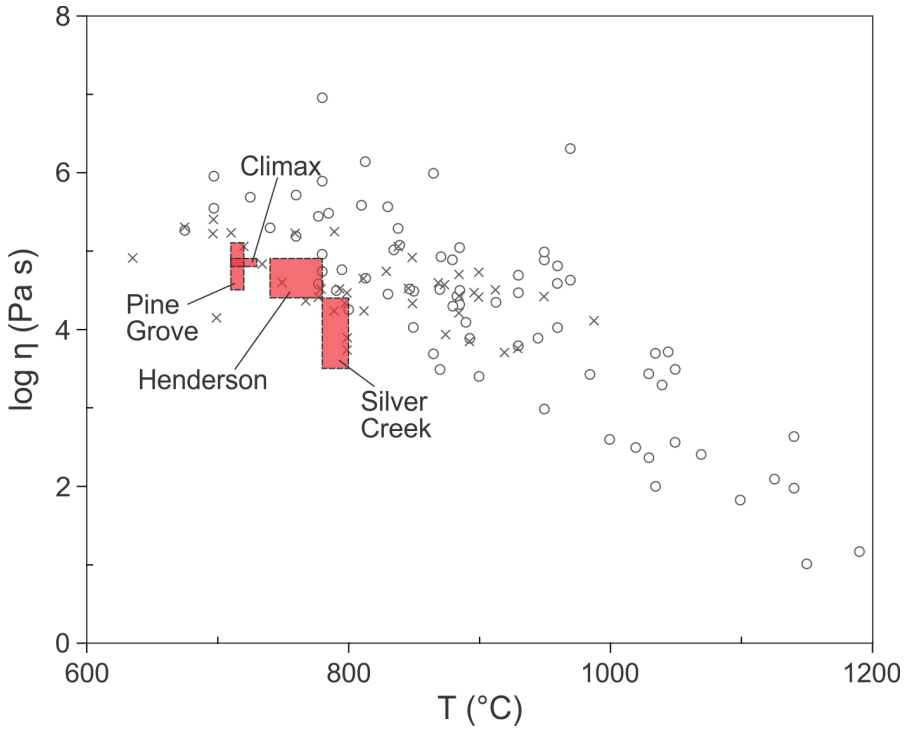

Fig. 3.2-19: Viscosities of rhyolite melts in Climax-type porphyry Mo deposits (red boxes), compared to viscosities of basaltic to rhyolitic melts reported in the literature (crosses and open circles).

3.3 Mineralogy, Crystal Chemistry and Phase Transformations

Mineralogical investigations of Earth's constituents continue to play an important role in our quest to understand the Earth's interior and its dynamics. An experimental approach is a mandatory part of the quest to clarify the *crystal chemistry* of constituent materials and their *phase stabilities and transformations*. Experiments can help to forge the link between microscopic properties of target materials and macroscopic observations of the Earth's interior. This chapter describes some of the most recent results using experimental approaches. These studies include application and development of high-pressure technology and fine probe techniques, such as single crystal X-ray diffraction, Brillouin scattering and infrared spectroscopy at extreme conditions, together with state-of-the-art *post mortem* chemical analysis.

Iron, a constituent of the Earth's liquid outer core and solid inner core, continued to attract attention. The martensitic transition of iron from the α-phase to the ε-phase was investigated at high pressure by single crystal X-ray diffraction. Pre-melting effects on the elastic properties of iron are also important, and these were addressed through a combined Brillouin scattering and X-ray diffraction study on argon as an *fcc* analogue. The elastic properties of bridgmanite and akimotoite, constituent minerals of the lower mantle and transition zone, respectively, were also under the spotlight. The structure of $LiNbO_3$-type $Mg_3Al_2Si_3O_{12}$ was refined as a metastable product formed during the back-transformation from the perovskite structure. Synthesis of high-quality large single crystals of OH-bearing phases gave information on their crystal chemistry and compressional behaviour. The discovery of new phases of iron oxide and Mn-carbonate revealed a potential new host of ferric iron in the mantle and the existence of tetrahedral carbon in the carbonate structure.

Phase stabilities of constituent minerals and mineral assemblages in the lower mantle further link microscopic properties to macroscopic observations to provide better constraints on seismic discontinuities and deep volatile cycles. The thickness of the 660 km discontinuity is related to the extent of the three-phase field ringwoodite + bridgmanite + ferropericlase and new development of a high-pressure cell assembly for *in situ* X-ray diffraction promises a more precise determination of the stability field. The Al_2O_3 solubility in bridgmanite as a function of pressure and temperature can place constraints on MORB subduction into the lower mantle. Results from a single crystal study of clinoferrosilite can be linked to metastable pyroxene in cold slabs. Ferropericlase inclusions in diamond may provide a geobarometer for deep diamonds and iron-bearing carbonate phase transformations can also place constraints on the deep carbon cycle. Similarly, structural and spectroscopic studies of Phase E and OH in rutile provide information relevant to the deep water cycle.

a. *Iron at high pressure: A single-crystal study (R. Huang, T. Boffa Ballaran, S. Petitgirard and D.J. Frost)*

The Earth's liquid outer core and solid inner core are mainly composed of an iron-nickel alloy with a small proportion of light elements. Fe adopts a bcc structure (α-phase) at ambient

conditions. At least 6 phases have been proposed for iron at high-pressure and high-temperature conditions (α, γ, δ, ε, double-hcp phase and an orthorhombic phase). In most of the studies, the ε-phase of iron, hexagonal close packed (hcp), has been considered to be stable over a wide P–T range approaching the Earth's core conditions. The high-pressure martensitic α→ ε phase transition has been the subject of numerous studies, however only recently the mechanism of the transformation has been determined using single-crystal X-ray diffraction. During the transition the α-phase Fe crystal gave rise to a mixture of ε-phase Fe single crystals with a few different orientations. If this is the case, it should be possible to treat each of these single crystals separately and obtain structural information and an accurate equation of state for ε-phase Fe at high pressure.

In order to obtain crystals of ε-phase Fe we compressed a single-crystal of α-phase Fe above 14 GPa in He and Ne as pressure-transmitting media to ensure hydrostatic conditions. Focused ion beam (FIB) was used to cut an α-Fe piece with dimensions 45 x 35 x 7 μm^3 from a large single crystal for the high-pressure X-ray diffraction study. The crystal was loaded in a diamond anvil cell with 350 μm culet diamonds. A rhenium gasket with a hole of 175 μm diameter and a ruby chip were used as sample chamber and pressure calibrant, respectively. Intensity data were collected every 1-2 GPa up to 15.8 GPa using an Xcalibur diffractometer with MoKα radiation and a CCD detector. At first, He was loaded as the pressure-transmitting medium. However, at ~ 5.6 GPa, the hole became very small, therefore we reloaded the same crystal in a Ne pressure-transmitting medium to minimise shrinkage of the gasket hole. The unit-cell parameters of α-Fe were obtained using up to 60 reflections. Structural refinements were performed in $Im\bar{3}m$ space group using 9 unique reflections for 2 parameters.

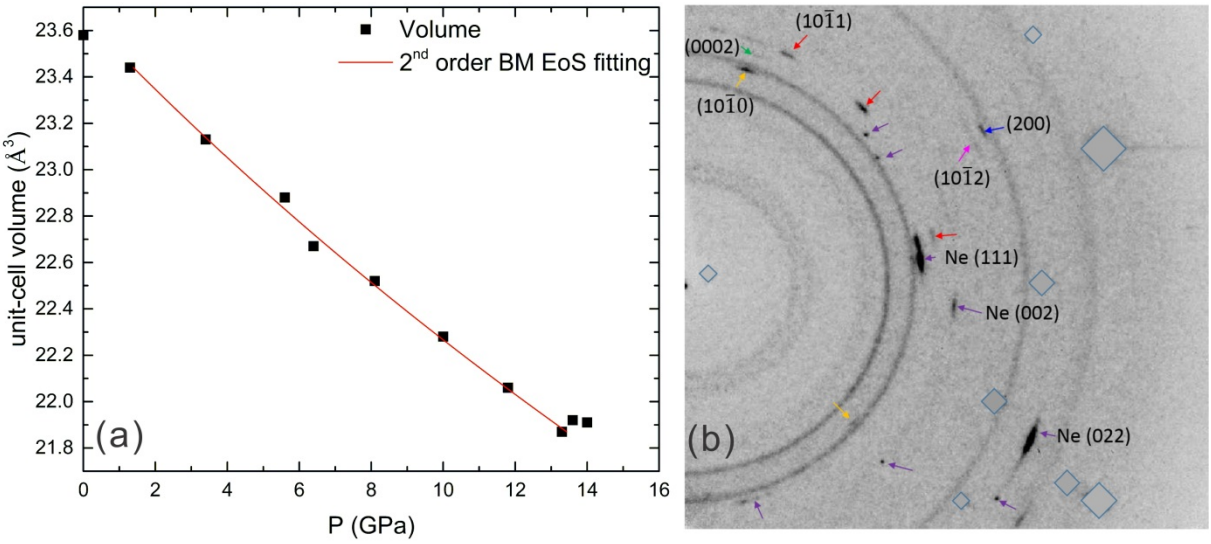

Fig. 3.3-1: (a) Influence of pressure on the unit-cell volume of the α-phase of iron. (b) Composite X-ray diffraction image at 14.5 GPa where the α- and ε-phases coexist. The red, pink, green and yellow arrows represent different planes of the ε-phase crystals as indicated. The blue arrow indicates the remaining (200) reflection of the α-phase. Reflections from Ne are indicated by purple arrows; whereas those of the diamonds are masked with grey diamonds outlined in blue.

The α-phase is stable up to 14.0 GPa as expected for hydrostatic conditions. The pressure-volume relationship and fitting using a 2nd order Birch–Murnaghan isothermal equation of state are shown in Fig. 3.3-1a. The α→ ε phase transition occurs between 14.0 and 14.5 GPa. At 14.5 GPa, the α- and ε-phases coexist (Fig. 3.3-1b), and at 15.8 GPa, only peaks from the ε-phase can be seen. However, the ε-Fe sample is not a single crystal after the transition. This α-ε phase transition is martensitic. From the Burgers path, the bcc→hcp transition consists of a lattice distortion and a shuffle. The original $(110)_{bcc}$ plane corresponds to the $(0001)_{hcp}$ planes. Thus six equivalent $(110)_{bcc}$ planes will form six variants of hcp crystals. And by rotation of $(1\bar{1}00)_{hcp}$ and $(01\bar{1}0)_{hcp}$ of ±5 ˚along the *c* axis, the ε-phase can grow in 12 different crystal orientations. As indicated in Fig. 3.3-1b, there are several reflection spots from planes with the same Miller indices and different azimuthal angles. The reflections cover a few degrees of azimuthal angles, suggesting that the crystals are highly strained. Such strains (if still elastic) may be relaxed by heating. We will therefore use an electrical heater inserted in the diamond anvil cell to reach ~ 500 °C and recover good quality single-crystals of the ε-phase.

b. *Pre-melting in rare gases (M.G. Pamato, L. Vočadlo, D.P. Dobson and I.G. Wood/London; A. Kurnosov, A. Pakhomova and T. Boffa Ballaran)*

The Earth's inner core is considered to be made of an iron-nickel alloy with a few percent of light element(s), but its exact structure and composition are still unknown. Seismological and mineralogical models for the Earth's inner core do not agree, where mineralogical models derived from *ab initio* calculations predict shear-wave velocities up to 30 % greater than seismically observed values. Recent computer simulations at Earth's core conditions revealed that the shear modulus, and therefore the seismic velocities of iron, decrease drastically just before melting. These findings provide a new explanation for the discrepancy between mineralogical models and seismic data.

The only results on pre-melting with direct applicability to the Earth's core are state of the art computer calculations. It is vital, therefore, that the role of pre-melting in the inner core is systematically tested at a range of P-T conditions as well as for iron alloyed with both nickel and light elements. It is extremely challenging to measure the pressure dependence of pre-melting effects on the elastic properties of iron under inner core conditions to the required precision. We will therefore experimentally determine the extent to which pre-melting behaviour occurs in the elastic properties of other materials at less experimentally challenging conditions and combine these studies with computer simulations of the same materials.

In this study, we investigated the elastic properties of single crystals of argon prior to melting. If pre-melting in this system occurs, we expect to observe a non-linear softening of the elastic constants and velocities just before the melting temperature. Ar is an ideal test material since it crystallises in a simple monatomic cubic face-centred structure which is easily modelled

using classical potentials or *ab initio* methods. In addition, the compressibility of Ar is large and the temperature range required is within the capabilities of externally heated diamond anvil cells so high pressures and temperatures close to the melting point can be readily achieved.

The elastic constants, anisotropy, and the crystal orientation at each pressure and temperature are accurately determined by combining Brillouin scattering measurements with X-ray diffraction. One of the main advantages of using Brillouin scattering is that it allows an unambiguous discrimination between signals from solid and liquid components in partially-molten samples (see Fig. 3.3-2) which would be difficult (or perhaps impossible) using other techniques such as ultrasonic interferometry.

To this end, Ar was loaded using a high-pressure gas loading device in a diamond anvil cell with large opening angle of 80° and Almax- Böhler type anvil diamonds with culets of 500 µm in diameter. A specially designed internal resistive heater was placed around the diamonds for high-temperature measurements. Additionally, a single crystal of Sm:YAG combined with ruby chips was used as combined pressure and temperature sensors within the pressure cavity. We will establish the circumstances under which the pre-melting behaviour occurs, the extent to which it is prevalent and the mechanism(s) by which it occurs.

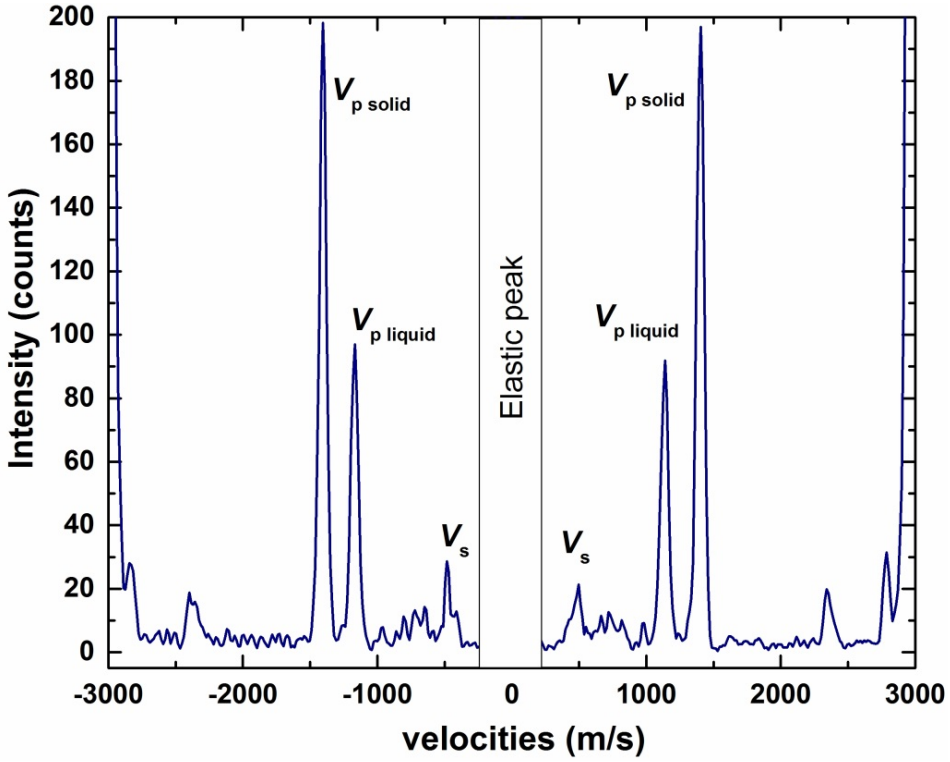

Fig. 3.3-2: Representative Brillouin spectrum of argon measured at a selected angle at 1.8 GPa and 367 K in the diamond anvil cell showing the signals from both solid and liquid components in a partially-molten sample.

c. *The effect of Fe-Al substitution on $MgSiO_3$ bridgmanite (R. Huang, T. Boffa Ballaran, C.A. McCammon and D.J. Frost)*

Magnesium silicate perovskite-type structure $(Mg,Fe)SiO_3$ bridgmanite, the dominant phase in the Earth's lower mantle, can accommodate a substantial amount of Fe and Al. The oxidation state of Fe (2+ or 3+) and the distribution of Fe and Al over the A and B sites of the bridgmanite structure are important for understanding transport properties, cation diffusion and possible spin transitions at lower mantle conditions. Also, the Fe-Al substitution influences the distortion of the perovskite framework. The aim of this study is to characterise the crystal chemistry of bridgmanite with different Fe-Al contents.

Eight bridgmanite single crystals with different Fe-Al concentrations up to 40 mol. % synthesised in multianvil runs at 25 GPa and between 1300 and 2000˚C were selected for this study. For comparison two samples, one of pure $MgSiO_3$ bridgmanite and the other with 4 mol. % of Fe^{2+} and with no Al, were also analysed. Chemical analysis and $Fe^{3+}/\sum Fe$ determination were made using the electron microprobe and Mössbauer spectroscopy, respectively. The reflection intensity data were collected using an Xcalibur diffractometer with MoKα radiation and a CCD detector. The unit-cell parameters were determined using the eight-position centring method on a HUBER four-circle diffractometer. Structural refinements were performed using up to 724 independent reflections to determine atomic positions, Fe occupancy and anisotropic displacement parameters.

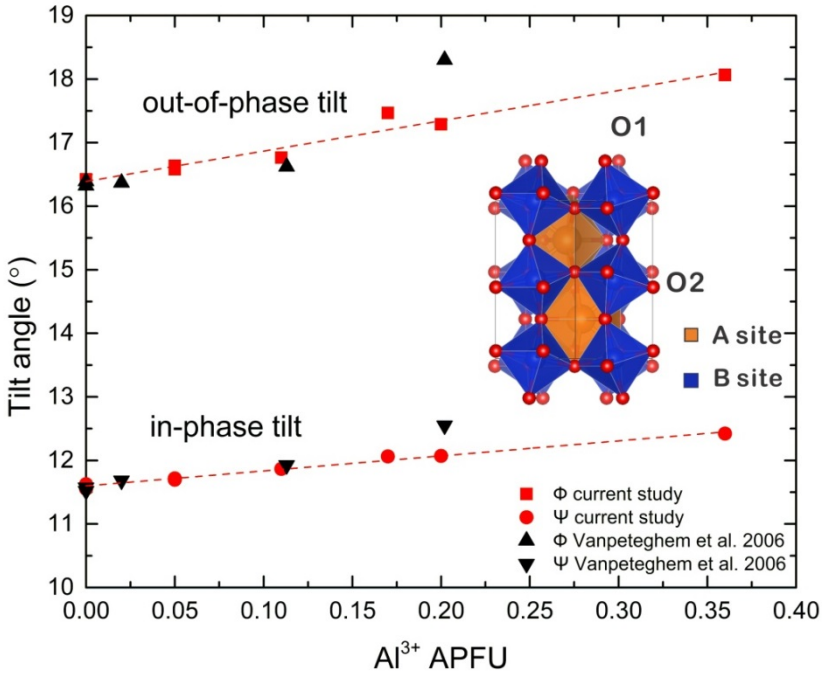

Fig. 3.3-3: Variation of the out-of-phase tilt angle Φ and in-phase tilt angle Ψ with Al^{3+} content expressed in atoms per formula unit (APFU) of $(Mg,Fe)(Si,Al)O_3$ bridgmanite. The calculation of these tilting angles is based on the oxygen atomic positions obtained from the structural refinements. Previous data [Vanpeteghem *et al.* 2006, *Phys. Earth Planet. Inter.* 155: 96-103] also are shown. The crystal structure of bridgmanite is depicted in the inset.

The perovskite (ABO_3) structure consists of corner-linked octahedra (B-site) sharing triangular faces with dodecahedra (A-site) (Fig. 3.3-3). The refined Fe fractional occupancies on the A site are in agreement with the electron microprobe results within their respective uncertainties, indicating that all Fe (Fe^{2+} and Fe^{3+}) occupies the A site of bridgmanite. In all experiments, a large amount of Fe is trivalent according to Mössbauer spectroscopy. The structural refinement shows that with increasing Fe+Al content: (1) the unit-cell lattice parameters of bridgmanite increase; (2) the average <A-O> bond distance increases; (3) the average <B-O> bond distance increases; (4) the B-O1 bond distance increases more than the two B-O2 distances, and the O1-B-O2 angle increases with consequent increase of the octahedral distortion; (5) the in-phase tilt (along [001]) and out-of-phase tilt (along [111]) become larger (Fig. 3.3-3), indicating an increase in the orthorhombic distortion of bridgmanite with Fe and Al substitution. The previous study with Al content of 0.202 deviates from the linear fit of our data likely because of its larger Fe^{2+} content (~ 0.085 atoms per formula unit, APFU) (Fig. 3.3-3).

d. *Synthesis of a large single-crystal of akimotoite using hydrous starting compositions (A. Adams and T. Boffa Ballaran)*

Akimotoite, $MgSiO_3$ with ilmenite structure, may be present in the Earth near subducting slabs in the lower transition zone and uppermost lower mantle. Because akimotoite is highly anisotropic compared to the other mineral constituents of this region, its elastic properties may significantly influence the dynamics of subducting slabs at these depths. Experimental techniques (*e.g.*, Brillouin spectroscopy) could be used to better constrain the elastic properties of this mineral phase, but a large (50-60 μm) single-crystal of akimotoite must first be synthesized. The goal of this study was to explore different hydrous starting compositions to optimize akimotoite grain growth at 1600 °C and 22 GPa in a multianvil press.

Different amounts of water (from brucite powder or liquid H_2O) were used as a flux to facilitate grain growth from a partial melt beginning at temperatures lower than for dry compositions. Mixtures of $MgSiO_3$ from oxide powders (MgO and SiO_2) were combined with brucite ($Mg(OH)_2$) to obtain compositions with 5, 6.5, 10, and 15 wt. % water. Different multianvil capsule types (folded Re-capsules, a spark-eroded multi-chamber Pt capsule, and welded Pt capsules) were explored to contain the water within the capsule at high P-T conditions.

X-ray diffraction and energy dispersive X-ray spectroscopy chemical analyses indicated a region with up to 30 μm-sized akimotoite grains in the sample with $MgSiO_3$ + 10 wt. % water synthesized from oxide powders in a Re-capsule (Fig. 3.3-4). Significant power instabilities were observed during heating, and this was considered to be due to water leakages from the folded Re-capsule coming in contact with the heater. Additional experiments with $MgSiO_3$ + 10 wt. % water synthesized from oxide powders at 1600 °C for longer durations using leakage-resistant capsule types could produce large enough single crystals to be used for elasticity measurements.

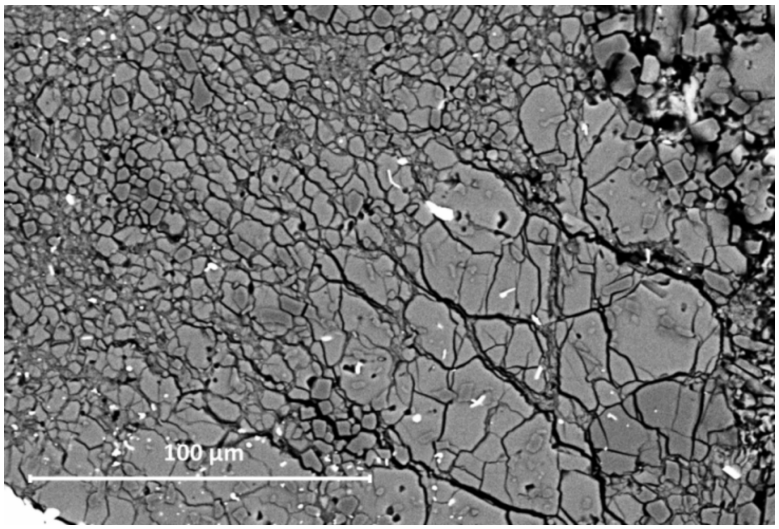

Fig. 3.3-4: Back-scattered electron image of a run product from $MgSiO_3$ + 10 wt. % H_2O showing a region of akimotoite grains on the right.

e. *Synthesis of $LiNbO_3$-type $Mg_3Al_2Si_3O_{12}$ at 45 GPa and 2000 K with a large volume press and subsequent Rietveld refinement (T. Ishii, R. Sinmyo/Tokyo, T. Komabayashi/Edinburgh, T. Boffa Ballaran, T. Kawazoe, N. Miyajima and T. Katsura)*

$LiNbO_3$-type $Mg_3Al_2Si_3O_{12}$ (py-LN) is formed by back-transformation of bridgmanite (Brg) with the same composition synthesized at 45 GPa and 2000 K during decompression. Although some compounds with the LN-structure are known (*e.g.*, $FeTiO_3$ and $MnTiO_3$), the structural features of LN-type silicate phases are not yet clear because of difficulties to synthesise large enough samples with sufficient quality to analyse the structure. In this study, the synthesis of a high-quality aggregate was conducted using a large volume press and structure analysis was performed with powder synchrotron X-ray diffraction data.

Py-LN was synthesized by the following three steps. Firstly, a glass with an $Mg_3Al_2Si_3O_{12}$ composition (py-glass) was synthesized from a mixture of MgO, Al_2O_3 and SiO_2 with a 3:1:3 molar ratio by quenching into water after melting at a temperature of 1950 K for 1 hour. The py-glass was then converted to a sintered aggregate of ilmenite-type $Mg_3Al_2Si_3O_{12}$ (py-Ak) at 26 GPa and 1170 K for 1 hour. A sintered aggregate of LN-type $Mg_3Al_2Si_3O_{12}$ (py-LN) was synthesized by compressing the sintered py-Ak aggregate with a press load of 15 MN, heating to 2000 K for 3 hours, quenching to ambient temperature, and then decompressing to ambient pressure. These high P-T syntheses were conducted using the IRIS-15 multianvil press at BGI. The composition was determined to be $Mg_{2.98(2)}Al_{1.99(2)}Si_{3.02(2)}O_{12}$ by electron microprobe analysis.

The Rietveld refinement was conducted using synchrotron X-ray diffraction data collected at SPring-8 (BL10XU) in Japan (Fig. 3.3-5). The lattice parameters were determined to be a = 4.8194(3) Å, c = 12.6885(8) Å, V = 255.23(3) Å^3 and Z = 6 (hexagonal, $R3c$). The average A-O and B-O distances in AO_6 and BO_6 octahedra are 2.043 Å and 1.840 Å, respectively, which are similar to the sums of ionic raidii of the averaged A- and B-site cations and oxygen (2.073 and 1.833 Å). The present compound has B-site cations in the octahedral site largely shifted

along the *c* axis compared with other $LiNbO_3$-type phases formed by back-transition from the perovskite structure, and as a result, the coordination number is almost three. The present compound might occur in shocked meteorites as well as LN-type $FeTiO_3$. This synthesis approach could also be useful to explore novel materials.

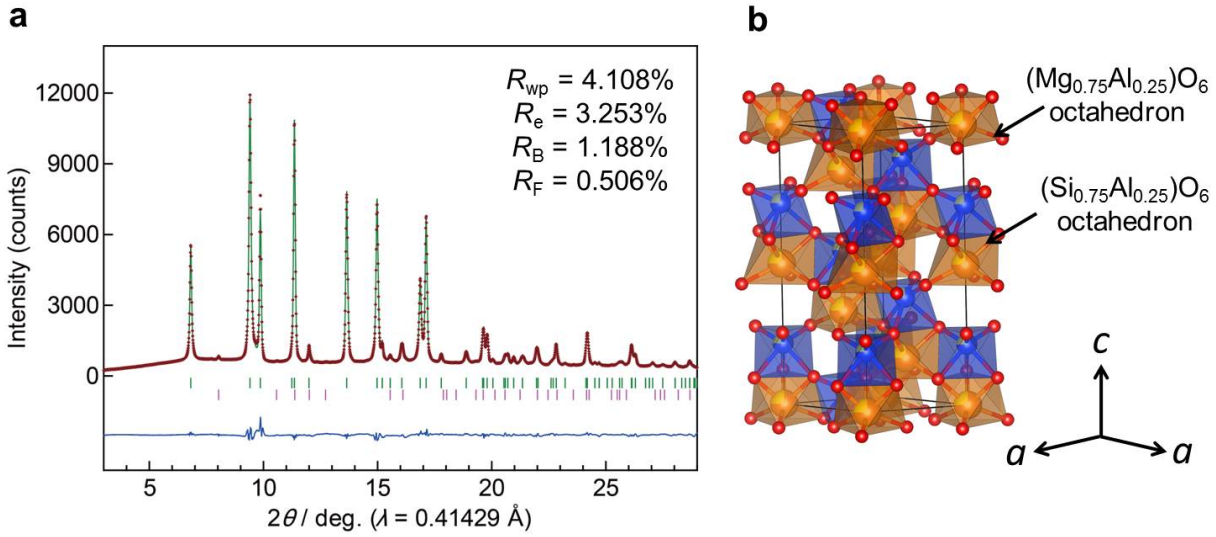

Fig. 3.3-5: $LiNbO_3$-type $Mg_{2.98(2)}Al_{1.99(2)}Si_{3.02(2)}O_{12}$: (a) X-ray diffraction pattern with Rietveld refinement; (b) polyhedral representation of the refined crystal structure

f. *Single crystal synthesis of δ-(Al,Fe)OOH (T. Kawazoe, I. Ohira/Sendai, T. Ishii, T. Boffa Ballaran and C.A. McCammon; A. Suzuki and E. Ohtani/Sendai)*

δ-AlOOH is an important hydrous phase for understanding the water cycle in the deep Earth because: (1) a large amount of water can be incorporated in its crystal structure; (2) this phase can exist in hydrous pyrolite mantle, hydrous basalt and hydrous sediment components of descending slabs in the mantle transition zone and the lower mantle; (3) this phase can carry water to the core-mantle boundary; and (4) chemical reaction between δ-AlOOH and Fe-Ni alloy can provide hydrogen to the Earth's core. Consequently, properties of δ-AlOOH are fundamentally important for addressing the water cycle in the mantle transition zone, the lower mantle and the core.

Single crystals of δ-AlOOH and Fe-bearing δ-AlOOH with dimensions up to ~ 0.6 mm were synthesized by a high-pressure hydrothermal method (Fig. 3.3-6). Synthesis experiments were performed at 21 GPa and 1480 K for 4 h using a Kawai-type multianvil apparatus. Mössbauer spectra showed 95-100 % $Fe^{3+}/\Sigma Fe$ at the octahedral site in Fe-bearing δ-AlOOH. Unit-cell parameters of δ-AlOOH were consistent with those of previous studies, and they increased linearly with Fe/(Al+Fe) of the starting materials. These results demonstrate that δ-AlOOH can form a solid solution with ε-FeOOH. The crystals contained a small number of fluid inclusions. Synthesis of large single crystals of δ-(Al,Fe)OOH will facilitate investigations of their phase stability, physical properties including elasticity and elastic anisotropy and

behaviour of hydrogen bonding, which will improve models of the water and oxygen cycles in the deep Earth.

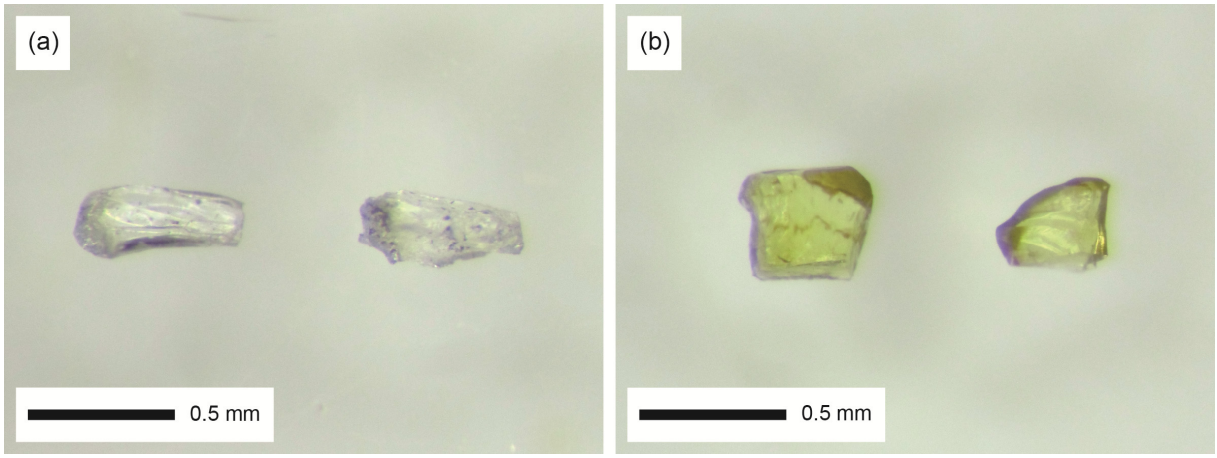

Fig. 3.3-6: Photographs of the single crystals: (a) δ-AlOOH, (b) Fe-bearing δ-AlOOH, where Fe/(Al+Fe) of the starting material was 0.06.

g. *High-pressure behaviour of δ-AlOOH and Phase D (D. Simonova, E. Bykova, M. Bykov, T. Kawazoe and L.S. Dubrovinsky)*

Water plays an important role in the dynamics of the Earth's interior. If water is transported into the deep mantle, properties of mantle phases including viscosity, melting temperature and atomic diffusion can be considerably affected. The properties of high-pressure hydrous minerals thus play an important role in understanding the petrology and geochemical evolution of the mantle. In this context water-bearing dense phases like Phase D and δ-AlOOH are interesting targets of investigation at elevated pressure (and eventually at both high pressure and high temperature). So far high-pressure studies of Phase D and δ-AlOOH have been performed on powder materials up to about ~ 25 GPa and on single crystals (in the case of δ-AlOOH) at relatively low pressures (below 12 GPa). This limited amount of structural information about the phases can affect the accuracy of determination of their equations of state. We therefore performed high-pressure single-crystal X-ray diffraction on these phases using diamond anvil cells.

High-quality single crystals of Phase D and δ-AlOOH were synthesized at high-pressure high-temperature conditions at BGI. Single crystals of Phase D were grown at 26 GPa and 1500 °C in a 1200 ton multianvil Sumitomo press by heating for 10 min. Single crystals of δ-AlOOH were obtained by decomposition of $Al(OH)_3$ at 21 GPa and 1050 °C during heating over 4 h in a 1000 ton multianvil Hymag press. The as grown single crystals were examined by X-ray diffraction employing a three-circle Bruker diffractometer equipped with a SMART APEX CCD detector and a high-brilliance Rigaku rotating anode (Rotor Flex FR-D, Mo-Kα radiation) with Osmic focusing X-ray optics. High-pressure single-crystal X-ray diffraction measurements were performed at the Extreme Conditions Beamline P02.2 at PETRA III

(Hamburg, Germany) using a wavelength of 0.28995 Å. δ-AlOOH single crystals with 30 µm diameter and Phase D single crystals with 40 µm diameter were put together in a diamond cell (250 µm diameter culets) along with ruby for pressure calibration. Neon was used as a pressure-transmitting medium. Diffraction data were collected at room temperature up to 30 GPa with pressure steps of 2 to 4 GPa.

Phase D at ambient conditions has trigonal symmetry and unit-cell parameters a = 4.7453(4) Å, c = 4.3450(5) Å, and V = 84.74(3) Å^3/unit cell. δ-AlOOH is orthorhombic with unit cell parameters a = 2.827(2) Å, b = 4.2022(4) Å, c = 4.709(1) Å, and V = 55.59(3) Å^3/unit cell. The room temperature P-V data for both samples were fitted using a second order Birch-Murnaghan equation of state. The results for Phase D gave an ambient unit-cell volume V_0 = 84.73 (2) Å^3 and an isothermal bulk modulus K_0 = 162 (3) GPa for K_p = 4 (Fig. 3.3-7), while for δ-AlOOH the values are V_0 = 55.83 (2) Å^3 and K_0 = 140.9 (2) GPa with K_p = 4 (Fig. 3.3-8).

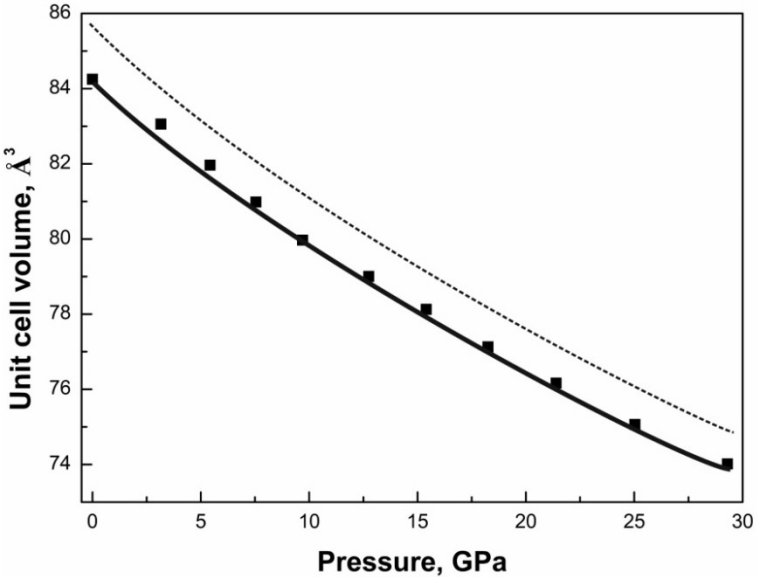

Fig. 3.3-7: Compressibility data for Phase D synthesised in this study (filled squares) compared with the trend of literature data (dashed line) [Frost & Fei 1999, *Phys. Chem. Minerals* 26: 415-418].

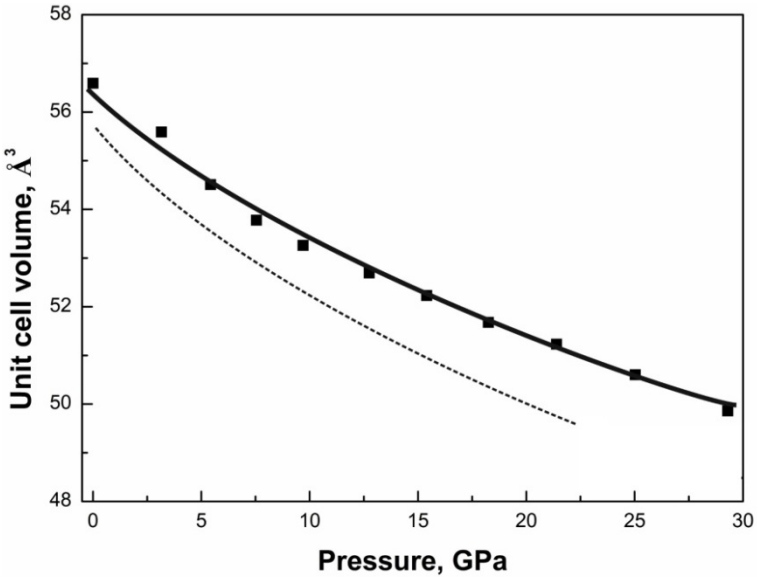

Fig. 3.3-8: Compressibility data for δ-AlOOH synthesised in this study (filled squares) compared with the trend of literature data (dashed line) [Vanpeteghem *et al*. 2002, *Geophys. Res. Lett*. 29, DOI: 10.1029/2001GL014224].

h. *Observation of a novel high-pressure high-temperature phase of Fe_3O_4 (E. Bykova, N.A. Dubrovinskaia/Bayreuth, L.S. Dubrovinsky, M. Bykov, C.A. McCammon, S.V. Ovsyannikov, M. Hanfland/Grenoble, H.-P. Liermann/Hamburg and V. Prakapenka/Argonne)*

At ambient conditions Fe_3O_4 (magnetite) has the cubic crystal structure of inverse spinel (space group $Fm\bar{3}m$, No. 225). In previous experiments based on powder X-ray diffraction (XRD) and Mössbauer spectroscopy in diamond anvil cells, magnetite was shown to transform into a high-pressure phase (*HP*-Fe_3O_4) above 19 GPa, but its crystal structure has remained the subject of debate. At least four candidates have been proposed for the high-pressure polymorph of Fe_3O_4, including a monoclinic structure with octahedrally coordinated iron atoms, a $CaMn_2O_4$-type, and a $CaTi_2O_4$-type (space group *Bbmm*, No. 63). Using single crystal XRD data collected at 44.5(5) GPa after heating at 2400(100) K, we were able to finally establish that *HP*-Fe_3O_4 has a $CaTi_2O_4$ structure type (*Bbmm, a* = 9.309(3), *b* = 9.282(2), and *c* = 2.6944(9) Å, R_1(all data) = 6.91 %). The crystal structure is composed of FeO_6 octahedra and trigonal prisms (Fig. 3.3-9).

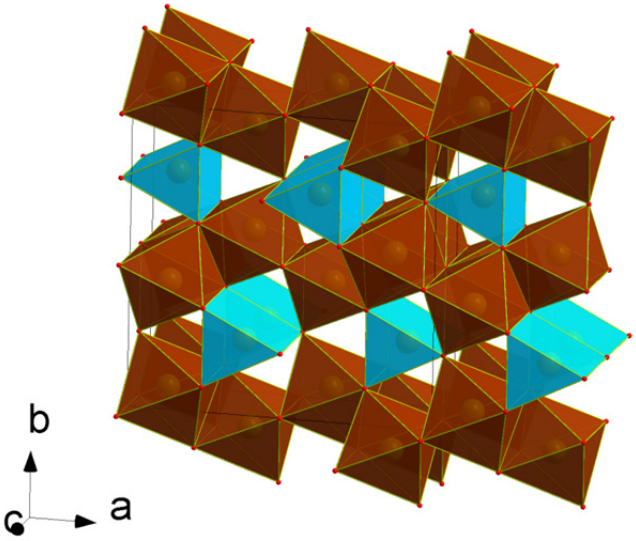

Fig. 3.3-9: Crystal structure of the high-pressure polymorph of Fe_3O_4 with the $CaTi_2O_4$ structure. The crystal structure is composed of FeO_6 octahedra (brown) and trigonal prisms (light blue) connected via common edges and corners.

Laser heating of *HP*-Fe_3O_4 at 2350(100) K and pressures up to 50 GPa did not result in any chemical or structural modifications. Moreover, we identified reflections belonging to *HP*-Fe_3O_4 in the products of thermal decomposition of siderite, $FeCO_3$ at 50(1) GPa and 2400(100) K). This finding confirms the wide pressure range of stability of *HP*-Fe_3O_4. At higher pressures, however, the behaviour of Fe_3O_4 changes. After laser heating at 80(1) GPa above 2900 K we observed the appearance of new XRD reflections. Also, reflections with similar *d*-spacing were found in the products of thermal decomposition of $FeCO_3$ at 75(1) GPa after laser heating to 2200(150) K and at 91(1) GPa after heating to 2500(200) K. The samples were characterized by X-ray diffraction. The single-crystal X-ray diffraction experiments were conducted at the ID09A beamline at the European Synchrotron Radiation Facility, Grenoble, France (MAR555 detector, λ=0.4126 Å); at the P02.2 beamline at PETRA III, Hamburg, Germany (PerkinElmer flat panel detector, λ=0.2904 Å); and at the 13-IDD beamline at the Advanced Photon Source, Chicago, USA (MAR165 CCD detector,

λ=0.3344 Å). Integration of the reflection intensities and absorption corrections were performed using CrysAlisPro software. The structure was solved by the direct method and refined by full matrix least-squares using SHELXTL software.

The new high-pressure high-temperature modification of Fe_3O_4 (*mI*-Fe_3O_4) has monoclinic symmetry (space group *I*2, No. 5, a = 5.951(8), b = 5.8176(16), c = 5.859(11) Å, β = 91.22(19)°). The crystal was slightly twinned, therefore refinement of the crystal structure could be performed only up to R_1 = 10.5 % (all data). The atomic arrangement is characteristic for a distorted Th_3P_4 structure type (Fig. 3.3-10). The asymmetric unit contains four independent iron atoms: Fe1 and Fe2 are sitting on a two-fold axis, while Fe3 and Fe4 are located in general positions. Each iron atom is surrounded by eight oxygen atoms with Fe-O distances varying from 1.86(2) to 2.37(2) Å. Each FeO8 polyhedron has eight FeO8 neighbouring units connected through common triangular faces. Unlike *HP*-Fe_3O_4, the crystal structure of *mI*-Fe_3O_4 is built solely from 8-coordinated Fe atoms, which follows the common trend of increasing atomic coordination with pressure in high-pressure phases in order to increase packing density.

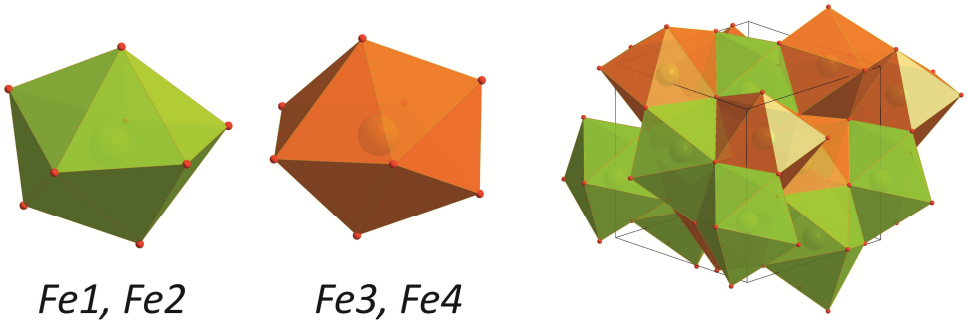

Fig. 3.3-10: Crystal structure of the high-pressure high-temperature polymorph of Fe_3O_4 with the distorted Th_3P_4 structure (right). The asymmetric unit contains four independent Fe atoms, Fe1 and Fe2 (green) are sitting on a two-fold axis, while Fe3 and Fe4 (orange) are located on general positions. Each iron atom is surrounded by eight oxygen atoms.

i. *A new tetrahedrally coordinated carbonate in the lower mantle: MnC_2O_5 (S. Chariton, E. Bykova, M. Bykov, V. Cerantola, I. Kupenko/Grenoble, G. Aprilis, C.A. McCammon and L.S. Dubrovinsky)*

During the past decade, alkaline earth and transition metal carbonates such as calcite ($CaCO_3$), magnesite ($MgCO_3$), siderite ($FeCO_3$) and rhodochrosite ($MnCO_3$) have been of great interest to deep carbon cycle-related studies. Interest in the high-pressure behaviour of carbonates has been enhanced by recent discoveries of novel compounds that consist of tetrahedral CO_4^{4-} units. According to theoretical predictions, the existence of CO_4-bearing carbonates raises intriguing possibilities concerning potential silicate analogues as well as implications for the complex mineralogy of the D″ region and crystal chemical reactions between silicates and carbonates at depths greater than 1600 km within the Earth. Tetrahedrally-coordinated carbonates are a relatively new study area, which although highly promising, remains poorly

explored so far. In our efforts to study the high-pressure structures of transition metal carbonates, and in particular $MnCO_3$, we discovered novel phases including a new manganese tetracarbonate phase reported here for the first time.

We synthesized pure $MnCO_3$ single crystals at 18 GPa and 1600 K using a Sumitomo multianvil press at BGI. Diamond anvil cells were employed to generate high pressures and Ne gas was used as pressure-transmitting medium to promote hydrostaticity. A portable double-sided laser heating system was used to heat the sample at ~ 2000(150) K. Single crystals X-ray diffraction measurements up to ~ 66 GPa were conducted at the ID09A beamline at the European Synchrotron Radiation Facility, Grenoble, France.

Our first results indicate that rhodochrosite undergoes a structural transformation above ~ 44 GPa. Specifically the calcite-type structure ($R\bar{3}c$) of $MnCO_3$ transforms to the triclinic structure ($P\bar{1}$) of $MnCO_3$-II, which is isostructural to $CaCO_3$-VI. The structural transition in the $MnCO_3$-II phase is accompanied by a ~ 5 % volume collapse (Fig. 3.3-11). At 65.9(1) GPa and after heating at 2000(150) K, $MnCO_3$-II thermally decomposes and three new phases are found, one of which is monoclinic ($P2_1/c$) $MnCO_3$. The second phase is the novel oxide Mn_5O_7 ($C2/m$) and the third and most important phase is the new tetrahedrally coordinated carbonate MnC_2O_5 ($Fd\bar{3}m$) (Fig. 3.3-12). In order for this exotic phase to form, oxygen must be released from $MnCO_3$-II during heating. Consequently, the excess of oxygen forms the oxide Mn_5O_7. MnC_2O_5 consists of highly distorted MnO_6 edge-shared octahedra surrounding CO_4^{4-} corner-shared tetrahedra in a 3-fold symmetry (Fig. 3.3-12).

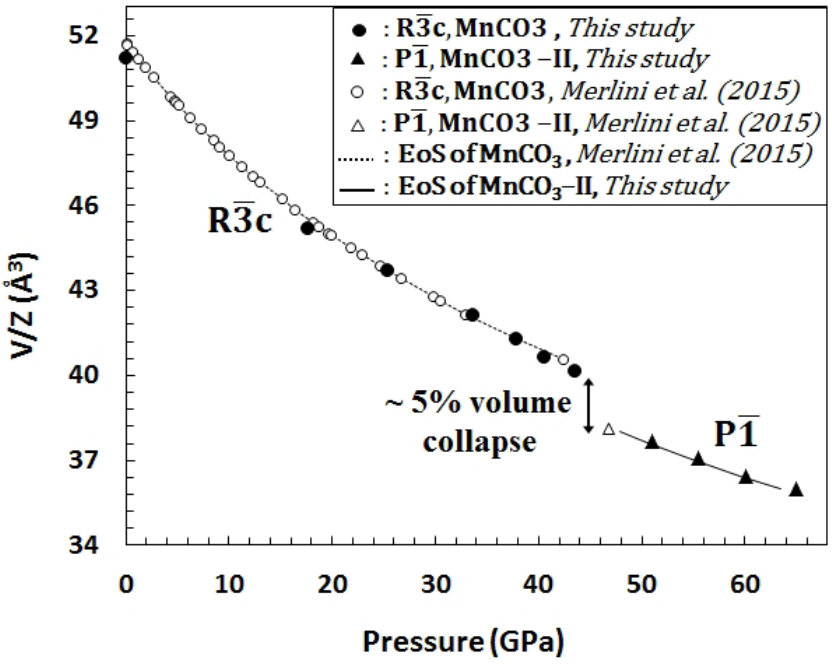

Fig. 3.3-11: Volume data of rhodochrosite with increasing pressure and the equation of state for magnesite-type $MnCO_3$ and triclinic $MnCO_3$-II. Data from this study are shown as well as from the literature [*Merlini et al., 2015, Am. Mineral., 100, 2625-2629*]. Error bars are indicated and in some cases are smaller than the symbols.

Previous reports on siderite and ferromagnesian carbonate have detected similar tetrahedrally coordinated carbon structures coexisting with complex oxides in the pressure range 76 - 135 GPa (~ 2000-2900 km). Our findings demonstrate that CO_4^{4-}-bearing carbonates can form at even shallower depths (> 1600 km). In order to better understand and fully constrain the

crystal chemistry of tetrahedrally coordinated carbonate structures, further experiments are required to uncover the new high-pressure carbonate phases that are waiting to be discovered.

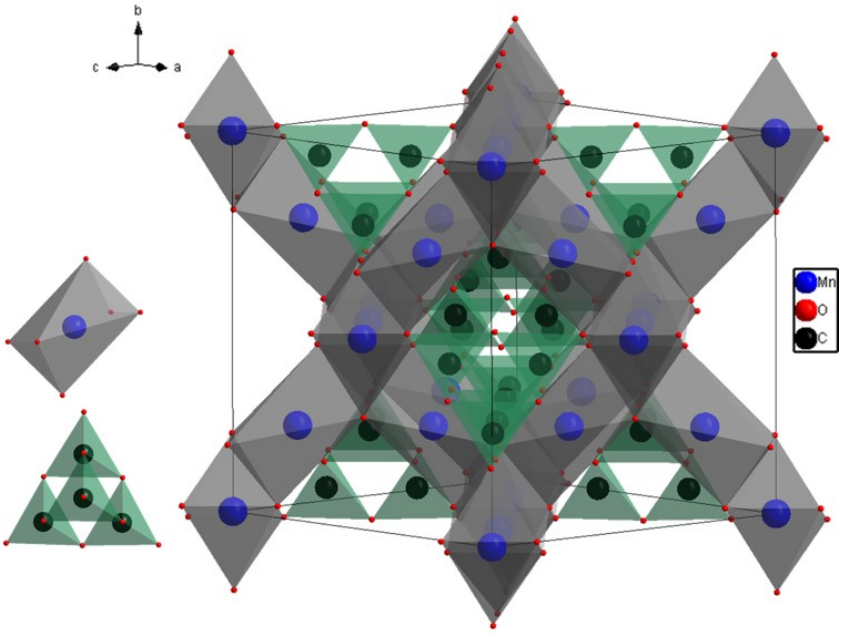

Fig. 3.3-12: Schematic representation of the new MnC_2O_5 structure at 65.9(1) GPa.

j. *Precise determination of the post-spinel transition binary loop in the MgO-FeO-SiO_2 system by* in situ *X-ray diffraction (T. Ishii, H. Fei, Z.D. Liu, T. Kawazoe, N. Tsujino/Misasa, T. Takafumi/Hiroshima, L. Wang, D. Druzhbin, E. Kulik/Hamburg; F. Maeda, Y. Higo and Y. Tange/Kouto; T. Katsura)*

The 660-km seismic discontinuity (D660) is one of the keys to understanding the structure and dynamics of the Earth's mantle. D660 is considered to be caused by the dissociation of $(Mg,Fe)_2SiO_4$ ringwoodite to $(Mg,Fe)SiO_3$ bridgmanite + (Mg,Fe)O ferropericlase (post-spinel transition). According to seismic observations, the depth interval of D660 is less than 2 to 4 km, corresponding to 0.1 to 0.15 GPa, which means that D660 is extremely sharp. The correspondence between the pressure interval of the post-spinel transition and the depth interval of D660 is not yet clear due to experimental challenges. In this study, the post-spinel transition binary loop in the MgO-FeO-SiO_2 system was carefully examined with a precision in pressure better than achieved so far by *in situ* X-ray diffraction.

Energy-dispersive X-ray diffraction experiments under high pressure and temperature were carried out using a Kawai-type multianvil press with DIA-type guide blocks, SPEED-*Mk*.II, at the synchrotron radiation facility, SPring-8, Japan. Second-stage WC anvils (TF05, Fujilloy Co., Ltd) with truncations of 4 mm and tapers of 1.0 degree were used. Sintered mixtures of Mg_2SiO_4 + $MgSiO_3$ + MgO (Fo_{100}) and $(Mg,Fe)_2SiO_4$ + $(Mg,Fe)SiO_3$ + (Mg,Fe)O with overall composition Fe/Mg+Fe = 0.7 with 5 wt. % Fe metal (Fo_{70}) were used as starting materials. Figure 3.3-13 shows cross sections of the cell assembly. Generated pressures were calibrated using an MgO equation of state from the literature. Sintered MgO pressure

calibrants and two starting materials were put at the centre of a MgO sleeve in a Re cylindrical heater to collect diffraction data of samples with different compositions simultaneously (Fig. 3.3-13c). Temperatures up to 1700 K were measured at the centre of sample chambers with a W3%Re-W25%Re thermocouple. Samples were first compressed at room temperature, and then gradually heated to 1100 K. Samples were then rapidly heated to 1700 K. On reaching 1700 K, loads were applied to maintain target pressures of 22-24 GPa at 1700 K.

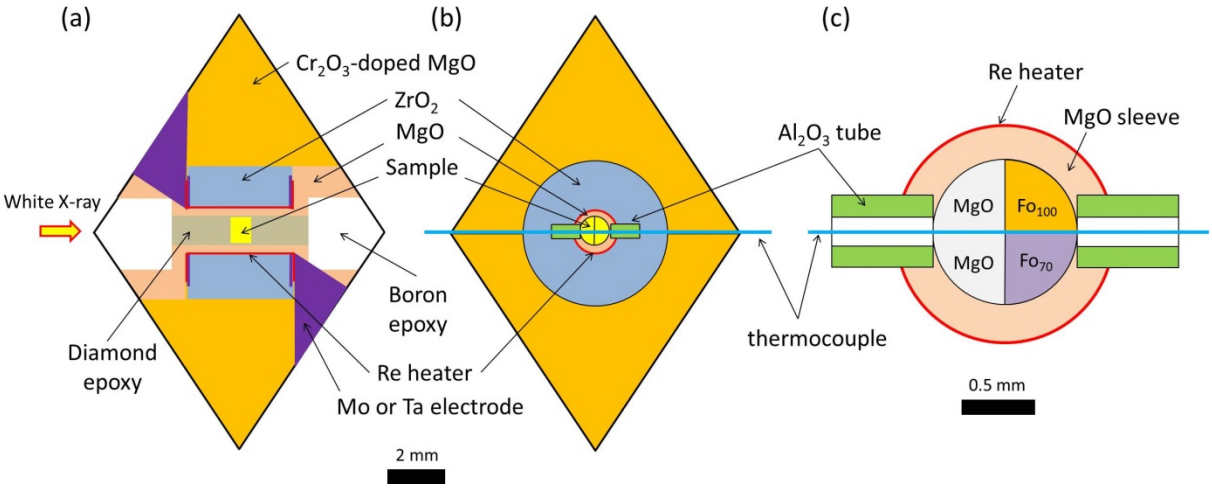

Fig. 3.3-13: Cross sections of the cell assembly used for the *in situ* X-ray diffraction experiment: (a) view parallel to incident X-ray, (b) view normal to incident X-ray, and (c) part containing the sample.

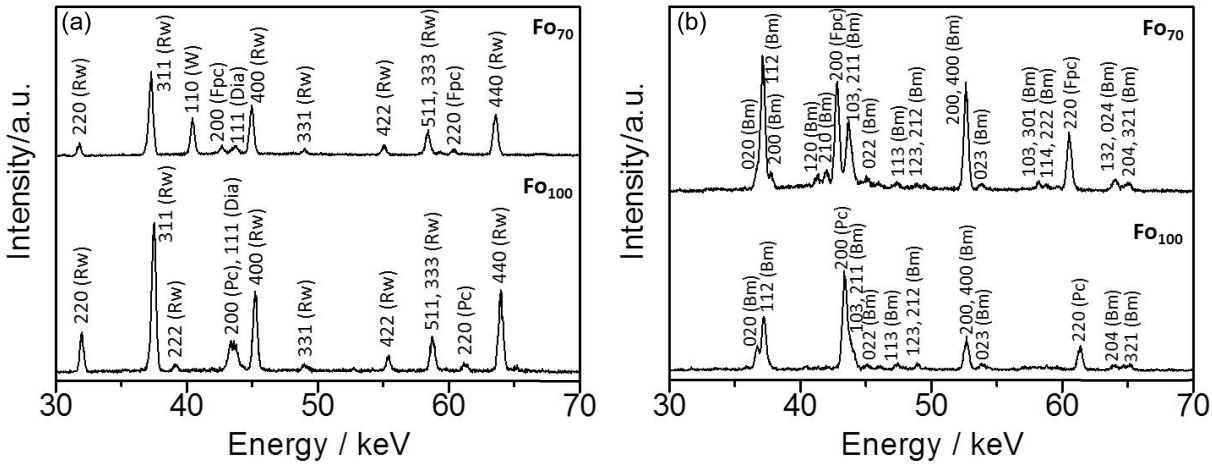

Fig. 3.3-14: *In situ* X-ray diffraction patterns of run products at 1700 K: (a) 22.6 ± 0.07 GPa and (b) 24.0 ± 0.04 GPa. Lines are marked as follows: Rw, ringwoodite; Pc, periclase; Fpv, ferropericlase; Dia, diamond epoxy; Bm, bridgmanite; St, stishovite.

Representative *in situ* X-ray diffraction patterns of the samples are shown in Fig. 3.3-14. The patterns were collected on the low- and high-pressure sides of the post-spinel transition binary

loop with a high precision of pressure less than 0.1 GPa. So far in this study we have successfully constructed an appropriate cell assembly for this project. In work to come we will determine the pressure interval of the post-spinel transition binary loop.

k. *Al_2O_3 solubility in bridgmanite as a function of pressure and temperature in the lower mantle (Z.D. Liu, T. Katsura, T. Ishii, H. Fei, N. Miyajima, L. Wang; T. Irifune, M. Nishi, H. Ohfuji and T. Sakai/Matsuyama; Y. Tange and Y. Higo/Hyogo)*

Aluminium is the fifth most abundant element in the Earth's mantle. It has been in the spotlight because of its importance for understanding the mineralogy of the Earth's mantle. A previous study showed that all Al_2O_3 can be incorporated into $(Mg,Fe)SiO_3$ bridgmanite under lower mantle conditions, with no need for other new aluminous mineral phases in a pyrolitic lower mantle. Al_2O_3 can affect the iron valence and content in bridgmanite, and also it changes the Mg-Fe partitioning in bridgmanite and magnesiowustite; hence it can influence chemical heterogeneity in the lower mantle. Investigation of the effect of Al_2O_3 on the chemical and physical properties of bridgmanite is thus important for understanding the chemical and physical state of the lower mantle.

We studied the Al_2O_3 solubility in bridgmanite up to lower mantle conditions using *in situ* synchrotron X-ray diffraction measurements combined with sintered diamond (SD) anvils in a multianvil apparatus. Quench experiments at pressures lower than 27 GPa were conducted using an IRIS-15 multianvil apparatus at BGI (Fig. 3.3-15). At pressures above 27 GPa, the coexisting mineral assemblage is aluminous bridgmanite and Al_2O_3 corundum (Fig. 3.3-16). The solubility of Al_2O_3 in bridgmanite was found to depend significantly on temperature and pressure. The solubility of Al_2O_3 in bridgmanite increases from 9 mol. % at 1700 K to 22 mol. % at 2500 K at ~ 27 GPa, and bridgmanite becomes more aluminous with increasing pressure up at 1700 K, from 9 mol. % at 27 GPa to ~ 24 mol. % at 48 GPa.

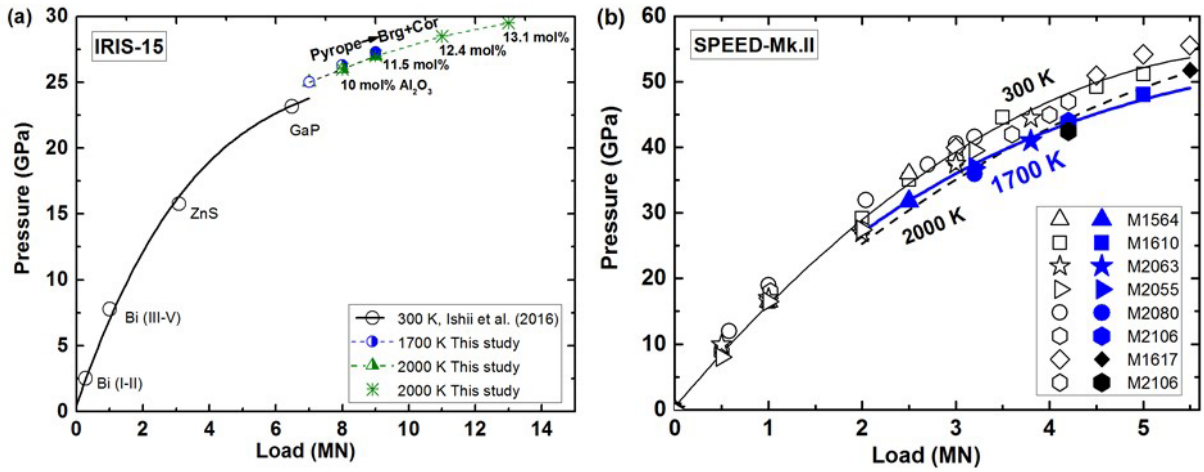

Fig. 3.3-15: (a) Pressure calibration of quench experiments in an IRIS-15 (1500 ton) multianvil apparatus at 1700 and 2000 K. (b) Pressure calibration of *in situ* SD experiments at 300, 1700 (this study) and 2000 K (Liu *et al.* 2016), respectively.

Bridgmanite can incorporate higher contents of Al_2O_3 in pyrope-type bridgmanite, *e.g.*, 30 mol. % at 52 GPa and 2000 K (Fig. 3.3-17). Al_2O_3 corundum can also incorporate a large amount of $MgSiO_3$ depending on pressure and temperature. The present results provide a good pressure reference at pressures higher than 30 GPa at high temperature for in house quench experiments. These new phase diagrams in the system $MgSiO_3$–Al_2O_3 confirm that bridgmanite is the dominant host mineral for Al_2O_3 in a peridotitic or pyrolitic lower mantle.

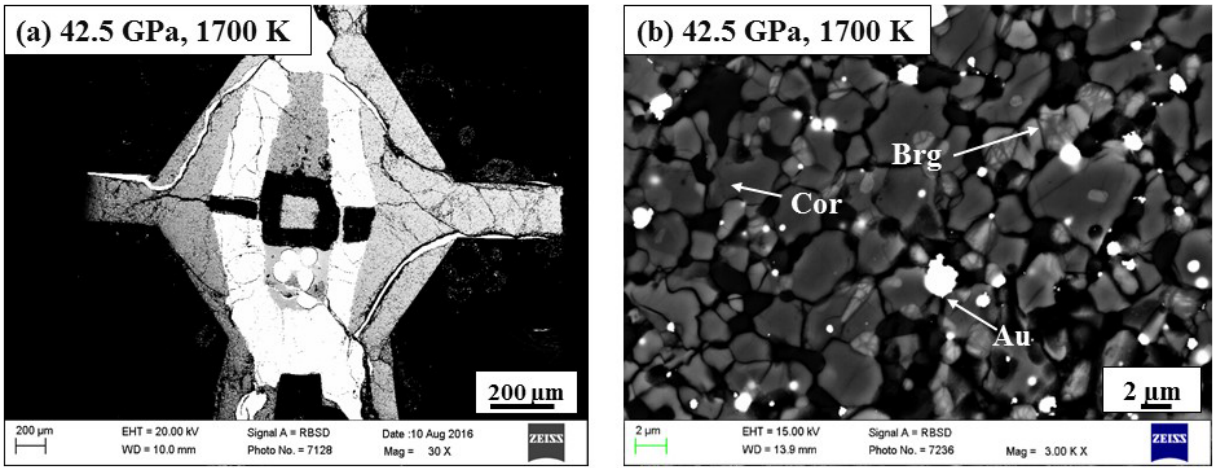

Fig. 3.3-16: Electron back-scattered images of (a) the cell assembly and (b) the sample quenched from 42.5 GPa and 1700 K.

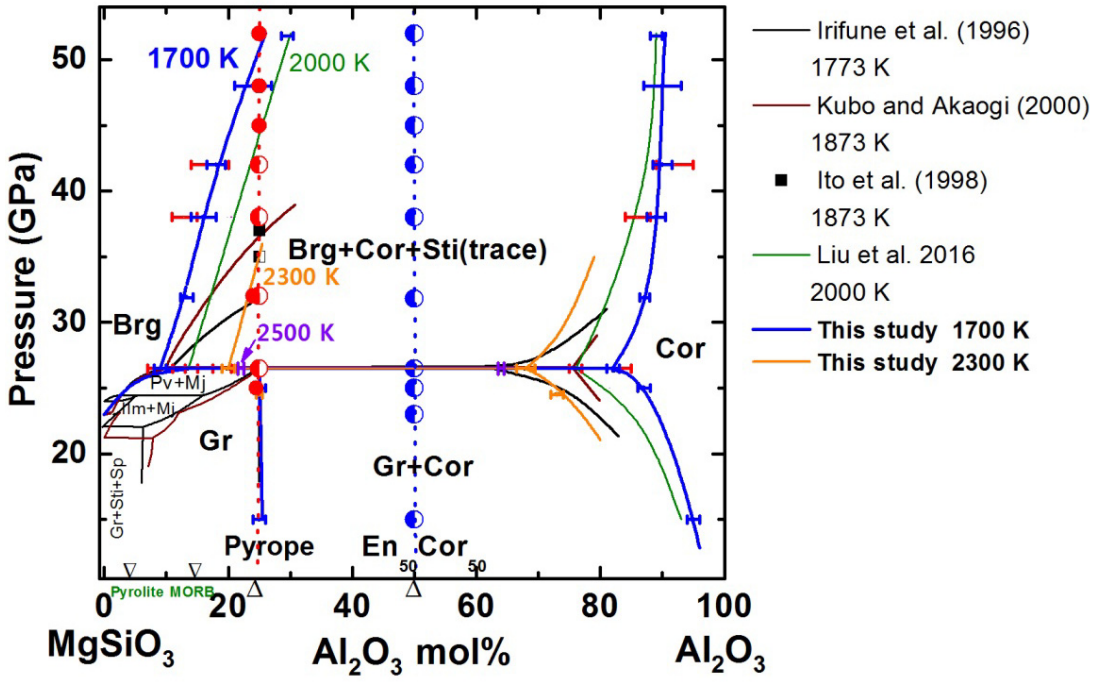

Fig. 3.3-17: Phase relations in the system $MgSiO_3$-Al_2O_3 at pressures of 15 to 48.2 GPa at 1700-2300 K.

l. *A new high-pressure phase transition in clinoferrosilite:* In situ *single-crystal X-ray diffraction study (A.S. Pakhomova, L. Ismailova/Bayreuth, E. Bykova, M. Bykov, T. Boffa Ballaran and L.S. Dubrovinsky)*

Pyroxenes are one of the major constituent minerals in the Earth's upper mantle. Depending on the petrological model, orthopyroxenes comprise between 17 and 27 % of the upper mantle; whereas the abundance of clinopyroxenes varies in the range 16-20 %. Given these proportions, pyroxenes may have a major influence on the thermodynamics of the upper mantle. Therefore, a well-constrained correlation between chemical composition, crystal structure and elastic properties is extremely important for modelling the behaviour of pyroxenes in the Earth's interior. Here we report the results obtained from a single-crystal X-ray diffraction investigation on the compressional behaviour of clinoferrosilite, $Fe_2Si_2O_6$, up to 45 GPa.

Single crystals of clinoferrosilite were synthesized at 9.5 GPa and 1100 °C using a split-sphere type multianvil apparatus at the Bayerisches Geoinstitut. Three separate *in situ* high-pressure single-crystal diffraction experiments using diamond anvil cells (DAC) were performed at the experimental stations P02.2 at PETRA III (Hamburg, Germany) and ID09 at the European Synchrotron Radiation Facility (Grenoble, France). Ferrosilite crystals along with ruby spheres were placed inside the pressure chamber of the DACs. To achieve quasi-hydrostatic conditions, the DACs were loaded with neon as pressure-transmitting medium. Pressures were determined using both the equation of state of neon and ruby fluorescence.

The experiments performed up to 45 GPa revealed the occurrence of two phase transitions of clinoferrosilite. A $P2_1/c$ to $C2/c$ transition occurs between 1.3(1) and 3.0(1) GPa, in agreement with previous observations. The phase transition results in a sudden decrease of all unit-cell parameters with a resulting volume discontinuity of ~ 3 % (Fig. 3.3-18). Upon further compression all the unit-cell parameters decrease continuously until a further sudden change is observed between 30.0(1) and 35.9(1) GPa due to the occurrence of a second transition to a HP-$P2_1/c$ phase. At the transition, the *b* and *c* axes decrease whereas *a* and *a* sin β increase. This first-order transition is accompanied by a 5 % decrease in volume.

The measured *P-V* data were used to determine the equations of state of the $C2/c$ and HP-$P2_1/c$ phases. Fitting the data for the $C2/c$ phase using a third-order Birch-Murnaghan equation of state (BM EoS) resulted in the following parameters: V_0 = 426.2(2) Å^3, K_{T0} = 113(3) GPa and K' = 6.3(3) GPa. For the HP-$P2_1$/c phase the available four pressure points were insufficient to properly constrain an equation of state. Therefore, the pressure point at 35.9 GPa was chosen as a reference state for the fitting. The values of the unit-cell volume, V_{36}, and of the bulk modulus, K_{36}, were thus determined at 35.9 GPa by fitting a second-order BM EoS. The obtained EoS parameters of the two $Fe_2Si_2O_6$ phases at 36 GPa indicate that the HP-$P2_1/c$ phase is more compressible than the $C2/c$ phase.

Structural data were obtained for clinoferrosilite at 15 pressure points from ambient conditions up to 45 GPa. The crystal structure of the $C2/c$ phase is based on three

crystallographically distinct polyhedra: two octahedra, $Fe1O_6$ and $Fe2O_6$, and one tetrahedron, SiO_4. The tetrahedra are connected via bridging O3 atoms to form chains running along the *c* axis. The $Fe1O_6$ octahedra share a common edge, forming dense chains parallel to the same direction. The Fe2 atoms occupy the space between the tetrahedral chains and the chains of $Fe1O_6$ octahedra. With increasing pressure all structural units undergo an anisotropic distortion. The lowering of the symmetry to a HP-$P2_1/c$ phase above 30 GPa is due to the rearrangement of half of the layers of corner-sharing SiO_4 tetrahedral chains to octahedrally coordinated Si (Fig. 3.3-19). This forms a new type of layer by polymerization of Si_2O_6 polyhedra via common edges. The remaining Si chains (Si1) retain their tetrahedral coordination. The new configuration of ^{VI}Si layers suggests the possibility of a progressive transformation of the pyroxene structure into an ilmenite-type structure. The persistence of metastable pyroxene up to pressures higher than expected and its feasible direct transformation to ilmenite are of special interest for understanding the dynamics of cold subducting slabs.

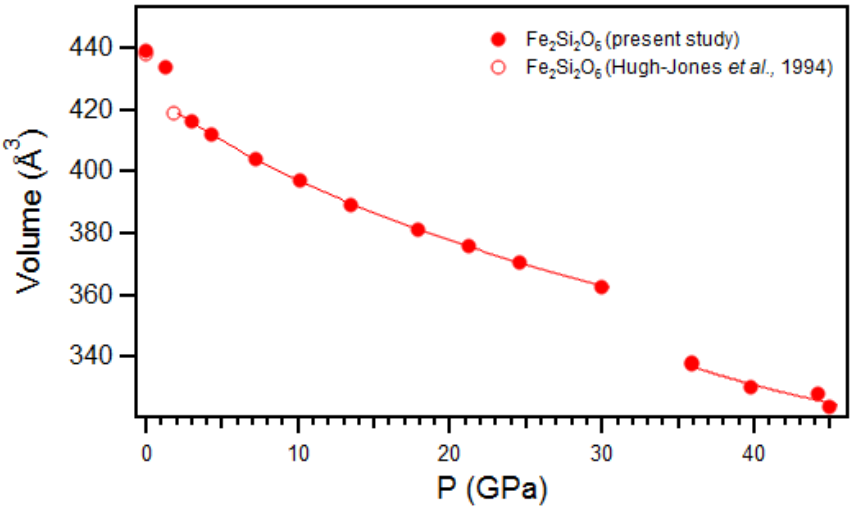

Fig. 3.3-18: High-pressure evolution of the unit-cell volume of clinoferrosilite.

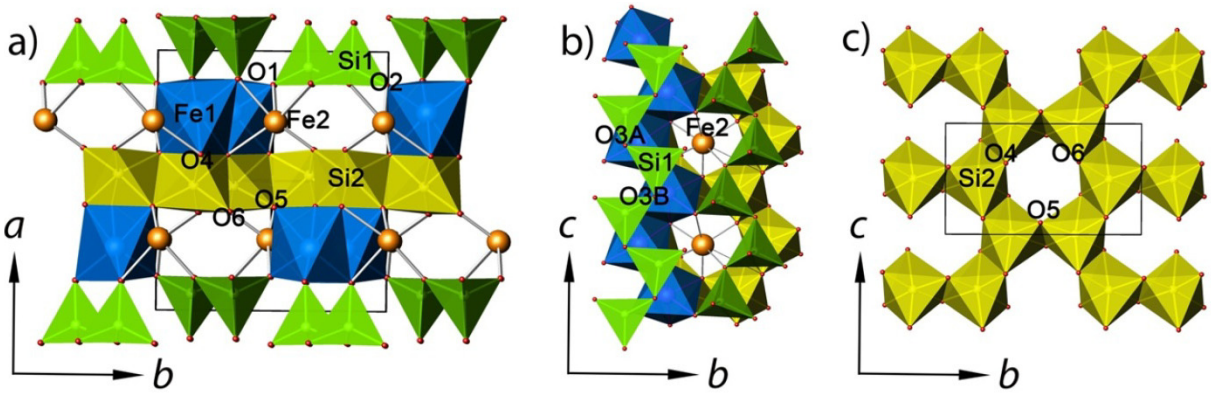

Fig. 3.3-19: Crystal structure of the HP-$P2_1/c$ phase of clinoferrosilite at 35.9 GPa. $Fe1O_6$ octahedra, $Si2O_6$ octahedra and $Si1O_4$ tetrahedra are indicated in blue, yellow and green, respectively. Fe2 atoms are shown as orange spheres.

m. *Exploring a new geobarometer for ferropericlase inclusions in diamond from the lower mantle (C. Melai, C.A. McCammon, K. Marquardt and K. Armstrong)*

Ferropericlase (Mg,Fe)O is the most abundant non-silicate oxide in the Earth's lower mantle and is one of the most common mineral inclusions in diamonds and super-deep diamonds. Although (Mg,Fe)O is absent in common upper mantle rocks, only the coexistence of ferropericlase with perovskite in diamonds can unequivocally provide evidence for lower mantle origin. Different approaches have been used to prove or disprove the potential lower mantle origin of ferropericlase, including the presence of magnesioferrite exsolution. The experimental determination of pressure and temperature constraints for magnesioferrite exsolution could lead to a barometer for lower mantle phase assemblages.

The aim of the study was to investigate the formation conditions (*e.g.*, pressure, temperature and oxygen fugacity) of magnesioferrite from ferropericlase as a potential barometer. We made multianvil syntheses of ferropericlase at different pressures (15 to 25 GPa) and fixed temperature and oxygen fugacity conditions (Re-ReO_2 buffer). Six multianvil runs were performed with two compositions, $(Mg_{0.75}Fe_{0.25})O$ and $(Mg_{0.55}Fe_{0.45})O$. Mössbauer spectroscopy and TEM analysis was performed to document the presence of the spinel phase. Mössbauer results showed the presence of an additional magnetic phase in one of the run products. The observed magnetic sextet is consistent with the magnetic components expected in the spinel phase and previously reported in the literature. The sextet is consistent with TEM analysis for the same sample that showed additional diffraction spots confirming the topotaxial relation of spinel and ferropericlase. In contrast, no unambiguous proof of spinel was observed in other samples using Mössbauer spectroscopy. However, some electron diffraction patterns showed evidence of streaking, suggesting the beginning of exsolution. Overall the two compositions show opposite trends with pressure (Fig. 3.3-20). One possible explanation could be a change in oxygen fugacity during one of the multianvil runs. More experiments are needed. We note that for the $(Mg_{0.75}Fe_{0.25})O$ composition, all run products at all pressures showed evidence for the additional phase by TEM.

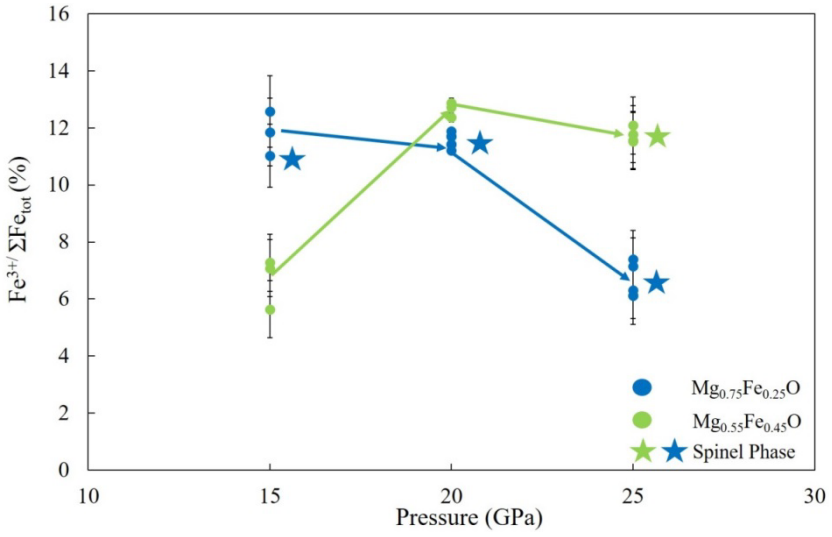

Fig. 3.3-20: Variation of relative Fe^{3+} abundance with pressure for two compositions of ferropericlase. Stars indicate where magnesioferrite was observed using TEM.

n. *Iron-bearing carbonate stability in the Earth's deep interior (V. Cerantola, E. Bykova, I. Kupenko/Münster, M. Merlini/Milan, L. Ismailova/Bayreuth, C.A. McCammon, M. Bykov, A. Chumakov/Grenoble, S. Petitgirard, I. Kantor/Lund, V. Svitlyk and J. Jacobs/Grenoble, C. Prescher/Köln, R. Rüffer/Grenoble and L.S. Dubrovinsky)*

In the last century, the rapid increase in the amount of CO_2 in the atmosphere together with the observed correlation in climate change have increasingly focused scientists' attention on the carbon cycle and its evolution at the Earth's surface. The carbon cycle, however, has roots well below the surface, where recent estimations suggest that up to 90 % of the Earth's carbon budget may be shared between the Earth's mantle and core. Due to the dynamic nature of processes within our planet's interior, such as upwelling and downwelling of material via convection and subduction, there is a constant recycling of carbon between the Earth's surface and its deep interior. Subduction is considered so far to be the only mechanism capable of dragging a considerable amount of carbon to the deep Earth. In this study we focussed our attention on carbonate phases, which are the main carbon-bearing minerals in subducting slabs, and in particular on the stability of Fe-carbonates such as siderite ($FeCO_3$). Indeed, a previous experimental investigation on $MgCO_3$ revealed its stability at pressures and temperatures down to the core-mantle boundary. Due to the extensive solid solution formed between $MgCO_3$ and $FeCO_3$ at ambient conditions and the spin transition of Fe at high pressures which could influence the stability of the phase itself, we performed high P,T experiments on $FeCO_3$ in order to study its stability and potential decomposition and transformation products at the relevant pressure and temperature conditions.

Experiments were performed using synthetic $FeCO_3$ crystals at pressures and temperatures over 110 GPa and 2500 K, respectively. High pressure and high temperature were achieved by means of diamond anvil cells and by double-sided laser heating. Neon was employed as a pressure medium in order to preserve the single crystal nature of the sample even after short laser heating periods from a few minutes to more than one hour. X-ray single crystal diffraction and Synchrotron Mössbauer Source experiments were performed at the European Synchrotron Radiation Facility, Grenoble, France and the Advanced Photon Source, Argonne, USA.

Our results show that upon heating $FeCO_3$ to temperatures along the geotherm at pressures up to about 50 GPa, it partially dissociates to form different iron oxides (Fig. 3.3-21). In particular, we found that below and above ~ 30 GPa, dissociation leads to the formation of α-Fe_2O_3 and hp-Fe_3O_4. As reported by previous authors, Fe_2O_3 and hp-Fe_3O_4 form as the result of partial redox dissociation of liquid $FeCO_3$, leading to dissolved Fe^{3+} and CO_2 in the carbonate melt. At pressures above ~ 75 GPa, we discovered and solved the structures of two new compounds – tetrairon (III) orthocarbonate, $Fe_4^{3+}C_3O_{12}$, and diiron (II) diiron (III) tetracarbonate, $Fe_2^{2+}Fe_2^{3+}C_4O_{13}$. Both phases contain CO_4 tetrahedra, and the former in particular is characterized by a previously unknown structure, thus indicating that high-pressure carbonates might not be similar to other compounds (including silicates). Based on the data we infer that the orthocarbonate, $Fe_4C_3O_{12}$, forms directly from heating $FeCO_3$ at T > 1400 K following the reaction $4FeCO_3 \rightarrow Fe_4C_3O_{12} + C$. The tetracarbonate, $Fe_4C_4O_{13}$,

appears upon prolonged heating of $Fe_4C_3O_{12}$ above ~75 GPa, but at temperatures significantly higher than those needed for the synthesis of the orthocarbonate (Fig. 3.3-21) following the possible reaction $8Fe_4C_3O_{12} \rightarrow 6Fe_4C_4O_{13} + 4Fe_2O_3 + 3O_2$. This means that iron is reduced by oxygen, which has already been observed in studies of iron(III) oxide at pressures above ~70 GPa. Thus, we conclude that the tetracarbonate is the product of chemical evolution of the orthocarbonate. Moreover, $Fe_4C_4O_{13}$ was found to survive along the entire geotherm to depths corresponding to at least 2500 km, demonstrating that self-oxidation-reduction reactions do not lead to the destruction of carbonates in the Earth's lower mantle.

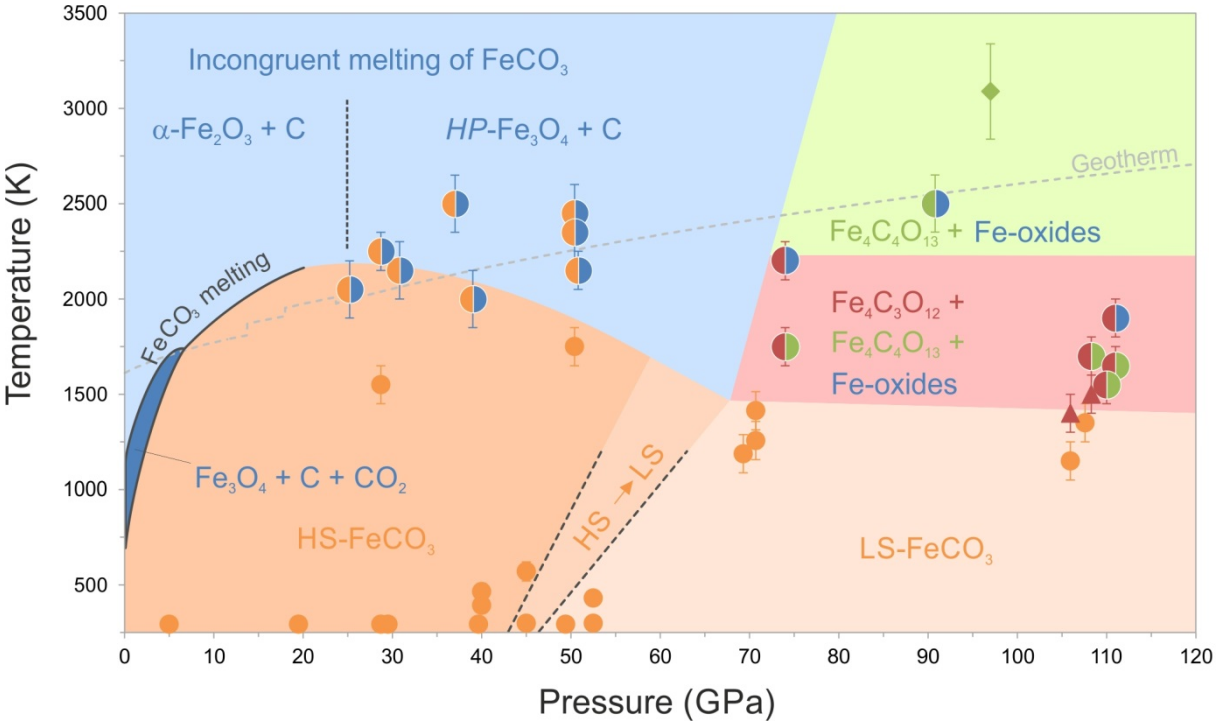

Fig. 3.3-21: Transformational phase diagram of $FeCO_3$ at high pressure and temperature. Symbols represent experimentally observed phases as follows: siderite, magnesite-structured $FeCO_3$ (orange circles), oxide(s) and recrystallized siderite (orange-blue circles), orthocarbonate $Fe_4C_3O_{12}$ (red triangles), tetracarbonate $Fe_4C_4O_{13}$ + $Fe_4C_3O_{12}$ + oxide(s) (red-green circles), $Fe_4C_4O_{13}$ + oxides (green-blue circles), $FeCO_3$ decomposition to $Fe_3O_4 + C + CO_2$ (dark blue area), high- and low-spin $FeCO_3$ (dark and light orange area), incongruent melting of $FeCO_3$ (light blue area), and formation of HP-carbonates $Fe_4C_3O_{12}$ and $Fe_4C_4O_{13}$ (red and green area). The vertical dashed black line separates the regions in which the formation of α-Fe_2O_3 and hp-Fe_3O_4 was observed upon incongruent melting of $FeCO_3$.

o. *Stability, composition and crystal structure of DHMS Phase E in the transition zone (J.R. Smyth and L. Zhang/Boulder; T. Kawazoe)*

Phase E is a stable dense hydrous magnesium silicate (DHMS) phase at near-geotherm temperatures through much of the upper part of the Earth's transition zone at depths of 400 to

about 550 km. Its potential role in the transition zone and importance as a hydrous phase motivated a detailed study of its crystal structure and crystal chemistry.

We synthesized Phase E at 18 and 19 GPa and 1400 °C with heating duration time up to 27 h. We measured the chemical composition by electron microprobe, collected Raman spectra and determined the crystal structure by single-crystal X-ray diffraction for Phase E, showing that it can coexist with ringwoodite, wadsleyite, pyroxene, and majorite in hydrous pyrolite compositions at temperatures to at least 1400 °C.

X-ray diffraction analyses show that the space group of Phase E is R-3m, with a = 2.9650 (13) Å; c = 13.870 (4) Å; V = 105.60 (4) Å^3; ρ = 2.92 g/cm^3. The composition is approximately $(Mg_{2.00}Fe_{0.22})Si_{1.18}H_{2.8}O_6$. As previously observed, the structure is significantly disordered. The Mg1 site in octahedral coordination is about 72 % occupied, whereas Mg2 which is also octahedral but near the Si position is only about 2 % occupied. Si is in a tetrahedral site with unusually long Si-O distances (average 1.78 Å).

Raman spectra of Phase E samples at ambient conditions are characterized by several broad bands between 80 cm^{-1} and 1100 cm^{-1}, of which the most intense occur at about 240 cm^{-1}, 370 cm^{-1}, 680 cm^{-1}, and 900 cm^{-1} (Fig. 3.3-22). In the O-H stretching region (from 2500 to 3700 cm^{-1}), we observe two broad bands which occur at about 3610 cm^{-1} and 3420 cm^{-1}.

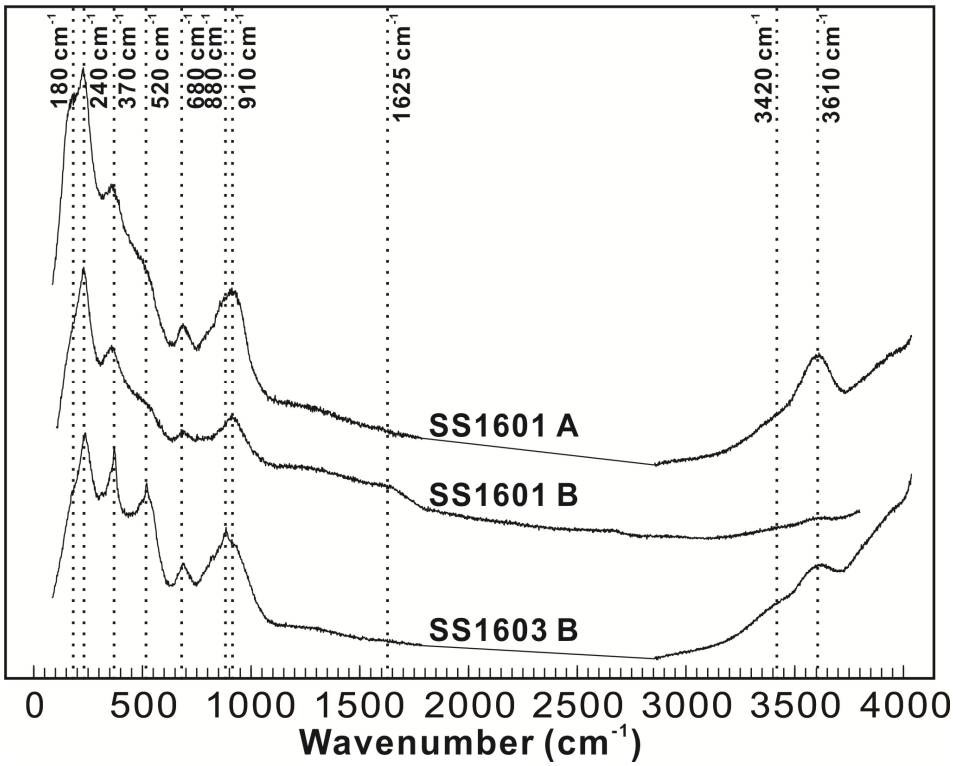

Fig. 3.3-22: Representative Raman spectra of Phase E samples collected at ambient conditions.

Electron microprobe analyses show that Phase E can incorporate a significant amount of Fe and Al (up to 6.8 and 1.47 wt. % for FeO and Al_2O_3, respectively), and the Phase E samples which coexist with ringwoodite have higher average Al_2O_3 content (1.4 wt. %) than those that coexist with wadsleyite (average Al_2O_3 content is 0.6 wt. %) (Fig. 3.3-23). This observation implies that Al^{3+} is able to stabilise the Phase E structure to higher pressure.

In this study, Phase E is somewhat denser than previously reported and occurs at relatively high temperature (near the geotherm). The long heating duration indicates that Phase E is a stable component of the mantle and not a metastable phase under very hydrous compositions. The relatively high temperatures and pressures of synthesis imply that Phase E is a potential component of the transition zone under extremely hydrous conditions.

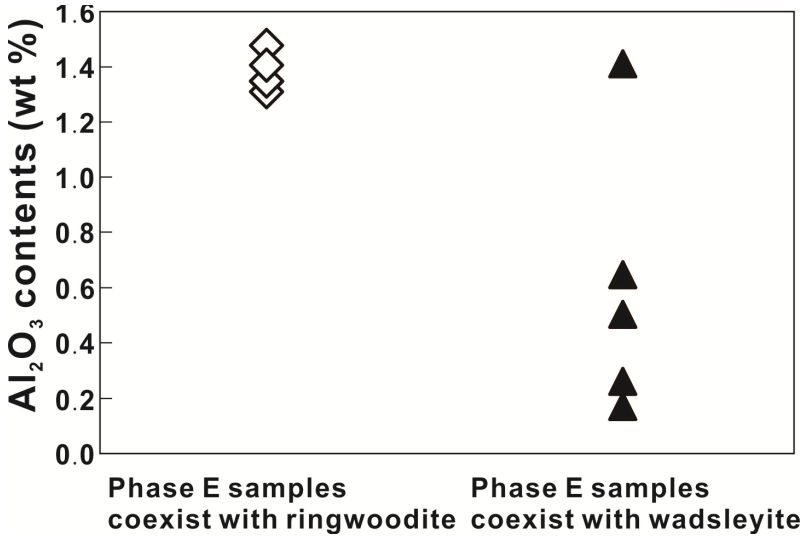

Fig. 3.3-23: Graphic representation of the Al_2O_3 contents of Phase E samples that coexist with ringwoodite and wadsleyite.

p. In situ *infrared spectra of OH in rutile at high temperature (H. Guo and H. Keppler)*

Among all nominally anhydrous minerals occurring in mantle xenoliths, rutile (TiO_2) often has the highest water contents, with maximum values reaching nearly 1 wt. %. Despite its low modal abundance, rutile may therefore be a significant carrier of water in eclogite during subduction into the mantle. Water incorporation into rutile appears to be strongly enhanced by the coupled substitution of H^+ and trivalent cations, such as Al^{3+} and Ti^{3+} for Ti^{4+}. Due to the coupling of Ti^{3+} and H^+, it has also been suggested that the OH content of rutile may actually be useful as a sensor of oxygen fugacity, *i.e.*, as an oxybarometer. Another interesting experimental observation is that particularly in rutile containing elevated Ti^{3+} concentrations, the diffusion of hydrogen appears to be unusually fast. In order to better understand these effects, we have measured high-temperature infrared spectra of OH in Al-doped and pure rutile to constrain H speciation at mantle conditions.

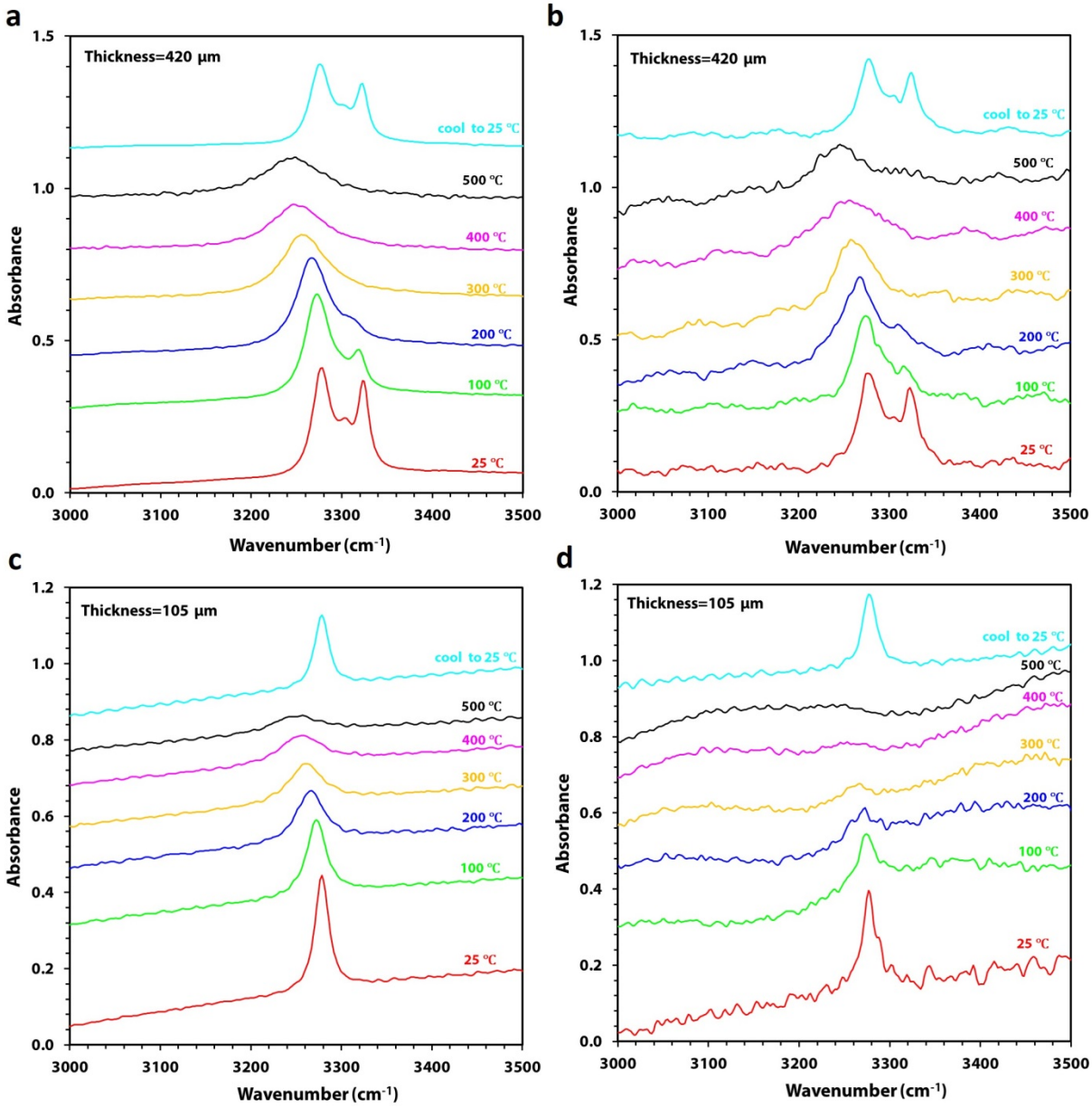

Fig. 3.3-24: FTIR spectra of hydrous rutile at various temperatures: (a) unpolarised spectra of Al-doped rutile; (b) polarised spectra (*E* // *a*) of Al-doped rutile; (c) unpolarised spectra of pure rutile; (d) polarised spectra (*E* // *a*) of pure rutile. The initial water contents in the Al-doped rutile and pure rutile are ~ 197 and 156 ppm.

The hydrous samples were prepared by annealing crystallographically oriented, synthetic Al-doped and pure rutile at 200 MPa and 800-900 °C in cold seal pressure vessels. The *in situ* unpolarised and polarised infrared spectra were measured from room temperature to 500 °C at 1 bar using a heating stage (Fig. 3.3-24). The spectra show only one band at ~ 3278 cm^{-1} in pure rutile, and additionally two satellite bands at ~ 3303 and ~ 3323 cm^{-1} in Al-doped rutile at room temperature. The Al-associated band at ~ 3323 cm^{-1} loses intensity as temperature rises and nearly disappears by 300 °C, suggesting that H becomes decoupled from Al at high

temperature and the defect observed in room-temperature spectra only forms during cooling. All OH bands shift to lower wavenumbers at elevated temperatures with different rates. The downshift of these bands is very unusual when compared to other oxides and silicates. The room-temperature band position implies very significant hydrogen bonding. Since with increasing temperature, O-O distances in rutile increase due to thermal expansion, one would expect a weakening of the hydrogen bonds, which should result in a shift of the bands to higher frequency, the opposite of what was observed. Very likely, the downshift in frequency implies an intrinsic weakening of O-H bond strength with temperature. The observed line broadening could at least partially be due to lifetime effects, implying rapid exchange of protons between adjacent oxygen atoms. Overall, these spectral changes at high temperature show that water speciation models in rutile from infrared spectra at ambient conditions may not be fully applicable for subduction zone and upper mantle conditions.

3.4 Physical Properties of Minerals

By developing a systematic understanding of the physical properties of minerals and rocks at pressure and temperature conditions typical of the Earth's deep interior, we improve our ability to link geophysical observables, such as seismic wave velocities or electrical conductivity, to the structure and composition of the Earth. This quantitative understanding also is key to improve large-scale models that aim at providing constrains on the dynamic evolution of our planet.

The first contribution of this section aims at understanding the origin of high electrical conductivity layers at 70-120 km depth beneath young oceanic plates as depicted by magnetotelluric studies. The measured conductivity is higher than expected for dry olivine and cannot be explained through proton migration in hydrous olivine. In this contribution, the diffusion rate of Mg (D_{Mg}), which is a measure for the expected electrical conductivity, has been determined as a function of pressure, temperature, and water content and the results have been used to show that the high conductivity observed beneath young oceanic plates can be explained by water-enhanced ionic conduction due to the migration of Mg vacancies.

In the second contribution, two crystals of wadsleyite with different crystallographic orientations were loaded together in a diamond anvil cell in order to determine the effect of possible non-uniform stress on their compression behaviour. The two crystals have identical compressibility up to the maximum pressure reached in the study. This suggests that they are experiencing a uniform stress field inside the diamond anvil cell.

The next five contributions focus on determining the elastic wave velocities of different mantle minerals in order to constrain seismological observations of the Earth's mantle. The first three of these contributions show how the simultaneous loading of several double polished crystals with different crystallographic orientations cut using a focused ion beam (FIB) is a valuable tool for better constraining the effect of cation substitution on the elastic properties of end-member minerals. The advantage of this method resides in the ability to measure both phonon velocities with Brillouin spectroscopy and X-ray diffraction of all crystals at exactly the same conditions of pressure and temperature. In this way, the elastic tensor of low symmetry materials can be determined with high precision as in the case of wadsleyite and bridgmanite (third and fourth contributions) for which the effect of Fe incorporation and of Fe/Al coupled substitution, respectively, has been accurately characterized. In the fifth contribution, the simultaneous measurement of four crystals has been used to determine changes associated with small variations in water content in Fe-bearing ringwoodites.

In case of non-transparent samples, sound wave velocities can be measured using nuclear inelastic scattering. This technique has been used in the sixth contribution to obtain information about the influence of the skiagite component on the wave velocities of garnets. These minerals are present in diamond inclusions and have large amounts of Fe^{3+}. In the

seventh contribution the same technique has been used to show that Fe substitution in magnesite significantly decreases the bulk sound velocity of this carbonate mineral, although such effect is less evident at high pressure where Fe adopts the low spin state.

Since elasticity measurements at lower-mantle conditions remain challenging, coupling theoretical calculation with experiments can give more robust results and can help to reveal experimental errors. This is well demonstrated in the eights contribution of this section which makes use of density functional theory calculations to understand previously reported results from nuclear inelastic scattering on iron-rich post-perovskite. The calculations suggest that the velocity results reported in the literature may be significantly too low as a result of experimental artifacts.

Glasses often serve as proxies for describing the behavior of melts which can be present in the Earth's mantle. The density of SiO_2 glass has been measured up to 90 GPa by means of X-ray absorption using a diamond anvil cell. The results presented in the ninth contribution of this section show that the measured high-pressure densities of SiO_2 and $MgSiO_3$ are identical at room temperature and differ by less than 1 % along a 4000 K isotherm. Therefore, the silica content of the melt plays only a secondary role in determining its buoyancy at lowermost mantle conditions.

The last contribution in this section discusses results of hardness measurements conducted on different garnets. Samples of gem-quality polycrystalline garnet have been synthesized at 18 GPa and 2100 K along the majorite-pyrope solid solution and characterized by means of powder X-ray diffraction. The Vickers hardness has been measured by indentation tests and appears to increase with the pyrope content.

a. *Water-enhanced ionic conduction accounts for the high electrical conductivity at the top of oceanic asthenosphere (H. Fei, S. Koizumi/Tokyo; N. Sakamoto, M. Hashiguchi and H. Yurimoto/Hokkaido; T. Katsura)*

The electrical conductivity of olivine occurs according to three major mechanisms: small polaron conduction (σ_h) through the hopping of electron holes ($h^{\bullet}$) between ferrous and ferric iron, proton conduction (σ_p) due to the migration of free protons, and ionic conduction (σ_i) due to migration of Mg vacancies. Magnetotelluric studies have depicted high-conductivity layers (HCL) at 70-120 km depth beneath young oceanic plates; such a conductivity anomaly is higher than σ_i and σ_h in dry olivine by about one order of magnitude and was once attributed to water-enhanced σ_p in hydrous olivine. However, recent experimental results suggested that the magnitude of σ_p is insufficient to account for that anomaly. In addition, although carbonate melt might enhance the bulk conductivity of peridotite, using carbonate melt to explain the HCL requires significantly larger CO_2 concentrations than those expected in mid-ocean ridge basalts. These arguments lead us to investigate the role of ionic conduction in oceanic asthenosphere.

Incorporation of water into an olivine crystal structure increases the Mg defect concentration and thus enhances Mg diffusion. Based on the proportionality of σ_i and Mg diffusivity in olivine indicated by the Nernst-Einstein relation, water is expected to enhance not only σ_p but also σ_i. Due to the high-temperature conditions in the asthenosphere, σ_i in olivine may play an essential role in mantle conduction because it dominates at higher temperatures with respect to σ_h and σ_p. However, it is extremely difficult to directly determine σ_i in water-rich olivine at asthenospheric temperatures due to water loss from the sample and to the high conductivity path produced by the resulting fluid phase during the σ_i measurements. In order to overcome this problem, we measured the diffusion rate of Mg (D_{Mg}) as a function of pressure, temperature, and water content in this study instead of directly measuring the conductivity. Our results indicate that D_{Mg} systematically increases with temperature and water content, and decreases with pressure. The activation enthalpy, activation volume, and water-content exponent are found to be 280 ± 30 kJ/mol, 4.3 ± 0.3 cm^3/mol, and 1.2 ± 0.2, respectively.

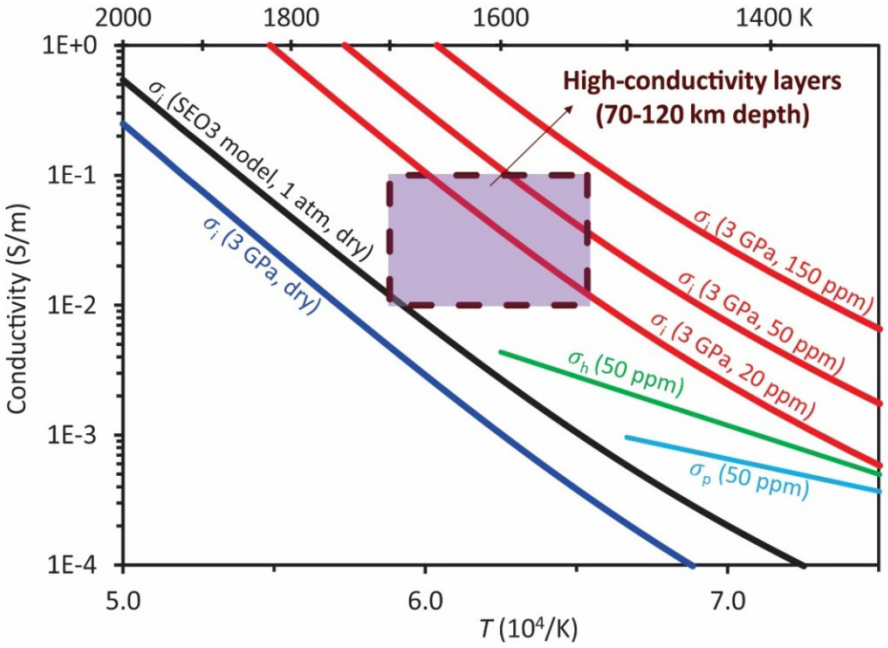

Fig. 3.4-1: The high conductivity layers beneath young oceanic plates at 70-120 km depth corresponding to 2-4 GPa and 1550-1700 K is well explained by the water-enhanced ionic conduction in hydrous olivine. The SEO3 model is from Constable (Geophys. J. Int. 166, 435-437, 2006). The σ_h and σ_p data are taken from Yoshino *et al.* (EPSL 288, 291-300, 2009).

By assuming that Mg diffusion controlles σ_i in olivine, we estimated the σ_i under various pressure, temperature, and water-content conditions based on the standard olivine conductivity model (SEO3) (Fig. 3.4-1). The results show that σ_i in dry olivine at 1 atm is lower than that observed in the high-conductivity layers beneath young oceanic plates. With pressure correction to 3 GPa corresponding to the top of the oceanic asthenosphere, the σ_i becomes even lower. However, considering a water content of ~ 20-150 wt. ppm, which is the

typical water-content condition in the asthenosphere, σ_i becomes much larger than σ_p and σ_h, and essentially identical to the observed mantle conductivity at the top of oceanic asthenosphere. Therefore, the high conductivity observed beneath young oceanic plates is well explained by the water-enhanced ionic conduction.

b. *Anisotropic compression of $(Mg_{0.89}Fe_{0.1})_2SiO_4$ wadsleyite reveals the stress conditions inside a diamond anvil cell (J. Buchen, H. Marquardt, T. Kawazoe and T. Boffa Ballaran)*

In the pyrolite model for Earth's mantle, the mineral wadsleyite contributes with about 60 vol. % to a mantle rock at depths between 410 km and 520 km depth. This depth range corresponds to the upper part of the transition zone, a layer in the Earth's mantle delimited by major seismic discontinuities and apparently responsible for the selective fate of subducted lithospheric slabs. Both the extent of phase stability in pressure-temperature-composition space and the speed of seismic waves through a wadsleyite-bearing rock depend on the compression behavior of this mineral. For an elastically anisotropic mineral such as wadsleyite, a description of the compression behavior should ideally include the changes in shape and volume of the unit cell with increasing pressure. We determined volume and axial compression curves for $(Mg_{0.89}Fe_{0.11})_2SiO_4$ wadsleyite at room temperature for pressures relevant to the expected stability field using single-crystal X-ray diffraction. The equations of state (EOS) resulting from isotropic and anisotropic finite strain analyses show mutual consistency and contribute to clarify the impact of chemical composition on the compressional behavior.

Gem quality wadsleyite crystals were synthesized from San Carlos olivine powder at 16 GPa and 1600 °C in a multianvil apparatus. Electron microprobe analysis demonstrated chemical homogeneity across individual crystals and among different crystals from the same synthesis run with Fe/(Mg+Fe) = 0.112(2). Crystals with low mosaicity were selected and oriented by means of X-ray diffraction. Sections with a final thickness of 10 μm were cut from these crystals and characterized with polarized Fourier-transform infrared spectroscopy. Structurally bonded hydroxyl groups appear to be homogeneously distributed throughout the crystals with a concentration of 0.25(3) wt. % H_2O. Semicircular disks were cut out of thin sections with different orientations using a focused ion beam and subsequently loaded together into the same diamond anvil cell (DAC) to exclude bias arising from a combined effect of deviatoric stresses and anisotropic compression. We added a ruby sphere for pressure calibration and loaded neon as a pressure-transmitting medium. The unit-cell lattice parameters were determined by means of single-crystal X-diffraction at 10 different pressures up to 20 GPa. The resulting compression behavior is shown in Fig. 3.4-2a. By compressing two crystals along different crystallographic directions inside the same DAC, we aimed at resolving any potential difference in the anisotropic response of the crystals to the applied stress field.

The variation with pressure of the unit-cell parameters are identical within errors for the two crystals suggesting homogeneous stress conditions throughout the pressure chamber of the

DAC and no detectable influence of crystal orientation on the derived EOS parameters. A finite strain analysis of the axial compression curves using a Reuss bound formalism leads to a value of the bulk modulus identical to that obtained from the unit-cell volume data (Fig. 3.4-2a). This consistency supports the assumption of a uniform stress field across individual crystals as captured by the Reuss bound. Local deviatoric stresses inside the DAC chamber likely started to develop above 10 GPa as indicated by broadening of individual X-ray rocking curves observed above this pressure (Fig. 3.4-2b), however the response of the crystals to such stresses appears to be still in the elastic regime, and is not influencing the compressional behavior at least up to the maximum pressure reached in this study.

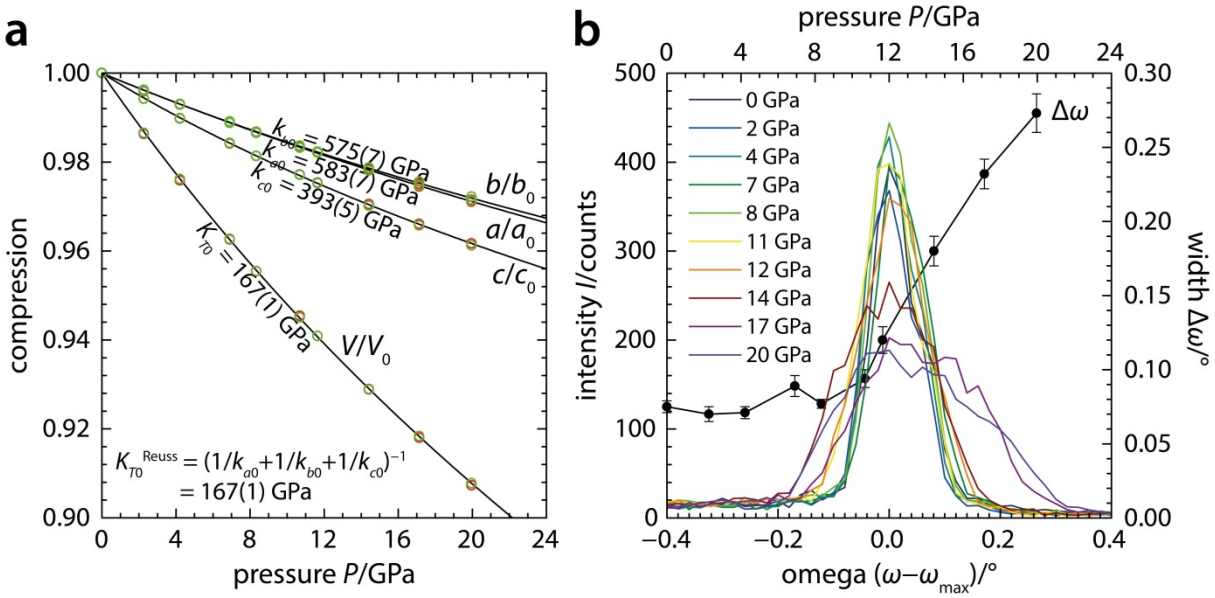

Fig. 3.4-2: (a) Unit-cell volume and axial compression curves for two $(Mg_{0.89}Fe_{0.11})_2SiO_4$ wadsleyite crystals having different orientations inside the same DAC (red and green circles). Note that the K_{T0} derived from the unit-cell volume compression is identical to the bulk modulus computed from the axial compression using the Reuss bound; (b) rocking curves for the 240 reflection at different pressures; broadening occurs at pressures above 10 GPa.

c. *Internally consistent elasticity measurements of single-crystals of $(Mg_{0.9}Fe_{0.1})_2SiO_4$ wadsleyite at high pressures and high temperatures: Hydrous transition zone or non-pyrolitic mantle? (J. Buchen, H. Marquardt, T. Kawazoe, A. Kurnosov, S. Speziale/Potsdam and T. Boffa Ballaran)*

Located at depths between 410 km and 660 km, the transition zone controls material exchange between Earth's lower and upper mantle. In the $(Mg,Fe)_2SiO_4$ system, a cascade of phase transitions from olivine to wadsleyite at 410 km depth and to ringwoodite around 520 km depth entails changes in density and physical properties. Together with the dissociation of $(Mg,Fe)_2SiO_4$ to ferropericlase and bridgmanite at 660 km depth, these phase transitions give rise to major discontinuities in seismic wave velocities that can serve as anchor points to

constrain mineralogical and thermodynamic models of the Earth's mantle. These models are based on thermo-elastic properties of candidate minerals. Combining Brillouin spectroscopy with single-crystal X-ray diffraction, we are determining an internally consistent description of the thermo-elastic behavior for $(Mg_{0.89}Fe_{0.11})_2SiO_4$ wadsleyite based on the measurement of single-crystal elastic stiffnesses and densities at high pressures and high temperatures.

San Carlos olivine powder was transformed to wadsleyite at 16 GPa and 1600 °C in a multianvil apparatus. The run product was analyzed with an electron microprobe and shows Fe/(Mg+Fe) = 0.112(2), as expected for a pyrolitic mantle composition. Recovered gem quality wadsleyite crystals were oriented using X-ray diffraction and cut to thin sections. Polarized Fourier-transform infrared absorption spectroscopy revealed small amounts of structurally bonded hydroxyl groups in the wadsleyite crystals (0.25(3) wt. % H_2O). We used a focused ion beam to cut semicircular disks out of the oriented thin sections and mounted two sections of complementary orientations into the same diamond anvil cell (DAC). This two-crystal approach allows us to determine all nine independent single-crystal elastic stiffness coefficients at the same conditions of pressure and temperature. Neon is used as pressure-transmitting medium whilst a ruby sphere and a chip of Sm:YAG have been inserted as independent pressure and temperature sensors. Brillouin spectra and X-ray diffraction data have been collected on both crystal sections up to pressures relevant for the transition zone. From an integration of single-crystal elasticity and volume compression, we derived an internally consistent set of thermo-elastic parameters based on finite strain theory and absolute pressure.

The evolution of the elastic moduli and density of $(Mg_{0.89}Fe_{0.11})_2SiO_4$ wadsleyite with pressure is shown in Fig. 3.4-3a. In comparison with the Mg_2SiO_4 end-member, the bulk modulus K_S for the composition $(Mg_{0.89}Fe_{0.11})_2SiO_4$ appears to be essentially unchanged while the shear modulus falls significantly below the one of the magnesium end-member, at low pressures, but show a larger first pressure derivative than Mg_2SiO_4. In addition, we have so far performed high-pressure and high-temperatures experiments at 11 GPa and at 500 K, at 11.9 GPa and 640 K and at 19 GPa and 460 K, in order to obtain the temperature derivatives of the elastic moduli and of the elastic tensor. As an example for these experiments, the angular dispersion of single-crystal sound wave velocities collected at 11.9 GPa and 640 K is shown in Fig. 3.4-3b. P-wave and S-wave velocities determined for the two crystals as a function of rotation angle are shown in the inset. From the elastic moduli and the density directly constrained by our measurements, aggregate sound wave velocities can be calculated at pressures and temperatures relevant for the Earth's transition zone.

Future work will involve experiments at combined high pressures and high temperatures as well as the formulation of an anisotropic thermo-elastic model for wadsleyite. To better constrain the impact of hydration on the thermo-elastic properties of wadsleyite, we are currently conducting a comparative study following the principles outlined above but with four crystal sections inside the DAC, two of wadsleyite with 0.25 wt. % H_2O and two of wadsleyite with 0.75 wt. % H_2O.

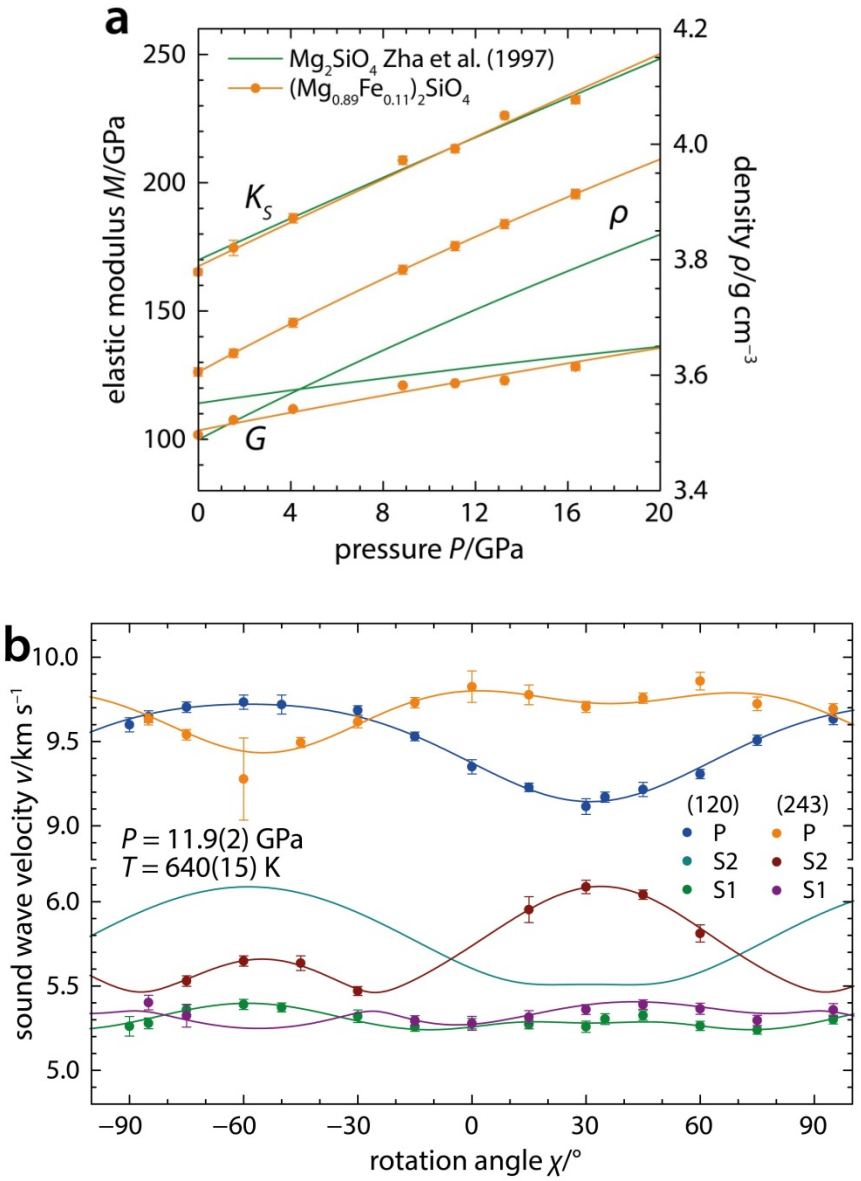

Fig. 3.4-3: (a) Elastic moduli and density of $(Mg_{0.89}Fe_{0.11})_2SiO_4$ wadsleyite as a function of pressure at room temperature; the elasticity model from Zha *et al.* (1997) *Earth Planet. Sci. Lett.* 147: E9-E15 for iron-free wadsleyite is shown for comparison; (b) experimental and fitted sound wave velocity dispersion curves for two wadsleyite crystals at 11.9 GPa and 640 K; the inset shows a view into the DAC loaded with the two crystals with indicated orientations, Sm:YAG (Y), and ruby (R).

d. *High-pressure single-crystal elasticity measurements of Al-Fe-bridgmanite up to lower mantle pressures (A. Kurnosov, H. Marquardt, D.J. Frost, T. Boffa Ballaran and L. Ziberna)*

The chemical composition of the Earth's lower mantle can be constrained by combining seismological observations with mineral physics elasticity measurements. However, the lack of laboratory data for Earth's most abundant mineral (Mg,Fe,Al)(Al,Fe,Si)O_3 bridgmanite has hampered any conclusive result. Here, we report single-crystal elasticity data on Al-Fe-

bearing bridgmanite $(Mg_{0.9}Fe_{0.1}Si_{0.9}Al_{0.1})O_3$ using single-crystal high-pressure Brillouin spectroscopy and X-ray diffraction in a novel self-consistent approach. Our measurements show that the elastic behavior of Fe-Al-bearing bridgmanite is markedly different from the behavior of the $MgSiO_3$ endmember reported previously.

Two crystals of $(Mg_{0.9}Fe_{0.1}Si_{0.9}Al_{0.1})O_3$ bridgmanite with different crystallographic orientations were cut using a focused ion beam and were loaded in the pressure chamber of a single diamond anvil cell using helium as pressure-transmitting medium (Fig. 3.4-4a). Elasticity and density measurements were performed at high pressures and room temperature on both samples using a combined Brillouin scattering and X-ray single crystal diffraction system at BGI. A Brillouin spectrum collected at 31.8 GPa is shown in Fig. 3.4-4b as example. All acoustic velocities and in particularly V_p which is close to the diamond signal are still perfectly visible.

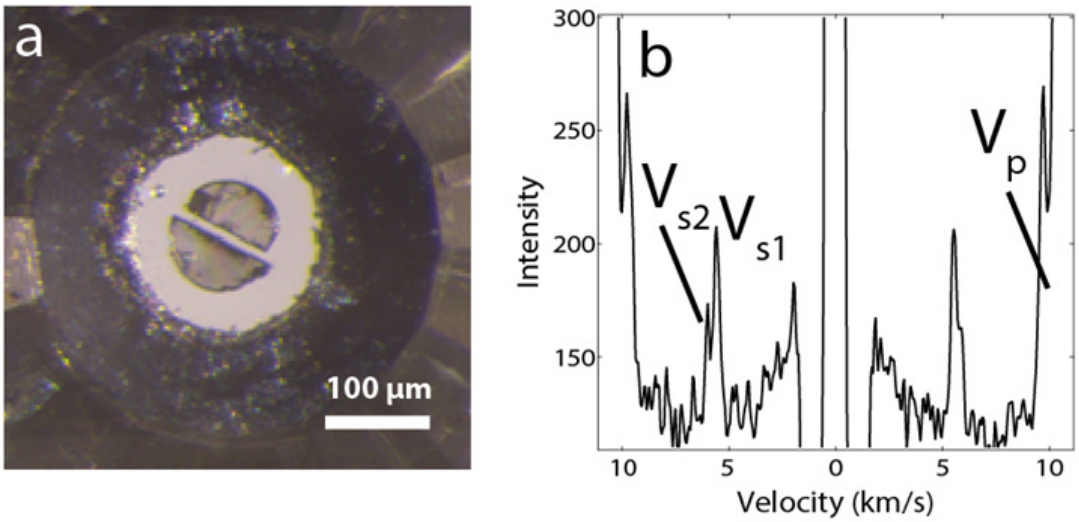

Fig. 3.4-4: (a) Two crystals with different crystallographic orientations cut with a focused ion beam and loaded together in the pressure chamber of a diamond anvil cell; (b) Brillouin spectrum collected at 31.8 GPa. Brillouin measurements were performed on both samples as a function of rotation angle.

A global fit of all the experimental data collected at different pressures was performed combining the usually employed Christoffel equation that relates elastic tensor and density to direction-dependent acoustic wave velocities with a finite strain formalism to derive values and uncertainties of the bulk and shear moduli, K_0 and G_0, of their first pressure derivatives, K_0' and G_0' as well as of the elastic stiffness coefficients, C_{ij} and absolute pressure. Input data for this fit were the experimentally measured acoustic velocities (about 100-150 individual velocities for each pressure point), the crystallographic orientations of the two sample platelets determined by *in situ* X-ray measurement, and the unit-cell volume (or density) for every pressure point.

A comparison between the aggregate sound velocities of Al-Fe-bearing bridgmanite and those obtained from polycrystalline samples of $MSiO_3$ end-member bridgmanite, of Fe-bearing and of Al-bearing bridgmanites is reported in Fig. 3.4-5. The Fe/Al substitution in the $MgSiO_3$ structure reduces the acoustic velocities at room pressure. The compressional wave velocities remain smaller at all pressures due to the similar K_0' values of all compositions, whereas the larger pressure dependence of the shear wave velocities obtained for our sample leads to a shear velocity crossover with $MgSiO_3$ bridgmanite at pressures above 35 GPa.

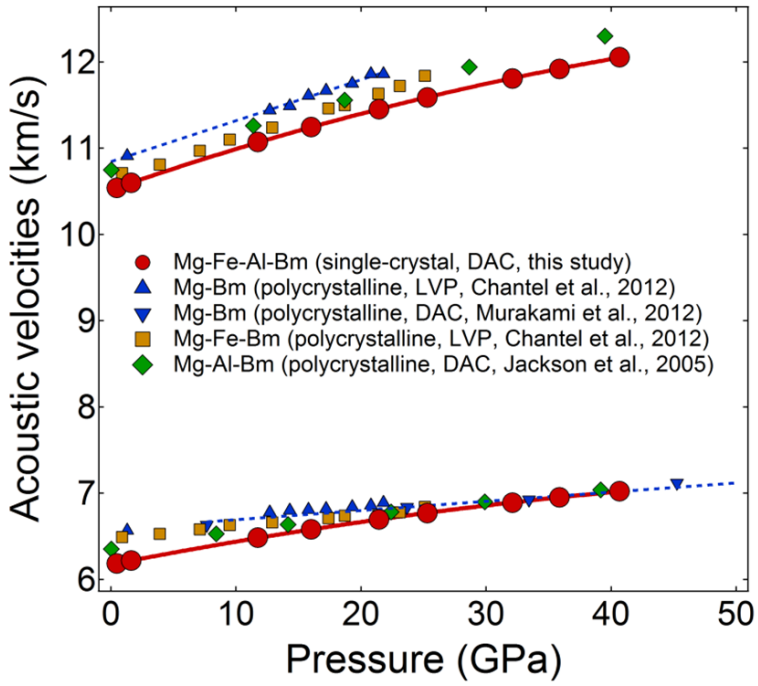

Fig. 3.4-5: Pressure dependence of the aggregate sound wave velocities of Al-Fe-bearing bridgmanite (red circles). The uncertainties in acoustic velocities are smaller than the symbol size. Previously published data measured on polycrystalline bridgmanites with different chemical compositions (Chantel *et al.*, Geophys. Res. Lett., 39, L19307 (2012); Jackson *et al.*, Geophys. Res. Lett., 32, L21305 (2005); Murakami *et al.*, Nature, 485, 90-94 (2012)) are shown for comparison. The blue dotted lines indicates the pressure trend of the $MgSiO_3$ end-member bridgmanite

e. *Direct determination of the chemical effects on the high-pressure single-crystal elasticity of ringwoodite (K. Schulze, H. Marquardt, A. Kurnosov, T. Kawazoe and T. Boffa Ballaran, in collaboration with M. Koch-Müller/Potsdam)*

The elastic properties of ringwoodite depend on its iron content and its hydration state. So far a quantitative description of this dependencies has been difficult due to uncertainties arising from different experimental conditions and slight chemical variations. To minimise these uncertainties we developed a method for measuring single-crystal Brillouin spectroscopy and X-ray diffraction simultaneously on four samples of single-crystals of ringwoodite loaded together in the pressure chamber of one diamond anvil cell.

The four-sample DAC-loading, described in details in the annual report 2015, contains three iron bearing ringwoodites with different OH-contents and one Mg_2SiO_4 ringwoodite end-member. Three ruby spheres were added to the loading as pressure standards. Upon compression to a pressure of 18.4 GPa, 18 X-ray diffraction and seven Brillouin spectroscopy measurements were performed. The variations with pressure of the unit-cell volumes of all four samples are shown in Fig. 3-4.6. As expected, the unit-cell volume of the Mg_2SiO_4 ringwoodite end-member is smaller than that of the iron bearing samples, moreover, at room pressure the unit-cell volumes of Fe-bearing ringwoodites increase with increasing hydration. With increasing pressure, however the difference between the three Fe-bearing samples decreases due to the larger compressibility of the ringwwodite crystals with larger H_2O content. All four unit-cell volume data sets were fitted with a third order Birch-Murnaghan equation of state. Comparison of the Fe-bearing ringwoodites shows a decrease in the isothermal bulk modulus *K0* and its pressure derivative *K′* with increasing hydration state. The Mg_2SiO_4 ringwoodite end-member has the larger bulk modulus, but the smallest *K*'.

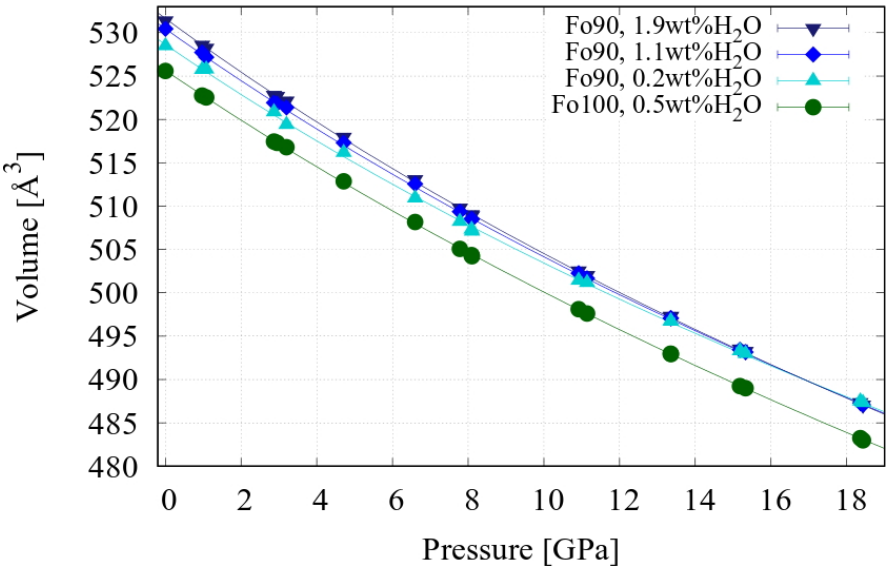

Fig. 3.4-6: Variation of the unit-cell volumes of three Fe-bearing and one Mg_2SiO_4 end-member single-crystals of ringwoodite up to 18.4 GPa. Third-order Birch-Murnaghan equations of state were fitted to each dataset and are reported as solid curves.

Single-crystal Brillouin spectroscopy measurements for each crystal were conducted at seven different pressures. In Figure 3.4-7, the transverse velocities measured at 3.2 GPa are exemplarily plotted for all four compositions, the range between the [110] and [1-10] orientation is equivalent to a 90° rotation. The velocities of the Fe-bearing samples increase with decreasing hydration state. The hydration state does not seem to significantly influence the anisotropy in V_S. The iron content of ringwoodite has a much greater effect on the measured transverse velocities and a slight impact on the elastic anisotropy. The Mg_2SiO_4 ringwoodite end-member shows higher transverse velocity and larger anisotropy with respect to the Fe-bearing samples.

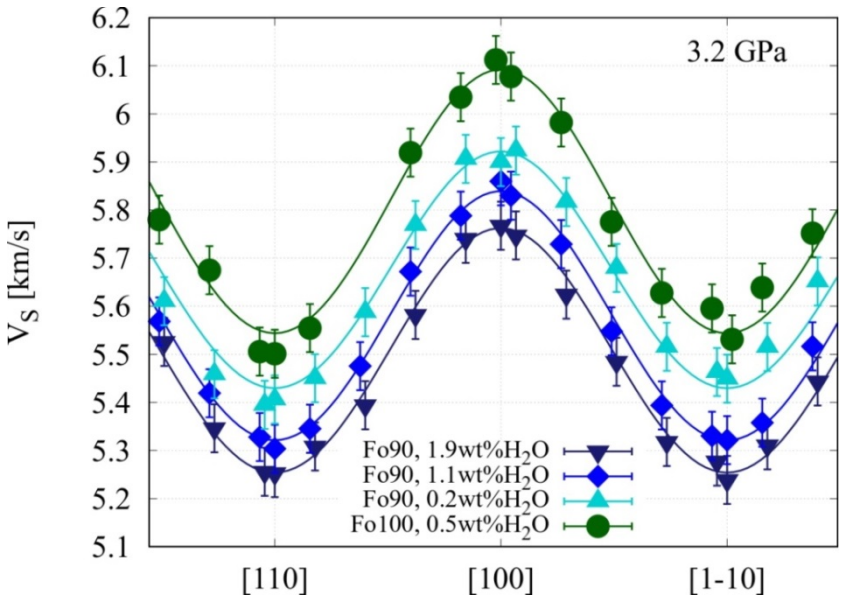

Fig. 3.4-7: Orientation dependent single-crystal Brillouin measurements at 3.2 GPa of the four single-crystals of ringwoodite with different chemical compositions. Solid curves represent the results from the fits to the Christoffel equation.

f. *Sound velocities of skiagite-iron-majorite solid solution at high pressure (D. Vasiukov/Bayreuth, I. Kupenko/Münster, L. Ismailova/Bayreuth, V. Cerantola, C.A. McCammon, A.I. Chumakov/Grenoble, L.S. Dubrovinsky and N.A. Dubrovinskaia/Bayreuth)*

Garnets are major rock forming minerals of the Earth's upper mantle and transition zone (MTZ). Their fraction in peridotite and eclogite rocks varies between 35 and 95 vol. %, respectively, at MTZ conditions, as pyroxenes progressively dissolve into the garnet structure with depth. Therefore the elastic properties of garnets are very important for interpreting seismic observation of this region. Such properties will depend on the garnet chemical composition which involves several chemical substitutions. In particular, a recent experimental study of majoritic garnet present as inclusions in diamonds has shown that the amount of Fe^{3+} increases considerably with depth (up to 25 % of the total iron content is ferric at 500 km depth).

To elucidate the effect of trivalent iron on the seismic wave velocities of majoritic garnet, we have carried out at the Nuclear Resonance Beamline ID18 of European Synchrotron Radiation Facility (Grenoble, France) a nuclear inelastic scattering (NIS) study at different pressures on a sample along the skiagite-iron-majorite solid solution, namely $(Fe_3(Fe_{1.766(2)}Si_{0.234(2)})(SiO_4)_3)$.

The obtained longitudinal, V_p, and shear, V_s, wave velocities are reported in Fig. 3.4-8 as a function of pressure. Linear fits through the data gives the following pressure dependencies of sound velocities at ambient temperature:

$$V_p = 7.43(9) + 0.039(4) \times P, \qquad V_s = 3.56(12) + 0.012(6) \times P$$

where V_p and V_s are in km/s and pressure in GPa.

The values of sound velocities obtained for the skiagite-iron majorite garnet are substantially lower than those reported for all other garnet end-members (grossular, pyrope, majorite, andradite and almandine), but have a similar dependence on pressure (Fig. 3.4-8).

Most of the Earth's upper mantle and transition zone models do not take into account the effect of Fe^{3+} which appears, however, to have a significant influence on the wave velocities of garnets with complex compositions as those reported in this study, especially for those having a large skiagite component.

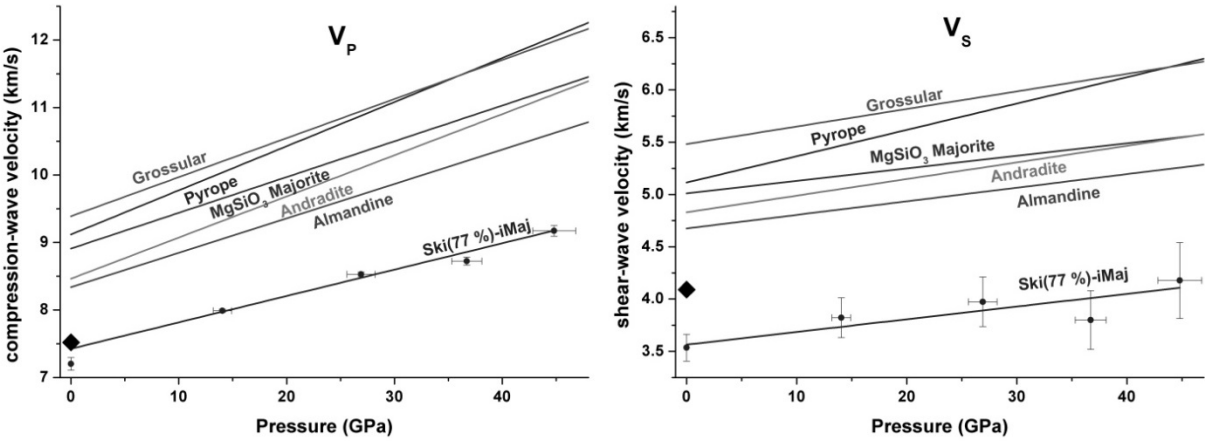

Fig. 3-4-8: Variation with pressure of the sound velocities of a garnet belonging to the skiagite-iron-majorite solid solution (this study). Values taken from the literature for silicate garnet end-members also are reported for comparison. The black diamonds are the estimated sound velocities of pure skiagite, taking into account the results from this study.

g. *Elastic wave velocities of Fe-bearing carbonates using nuclear inelastic scattering (S. Chariton, C.A. McCammon D. Vasiukov, V. Cerantola/Grenoble, I. Kupenko/Münster, G. Aprilis, A. Chumakov/Grenoble and L.S. Dubrovinsky)*

There is much evidence of carbon cycling through the Earth, with carbon being stored in accessory phases such as diamonds, carbides, methane and carbonates. The precise size of the net sink of carbon and carbonates at subduction zones is still unknown. In order to characterise which are the most abundant accessory phases incorporating carbon and how they influence the dynamical processes that operate inside the Earth, investigations on the vibrational, elastic and thermodynamic properties of these phases are crucial for interpreting the seismological observations.

Recently, nuclear inelastic scattering (NIS) has proved to be a useful tool to access information on lattice dynamics as well as to determine Debye sound velocities of Fe-bearing

materials. In the present work we present our results on the sound velocities of the carbonate Fe end-member (siderite) and different Fe-bearing solid solutions up to ~ 70 GPa by means of NIS in diamond anvil cells (DACs). The scope of our study is to detect *in situ* the effect of the spin transition of Fe^{2+}, the crystal orientation and the chemical composition on the elastic and vibrational properties of carbonates at high pressures.

Single crystals and/or powder of $^{57}FeCO_3$, $(Mg_{0.9}, {}^{57}Fe_{0.1})CO_3$ and $(Mg_{0.7}, {}^{57}Fe_{0.3})CO_3$ were synthesized using a multi anvil apparatus available at BGI. In addition, crystals were oriented along two crystallographic orientations and then they were loaded into specially designed DACs for NIS measurements. NIS experiments were performed at the Nuclear Resonance beamline, ID-18, at European Synchrotron Radiation Facility, Grenoble, France.

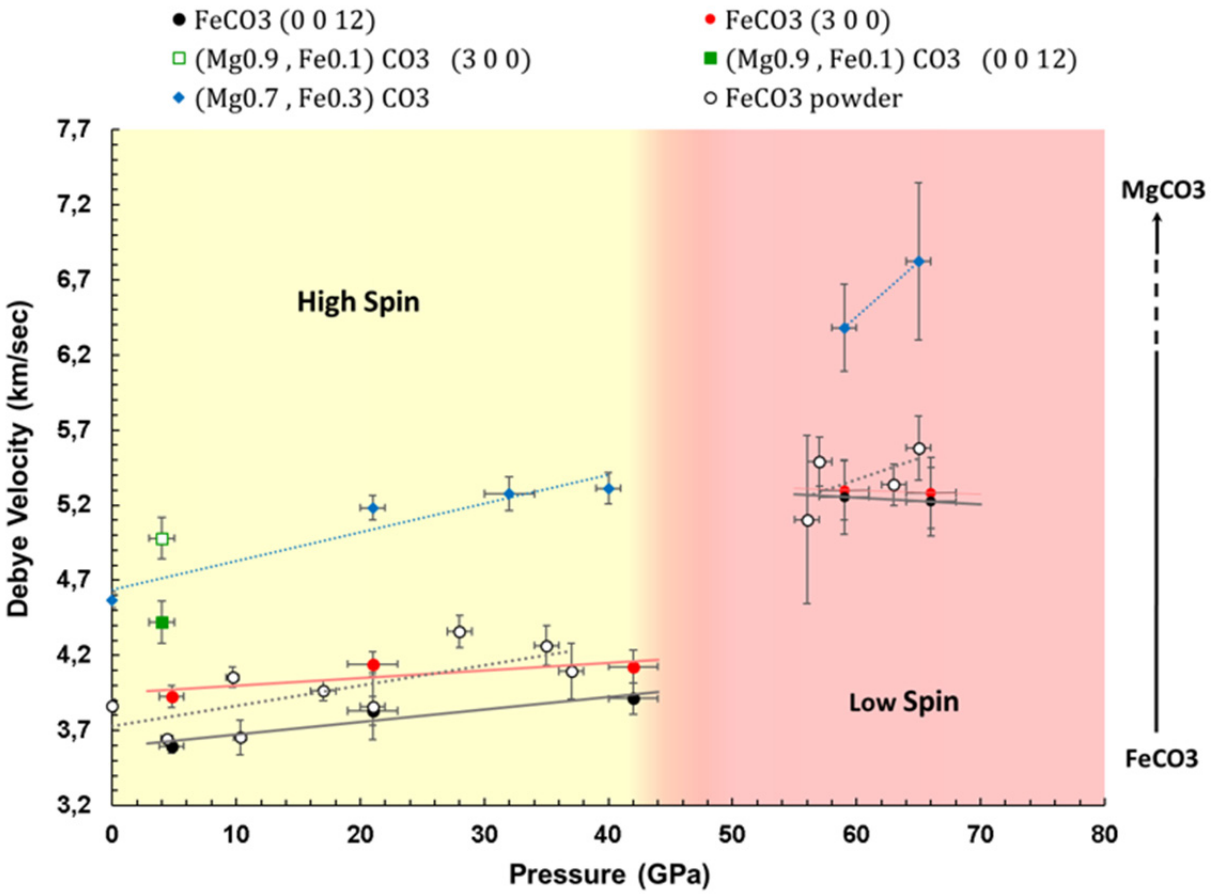

Fig. 3.4-9: Calculated Debye sound velocities of siderite ($FeCO_3$) and its solid solution with magnesite ($MgCO_3$) by NIS. The velocities for the latter are greater than those of $FeCO_3$. Different crystallographic orientations give distinct velocities, reflecting the highly anisotropic nature of the calcite-type structure ($R\bar{3}c$). Velocities increase when Fe^{2+} undergoes a spin transition above 50 GPa.

Concerning the effect of the spin transition, our results provide clear evidence of an increase in velocities by nearly 25 % above 50 GPa (Fig. 3.4-9). This observation has potential

implications for subducting slabs that penetrate the lower mantle at depths greater than 1200 km. Further, we note that different crystal orientations result in different velocities, which reflects the highly anisotropic nature of rhombohedral carbonates. In particular, velocities along (3 0 0) and (0 0 12) planes differ by 3-5 %, and values for the latter are always lower (Fig. 3.4-9). This indicates that waves propagate faster along the *a*-axis compared to the *c*-axis, which is nearly three times greater in length. Experiments on powder $^{57}FeCO_3$ (Fig. 3.4-9) give only the aggregate bulk sound velocity provided that there is no preferred orientation of the sample. Although there is a remarkable velocity contrast for different orientations below 40 GPa, the contrast abruptly diminishes once Fe^{2+} adopts the low-spin state (Fig. 3.4-9). Thus, the anisotropic behavior along the *a*- and *c*- axes is greatly reduced and therefore crystal orientation will play only a minor role at depths greater than 1200 km. We also performed experiments in the binary system $FeCO_3$-$MgCO_3$ and observed that velocities differ essentially depending on chemical composition. Ferromagnesian carbonates have greater velocities than siderite ($FeCO_3$) (Fig. 3.4-9); samples with the lowest Fe concentration have the largest velocities. Further experiments are required to accurately determine the likely seismic signatures of Fe-bearing carbonates, leading us one step closer to the seismic detectability of carbonates and the size of the net carbon sink in the Earth's interior.

h. *Sound velocities of post-perovskite from calculated density of states (C.A. McCammon and R. Caracas/Lyon)*

Regions of heterogeneity at the core-mantle boundary have long been a focus of interest. Most hypotheses to explain these seismic heterogeneities are based on comparison of seismic data with experimental and computational mineral physics studies of the relevant phases. Shear wave velocities are particularly important, and nuclear inelastic scattering (NIS) offers the attractive possibility to measure these velocities for iron-containing minerals in a laser-heated diamond anvil cell through direct measurement of the partial density of states (DOS). Complementary determination of the partial DOS using density functional theory (DFT) has shown the potential to identify experimental features that impact the velocity determination as demonstrated by our recent study on bridgmanite. In this work we focus on the origin of ultralow velocity zones (ULVZs) which have shear velocities that are up to 30 % lower than surrounding material. We combine DFT calculations of iron-bearing post-perovskite with experimental NIS post-perovskite data from the literature to assess potential explanations for ULVZs.

We performed first-principles calculations based on the local density approximation of DFT to determine the iron partial DOS for $Mg_{0.75}Fe_{0.25}SiO_3$ post-perovskite at 100, 120 and 160 GPa and 0 K. We calculated Debye sound velocities (which are closely related to the shear wave velocities) using the same approach as for experimental NIS data, namely from the limit of $DOS(E)/E^2$ as energy goes to zero. We obtained velocities for $Mg_{0.75}Fe_{0.25}SiO_3$ post-perovskite that are consistent with literature values for $MgSiO_3$ and $FeSiO_3$ post-perovskite that were also calculated using DFT. In contrast, the experimentally determined Debye sound velocity from NIS reported in the literature is 35 % lower than our calculated value, which led

previous authors to suggest that ULVZs originate from regions containing iron-rich post-perovskite. We note, however, that the lower velocities in the NIS post-perovskite data arise from a similar effect to NIS bridgmanite data, which may be an artefact (Fig. 3.4-10). The velocity is inversely proportional to the slope of the DOS at low energy, hence steeper slopes mean lower velocities. In both bridgmanite and post-perovskite DOS derived from NIS data, there are modes at low energies that significantly steepen its slope compared to the DFT DOS (indicated by blue arrows in Fig. 3.4-10). The velocities derived from the DFT DOS of both bridgmanite and post-perovskite are consistent with seismic velocities of the bulk lower mantle, suggesting that ULVZs are likely not caused by iron-rich post-perovskite. Instead we suggest that dense melts as proposed by other authors are a more plausible explanation.

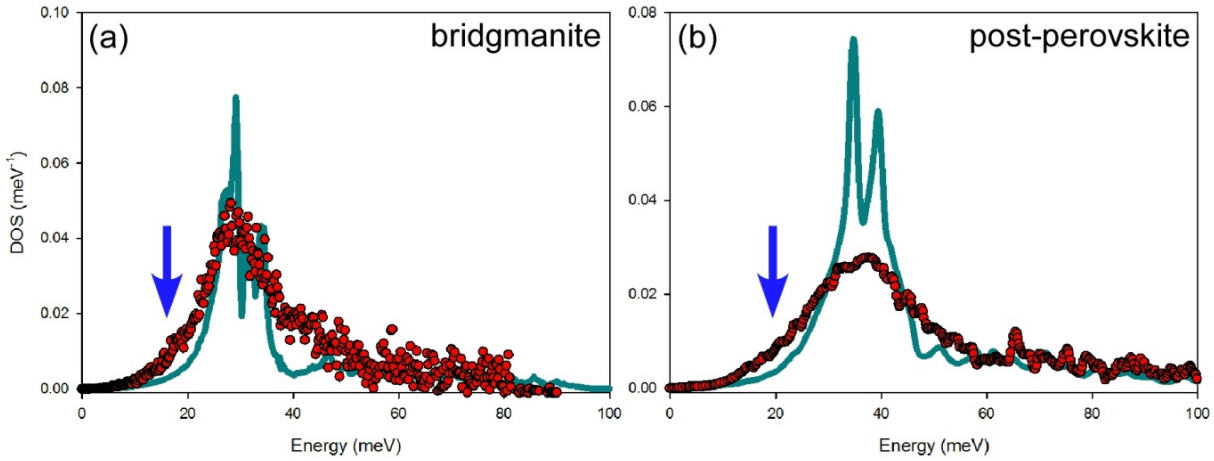

Fig. 3.4-10: Comparison of iron partial DOS determined by experiment and calculation. Experimental data (red) are from room temperature NIS spectra for (a) $Mg_{0.6}Fe_{0.4}Si_{0.63}Al_{0.37}O_3$ bridgmanite at 53 GPa [McCammon *et al.* 2016, *Prog. Earth Planet. Sci*., DOI 10.1186/s40645-016-0089-2] and (b) $Mg_{0.6}Fe_{0.4}SiO_3$ post-perovskite at 130 GPa [Mao *et al.* 2006, *Science* 312: 564-565]. Theoretical data (cyan) are from DFT calculations at 0 K of (a) antiferromagnetic $FeSiO_3$ perovskite at 60 GPa and (b) $Mg_{0.75}Fe_{0.25}SiO_3$ post-perovskite at 120 GPa. Blue arrows indicate additional modes in the experimental data but not present in the theoretical data that lead to 30-35 % lower velocities.

i. *Density of SiO_2 glass at lower mantle pressure (S. Petitgirard, W.J. Malfait/Zurich, B. Journaux/Grenoble, I.E. Collings/Bayreuth, L. Hennet/Orléans, T. Dane/Grenoble, M. Burghamer/Grenoble and D.C. Rubie)*

The concentration of SiO_2 exceeds 45 mole per cent in the Earth's mantle, and the properties of minerals and melts are greatly influenced by the behaviour, arrangement and coordination of silicon atoms in the structure of such compounds. Therefore, the SiO_2 reference system is seminal for constraining the density, compressibility, and atomic coordination changes of the more complex silicate melt compositions that can be found in the deep interior of the Earth and other rocky planets. However, the density of SiO_2 (glass or melt) has not been measured

beyond 55 GPa in spite of its importance in constraining the properties of melts with different SiO_2 content at greater depth.

Using the X-ray absorption method that we recently adapted to the small environment of the diamond anvil cell (DAC), we measured the density of pure SiO_2 glass up to 90 GPa. Our results (Fig. 3.4-11) show that the measured densities of SiO_2 and $MgSiO_3$ glasses at high pressure and room temperature are identical and are within less than 1 % when considering an isotherm of 4000 K. Therefore the different SiO_2 content at high pressure depending on whether a pyrolitic or a basaltic system is considered will have at most a minor effect on the final density of the respective melts.

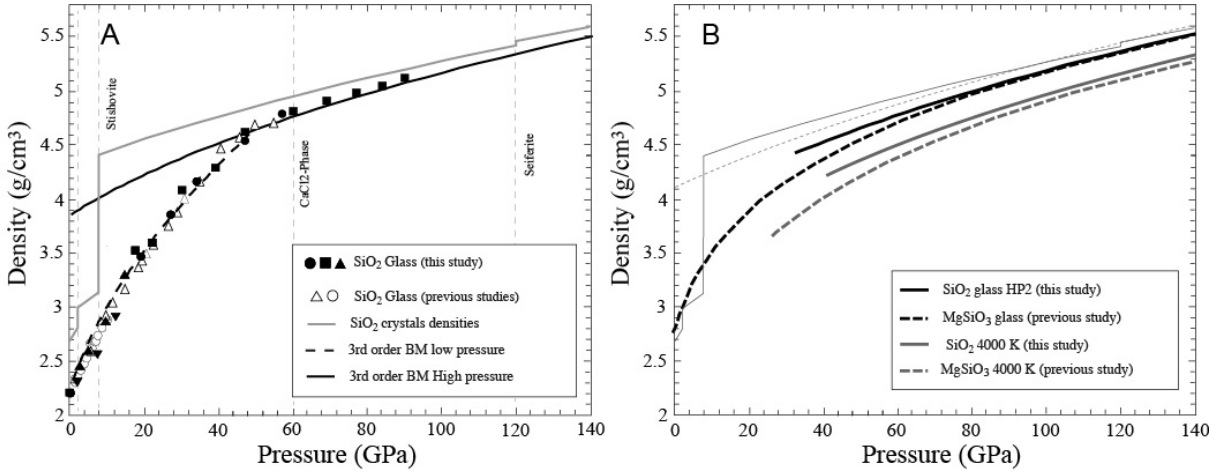

Fig. 3.4-11: A) SiO_2 glass density results obtained using the X-ray absorption method. Filled symbols: SiO_2 glass density measured in this study, empty symbols: previous measurements. The grey line is the density of the SiO_2 crystalline phases, the thick dark line is the equation of state (EoS) calculated form our high-pressure measurements (above 40 GPa) and the dashed dark line represent the EoS calculated using the low pressure-data (below 40 GPa). B) High-temperature EoS for SiO_2 and comparison with the EoS of $MgSiO_3$ at 300 K and 4000 K. The density of SiO_2 and $MgSiO_3$ glasses at 300 K are identical above 80 GPa, whereas SiO_2 glass is less than 1 % denser at 4000 K than $MgSiO_3$ glass.

Thus, we conclude that the main factor controlling melt buoyancy in the lowermost mantle is the partitioning of iron between the melt and the coexisting mineral phases, with the silica content of the melt playing only a minor role.

j. *Hardness and bonding of garnets in the majorite-pyrope system (Z.D. Liu, T. Boffa Ballaran, R. Huang, N. Cai/New York, S. Greáux, T. Shinmei and T. Irifune/Matsuyama)*

Garnet, $X_3Y_2Z_3O_{12}$ (where X^{2+} = Mg, Fe, Ca, Mn; Y^{3+}= Al, Fe, Cr; Z^{4+}= Si, Ge), is one of the most abundant rock-forming minerals in the Earth's crust, upper mantle, and mantle transition

zone. Garnet in the Earth's mantle usually exists as solid solutions, among which the majorite ($Mg_4Si_4O_{12}$) – pyrope ($Mg_3Al_2Si_3O_{12}$) system is the most dominant. Because of its hardness and its optical and conductive properties, garnet also shows great industrial applications such as excellent abrasive, gemstones, laser material and optical element. Therefore, accurate knowledge about the crystal structure, hardness, and thermodynamic properties of garnets in the majorite-pyrope system is of great interest not only in geophysics but also in physics and materials science.

Here, we synthesized samples of gem-quality polycrystalline garnet in the majorite-pyrope system at 18 GPa and 2100 K using a Kawai-type multianvil apparatus. A phase transition from a cubic to a tetragonal structure is clearly observed for garnets with pyrope content smaller than 26 mol. % as indicated by splitting of reflections in the X-ray powder diffraction patterns. Cation-oxygens bond lengths in cubic and tetragonal garnets were obtained from Rietveld structural refinements of the X-ray diffraction patterns (Fig. 3.4-12). In both cubic and tetragonal garnets, it is found that the bond length of Mg-O, Al-O and Si-O decreases with increasing pyrope contents (Fig. 3.4-13a), in agreement with results from single-crystal X-ray diffraction refinements present in the literature.

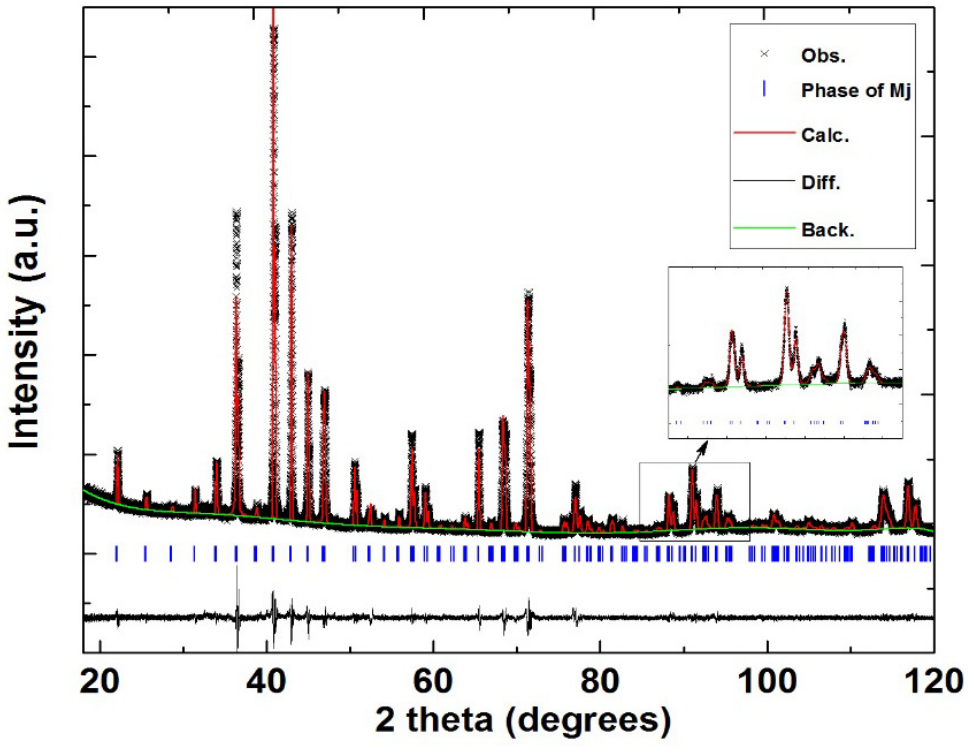

Fig. 3.4-12: Example of a Rietveld structural refinement of a powder X-ray diffraction pattern collected for a tetragonal $Mj_{90}Py_{10}$ garnet. Crosses represent the observed data, and red solid lines represent the fit obtained from the Rietveld structural refinements. The difference between calculated and observed intensities is shown below the spectrum. The vertical blue lines represent the reflection positions of the $Mj_{90}Py_{10}$ sample.

The Vickers hardness of some well-sintered garnets in this system has been measured by indentation tests. It is found that the hardness of these garnets increases with increasing pyrope contents along the majorite-pyrope system (Fig. 3.4-13b). The hardness of garnets in this system can be interpreted in terms of a chemical bond theory:

$$H_v(GPa) = 8.82\ (N_e^{\mu})^{2/3} E_h^{\mu} e^{-1.191 f_i^{\mu}} = H_v^{\mu}$$
$$= 350\ (N_e^{u})^{2/3} e^{-1.191 f_i^{\mu}} / (d^{\mu})^{2.5}$$

Where d^{μ} represents the bond length for the different coordinations μ-type bond, f_i^{μ} is the ionicity of the bonds, N_e^{u} is the covalent bond number per unit area. The hardness of these garnets can be calculated by a geometric average of all bonds in the garnet structure. Garnets presenting a high hardness have a smaller average bond length, while those with a lower hardness have a larger average bond length.

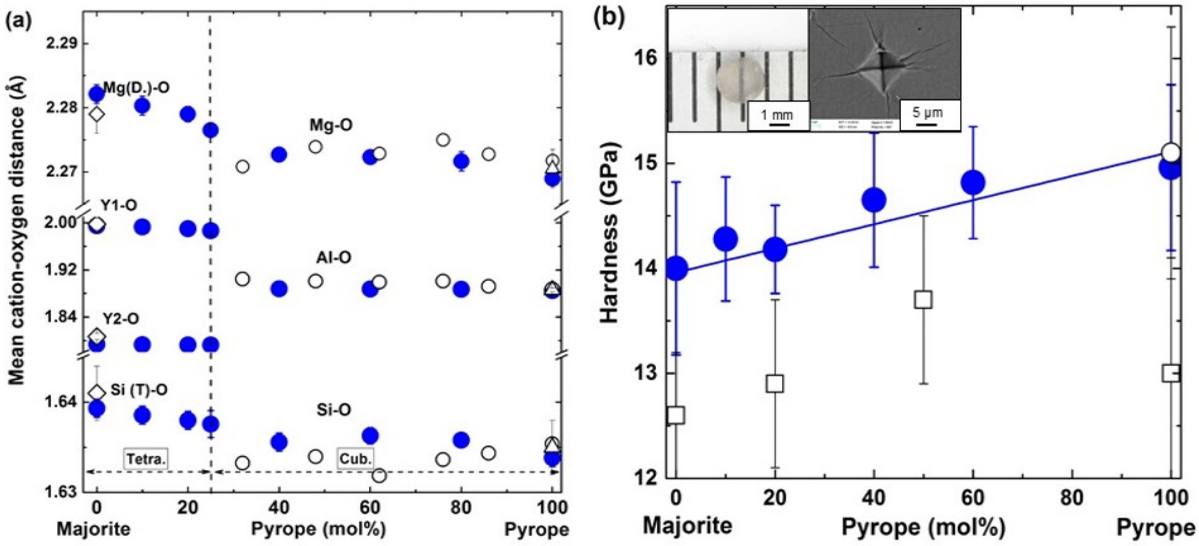

Fig. 3.4-13: (a) Compositional dependence of the cation-oxygen distances in the majorite-pyrope system. (b) Vickers hardness as a function of pyrope content along the majorite-pyrope system. Solid blue symbols represent results from this study, open symbols represent previous works. The optical micrograph of one well-sintered garnet and the electron back-scattered image after a Vickers indentation are shown in the inset.

3.5 Fluids, melts and their interaction with minerals

Hydrogen is likely the most important volatile element in Earth's interior, due to its strong effects on melting temperatures and many physical properties, such as electrical conductivity or deformation mechanisms. Usually, hydrogen is assumed to occur mostly in its oxidized form, as OH groups or H_2O molecules, stored as defects in mantle minerals, as a free aqueous fluid or as a dissolved component in silicate melts. However, under the very reducing conditions in the present deep mantle and throughout the entire mantle in early Earth history, molecular hydrogen (H_2) may prevail. Until recently, it was completely uncertain whether molecular H_2 could be dissolved in solid minerals and at which concentration level. The first contribution in this chapter solves this problem. Upper mantle minerals (olivine, garnet, and pyroxenes) were saturated with hydrogen in piston cylinder experiments and hydrogen concentrations were measured by infrared spectroscopy. Due to the interaction with the surrounding silicate matrix, a dipole moment in the H_2 molecule is induced, which makes it detectable by infrared spectroscopy. The data show a small, but significant solubility, which implies that some H_2 from the nebular gas may have been directly incorporated in the growing planet. In a companion study, the solubility of H_2 in silicate melts was systematically studied as a function of pressure, temperature, and melt composition. A third study looks at the effect of the redox state on the dissolution of OH in the transition zone minerals wadsleyite and ringwoodite. As OH and H_2O are reduced to H_2, the amount of OH dissolved in these minerals has to decrease, as observed in the experiments. Taken together, the three aforementioned studies will allow a much better understanding of how Earth acquired its hydrogen budget and how it evolved through geologic history. Another contribution reports on an ongoing experimental program to better constrain the effect of H_2O and CO_2 on mantle melting.

Experimental studies on nitrogen storage in the mantle have been pioneered at the Bayerisches Geoinstitut. One contribution in this chapter reports the first data on nitrogen solubility in transition zone and lower mantle minerals. Wadsleyite and ringwoodite may store nitrogen at the 50-200 ppm level, while nitrogen solubility in lower mantle minerals is lower. Taken together, these data suggest that as much as 40 atmospheric masses of nitrogen could be stored in the deep mantle. The capability of silicate melts to transport nitrogen back to the surface in subduction zones is studied in another contribution.

Based on recent measurements at the Bayerisches Geoinstitut, a numerical model for the electrical conductivity of NaCl-bearing aqueous fluids is developed and described in the last study of this section. This model allows a better interpretation of magnetotelluric data; in particular, it helps to distinguish silicate melts from aqueous fluids in zones of high conductivity in crust and mantle.

a. *Molecular hydrogen in mantle minerals (X. Yang/Nanjing and H. Keppler)*

Earth may have accreted in the presence of some nebular gas consisting mostly of H_2. It is therefore conceivable that some of Earth's hydrogen budget was acquired by the direct dissolution of nebular gas in a magma ocean or in solid minerals. Moreover, even today, the oxygen fugacity in the deep mantle is so low that a large fraction of H_2O and OH may be reduced to molecular hydrogen (H_2). The solubility of H_2 in upper mantle minerals (olivine, garnet, pyroxenes) was for the first time measured in piston-cylinder experiments (Fig. 3.5 - 1).

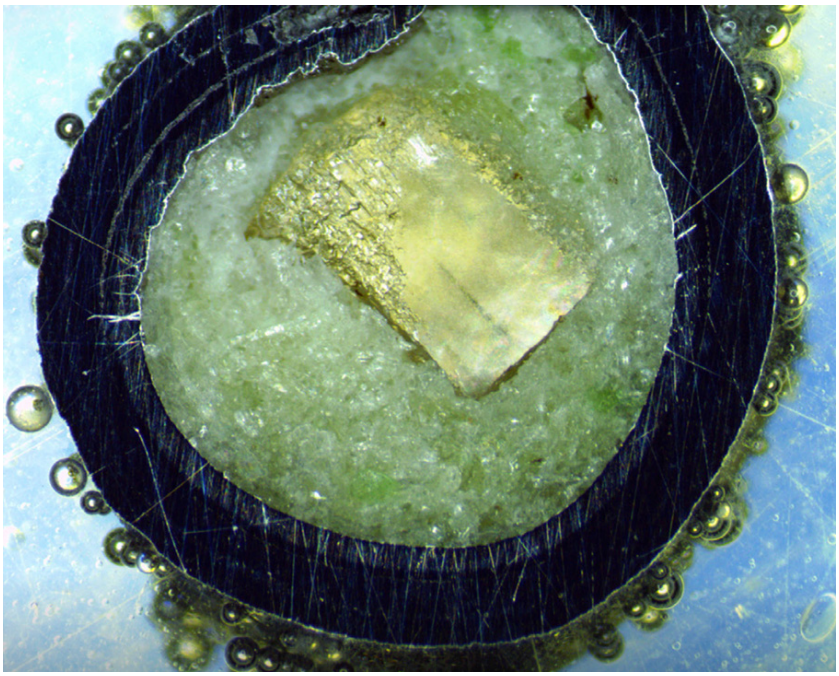

Fig. 3.5-1: A recovered single crystal of orthopyroxene inside a sample capsule from a piston-cylinder experiment on H_2 solubility in mantle minerals at 2 GPa and 1100 °C. The pyroxene crystal is surrounded by spinel peridotite powder and included in a double capsule, with a Pt capsule inside a Fe-capsule containing the Fe-FeO-H_2O buffer producing H_2. The width of the image is about 5 mm.

Starting materials in the experiments were gem-quality natural single crystals of olivine, garnet, orthopyroxene, and clinopyroxene. They were annealed in piston cylinder experiments at 2-7 GPa and 1100-1300 °C using a double capsule technique. Molecular H_2 was generated by a Fe-FeO-H_2O buffer included in an outer iron capsule.

The infrared spectra of the single crystals recovered after the experiment showed a new band due to molecular hydrogen at about 4062 cm^{-1} (Fig. 3.5-2) Molecular hydrogen becomes infrared active in a crystalline matrix due to a dipole moment induced by the interaction with the surrounding atoms. In order to quantify the amount of hydrogen represented by the 4062

cm^{-1} band, some samples were re-run under oxidizing conditions and the increase in infrared absorption due to OH was used to calibrate the extinction coefficient of the H_2 band. Ultimately, this procedure yielded H_2 concentrations equivalent to 15-50 ppm of dissolved H_2O. Solubility increases with pressure, but there is little systematic difference between the different minerals studied.

The experimental data imply that the deep, reducing part of the mantle may contain a very significant reservoir of hydrogen in the form of H_2. This could be particularly important for the lower mantle, where only little OH can be stored in minerals. Upon upwelling of material from the lower mantle, oxygen fugacity increases and H_2 is converted to OH or H_2O. This effect may explain why melts tapping lower mantle reservoirs often have elevated water contents, despite the difficulty to store OH in lower mantle minerals. Moreover, the data on H_2 solubility in minerals presented here imply that some H_2 from the nebular gas may have dissolved in a magma ocean early in Earth history and upon crystallization of the magma ocean, this H_2 was directly stored in minerals of the deep mantle.

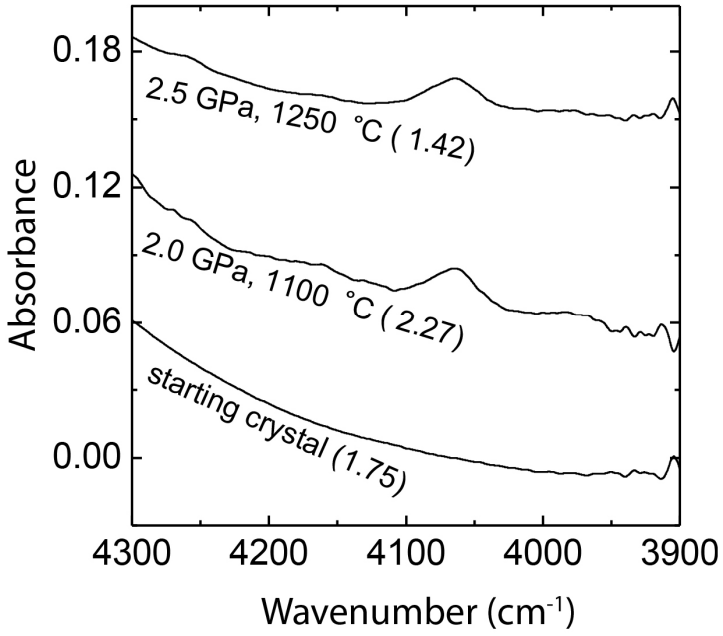

Fig. 3.5-2: Unpolarized infrared spectra of orthopyroxene, before and after saturation with H_2 at high pressure. The peak near 4062 cm^{-1} is due to molecular hydrogen. Numbers in parentheses give the thickness of the crystal studied.

b. *The solubility of molecular hydrogen in silicate melts (A. Chaudhari, M. Masotta/Rome, S. Shcheka and H. Keppler)*

After the accretion of the Earth, a magma ocean may have coexisted with a highly reducing atmosphere, containing abundant H_2. Accordingly, the solubility of H_2 in silicate melts may have contributed to the initial volatile budget of Earth's mantle. Quantifying H_2 solubility in

silicate melts, however, is hampered by uncertainties of the calibration of the infrared extinction coefficients of hydrogen. Moreover, the dependence of H_2 solubility of pressure, temperature, and melt composition requires further study.

H_2 solubility was studied in silicate melts of haplogranitic, andesitic, and basaltic (MORB) composition at 0.1 to 4 GPa and 1100-1400 °C. Some low-pressure experiments were carried out in TZM bombs using Pt capsules loaded with haplogranitic glass and H_2 gas. The other experiments were carried out in a piston-cylinder apparatus with a double capsule technique. An inner Pt capsule with the glass was sealed into an outer Fe capsule containing some FeO and H_2O as a source of H_2. Run products were investigated by FTIR spectroscopy.

Figure 3.5-3 shows infrared spectra of andesite glasses saturated with H_2 at 1400 °C and various pressures. The band near 4100 cm^{-1} is due to H_2, while the combination bands near 4500 and 5200 cm^{-1} are due to OH groups and molecular H_2O in the glass. Clearly, H_2 solubility increases with pressure; additional experiments showed a decrease of solubility with temperature. Melt composition also has a marked effect on solubility, which increases from basalt to andesite to haplogranite.

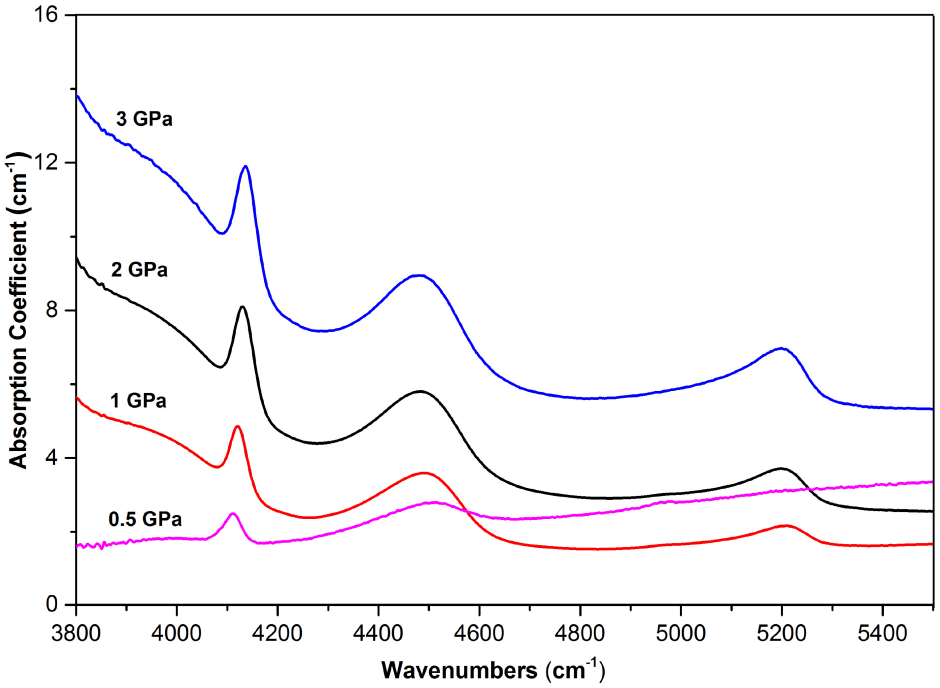

Fig. 3.5-3: FTIR spectra of quenched andesite melts, saturated with H_2 at 1400 °C, Fe-FeO buffer conditions and various pressures. The peak near 4100 cm^{-1} is due to molecular hydrogen (H_2). The peaks at 4500 and 5200 cm^{-1} are due to OH groups and molecular H_2O, respectively.

A thermodynamic analysis of the solubility data for haplogranitic composition constrained the enthalpy of dissolution of H_2 at ΔH = - 48.0 $kJmol^{-1}$ and the volume change of the melt upon

dissolution at ΔV_{melt} = 11.8 cm^3mol^{-1}. The quantification of absolute concentrations, however, depends on the infrared extinction coefficient of H_2. This coefficient has so far only be determined for quartz glass and the calibration method used may be unreliable. Some of the H_2-saturated haplogranitic glasses were therefore re-run together with pure O_2 loaded into the capsule, such that all H_2 was oxidized and the H_2 band completely disappeared in the run products. The corresponding increase in the infrared bands due to OH and H_2O was then used to calibrate the extinction coefficient of H_2. This calibration gives a much higher extinction coefficient than previously reported for quartz glass and suggests that H_2 solubilities in silicate melt may have been severely overestimated. More experiments are, however, necessary to reliably calibrate the infrared extinction coefficient of H_2 in glasses of variable composition.

c. *Water solubility in wadsleyite and ringwoodite as function of oxygen fugacity (D. Druzhbin, H. Fei and T. Katsura)*

The uppermost mantle is likely relatively oxidized, with an oxygen fugacity close to the fayalite-magnetite-quartz (FMQ) buffer. On the other hand, the mantle transition zone is considered to be much more reduced, near the iron-wustite buffer. However, the water content in the recently discovered ringwoodite inclusion in a transition zone diamond from Juina (Brazil) was estimated to be more than 1.4 wt. %, whereas the experimentally-determined maximum water contents in wadsleyite and ringwoodite are 2-3 wt. %. These observations indicate a hydrous transition zone, while the inferred low oxygen fugacity should reduce water to hydrogen. Possibly, the diamond inclusion from Juina is from a locally oxidized part of the transition zone, while in the reduced parts water solubility in minerals should be limited.

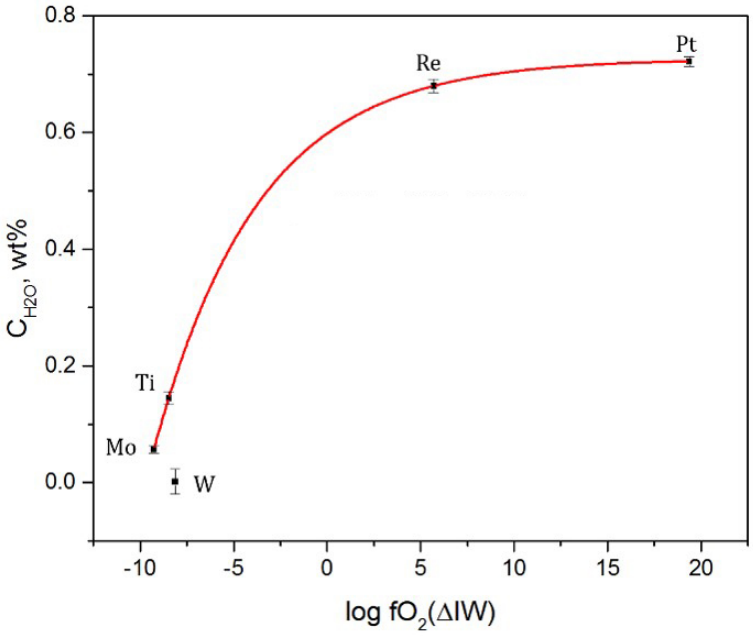

Fig. 3.5-4: Water solubility in wadsleyite at 21 GPa and 1570 K and variable oxygen fugacity. The data points labeled Mo, Ti, W Re and Pt refer to the Mo-MoO_2, Ti_2O_3-TiO_2, W-W_2O_3, Re-Re_2O_3, and Pt-PtO_2 buffers.

In order to constrain the dependence of water solubility on oxygen fugacity, we measured water (OH) contents in wadsleyite samples synthesized in experiments using various redox buffers, including Mo-MoO_2, Ti_2O_3-TiO_2, W-W_2O_3, Re-Re_2O_3 and Pt-PtO_2. Synthetic anhydrous forsterite powder was loaded together with a talc+brucite water source and various type of redox buffer into a platinum capsule and annealed at a nominal pressure of 21 GPa and a temperature of 1570 K. The water content in run products of Mg_2SiO_4 wadsleyite, as measured by FTIR spectroscopy, clearly shows a positive correlation with oxygen fugacity (Fig. 3.5-4), implying that at reduced conditions, the capacity of the transition zone to store water is limited. However, additional efforts, including reversed experiments, are necessary to fully constrain this effect.

d. *The role of volatiles (H_2O, CO_2) in the onset of melting in the Earth's upper mantle (P. Condamine and D.J. Frost)*

The purpose of this ongoing project is to provide a systematic study on the role of the volatiles H_2O and CO_2 on melting processes in the Earth's upper mantle. This includes the following two objectives: 1) Constraining the phase relations and melt compositions of peridotite as a function of volatile (H_2O, CO_2) contents at pressures and temperatures relevant for the genesis of groups I and II kimberlites, *i.e.*, from the diamond stability field to the base of the upper mantle. 2) Determining H_2O mineral-melt partition coefficients in H_2O and H_2O-CO_2 systems to better understand the onset of melting in the Earth's upper mantle down to the transition zone and to constrain the fraction of melting for a given source volatile content. These data are essential for the interpretation of geophysical observations of potential volatile induced partial melting.

Experiments are performed in multianvil apparatus in a range of pressures (6-15 GPa) and temperatures in a natural peridotitic assemblage. Because the bulk H_2O content of the mantle is very low, incipient melting of peridotite will not modify mineral compositions, except for the most incompatible elements. Thus, it is important to determine volatile partition coefficients at the very first degrees of melting. Conducting iterative sandwich experiments to study low-degrees of melting, using a high proportion of glass, helps to attain equilibrium and facilitates both melt and mineral analyses to study partitioning of H_2O and CO_2 at the onset of melting (Fig. 3.5 -5a).

A special melt extraction technique was developed to segregate small fractions of partial melt. Thin (≤60 μm) horizontal gold foils are placed in the middle of the experimental charges. During the experiments, the gold foil melts and retracts at the edges. As a consequence, melt migrates into the newly available space. Using this technique, we obtained melt layers up to 100 μm thick in equilibrium with residual peridotite (Fig. 3.5-5b). This technique is limited to temperatures significantly higher than the melting point of gold and may be used for melt fractions higher than 10 %. For lower temperatures, silver is a possible alternative to gold.

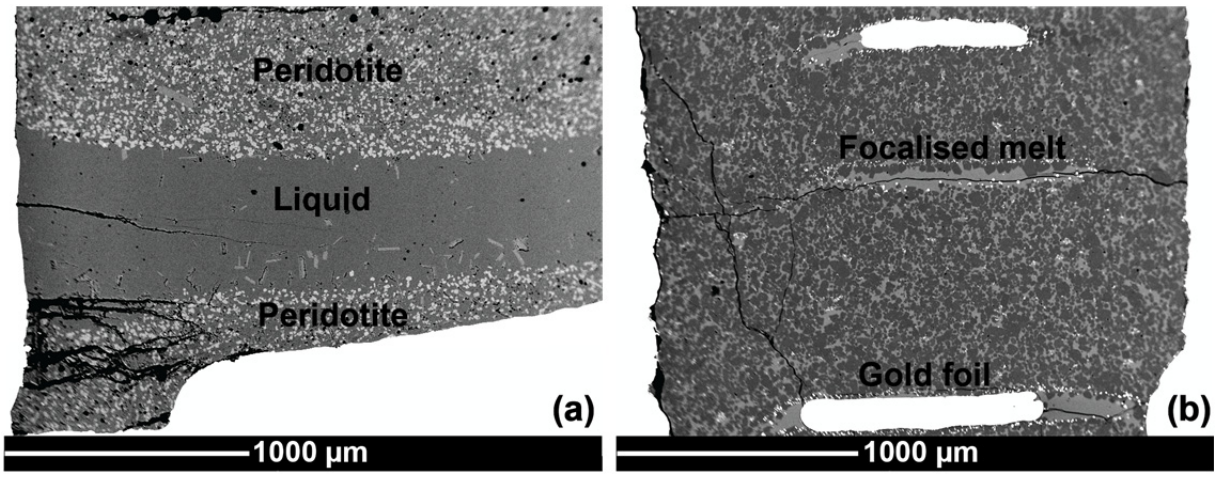

Fig. 3.5-5: BSE images illustrating experimental strategies employed in order to determine melt compositions under volatile-bearing conditions. (a) Iterative sandwich experiments are performed to obtain incipient melt in equilibrium with the peridotite. (b) Gold and silver foils are used at higher temperatures to extract moderate to high-degree of melting as thick layers in the peridotite.

e. *Nitrogen storage in the deep mantle (T. Yoshioka, M. Wiedenbeck/Potsdam, S. Shcheka and H. Keppler)*

Geochemical evidence suggests that there is presently much more nitrogen being recycled into the mantle in subduction zones than is degassed at mid-ocean ridges. Cosmochemical arguments also show that the bulk Earth may contain much more nitrogen than presently resides in the atmosphere. These observations imply that the deep nitrogen geochemical cycle may have evolved over time. However, it is still not well known where and how nitrogen may be stored in the solid Earth. To complement some pioneering studies on nitrogen solubility in upper mantle minerals that had been carried out at BGI in recent years, we started to investigate nitrogen solubility in transition zone and lower mantle minerals.

We synthesized nitrogen-saturated wadsleyite, ringwoodite, bridgmanite and Ca-silicate perovskite at 14-24 GPa and 1100-1600 °C in the multianvil apparatus from oxide mixtures or glasses using Pt and PtRh capsules. We included in the mixtures both a nitrogen-source (^{15}N-doped NH_4NO_3) and metallic iron, in order to buffer the oxygen fugacity close to the Fe-FeO buffer, consistent with the reducing conditions of the deep mantle. After the experiments, nitrogen contents in the minerals were quantified with the Cameca 1280-HR secondary ion mass spectrometer (SIMS) at GFZ Potsdam.

Figure 3.5-6 and Figure 3.5-7 show nitrogen solubilities in wadsleyite and ringwoodite. In both phases, especially in wadsleyite, solubility increases strongly with temperature, while the pressure effect is less pronounced. We also observed that nitrogen solubilities in Al-free bridgmanite and Ca-silicate perovskite at 24 GPa and 1600 °C were 22±18 and 63±46 ppm by weight, respectively. Furthermore, we synthesized samples in which two different mineral

phases were in equilibrium and obtained partition coefficients of $D_N^{wadsleyite/olivine} \approx 4$, $D_N^{ringwoodite/wadsleyite} \approx 0.5$ and $D_N^{bridgmanite/ringwoodite} \approx 0.25$. Nitrogen contents in coexisting Fe-Pt alloy were measured by electron microprobe. Partition coefficient between bridgmanite and metal were $D_N^{bridgmanite/metal} \leq 200$, and therefore, about 1/3 of the bulk nitrogen in the lower mantle is contained in the silicate phase, considering that the proportion of Fe-rich alloy in lower mantle is about 1 wt. %. These data imply that the transition zone and the lower mantle may store about 7 and 33 times more nitrogen than presently resides in the atmosphere, respectively (Fig. 3.5-8).

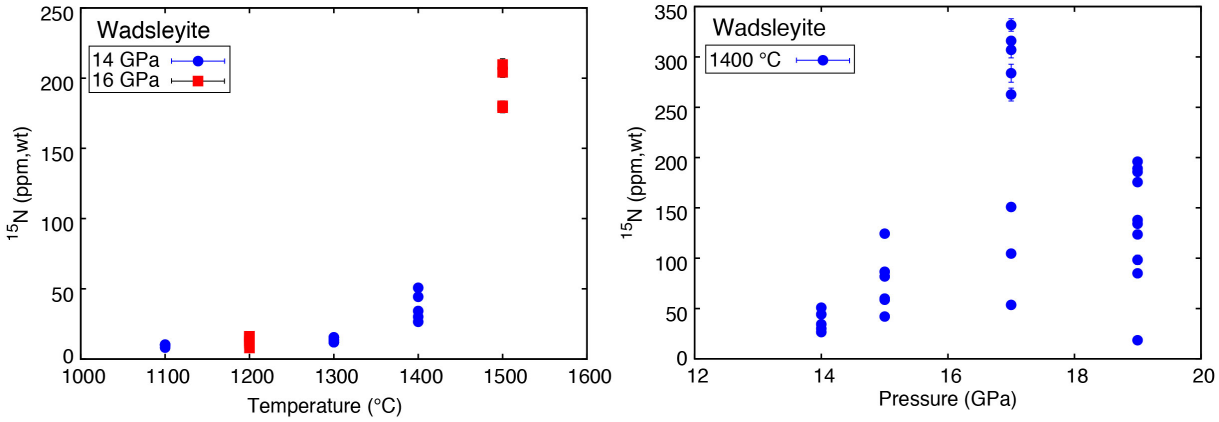

Fig. 3.5-6: Nitrogen solubilities in wadsleyite at various temperatures and pressures as quantified by SIMS

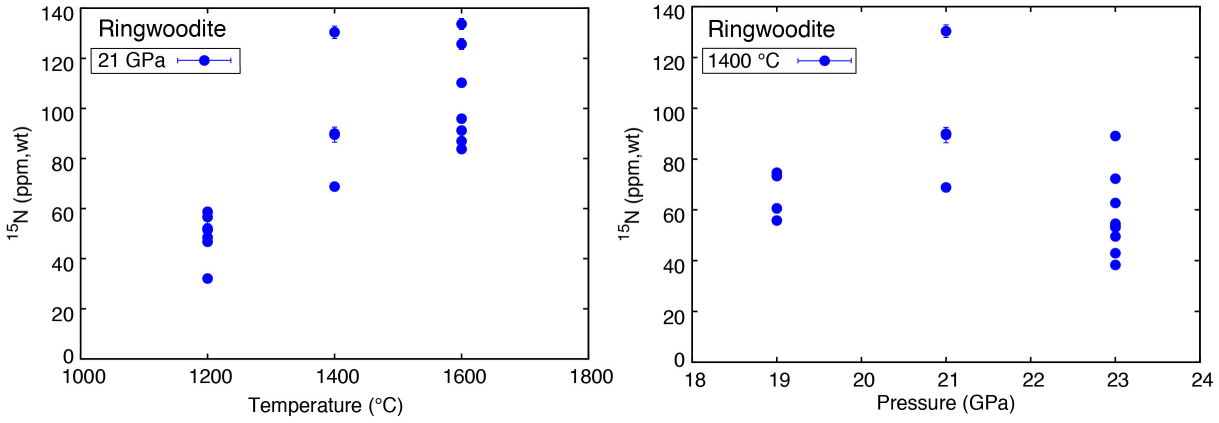

Fig. 3.5-7: Nitrogen solubilities in ringwoodite at various temperatures and pressures as quantified by SIMS.

Our study suggests that the deep, reduced mantle may be a major host of nitrogen in the Earth and it is by no means certain that the majority of the nitrogen in our planet resides in the atmosphere. Depending on the evolution of the deep nitrogen cycle over geologic time, it is quite plausible that atmospheric pressure may have largely fluctuated during the evolution of the Earth.

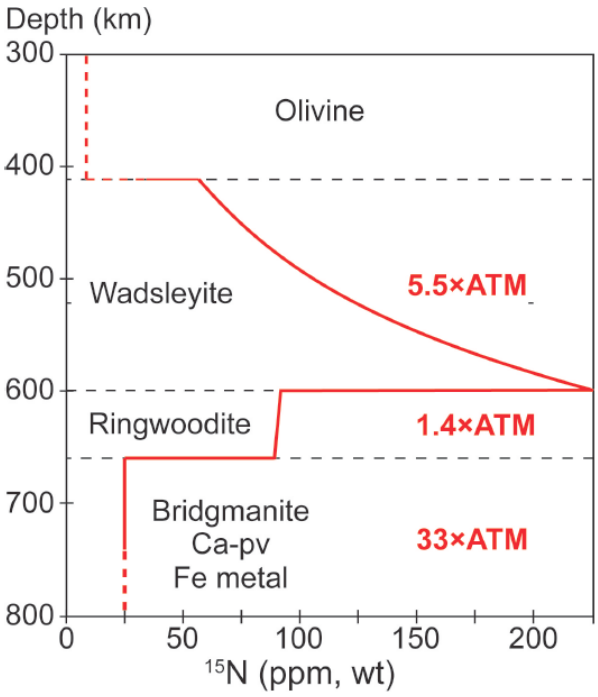

Fig. 3.5-8: A model of the nitrogen storage capacity in the mantle.

f. *Experimental determination of the nitrogen carrying capacity of subducted slab-derived melts (A. Mallik, M. Wiedenbeck/Potsdam and Y. Li/Guangzhou)*

Subduction zones are the principle tectonic setting for the recycling of nitrogen from the atmosphere into Earth's interior, as well as for the degassing of nitrogen from the mantle to the atmosphere via arc volcanism. The principle carriers of N in the slab are sediments and altered oceanic crust. Recent studies suggest an increased importance of slab-derived melt in arc magma genesis. Hence, we have determined the N carrying capacity of rhyolites (slab-derived melts) in order to understand the influx versus outflux of N via subduction processes. We performed experiments at 1300 °C, 2-4 GPa, buffered at fO_2 equivalent to NiNiO, to determine the solubility of nitrogen in rhyolites with variable dissolved H_2O concentrations. The N is dissolved in the rhyolites as molecular N_2, likely occupying the ionic porosity in the melt structure. The solubilities of N in the slab-melts vary from 0.4 wt. % to 1.1 wt. %. If a subducted slab carries 530-2400 ppm of nitrogen, a low degree slab melt should carry 0.2 to 1.1 wt. % N, assuming the partitioning of NH_4^+ in the slab minerals to be similar to Rb^+. The results from this solubility study indicate that it is possible for slab melts to carry this amount of nitrogen from the slab to the arc source. The amount of N released from subducted slabs via aqueous fluids and slab melts was determined along subduction zones globally by combining published fluid partitioning models with melt solubility data determined in this study and a range of partition coefficients for Rb^+ (as a proxy for NH_4^+). It is found that 18-27 % of N survive past the arc magmatism filter to enter the deep mantle together with the subducted slab. This is intermediate between previous estimates ranging from 0 % to 60-100.

Also, about 70 % of the N released from the subducted slabs by fluids and melt is sequestered in the mantle wedge and/or overriding arc crust. This sequestered N will also add to the amount recycled to the deep mantle and should be taken into account in future refinements of the recycling model.

g. *A model for the electrical conductivity of aqueous fluids in deep crust and mantle (R. Sinmyo/Tokyo and H. Keppler)*

Magnetotelluric data often show zones of elevated electrical conductivity in the deep continental crust, above subducting plates, and below active volcanoes. However, it is not always straightforward to decide whether these observations are due to the presence of silicate melts, aqueous fluids, or other effects. One main problem is here that electrical conductivity measurements of NaCl-bearing aqueous fluids, which may serve as a good model of aqueous fluids in crust and upper mantle, have been limited to 0.4 GPa and 800 °C. In order to overcome this limitation, a large number of conductivity measurements were carried in the NaCl-H_2O system at pressures up to 1 GPa, using a modified diamond anvil cell. In this apparatus, a perforated diamond platelet is placed between two gaskets, which serve as electrodes for the measurements. The data obtained were used, together with the low-pressure data from the literature, to derive a general model for the conductivity of aqueous saline fluids. This model is based on classical electrolyte theory with some simplifications.

The electrical conductivity σ (in S/m) of NaCl-bearing aqueous fluids may be described by the equation

$$\log \sigma = - 1.7060 - 93.78/T + 0.8075 \log c + 3.0781 \log \rho + \log \Lambda_0 (T,\rho)$$

where T is temperature in K, c is NaCl concentration in wt. %, ρ is the density of pure water at given pressure and temperature and Λ_0 (T,ρ) is the molar conductivity of NaCl in water at infinite dilution (in S cm^2 mol^{-1})

$$\Lambda_0 = 1573 – 1212\ \rho + 537\ 062/T – 208\ 122\ 721/T^2$$

Figure 3.5-9 compares predicted electrical conductivities of saline aqueous fluids in deep crust and upper mantle with the conductivity of dry and hydrous silicate melts. At typical lower crustal temperatures (600-800 °C), fluids are about two orders of magnitude more conductive than hydrous granitic melts. This means that a conductivity anomaly that would be consistent with extensive melting could also be produced by a very small fraction of a saline fluid forming an interconnected network. However, such a small fluid fraction would likely reduce seismic velocities much less than the presence of a large melt fraction, such that the effects of fluids and silicate melts in the deep crust likely can be distinguished by a combination of magnetotelluric and seismic data. However, at the high temperatures (> 1000

°C) in the mantle wedge above subduction zones, the conductivities of aqueous fluids and hydrous basaltic melts are similar, such that distinguishing these two phases from geophysical remote sensing data alone becomes difficult. However, the dependencies of conductivity on temperature are very different for these two phases, implying that a combination with thermal models may allow their effects to be distinguished.

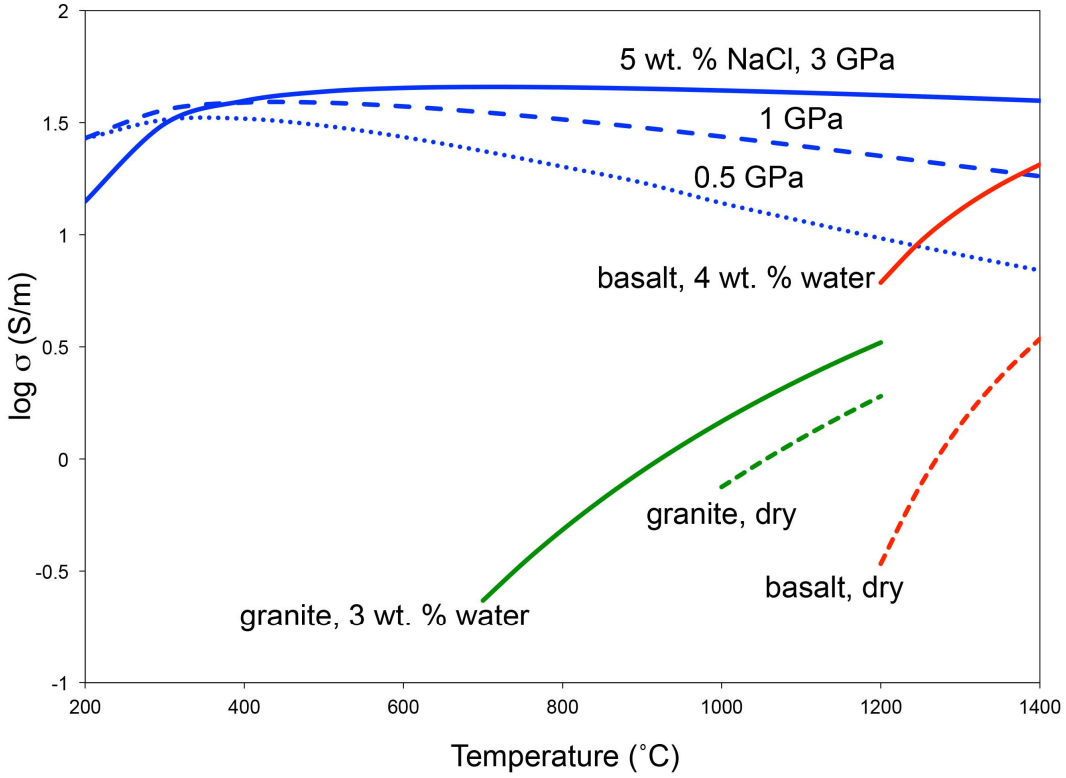

Fig. 3.5-9: Predicted electrical conductivity of aqueous fluid with 5 wt. % dissolved NaCl as function of pressure and temperature. Data for dry and hydrous granitic and basaltic melts are shown for comparison. The granite data are from Gaillard (2004; EPSL 218: 215), the basalt data from Ni *et al.* (2011; CMP 162: 637).

3.6 Rheology and Metamorphism

The dynamic motion in the Earth's interior is the driving force for global tectonics and the exchange of material between the surface and the deep interior of our planet. It causes catastrophic events such as earthquakes, explosive volcanism and enhances heat flow that in turn affects the thermal state of Earth's interior. The exact and quantitative description of rheological properties of the constituting materials of the upper and lower mantle of the Earth and their deformation mechanisms is indispensable for understanding the dynamic motion in the Earth's interior.

A most critical step in global tectonics is the initiation of localized deformation at the onset of subduction. Formation of boudinage, which is a form of strain localization in a special geometry, was investigated in the first contribution to this chapter. The presence of initial perturbations along the layered starting geometry seems to be a key aspect for boudinage and therefore strain localization. Eclogite layers at the base of mountain belts and at the top of subducted slabs are key positions in plate tectonics. The study presented in the second contribution reports that the bimineralic eclogite is weaker than pure garnet and possibly dunite. This is explained by weakening of clinopyroxene by change in deformation mechanism from (100) twinning at lower temperature to deformation accommodated by activation of multiple slip systems of {110}[001] and {110} ½ <110 > at higher temperature. The third contribution describes nucleation and growth of garnet under deviatoric stresses, as garnet is used to constrain pressure conditions of eclogite and peridotite. The structure of the newly formed garnets during metamorphism seems to be influenced not only by chemistry, but also by grain structures and deformation mechanisms, especially grain boundary sliding.

Plastic deformation of minerals by dislocation creep results in lattice-preferred orientation (LPO), which may cause seismic anisotropy. The fourth study determined the active slip system in periclase, which is the second most abundant mineral in the lower mantle by comparing results of deformation experiments with those of Elasto-Viscoplastic Self Consistent (EVPSC) modeling. The fifth study conducted deformation experiments on cubic $CaSiO_3$ perovskite, which is an important mineral in the transition zone and lower mantle, in a resistive-heated diamond-anvil cell after synthesis from wollastonite powder, whose results are also compared with results of EVPSC simulation to understand its slip system. The sixth contribution reports the results from high-temperature deformation experiments of ferropericlase at lower-mantle pressures. The previously observed strength increase of ferropericlase at ambient temperature is also observed at high temperature, although the increasing rate is smaller.

Olivine is a dominant mineral in the upper mantle and its mechanical properties have been investigated by many researchers. The seventh contribution attempts to develop a novel method to investigate effects of deviatoric stress on grain boundary migration of forsterite aggregates at high pressure and temperature, because the role of grain boundaries in

deformation of polycrystalline samples are still poorly understood. The eighth contribution presents diffusion studies at grain boundaries of forsterite by molecular dynamic simulation. A systematic relation between grain boundary excess free volume and diffusivity is observed, whereas the disorientation of adjacent crystals has no systematic influence on either, diffusivities or volume.

The ninth contribution is to study silicon self-diffusion in the wadsleyite lattice as a function of water content. This study tried to establish a procedure to obtain reliable diffusion profiles by coating single crystals with stable isotope enriched forsterite films. The last study of this section reports a negative relation between water-content and dislocation mobility in the olivine slip system [001](100). This relation was established by annealing simple-sheared single crystals of olivine containing different amounts of water to estimate dislocation mobility from dislocation annealing rates. This result suggests a possibility that the dislocation core structure might be changed by incorporation of water.

a. *Boudinage formation by deformation of layered olivine-orthopyroxene aggregates (R. Farla, F. Heidelbach and M. Urgese)*

Boudinage is a common pinch-and-swell structure in marble, gneiss, peridotite and eclogite deformed by dynamic metamorphism. Boudinage is a second-stage process that either immediately follows phase segregation in the same deformation cycle, or develops in pre-foliated rocks or pre-layered structures. Early attempts were made to understand the mechanisms of boudinage and buckle folding in the 1960s and 70s, and the generalized theory and models offered a tractable approach to quantify natural observations. A key observation, for instance, is that layers made of viscously contrasting minerals are stretched parallel to the foliation and compressed normal to the foliation plane, which produces “pressure gradients” in the softer layers, and pulls the harder layer apart. In the opposite sense, buckle folding of layers appears to be part of the same phenomenon. In addition, perturbations on layer interfaces are assumed to play a key role, because the growth rate of instability by perturbation can be high enough when materials are deformed by strongly nonlinear flow. In a sense, boudinage is a geometrical problem and a form of strain localization. Since it is considered that subduction of oceanic slabs is initiated by strain localization due to weak layers, understanding of boudinage should be vital for constructing numerical and large-scale geodynamical models, frequently employed in published studies.

In contrast, little attention has been given to experimental exploration of the onset and evolution of boudinage in layered Earth materials at high pressures and temperatures, which offers checks on numerical models. This study is based on natural observations of boudinaged pyroxenite dykes in dunite and experimental observations, suggesting orthopyroxene is harder than olivine (by a factor of 2 to 3). The samples are made of pre-sintered olivine and orthopyroxene layers and deformed to large strains (Fig. 3.6-1).

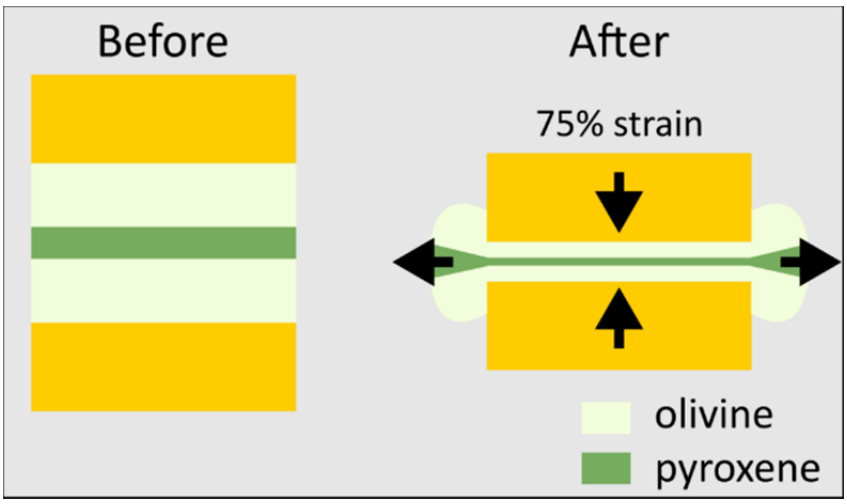

Fig. 3.6-1: Concept of the present boudinage experiment. Alternative layers of orthopyroxene and olivine are deformed by pure shear normal to the layering.

Boudinage experiments were conducted by tri-axial deformation using a large-volume multianvil press, because sufficient high-pressure conditions and large sample strains are essential for this project. Rock samples were composed of an orthopyroxene layer sandwiched by two olivine layers, or of alternate orthopyroxene and olivine layers. Their initial grains sizes were larger than 10 μm in order to prevent diffusion creep, which appears in polycrystalline samples with grain sizes smaller than 10 μm in laboratory deformation experiments. Theoretical considerations suggest power-law and exponential creeps favor boudinage, whereas linear (diffusion) creep hampers its formation. The grain sizes are less than 50 μm to avoid thinning layers with too few grains.

Preliminary experimental results show some evidence of pinch-and-swell in the multi-layered samples (Fig. 3.6-2). On the other hand, no necking was observed in a single orthopyroxene layer sandwiched by two olivine layers. The current hypothesis to explain this difference is that a single initially smooth layer may not possess sufficient perturbations on the interfaces to kick off the dynamic growth of layer instabilities, whereas the growth rate of layer instabilities may be amplified when multiple adjacent layers with a different distribution of perturbations are deformed simultaneously. These observations may imply that processes causing boudinage depend on not only viscosity contrast, spacing of the layers, and operating deformation mechanisms, but also on dynamic growth rate of instabilities on layer interfaces.

Another explanation for the absence of boudinage in samples with a single orthopyroxene layer is that boudinage could be hampered by a fine-grained matrix in the orthopyroxene layer, which results from dynamic recrystallization at high stresses/strain rates. Ongoing work is being carried out to address this complication by adding a small percentage of carbonate flux to Fe-bearing orthopyroxene synthesized from a laboratory precursor, which may enhance the grain growth kinetics (during annealing and deformation).

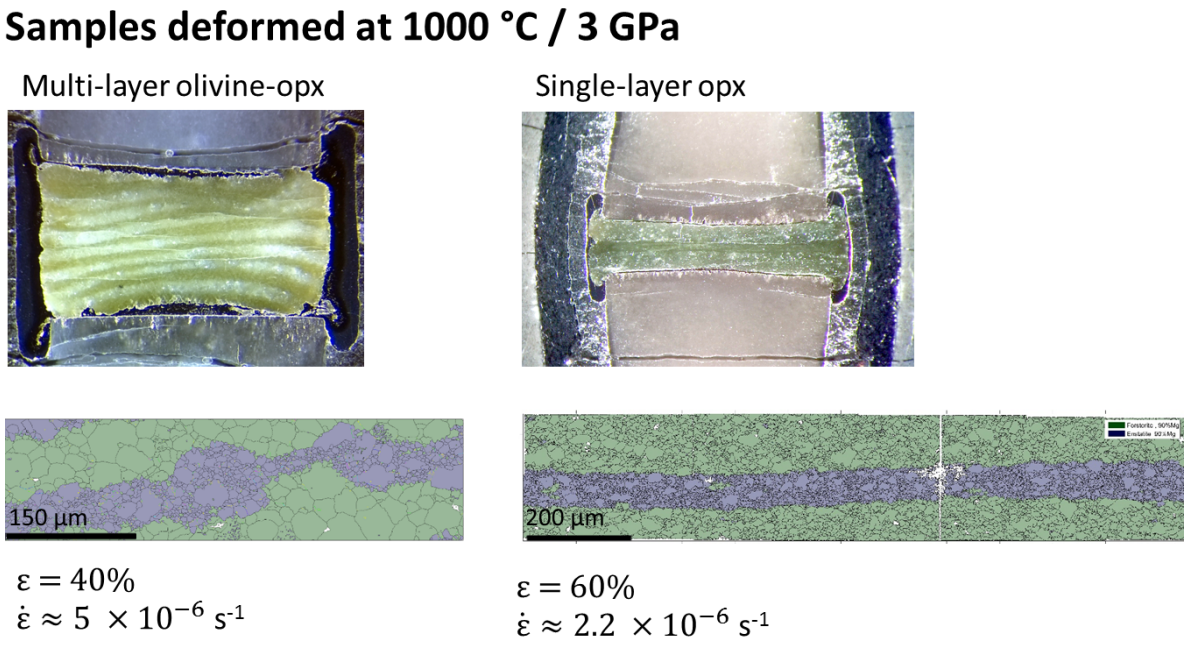

Fig. 3.6-2: (left) Optical micrograph and EBSD map of deformed multi-layered olivine (green) – orthopyroxene (blue) aggregate showing some form of boudinage. (right) Optical micrograph and EBSD map of deformation of a single orthopyroxene layer sandwiched by two olivine layers. The EBSD map highlights a distinct lack of boudinage in this sample.

b. *Deformation of residual eclogite in comparison with dunite, garnetite and clinopyroxenite (R. Farla, A. Rosenthal/Clermont-Ferrand, C. Bollinger, S. Petitgirard, J. Guignard/ Toulouse, W. Crichton/Grenoble, N. Miyajima, T. Kawazoe and D.J. Frost)*

Eclogite is composed mainly of garnet and clinopyroxene (omphacite), which exists as dense mafic cumulates at the bases of mountain belts, and as several-kilometer-thick layers at the top of subducted slabs. Due to its presence above the peridotite-dominated mantle, eclogite is expected to play a key role in plate tectonics. Since eclogite is not stable at low pressures, only a few classic deformation experiments were carried out at pressures of 2.5 to 3.5 GPa with large uncertainty in stress estimation. *In situ* synchrotron X-ray diffraction should allow the rheology of eclogite to be explored at high pressures. In this study, creep strength and microstructural evolution of eclogite aggregates composed of ~ 60 and ~ 40 wt. % of garnet and clinopyroxene, respectively, were investigated at pressures of 4.3 to 6.7 GPa, temperatures of 1050 to 1470 K and strain rates of 2×10^{-6} to 3×10^{-5} s^{-1}. Dunite (olivine) was simultaneously deformed with eclogite samples in series. Additional deformation experiments on garnetite and clinopyroxenite aggregates were performed to determine strengths of the constituent components of eclogite separately. The rheology of eclogite with three compositions was modeled using flow laws that describe relationships between the stress and strain rate. In spite of the relatively narrow range of experimental conditions, significant strength variation is observed, which is attributed to changes in the deformation mechanisms of the eclogite phases (Fig. 3.6-3).

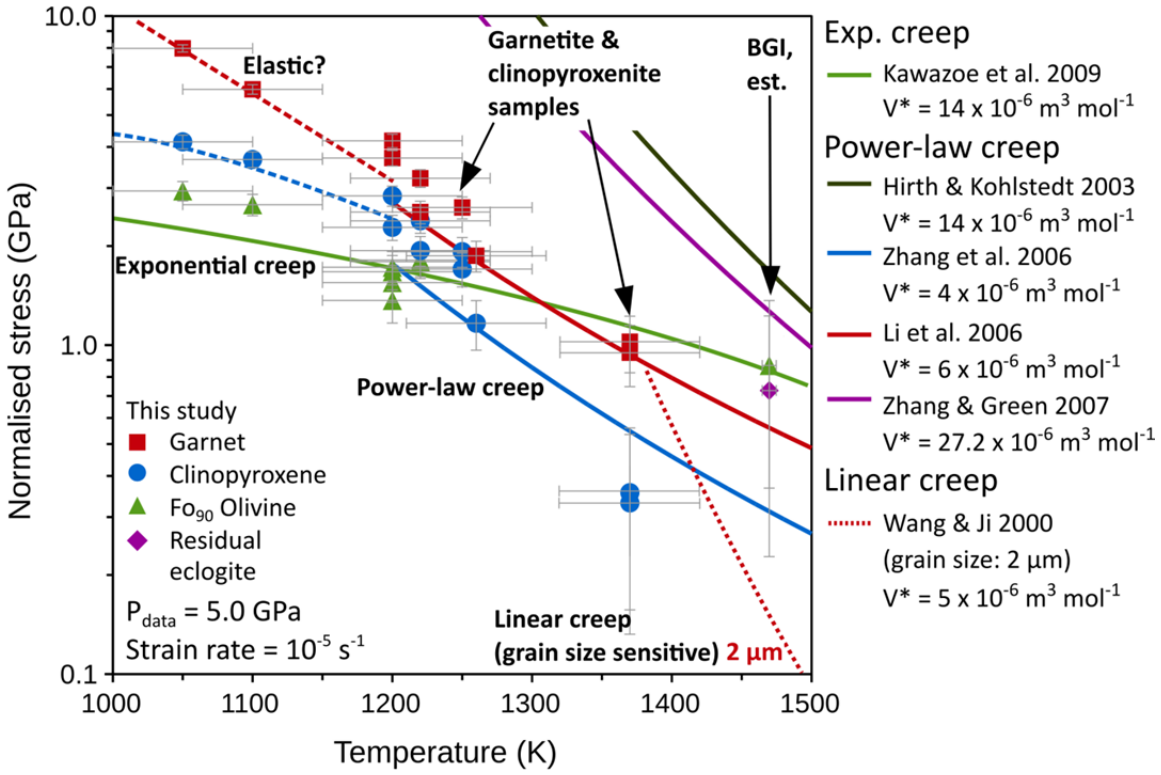

Fig. 3.6-3: Deviatoric stresses normalized by strain rate of 10-5 s-1 of all experiments against temperature. The curves indicate flow laws given in the literature. Colors denote constituent phases; red: garnet, blue: clinopyroxene, green: olivine, purple: bimineralic eclogite in average.

Assuming the rheology of garnet, clinopyroxene and olivine does not change significantly as a function of pressure, at temperatures below 1200 K, eclogite is by a factor of two stronger than olivine, likely due to the high strength of garnet. At temperatures greater than 1200 K, eclogite and olivine have approximately equal strengths. Clinopyroxene becomes significantly weaker at temperatures higher than 1250 K: Its rate of weakening by high temperature seems higher than those of olivine and garnet. These phenomena lead to reduction of the bulk strength of eclogite, dependent on the garnet fraction present (Fig. 3.6-3). The weakening of clinopyroxene is associated with a change in deformation mechanism from predominantly (100) twinning at lower temperatures to power-law dislocation creep at higher temperatures (Fig. 3.6-4). In the high-temperature regime, clinopyroxene grains were flattened by deformation, and exhibited strong lattice preferred orientation (LPO) characterized by [001] axes forming a girdle in the shear direction and [010] axes forming maxima in the plane normal to the shear direction. These observations agree with viscoplastic self-consistent modeling and TEM analysis in this study suggesting the activation of multiple slip systems: 1/2<110>{1 $\bar{1}$ 0}, [001]{110} and [001](100). Unlike clinopyroxene, garnet appears to accommodate only a small fraction of bulk strain by grain boundary sliding due to the small grain size, leading to phase segregation into layers. TEM and EBSD observations, respectively, demonstrated dislocation-free garnet grains and lack of LPO, which suggests limited dislocation activity in garnet. Stress estimations suggest that fine-grained garnetite

deformed elastically at lower temperatures and by Newtonian (linear) creep at temperatures higher than 1370 K. Note that strain partitioning between garnet and clinopyroxene in the eclogite was inferred from the deformation of garnetite and clinopyroxenite in series.

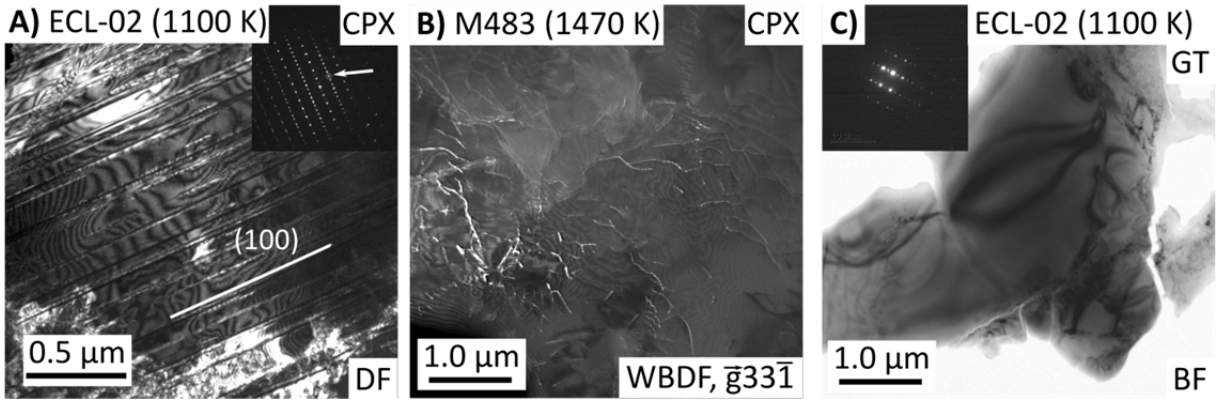

Fig. 3.6-4: TEM images of a twinned clinopyroxene grain deformed at 1100 K (A) one containing dislocations deformed at 1470 K (B) and a dislocation-free garnet grain apparently undeformed at 1100 K.

Unlike garnet and clinopyroxene, olivine seems to have deformed by a single deformation mechanism of exponential creep under the investigated temperature and strain rate conditions with deviatoric stresses higher than 1 GPa (Fig. 3.6-3). The change in deformation mechanism of olivine, which differs from eclogite, is not only due to difference in homologous temperature ($T_{\mathrm{H}} = T/T_{\mathrm{M}}$, T_{M} is the melting temperature) of olivine ($T_{\mathrm{H}} \cong 0.65$) and of eclogite ($T_{\mathrm{H}} \cong 0.95$), but also due to the higher temperature conditions of the transition (higher than 1500 K) to power-law dislocation creep in olivine at laboratory strain rates. It is noted that deviatoric stresses of eclogite estimated in this study are much lower than suggested by the previously reported flow law for eclogite, which significantly overestimated the stress sensitivity (Fig. 3.6-3, purple curve).

This study highlights the complexity in evaluating the flow strength of eclogite. Further experiments are necessary to reduce uncertainty in the flow law parameters of the mineral phases with careful consideration of pressure, temperature and solid solution compositions of the eclogite components. This study suggests that eclogite in the peridotite-dominated mantle may not necessarily exist as hard units or layers, and may affect mantle rheology by *e.g.*, placing an upper limit on the shear strength of the subducted oceanic crust.

c. *Experimental investigation of garnet nucleation and growth at high pressure under deviatoric stress (F. Heidelbach)*

Formation of garnet in high-pressure rocks such as eclogite and peridotite often provides constraints about pressure, and therefore depth conditions. Since diffusion of chemical

components is rather slow in garnet, its compositions are frequently used to determine pressure-temperature paths in metamorphic processes by assuming that garnet grows from a nucleus continuously at a constant rate to form roundish grains. In order to explore the nucleation and growth processes of garnet and the influence of concurrent deformation, we performed transformation experiments in simplified chemical systems, namely CaO-MgO-Al_2O_3-SiO_2 (CMAS) and CaO-MgO-Na_2O-SiO_2 (CMNAS) at high temperature and pressure.

In the CMAS system, we transformed a starting material representing spinel lherzolite into a garnet peridotite via the reaction of spinel + orthopyroxene + clinopyroxene → garnet + olivine for different durations at a pressure of 2.5 GPa and a temperature of 1100 °C under both static and deformed conditions. Garnet nucleated and then grew at the spinel-pyroxene interfaces (Fig. 3.6-5). Garnet gradually grew into pyroxene with time by consuming spinel through interdiffusion. Thickening of garnets, however, made diffusion distances longer and lowered the growth rate. As a result, rather large garnet grains contained small inclusions of spinel and clinopyroxene.

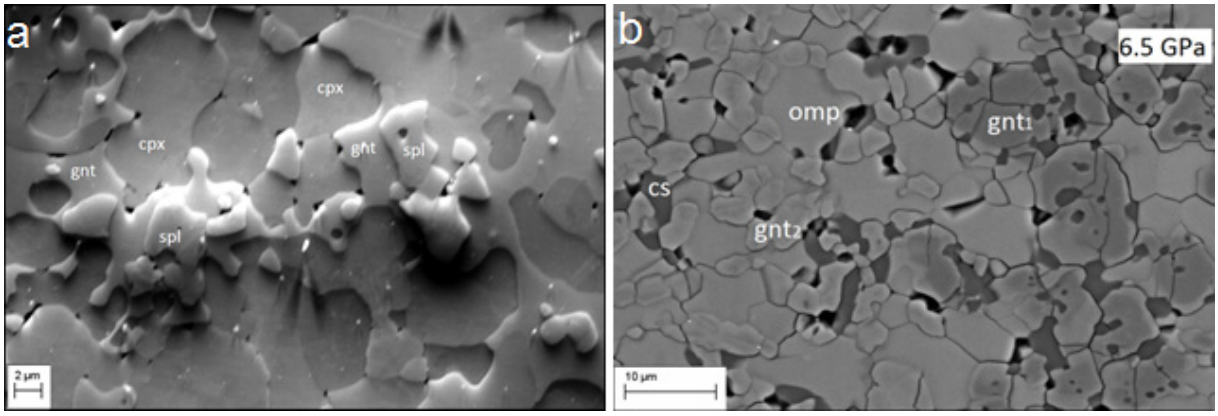

Fig. 3.6-5: a) Garnet growing around spinel gains in a sample statistically at 2.5 GPa and 1100 °C for 100 min in the CMAS system. b) Garnet formation in synthetic eclogite (CMNAS) transforming to garnetite by interdiffusion from omphacite (gnt1) and garnet nucleation and growth on omphacite grain boundaries (gnt2); run conditions 6.5 GPa, 1200 °C, 100 minutes run duration.

In the CMNAS system, we simulated the transition from eclogite to garnetite via dissolution of omphacite into garnet with increasing pressures. We found that increase in garnet fraction was achieved by rim growth of preexisting garnet (gnt1), and also by nucleation and growth of garnet newly formed on omphacite grain boundaries (gnt2) (Fig. 3.6-5). Compositions of both newly formed garnets are very similar with each other. They have higher CaO, Na_2O and SiO_2 contents than the original garnet. SEM-EBSD mapping of such samples revealed that seemingly separated nuclei of garnet on omphacite grain boundaries are three-dimensionally connected and showed relatively large amoeboid crystals enclosing omphacite and coesite (Fig. 3.6-6a). Due to these different formation mechanisms of garnet, some garnet grains are zoned (in case of overgrowth) or others are rather homogeneous in composition (in case of

nucleation at omphacite grain boundaries), even though their average compositions are similar. This fact is also seen from the chemical distribution maps of Ca (Fig. 3.6-6b). Ca distribution appears to be more correlated with the local growth environment rather than the bulk chemistry.

In both systems, the reaction rates increased when concurrent plastic deformation was imposed. Variations of microstructures by plastic deformation were, however, different between these systems. The garnet structure in the deformed CMAS samples displayed a continuous lattice bending indicated by a spread of orientations within one grain up to 15° with a rotational axis normal to the stress direction. This means that the garnet crystals are bent during the growth process. On the other hand, garnet grains in the deformed CMNAS samples showed no amoeboid structures, which was seen in the static samples, but rather compact roundish grains with clearly different orientations. It is likely that formation of garnet networks on grain boundaries was inhibited during the concurrent deformation, which was partly accommodated by grain boundary sliding. It is concluded that the structure and compositions of newly formed garnet during metamorphism are influenced not only by bulk chemistry, but also by grain structures and deformation mechanisms of reacting minerals.

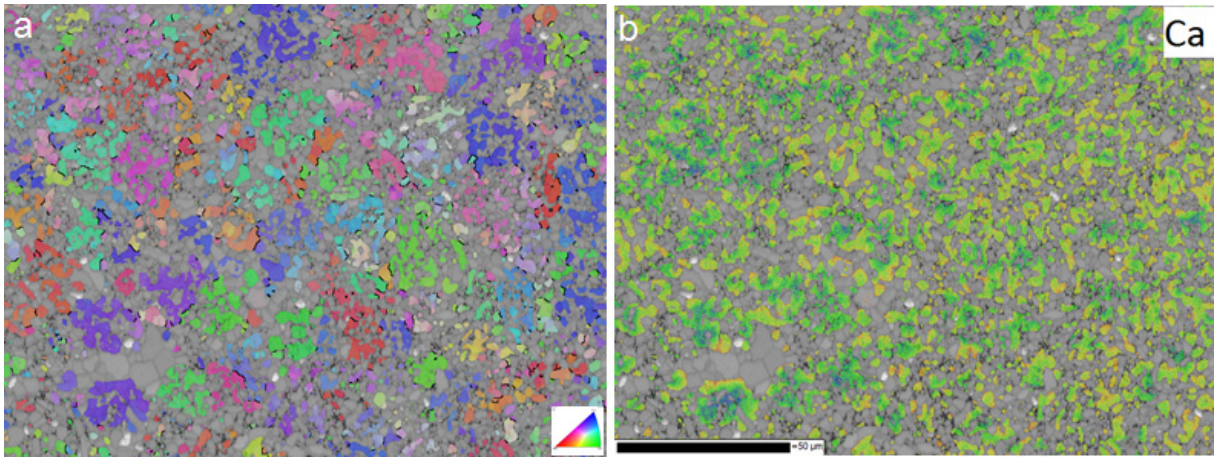

Fig: 3.6-6: a) An SEM-EBSD map showing garnet grain clusters in arbitrary orientation coloring; note larger clusters of seemingly separated garnet grains; b) An SEM-EDS map of Ca concentration in garnet for the same area; note the rather irregular distribution pattern due to the different formation mechanisms (*i.e.*, gnt1 and gnt2 of Fig. 3.6-5 b).

d. *Application of the Elasto-Viscoplastic Self Consistent (EVPSC) code to model texture and lattice strain evolution in periclase (F. Lin and L. Miyagi/Utah; H. Marquardt and J. Immoor; C. Tomé/Los Alamos; N. Hilairet and S. Merkel/Lille)*

Seismic anisotropy is observed in many regions of the lower mantle and is likely a result of plastic deformation of minerals by dislocation creep, which leads to grain rotations causing lattice-preferred orientation. In order to extract quantitative information about slip-system

activities from deformation experiments, especially conducted in DACs, numerical modelling is necessary. In this project, we applied the Elasto-Viscoplastic Self Consistent (EVPSC) approach to deformation data obtained using a deformation-DIA (D-DIA) apparatus, where deformation geometry and strain rate are better controlled than in DACs. After this benchmarking work, the EVPSC simulations will be applied to high-pressure and high-temperature deformation data collected in DACs in a radial diffraction geometry.

We focused our efforts on MgO, representative of the second most abundant mineral in the lower mantle, ferropericlase. It is well known that two main slip systems $\{110\}\langle 1\bar{1}0\rangle$ and $\{100\}\langle 011\rangle$ dominate deformation in periclase. In single-crystal MgO at ambient temperature and under high deviatoric stresses, critical resolved shear stresses (CRSS) for the $\{110\}\langle 1\bar{1}0\rangle$ slip systems are lower than the $\{100\}\langle 011\rangle$ slip system, making $\{110\}\langle 1\bar{1}0\rangle$ easier to glide.

Deformation experiments were performed in a D-DIA at the European Synchrotron Radiation Facility (ESRF) beamline ID06. Periclase was deformed at a pressure of 6 GPa and ambient temperature by pure shear to a total strain of 0.36 at average strain rates of 9.52×10^{-6}, 2.26×10^{-5} and 4.30×10^{-5} s^{-1}. Lattice strain and preferred orientation were obtained by means of *in situ* X-ray diffraction. Lattice strains were extracted using a software package Multi-fit/Polydefix and lattice preferred orientations were obtained by the Rietveld texture analysis with a software package Materials Analysis Using Diffraction (MAUD). During deformation, lattice strains on $\{200\}$ showed increase in strain in the early stage of the deformation followed by a fast drop upon further compression (Fig. 3.6-7). This could be caused by pinning by carbon introduced during sample sintering. Lattice strains on $\{200\}$ are significantly smaller than $\{111\}$ and $\{220\}$. Lattice strains on $\{220\}$ are slightly larger than $\{111\}$. It was also demonstrated that $\{100\}$ is concentrated in the direction of the pure shear with increasing total strain.

We tried to duplicate the above experimental results by means of the EVPSC simulation with an assumption of a high activity of the $\{110\}\langle 1\bar{1}0\rangle$ slip system. We optimized parameters such as CRSS for the various slip systems, strain hardening, initial grain shape and inclusion-matrix interaction for better duplication. As shown in Fig. 3.6-7, the EVPSC simulation with the assumed $\{110\}\langle 1\bar{1}0\rangle$ slip system almost perfectly duplicated the evolution of lattice strains of three crystallographic planes of $\{111\}$, $\{200\}$ and $\{222\}$. We also examined development of lattice preferred orientation by different slip systems, and demonstrated that high activity of $\{110\}\langle 1\bar{1}0\rangle$, $\{100\}\langle 011\rangle$ and $\{111\}\langle 110\rangle$ cause concentration of $\{100\}$, $\{110\}$ and also $\{110\}$, respectively, in the direction of pure shear. Thus, the concentration of $\{100\}$ shown by the deformation experiment implies a high activity of the $\{110\}\langle 1\bar{1}0\rangle$ slip system (Fig. 3.6-8).

We hope to simulate multiple sets of D-DIA data under different pressure and temperature range as well as diamond anvil cell results in order to quantify slip system activities at different pressure-temperature-conditions in the future. This knowledge will be applied for modelling seismic anisotropy observations in the lower mantle and depicting flow patterns in the deep Earth.

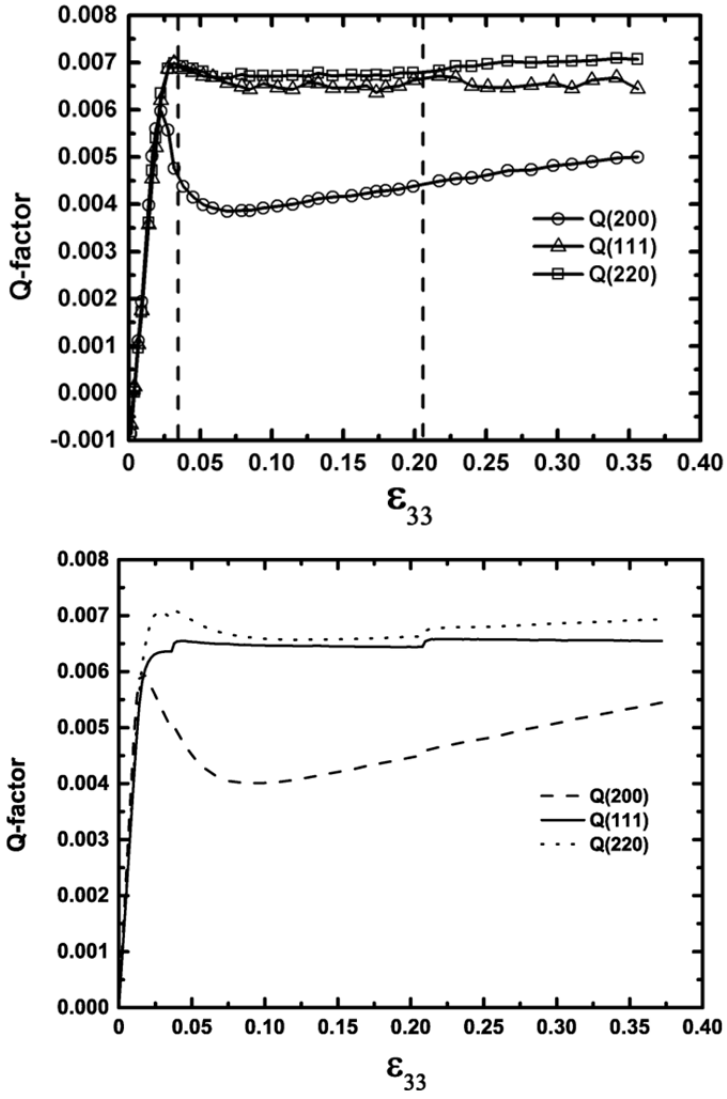

Fig. 3.6-7: Evolution of lattice strains (Q-factor) of (200), (111) and (200) planes against macroscopic strain $\mathcal{E}_{33}$. Top: Experimentally measured lattice strains. Bottom: Lattice strain evolution from the EVPSC simulation. Dashed lines indicate the strain where strain-rate was changed from 9.52×10^{-6} to 2.26×10^{-5}, then to 4.30×10^{-5} s^{-1}.

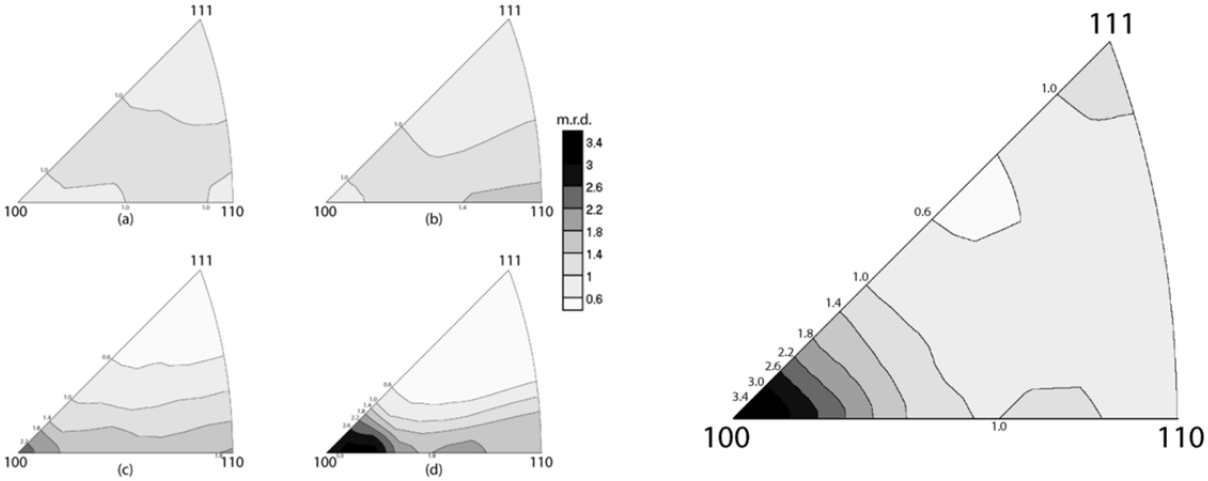

Fig. 3.6-8: Left: development of lattice preferred orientation of MgO in D-DIA experimental textures with increasing lattice strain. (a) 1 %; (b) 4 %; (c) 20 %; (d) 36 % strains. The {100} direction is more concentrated with increasing strain. Right: EVPSC texture modelling results for a fully activated $\{100\}\langle 1\bar{1}0\rangle$ slip system.

e. *Synthesis and experimental deformation of cubic $CaSiO_3$ perovskite in a resistive-heated diamond anvil cell (J. Immoor, H. Marquardt, L. Miyagi/Utah, S. Speziale/Potsdam and H.-P. Liermann/Hamburg)*

$CaSiO_3$ perovskite (Ca-Pv) is expected to be an important mineral in Earth's transition zone and lower mantle, where it is the third abundant minerals. In deeply subducted oceanic slabs, Ca-Pv may occupy up to 25 vol. % of basaltic crusts and will affect bulk rheological properties of lithospheric slabs. A recent computational study suggested that Ca-Pv shows a shear-wave anisotropy of 15 to 30 % under conditions of the lower mantle. Therefore, a strong lattice-preferred orientation of Ca-Pv may cause seismic anisotropy, in particular in the shallow parts of the lower mantle or the lower parts of the transition zone, where the intrinsic elastic anisotropy of Ca-Pv is stronger than in the deeper parts of the mantle.

Previous deformation studies on Ca-Pv have been limited to a pressure of 49 GPa and ambient temperature. At this temperature, Ca-Pv has a crystal structure with a tetragonal symmetry, whereas it has a cubic symmetry at temperatures typical for the lower mantle. Results from a recent computational study suggested lower shear moduli of cubic Ca-Pv than tetragonal Ca-Pv. Because the shear modulus is an indicator of plastic strength, lowering of shear modulus implies a reduction of plastic strength. Cubic Ca-Pv may exhibit different rheological properties from its tetragonal one, which was investigated in the previous study. Ca-Pv can be experimentally synthesized from $CaSiO_3$ wollastonite at pressures of about 20 GPa and temperature of about 1300 K, but is not quenchable to ambient conditions. This implies that studies of the physical properties of Ca-Pv need to be performed *in situ* and in the same pressure device used for its synthesis.

Here, powders of wollastonite were pressurized to about 40 GPa in customized Mao-Bell-type DACs without any pressure-transmitting medium using a gas membrane system. Ca-Pv was then synthesized by heating to temperatures higher than 1400 K using a resistive-heater made of graphite. Pressures determined by *in situ* X-ray diffraction using an internal pressure standard of platinum dropped by more than 10 GPa, once Ca-Pv started to grow. After synthesizing cubic Ca-Pv, the samples were deformed by further compression, and were measured by radial X-ray diffraction (Fig. 3.6-9), where the DAC was placed with the diamond axis normal to the incident X-rays, so that strain and textural development can be monitored. Experiments were performed at the Extreme Conditions Beamline (ECB) at PETRA-III, DESY. We collected experimental data at pressures up to 45 GPa and temperatures of 1600 K. The maximum pressure was limited to this pressure due to diamond failure. Collected data will be combined with the Elasto-Viscoplastic Self-Consistent (EVPSC) simulation to extract slip system activities of Ca-Pv, which can then be used to model seismic anisotropy in the uppermost lower mantle.

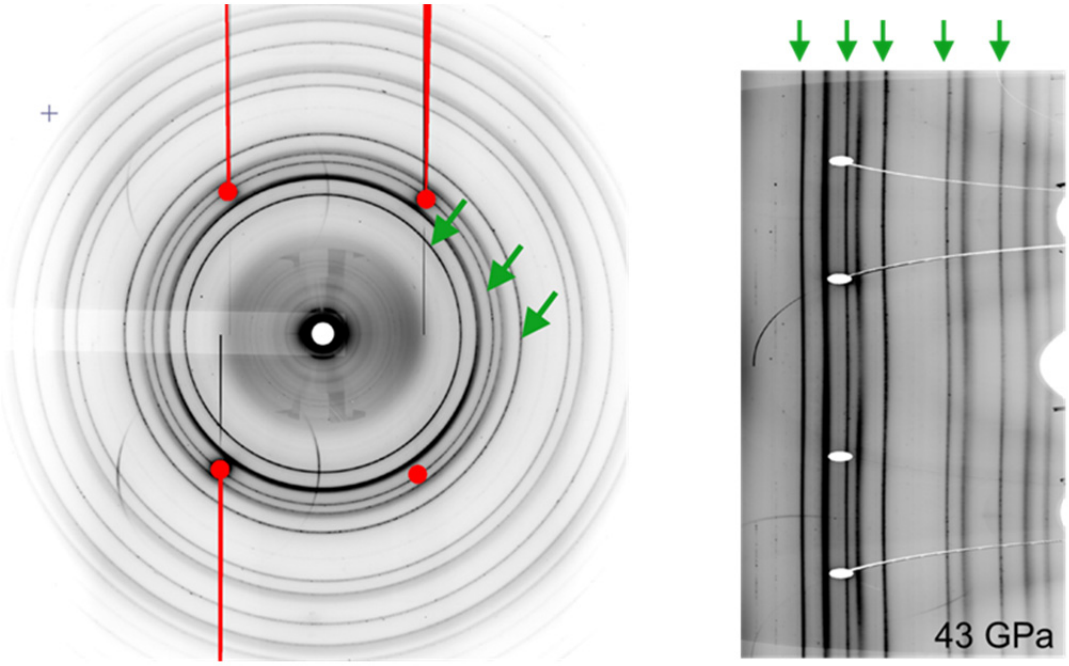

Fig. 3.6-9: Left: a powder X-ray diffraction pattern collected at a pressure of 27 GPa and a temperature of 1300 K after synthesis of $CaSiO_3$ perovskite (Ca-Pv) from wollastonite. All visible lines are from either cubic Ca-Pv or the pressure marker of platinum. Selected lines from Ca-Pv are highlighted by green arrows. The red areas mask Laue spots of diamond. Right: an unrolled diffraction image after deformation of cubic Ca-Pv at 1300 K. Green arrows highlight the diffraction lines from Ca-Pv. The curvatures of the lines are a measure of accommodated elastic strains, whereas intensity variations along the lines result from the lattice preferred orientation.

f. *High-temperature deformation experiments of (Mg,Fe)O ferropericlase at lower-mantle pressures (J. Immoor, H. Marquardt, L. Miyagi/Utah, S. Speziale/Potsdam and H.-P. Liermann/Hamburg)*

The lower mantle is dominated by bridgmanite and ferropericlase, along with $CaSiO_3$ perovskite. Deformation experiments have suggested that the creep strength of ferropericlase is lower than bridgmanite, and therefore it should accommodate the majority of bulk strain by deformation. As a result, ferropericlase may form an interconnected network and dominate lower-mantle rheology in high-strain regions. Recent deformation experiments at ambient temperatures suggested that the plastic strength of ferropericlase increases by a factor of 3 at pressures between 25 and 65 GPa. It has also been proposed that ferropericlase with lattice-preferred orientation may account for seismic shear wave anisotropy in the lowermost mantle. Slip system activities under high-pressure and high-temperature conditions need to be understood in order to examine this hypothesis. Previous experimental deformation studies at pressures of the lower mantle were, however, mostly limited to room temperature due to experimental difficulty. In this project, we determined slip systems of ferropericlase at temperatures up to 1700 K and pressures up to 79 GPa.

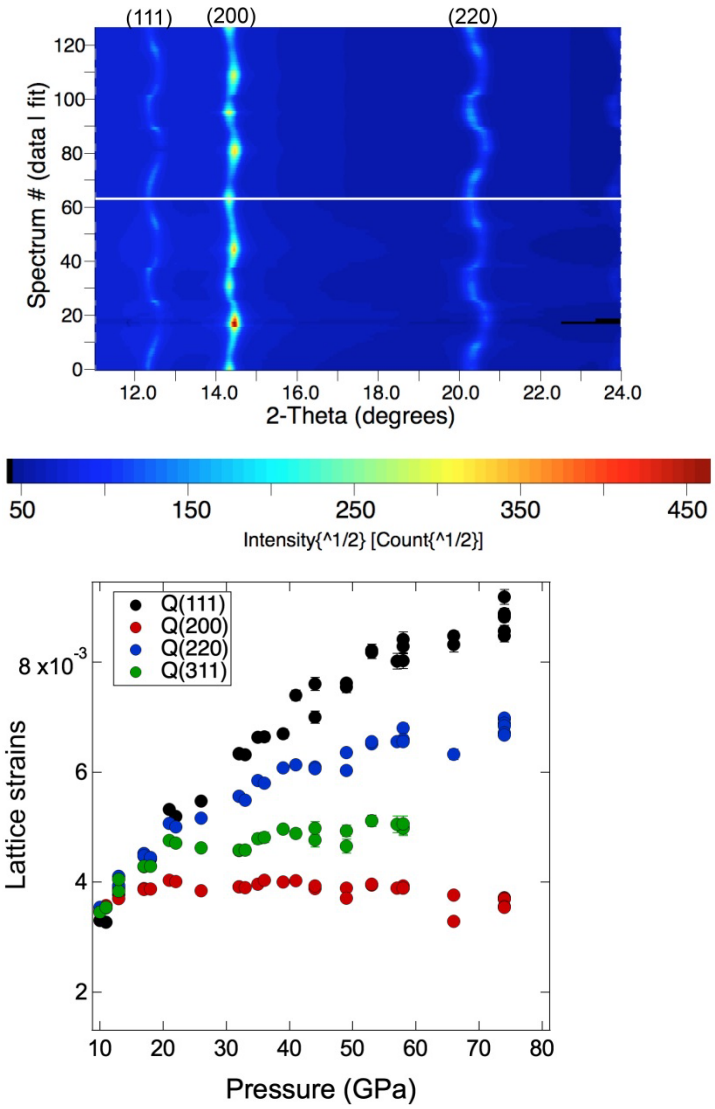

Fig. 3.6-10: Top: An unrolled radial X-ray diffraction pattern of ferropericlase at 75 GPa and 1150 K, showing differential strains indicated by curvature of the Debye rings and texture indicated by intensity variations along the Debye rings. Bottom: experimentally derived lattice strains of ferropericlase at a temperature of 1150 K as a function of pressure.

Deformation experiments were performed at the extreme conditions Beamline (ECB) in PETRA-III at DESY using *in situ* X-ray diffraction on powdered ferropericlase in a graphite resistive-heated DAC at simultaneously high pressures and high temperatures. The powders were loaded in customized Mao-Bell DACs with X-ray transparent amorphous or cubic boron nitride gaskets without any pressure-transmitting medium in order to enhance differential stress and resultant lattice-preferred orientation. Angle dispersive X-ray diffraction was conducted in a radial geometry using a Perkin Elmer detector in order to monitor stress and lattice-preferred orientation developed during compression. Pressure in the DAC was increased during heating using a gas-membrane device (Fig. 3.6-10). The limiting factor of this experiment is usually breakage of diamonds upon pressure increase at high temperatures.

Preliminary results at a pressure of 75 GPa and a temperature of 1150 K indicate no visible change in lattice-preferred orientation caused by pressure increase. On the other hand, significant changes in lattice strains were clearly observed during pressure increase. Determination of active slip systems requires detailed modelling of the experimental results by using the Elasto-Viscoplastic Self-Consistent (EVPSC) Code. Our results demonstrate that the strength of ferropericlase increases with increasing pressure at high temperatures, which is consistent with the former experimental results at ambient pressure (Fig. 3.6-11).

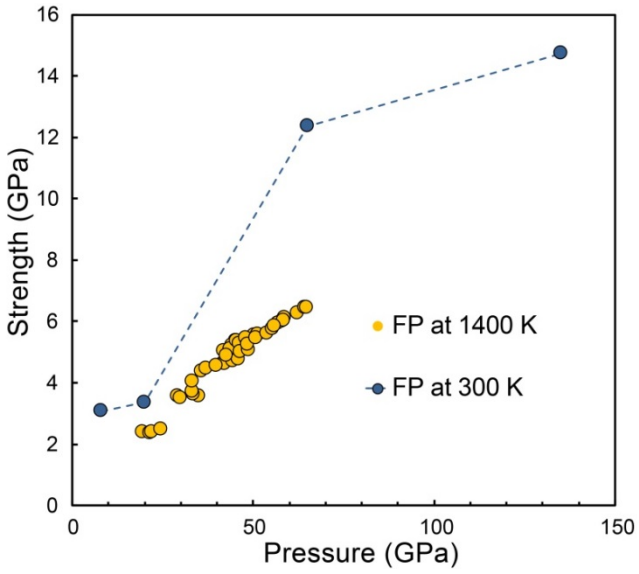

Fig. 3.6-11: Strength of ferropericlase at ambient temperature and at a high temperature of 1400 K against pressure. The strength increases with pressure at both temperatures. The strengths at high temperature are lower than at ambient temperature, as expected.

g. *Investigation of the behaviour of grain boundaries in response to deviatoric stress fields at high pressure and temperature (C. Bollinger, R. Farla, P. Knödler/Bayreuth and K. Marquardt)*

Plate tectonics is driven by large-scale convective motions in the upper mantle, in which olivine dominates by 60 % in volume. Olivine has a strong elastic anisotropy, which may be responsible for seismic anisotropy in the upper mantle down to 410-km depth. It is usually considered that the anisotropy is produced by dislocation creep in olivine grains.

Contributions of networks such as grain boundaries, triple junctions, and quadrupole junctions to deformation are generally ignored. Some experiments suggested that not only creep of crystals but also relative displacement between adjacent grains account for deformation of olivine aggregates. Previous studies particularly demonstrated the existence of a deformation regime with linear stress sensitivity and grain size dependence, which can be attributed to dislocation accommodated by grain boundary sliding (Dis-GBS). Hence, grain boundaries could play an essential role in deformation of polycrystalline olivine and grain boundary sliding will be an important deformation mechanism in addition to diffusion and dislocation creep. The contribution of this mechanism to bulk rock deformation is a function of grain size, strain rate, temperature and others. Therefore, we developed the following novel experimental technique to investigate effects of these factors on grain boundary sliding.

Samples for investigation were forsterite aggregates synthetized by flash sintering from oxide powders. The initial grain sizes ranged from 20 to 100 μm. Cylinders with 1.5 mm in length and 1.5 mm in diameter were cored from the forsterite aggregates. To follow and characterize strains, the cylinders were cut in the middle, and grids were engraved on the cutting faces using a focus-ion-beam (FIB). These grids were used as strain markers to measure displacements between adjacent grains. EBSD mapping provided orientations of grains and consequently planes of grain boundaries before deformation experiments.

Deformation experiments were performed on dry samples in molybdenum capsules in a pure shear geometry at pressures of 3 to 6 GPa and temperatures of 900 °C to 1300 °C, which correspond to physical conditions in the uppermost mantle, and a stain rate of 10^{-5} sec^{-1}, using a 6-ram multianvil apparatus. After the deformation experiments, distortions of grid markers in recovered samples were observed using SEM to measure relative displacement between adjacent grains as a response to applied constant displacement rates. Relative displacement should be a function of grain-boundary plane orientation, and therefore, EBSD examination was conducted to determine the change in interfacial relations associated with deformation.

Figure 3.6-12 shows an example of an experiment. Distortion of the grid by the deformation experiment can be clearly observed. Results will be analyzed using micromechanical modelling, including the contribution of grain-boundary sliding to deformation of olivine aggregates, to ultimately understand the contribution of grain-boundary sliding to mantle viscosity.

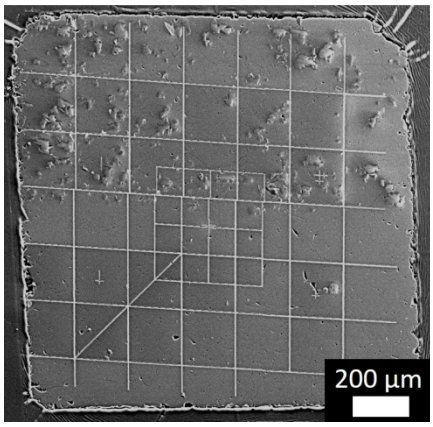

(a)

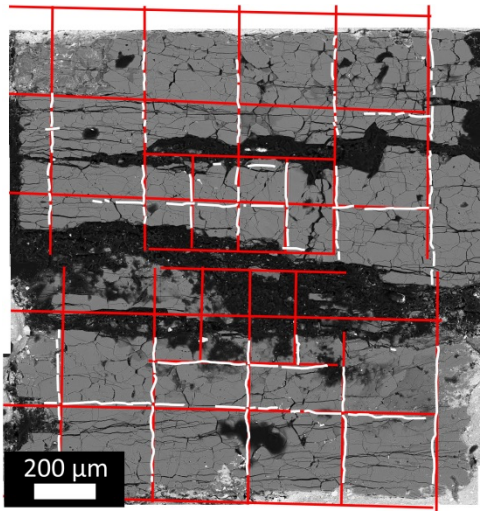

(b)

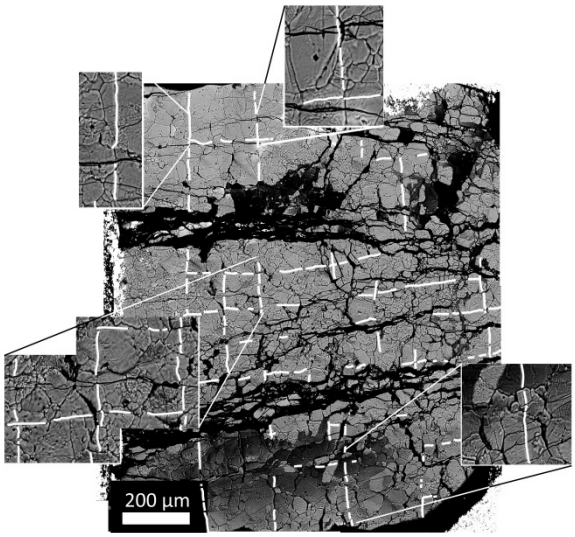

(c)

Fig 3.6-12: a) A secondary electron image of a sample with a grid width of 200 nm and intervals of 200 and 100 µm engraved by FIB before deformation. The oblique line was used as a reference. b) A back-scattered electron image of a sample after deformation at a pressure of 5 GPa, a temperature of 1100 °C and a strain rate of $2.0x10^{-5}$ s^{-1}. The total strain is 28 %. A supposed initial grid is drawn with red color, and the grid after deformation is with white color. c) A back- scattered electron image of the same starting sample as b) deformed at higher temperature of 1250 °C. The other conditions were identical. Some parts are zoomed.

h. *Self-diffusion coefficients in forsterite grain boundaries – insights from classical molecular dynamics simulations (J. Wagner/Potsdam, O. Adjaoud/Darmstadt, K. Marquardt, S. Jahn/ Köln)*

Deformation behaviour of minerals is based on diffusion, thus the latter has been the objective of many studies on olivine, due to its dominance in the upper mantle. Nevertheless, studies on grain boundary (GB) transport give controversial results. To solve these discrepancies we investigate the energy and geometry of individual GBs with the ultimate goal to understand transport in aggregates with lattice preferred orientation (LPO) where the presence and/or alignment of specific GBs over random GB distributions of undeformed rocks are favoured. Classical molecular dynamics simulations of a series of symmetric and one asymmetric tilt GBs of Mg_2SiO_4 (forsterite), ranging from 9.58° to 90° in misorientation and varying surface terminations were performed. Understanding structural characteristics of high and low angle grain boundaries and how the atomic structure influences grain boundary energy and self-diffusion processes lies at the heart of this study. Different GB geometries were generated by equilibration of the respective systems at ambient pressure and temperatures from 1900-2200 K, their evolution was traced for run durations of at least 1000 ps to extract self-diffusion rates. The mean square displacement of the different atomic species within the GB interface was traced and self-diffusion coefficients in their individual systems could be calculated. The GB self-diffusion coefficients for Mg and Si range from 10^{-18} to 10^{-20} m^3/s in agreement with extrapolations from low-temperature experimental data. These new data support that higher GB excess volumes enable faster diffusion rates; these two entities are positively correlated (Fig. 3.6-13). Furthermore, (self-) diffusion in dislocation cores which form for example low angle grain boundaries shows a strong anisotropy. Contrasting, diffusion in high angle grain boundaries is direction independent. Classical MD simulations are a viable tool to study diffusive processes within grain boundaries provided that long trajectories can be calculated.

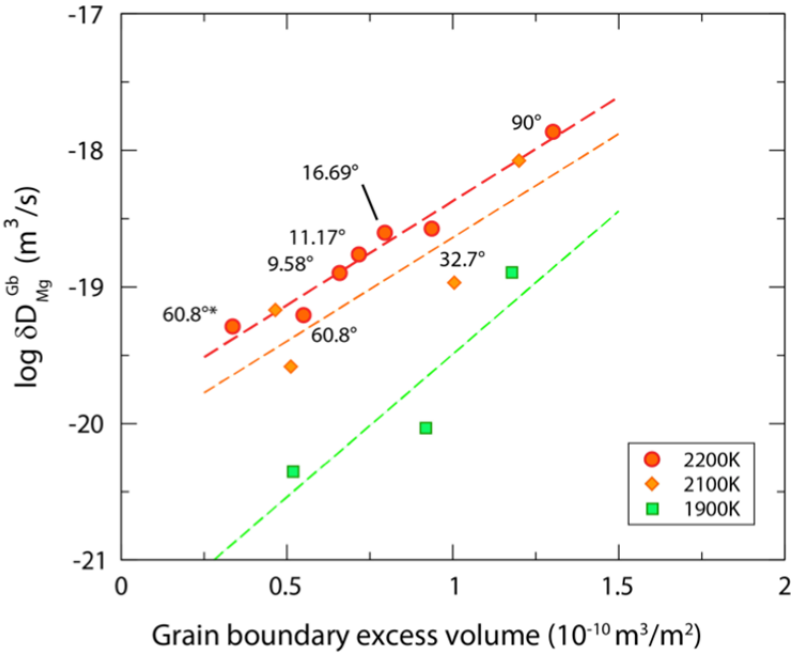

Fig. 3.6-13: Magnesium grain-boundary diffusion coefficient as a function of grain boundary excess volume at temperatures of 1900, 2100 and 2200 K. Dashed lines denote linear fit to the results of numerical simulation. *Asterisk* indicates results of simulation with asymmetrical grain boundaries.

i. *Silicon self-diffusion coefficient in wadsleyite as a function of water content (D. Druzhbin, T. Kawazoe, H. Fei, D.J. Frost and T. Katsura)*

Convection of the Earth's mantle results from plastic deformation of rocks, which is mainly driven by three mechanisms: diffusion creep, dislocation creep, and grain-boundary sliding. Both diffusion and dislocation creep at high temperatures are believed to be controlled by atomic diffusion. Hence, investigation of atomic diffusion of mantle minerals is vital for understanding mantle flow. Silicon is the slowest diffusing species in the majority of mantle minerals, and therefore considered rate-limiting for their creeps at high temperatures.

Wadsleyite, a high-pressure polymorph of olivine, is the most abundant mineral in the upper part of the mantle transition zone (410-520 km). Deformation experiments suggested that water incorporation significantly increases creep rates of wadsleyite. However, such experiment was conducted under many orders of magnitude higher stress conditions than that in the Earth's interior, which may cause misinterpretation. Diffusion experiments may solve this problem, because it is performed under hydrostatic conditions. The purpose of this work is to obtain silicon self-diffusion coefficient (D_{Si}) of wadsleyite, as a function of water concentration ($C_{\mathrm{H_2O}}$).

In order to avoid grain-boundary diffusion, measurement of diffusion coefficients should be conducted using single crystals. As reported previously, single crystals of both Fe-free and -bearing wadsleyite were already successfully synthesized. The crystals were oriented and polished on faces parallel to a (100), (010) or (001) plane using ¼-μm diamond powder and then alkali colloidal silica. The crystals were examined by etching using hydrofluoric acid diluted by acetic acid after alkali colloidal silica polishing to confirm that layers mechanically damaged by diamond powder were completely removed. ^{18}O- and ^{29}Si-enriched Mg_2SiO_4 thin films with thickness of 300-400 nm were deposited on the polished faces of Fe-free wadsleyite crystals using a pulsed laser deposition facility at Ruhr-Universität Bochum. For Fe-bearing samples, thin films with ^{18}O- and ^{29}Si-enriched $(Mg,Fe)_2SiO_4$ composition were produced.

Trial runs of diffusion annealing were conducted with careful design of sample environment explained below (Fig. 3.6-14). Crystals were embedded in dense CsCl pellets as a mechanical buffer to avoid crystals from mechanically breaking during compression. Usage of welded platinum capsules prevented wadsleyite crystals from significant dehydration. A serious problem was that roughness of crystal surfaces significantly increased and reached more than 600 nm during diffusion annealing. Such roughness does not allow measurement of diffusion profiles, because the expected diffusion lengths are less than 500 nm. A number of trial runs were made to suppress the surface roughness, and the following procedure was established. (1) Crystal faces must be exactly parallel to one of the major crystallographic planes. If not, a step-like structure would form. (2) Crystals must be placed on smooth faces of a hard material

(diamond disks in the present case). Without such hard faces, small crystals grow and develop crystallographic faces with rough surfaces. (3) Crystals on diamond disks must be wrapped by gold foil, without which fluid phases of water plus CsCl may intrude between the wadsleyite and diamond crystals to attack the surfaces of thin films on wadsleyite faces.

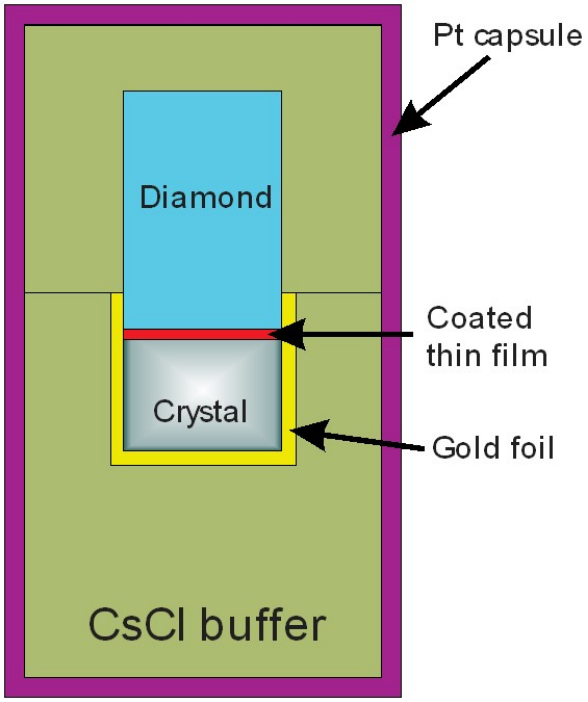

Fig. 3.6-14: A schematic drawing of a cross-section of a sample environment designed for diffusion annealing experiments.

j. *Negative water-content dependence of the dislocation mobility in the olivine [001](100) slip system (L. Wang, T. Kawazoe, N. Miyajima and T. Katsura)*

Deformation experiments on olivine suggest that water enhances the olivine creep rate significantly, in proportion to the 1.2 power of the water content. In addition, olivine fabric changes from A-type to E-type and then to C-type with increasing water content. However, the results from deformation experiments may have been biased by large stress conditions and the existence of free water on grain boundaries, which are not the case in the asthenosphere. In addition, recent Si self-diffusion experiments suggest that the water effect on olivine creep may be much smaller than that mentioned above. For better understanding of the water effects on rheology of mantle minerals, we conducted dislocation recovery experiments on olivine as a function of water content. Since the C-type fabric is dominant at high water content, we focused on the [001](100) slip system in this study.

Olivine single crystals were first annealed at dry/wet conditions so that olivine water contents ranged from 7 to 170 wt. ppm. Then, these crystals were simple-sheared to the [001] direction on the (100) plane to activate the target slip system at a pressure of 5 GPa and a temperature

of 1473 K under dry/wet conditions. The deformed olivine crystals were annealed under the same conditions for durations of 6 to 16 h to annihilate dislocations. In all annealing experiments, the olivine crystals were enclosed with graphite powder as a soft material to avoid their breakage. To produce dry/wet environments during annealing, different amounts of mixtures of talc and brucite were added. Dislocation densities before and after annealing were measured on the (001) planes by the oxidation-decoration technique using an SEM. The dislocation-annihilation rate constant (k) was obtained from the following equation, $k = (1/\rho_f - 1/\rho_i)/t$, where ρ_i and ρ_f are the dislocation densities before and after annealing, respectively, and t is the annealing time.

An example of the change in density of [001](100) dislocations is shown in Fig. 3.6-15. The dislocation-annihilation rate constants are shown against water content in Fig. 3.6-16. It was assumed that the dislocation mobility is proportional to the annihilation rate constant. Therefore, the water content dependence of dislocation mobility and annihilation rate constant should be identical. By fitting the data to the power law, the water-content exponent of dislocation mobility was found to be $r = -0.5(1)$. Therefore, water decelerates dislocation motion in olivine, instead of enhancing it. In addition, the fabric transition in olivine suggested by deformation experiment may be impossible in the real mantle.

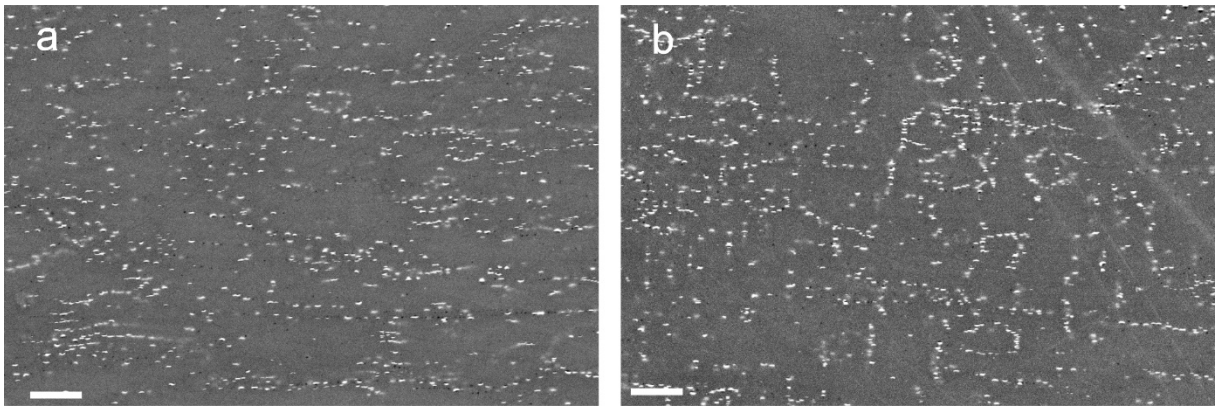

Fig. 3.6-15: Backscattered electron images of the oxidation-decorated olivine. The bright spots are expected to indicate the presence of dislocations. The scale bars denote 2 μm. (a) Before annealing. (b) After annealing. The water content before and after annealing was 161 wt. ppm H_2O. Annealing time was 8.5 h.

Dislocation mobility should be controlled by two factors, namely, shear modulus and dislocation core structure. Since incorporation of water does not change elastic moduli of olivine significantly, one possibility of negative water dependence of dislocation mobility is that water incorporation may change dislocation core structures. This needs to be examined by transmission electron microscopy (TEM) study as the next step.

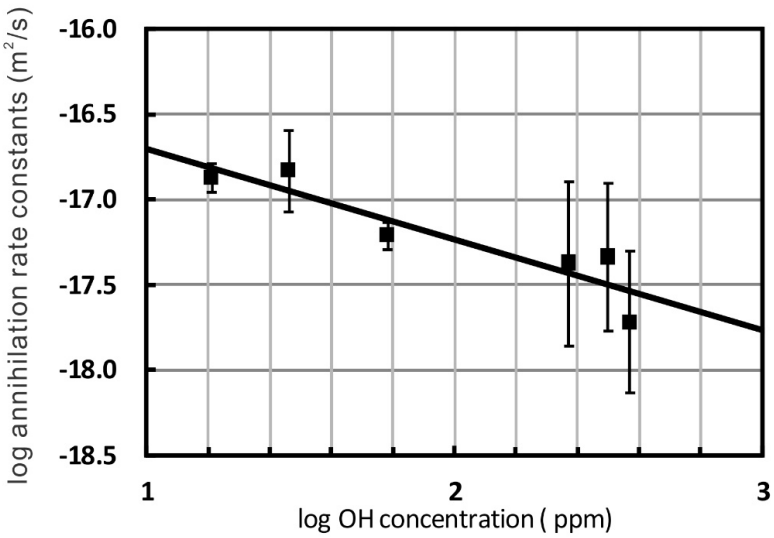

Fig. 3.6-16: Dislocation annihilation rate constants (k) in the [001](100) slip system against different water contents.

3.7 Materials Science

High-pressure material science, on the one hand, and mineral physics and petrology, on the other hand, not only share common synthesis methods, but also joint theoretical toolkits and methodologies of *in situ* investigations. The Bayerisches Geoinstitut combines scientists with unique experience and skills that work in both fields – Earth and materials sciences – and through their experience in mineral physics are also prepared to address challenging problems of solid state physics and chemistry, at the forefront of modern high-pressure material sciences.

Fe_4O_5 provides an example where a discovery first made in mineral sciences has subsequently become an important cornerstone of high-pressure materials research. Its discovery at high pressure as a new mixed valence Fe-oxide paved the way to the synthesis of a wide variety of unexpected iron oxides, while itself remaining an interesting subject of research, similar to the classical mixed valence example, Fe_3O_4 magnetite. Single-crystal high-pressure diffraction, combined with measurements of transport and magnetic properties of Fe_4O_5, reveals that it undergoes a unique charge-ordering transition below 150 K that involves competing Fe-dimers and trimers, ordered within chains of Fe ions. In particular, this electronic transition drives an intricate incommensurate distortion of its crystal structure.

The B-C and P_3N_5-P_2O_5 systems form similarly complex families, members of which are investigated here. They are important for their potential as ultra-hard phases and their extreme chemical stability, respectively. Both studies report *in situ* measurements in the diamond anvil cell. The structure and stability of $B_{13}C_2$ is examined by single-crystal X-ray diffraction and optical spectroscopy. Contrary to predictions, $B_{13}C_2$ is found to remain stable and not to change structure up to pressures beyond 70 GPa. Similarly, single crystal X-ray diffraction is performed on PON. In this study, a complex series of compression mechanisms are detected that show the transition from a framework to a close-packed structure by tetrahedra tilting alone.

In situ experiments under compression on two organic compounds follow, again performed in the diamond anvil cell: *simple* propane C_3H_8 and two complex metal-organic framework compounds. Propane, which is an important component of natural gas condenses to a solid at cryogenic temperature. The compression behaviour of this solid alkene is investigated by Raman spectroscopy. Three phase transitions can be observed below 40 GPa. They are associated with skeletal C-C and CH_2-CH_3 stretching, as well as CH_3 deformation.

Metal-organic framework (MOF) compounds show great potential as a new generation of multiferroic materials that can be used in multistate devices. Through the huge flexibility of their organic framework, different metal ions can be incorporated into the MOF to tune physical properties. Nevertheless, the structure-property relations remain poorly understood, and high-pressure studies can shed some light on them. By combining X-ray diffraction,

Mössbauer and Raman spectroscopy the polarity of the metal ions in the compounds can be characterized as a function of pressure and conclusions are drawn that can guide the design of dense MOFs, both at ambient and high pressure.

The final two contributions in the section deal with the high-pressure behaviour of a different material class, metals. Both contributions use computational techniques to look at properties of iron. With the failure of early density functional theory methods to correctly predict the stable phase of Fe at ambient pressure, high-pressure phase transitions, and the high-pressure equation-of-state for the hcp phase, iron has become a cornerstone in testing newly developed density functionals. Here, a newly developed method that accounts for exact electronic exchange is applied to compute the compression behaviour of the hcp phase, to test whether this approach can overcome the deficiency of other approaches. However, this is not the case which suggests that electronic correlations or magnetism play a significant role in the compression behaviour of hcp iron, despite ambiguous experimental evidence. Finally, molecular dynamics simulations, using a combination of density-functional-based and classical potential methods, are used to compute the structure of liquid Fe. The results presented pave the way towards an improved characterization of the compressibility of liquid iron at high pressure.

a. *A new type of charge-ordering transition in the novel iron oxide, Fe_4O_5 (S.V. Ovsyannikov, M. Bykov, E. Bykova, D.P. Kozlenko/Dubna, A.A. Tsirlin/Augsburg, A.E. Karkin and V.V. Shchennikov/Yekaterinburg, S.E. Kichanov/Dubna, H. Gou/Beijing; A.M. Abakumov, R. Egoavil and J. Verbeeck/Antwerp, C.A. McCammon; V. Dyadkin and D. Chernyshov/ Grenoble, S. van Smaalen/Bayreuth and L.S. Dubrovinsky)*

At ambient pressure, only three iron oxide polymorphs have been described: FeO, Fe_3O_4, and Fe_2O_3. Recently, several new iron oxide polymorphs with hitherto unknown stoichiometries, such as Fe_4O_5, Fe_5O_6, Fe_5O_7, Fe_7O_9, $Fe_{25}O_{32}$, have been prepared by means of high-pressure high-temperature (HP-HT) synthesis or discovered *in situ* at high-pressure conditions. These findings suggest the existence of a whole new class of iron oxide polymorphs to be uncovered. Among them, Fe_4O_5 looks particularly exciting since it can be readily quenched and it persists at ambient conditions as a metastable polymorph. This circumstance enables detailed investigations of its physical properties and suggests possible industrial applications along with the conventional iron oxides.

Using the multianvil presses at BGI we synthesized large polycrystals and microscopic single crystals of Fe_4O_5 at 15-20 GPa and 1300-1500 °C and investigated their properties. We have shown that below 150 K Fe_4O_5 undergoes a new type of charge-ordering phase transition involving the formation of competing dimer and trimer ordering within the chains of the octahedrally-coordinated Fe ions. This transition was probed by a single crystal X-ray diffraction (Fig. 3.7-1), by neutron diffraction, as well as by measurements of electrical

resistivity and magnetic susceptibility (Fig. 3.7-2). To date, such exotic and puzzling transitions have not been documented in any other materials. Thus, the phase transition discovered in Fe_4O_5 brings new perspectives on charge-ordered states in mixed-valent iron compounds and, in general, presents a new prototype of transitions related to charge-ordering.

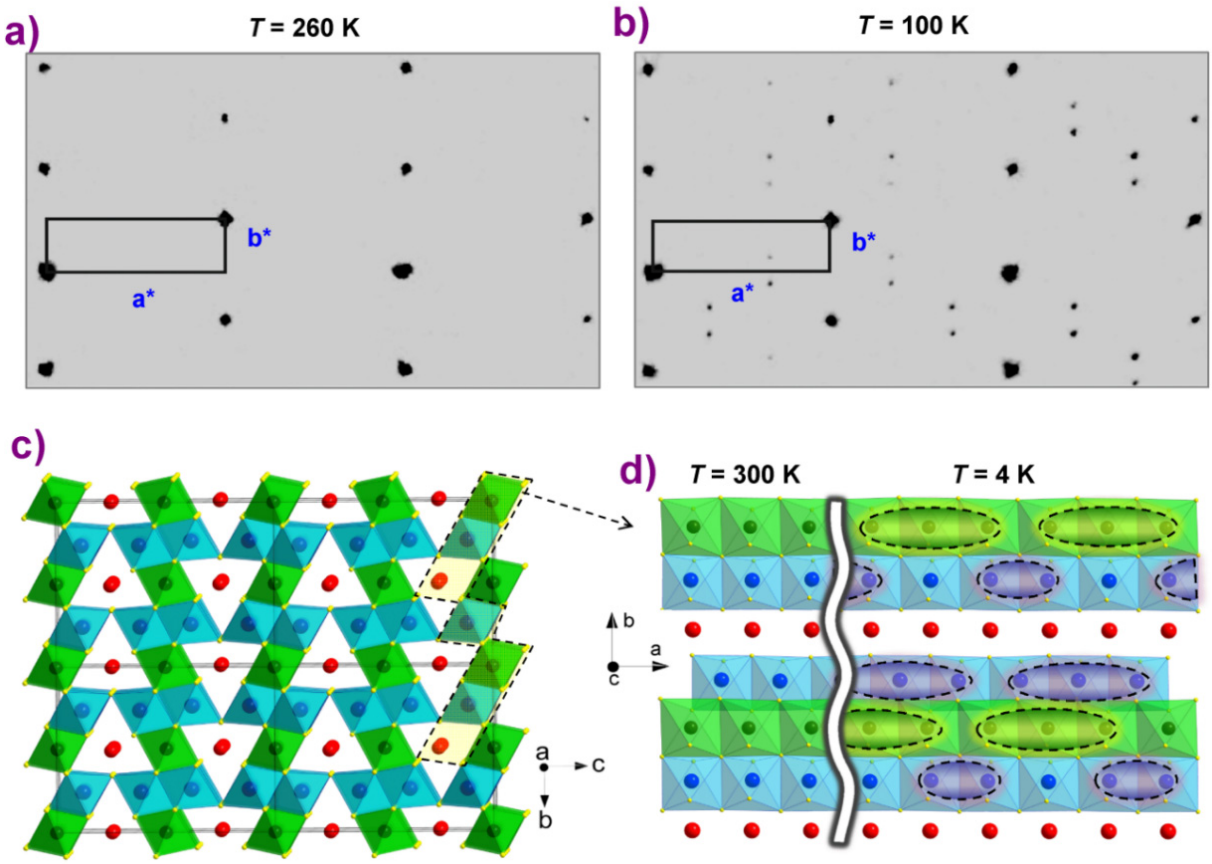

Fig. 3.7-1: Examples of reciprocal lattices of X-ray diffraction intensities of Fe_4O_5 at 260 K (***a***) and 100 K (***b***). *a** and *b** are the axes of the reciprocal lattice. (***c***) The crystal structure projected down the *a*-axis at room temperature. (***d***) The crystal structure projected down the *c*-axis at room and low temperatures. The low-temperature structure demonstrates the preference for dimer or trimer ordering in different Fe chains.

Recovered Fe_4O_5 crystallizes in a $CaFe_3O_5$-type crystal structure featuring linear chains of octahedrally-coordinated iron ions occupying two crystallographic positions, and linear chains of FeO_6 trigonal prisms along the *a*-axis (Fig. 3.7-1, c). This compound contains equal amounts of Fe^{2+} and Fe^{3+} ions, and similar to other mix-valent iron oxide, *e.g.*, magnetite (Fe_3O_4) it is a good electrical conductor (Fig. 3.7-2, a), owing to a charge transfer between Fe^{2+} and Fe^{3+}. Magnetite is known to undergo a charge ordering phase transition below ~ 125 K at which its electrical resistivity abruptly jumps by about two orders of magnitude. This transition in magnetite has been discovered by Verwey in 1939, but only recently the elusive charge ordering pattern in the low-temperature phase of Fe_3O_4 has been uncovered by means of single-crystal X-ray diffraction. It has been revealed that the charge ordering in magnetite

involves ‘three-site-distortions’, called ‘trimerons’. An analysis of the bond valence sums in the crystal lattice of Fe_4O_5 (Fig. 3.7-1, c) suggests that the octahedrally-coordinated iron ions have the average charges as of +2.7, whereas the cations in the prisms have the average charge as +1.92. In other words, the prisms are occupied by ferrous iron, while the octahedral positions host mixed valence states of Fe. Therefore, one should expect Fe_4O_5 to also undergo charge ordering at low temperatures.

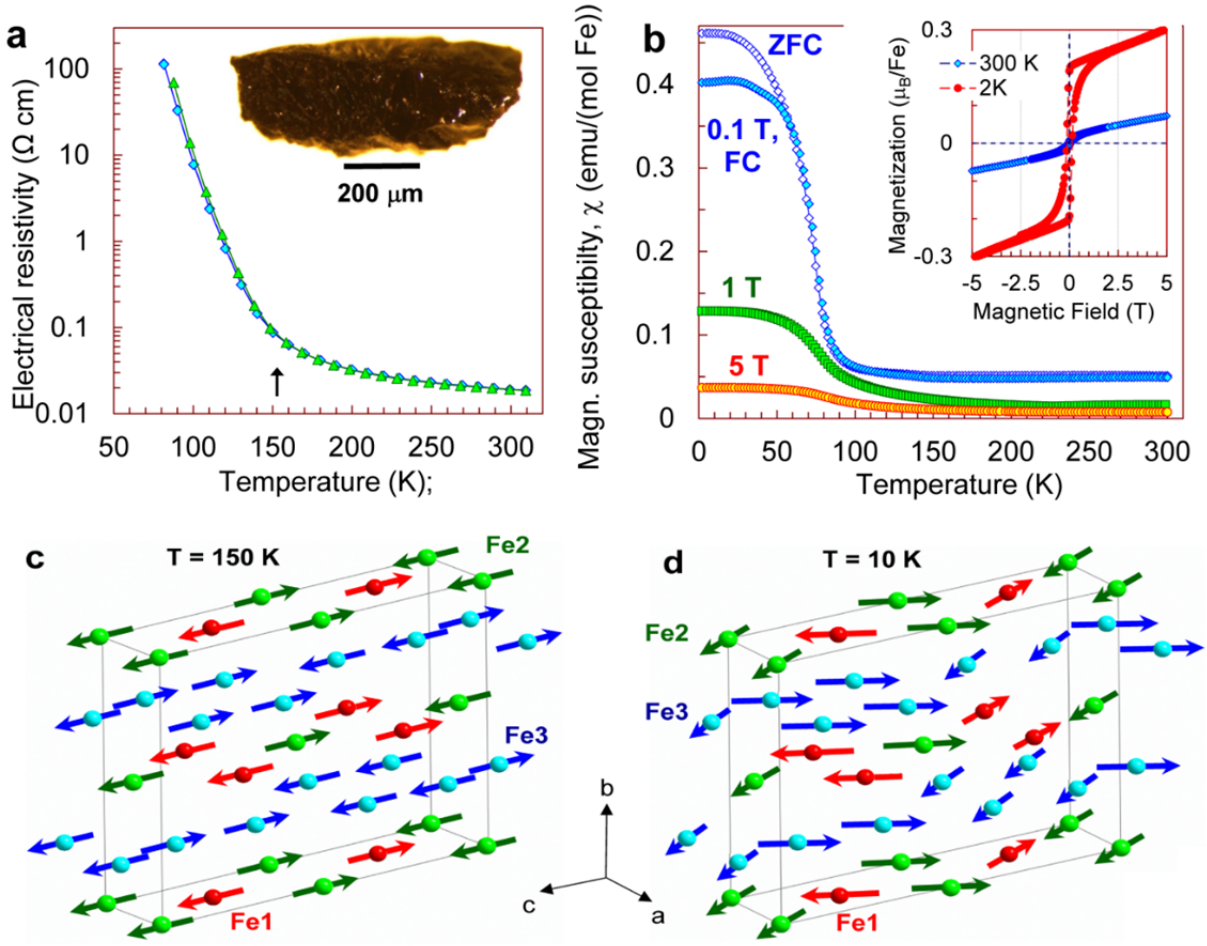

Fig. 3.7-2: Temperature-dependence of electrical resistivity (***a***) and magnetic susceptibility (***b***) of bulk samples of Fe_4O_5 measured at ambient pressure in different magnetic fields. The magnetic structures of Fe_4O_5 determined at two temperatures from neutron diffraction experiments, are shown in (***c***, ***d***). The insets in (***a***) and (***b***) are a photograph of a quasi-single crystalline sample and two magnetization curves of Fe_4O_5, respectively.

We collected high-quality single crystal X-ray diffraction for Fe_4O_5 at the SNBL beamline of ESRF. These data unambiguously demonstrated the appearance of superlattice reflections upon cooling below 150 K (Fig. 3.7-1, b). Indexing these superlattice reflections revealed that this structure is incommensurately modulated. We found that the main features of this transition in Fe_4O_5 involve the formation of Fe dimers and trimers within the chains of the

octahedrally-coordinated iron along the *a*-axis (Fig. 3.7-1, d). Meanwhile, the chains of the ferrous iron were only weakly modulated along the *c*-axis. A constant Fe-Fe distance of ~ 2.861 Å (at 4 K) in the triangular prismatic chains of the ferrous iron in the low-temperature structure (Fig. 3.7-1) serve as a reference point, enabling us to highlight the dramatic shortening of some inter-octahedra distances – marked by elongated ellipsoids in Fig. 3.7-1 (d). Each chain of the octahedral cations contains either dimers or trimers. The bond-valence-sum analysis suggests that the trimers are composed of one Fe^{2+} and two Fe^{3+} ions, similar to the trimerons in Fe_3O_4. The Fe ions in the dimers have an oxidation state of about +2.5, *i.e.*, the dimers are Fe^{2+}-Fe^{3+} pairs with one shared electron.

This unusual charge-ordering transition in Fe_4O_5 is concurrent with a significant increase in electrical resistivity (Fig. 3.7-2, a), and hence it may be described as of a "metal-insulator" type. The magnetic susceptibility measurements showed an abrupt transition to a ferrimagnetic state below 85 K (Fig. 3.7-2, b). The neutron diffraction studies established the formation of a collinear antiferromagnetic order above room temperature (Fig. 3.7-2, c) and a spin canting at 85 K (Fig. 3.7-2, a) that gives rise to the spontaneous magnetization observed in the magnetic susceptibility measurements (Fig. 3.7-2, b).

b. *High-pressure investigation of $B_{13}C_2$ single crystals (I. Chuvashova, E. Bykova, M. Bykov, L.S. Dubrovinsky, N.A. Dubrovinskaia/Bayreuth, V. Svitlyk/Grenoble; B. Gasharova and Y.-L. Mathis/Karlsruhe)*

Boron carbide is one of the most widely used hard materials, surpassed only by diamond and boron nitride. Due to its high melting point and thermal stability, high abrasion resistance, extreme hardness and low density, boron carbide is used for manufacturing shielding powders and coatings, and applied as energy absorbers for dynamic protection. Mechanical properties of boron carbide and limits of its stability under loading are thus of both scientific and practical interest for ballistic applications. Computations predicted a phase transition in boron carbide at 25 GPa, which may explain why it is destroyed upon dynamic tests at about this pressure. Recent XRD structural and Raman spectroscopy investigations of single crystals indicate a phase transition near 40 GPa that contradicts other experimental reports. Thus the question of structural stability of $B_{13}C_2$ under high pressure requires further investigation.

In the present work we study the behaviour of boron carbide of a stoichiometric composition, $B_{13}C_2$, under pressure using high-purity single crystals synthesized at high pressure and temperature in the large volume press. The crystals were placed into BX90-type diamond anvil cells with diamonds of culet diameters of 250 μm and neon as a pressure-transmitting medium. A single crystal of $B_{13}C_2$ has dark red or maroon color at ambient conditions that did not change upon compression up to 40 GPa at room temperature; further pressurization led to loss of color and full transparency of the crystal. This phenomenon is not explained so far.

Boron carbide is built of B_{12} icosahedra located in the corners of the rhombohedral unit cell and inter-icosahedral linear chains of three atoms oriented along its body diagonal. Single-

crystal X-ray diffraction data was collected at the beamline ID27 at the ESRF. The crystal structure of $B_{13}C_2$ was refined in the pressure range up to 68 GPa, and the bulk modulus of $B_{13}C_2$ was found to be K = 239(7) GPa, whereas the bulk modulus of individual B_{12} icosahedra appeared to be K_{ico} = 234(7) GPa. These values are very similar (Fig. 3.7-3).

IR and Raman spectroscopy investigations were partly stimulated by the interesting observation of the change of the optical properties of the single crystal upon compression as mentioned above. Infrared spectroscopy studies were done at ANKA Synchrotron Facility, Karlsruhe, Germany, up to 73 GPa at room temperature. The Raman spectra were collected *in house* on decompression of the same cell from 73 GPa. Vibrational properties of $B_{13}C_2$ investigated by IR and Raman spectroscopy gave evidence of the structural stability of the boron carbide within the pressure region studied. No evidence of a phase transitions in $B_{13}C_2$ was found.

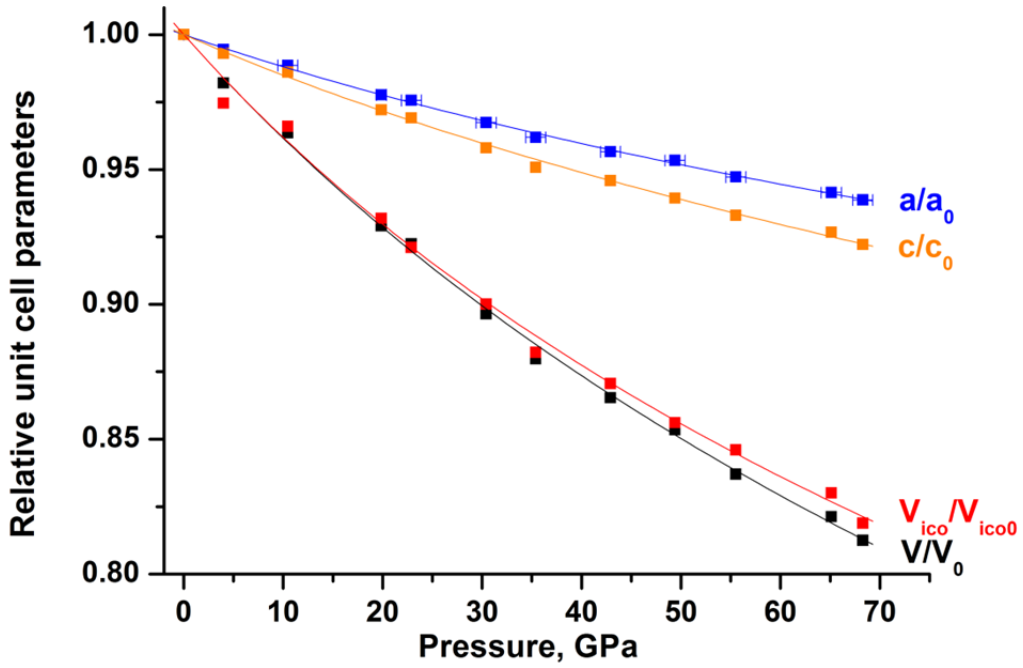

Fig. 3.7-3: Pressure-dependent evolution of unit cell volume, lattice parameters and volume of B_{12} icosahedra of $B_{13}C_2$ single crystals based on high-pressure single-crystal XRD data. Continuous lines show the fit of the pressure-volume data with the third-order Birch-Murnaghan equation of state.

c. *Anomalous compression of cristobalite-like phosphorus oxonitride (M. Bykov and E. Bykova; D. Baumann and W. Schnick/Munich; M. Hanfland/Grenoble; N.A. Dubrovinskaia/Bayreuth and L.S. Dubrovinsky)*

The pseudo-binary system P_3N_5/P_2O_5 has been investigated intensively because the properties of related ceramic materials are promising for industrial applications. A mid-member of this

system is phosphorus oxonitride (PON), whose chemical stability is essential for its use as an insulator or fireproofing material. This compound has attracted significant attention as a ternary base compound of electrolytes for rechargeable thin-film Li/Li-ion batteries. Phosphorus oxonitride is an isoelectronic analogue of silica (SiO_2) with the charge-balanced substitution $P^{5+} + N^{3-} = Si^{4+} + O^{2-}$. The crystal structures of the polymorphic forms of SiO_2 and PON are built of tetrahedral SiO_4 and PO_2N_2 units, respectively. At present, five modifications of PON have been identified. Four of them are isostructural to known silica polymorphs, α-quartz, β-cristobalite, moganite and coesite. The fifth one, δ-PON, has a structure type different from any of the silica modifications.

We have studied the high-pressure behaviour of *cri*-PON by means of single-crystal X-ray diffraction at 16 pressures in a range from 0.0001 to 55 GPa. The compression mechanism of *cri*-PON appears to be nontrivial. First of all, *cri*-PON possesses negative linear compressibility along the *c*-axis. Furthermore, the volume-pressure data cannot be adequately described by any available third-order equation of state. The compression of *cri*-PON can only be described by an EoS of at least fourth-order. Refined parameters for the fourth-order Birch-Murnaghan EoS are K_0 = 59.8(7) GPa, K_0' = 1.78(17), K_0'' = 0.054(5) GPa^{-1}. The anomalous positive value of K'' means that the rate, at which *cri*-PON becomes stiffer, increases with increasing pressure, which is unusual for standard materials.

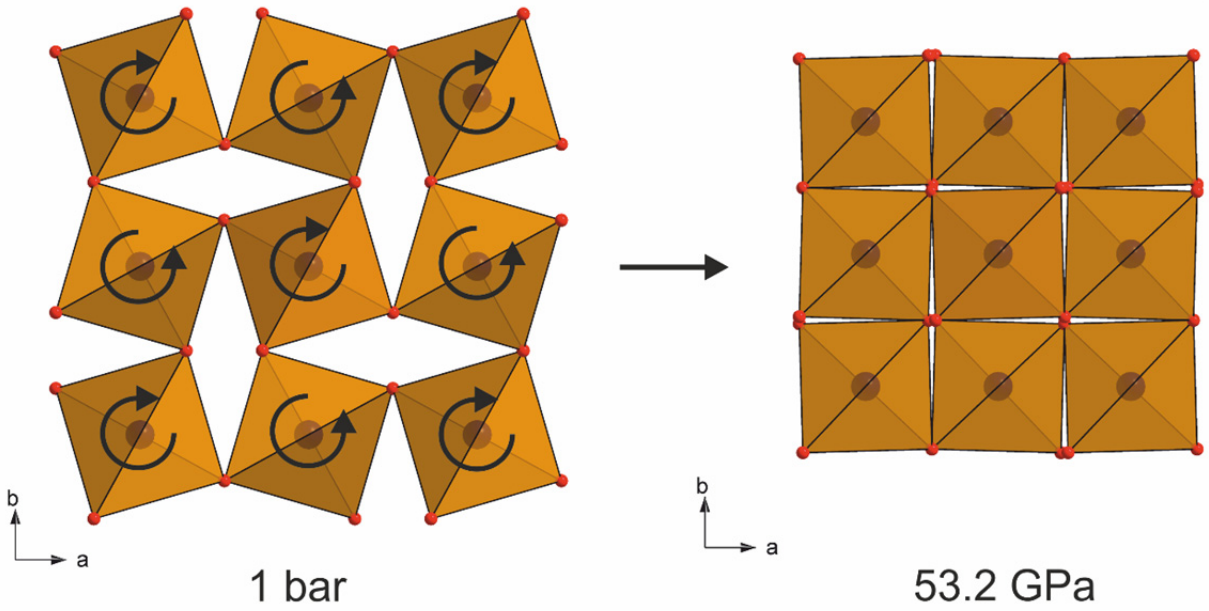

Fig. 3.7-4: Illustration of the compression mechanism of *cri*-PON.

At ambient conditions *cri*-PON has a distorted β-cristobalite structure. With increasing pressure the topology of *cri*-PON continuously changes towards a so-called collapsed cristobalite structure (Fig. 3.7-4). Below 25 GPa, the compression involves only tetrahedral

tilting with negligible changes of the intertetrahedral P-(O,N) distances. Only above 25 GPa, changes in the P-(O,N) distances start to play a noticeable role in the overall compression. At 53 GPa, the total change in the volume of P-$(O,N)_4$ tetrahedra is 5 %, while the total unit cell volume change is 35 %. The compression of *cri*-PON is an example of the collapse of a framework structure to a close-packed form in a continuous manner without an intervening phase transition. Such polyhedral tilting mechanisms are of great importance in determining the physical and thermodynamic properties of these ordered solids and result in continuous rather than abrupt changes in these properties. These processes may also play a role in the densification of glasses and amorphous solids.

d. *New phases of propane at pressure up to 40 GPa (D. Kudryavtsev and A. Serovaiskii/ Moscow, L.S. Dubrovinsky, V. Kutcherov/Stockholm)*

Propane, the three-carbon alkane, occurs in the gas phase at ambient conditions and is an important constituent of natural gas, used as a fuel for engines, blowtorches and domestic purposes, refrigeration agent, aerosol propellant, and feedstock for petrochemical industry. The wide range of thermodynamic conditions at which propane occurs in the universe warrants that it is studies at various pressures and temperatures. The high-pressure behaviour of hydrocarbons attracted significant attention in recent years most of all in connection with theory of petroleum of abiogenic origin and chemical stability. However, for propane only limited data up to 6 GPa is available.

We studied propane at pressures up to 40 GPa at ambient temperature using Raman spectroscopy. Vibrational, and particularly Raman, spectroscopy can serve as a powerful tool for investigation phase relations in hydrocarbons and may provide valuable information about intermolecular interactions in the condensed phases.

In our experiments, propane was loaded cryogenically in a BX-90-type diamond anvil cell, made from synthetic CVD type IIa diamonds with a culet size of 250μm. A rhenium gasket was indented to thickness of 35 μm, and a hole of 110 μm in diameter was drilled in the center, forming a cylindrical sample chamber. The Raman spectra were excited using He-Ne laser (632.8 nm) and were acquired by LabRam spectrometer with 2 cm^{-1} spectral resolution. Pressure was measured using the ruby gage.

Raman spectra of propane in the range 800 - 3250 cm^{-1} at different pressures are shown in Fig. 3.7-5. In spite of the simple chemical composition of C_3H_8, solid propane possesses a sufficient number of Raman bands reflecting the complexity of its internal vibrations. Still, our observations are limited due to Raman scattering of diamond anvils (the 1200-1400 cm^{-1} and 2100-2700 cm^{-1} regions are dominated by a diamond first- and second-order peak, respectively), and the weakness of lattice vibration modes below 800 cm^{-1}.

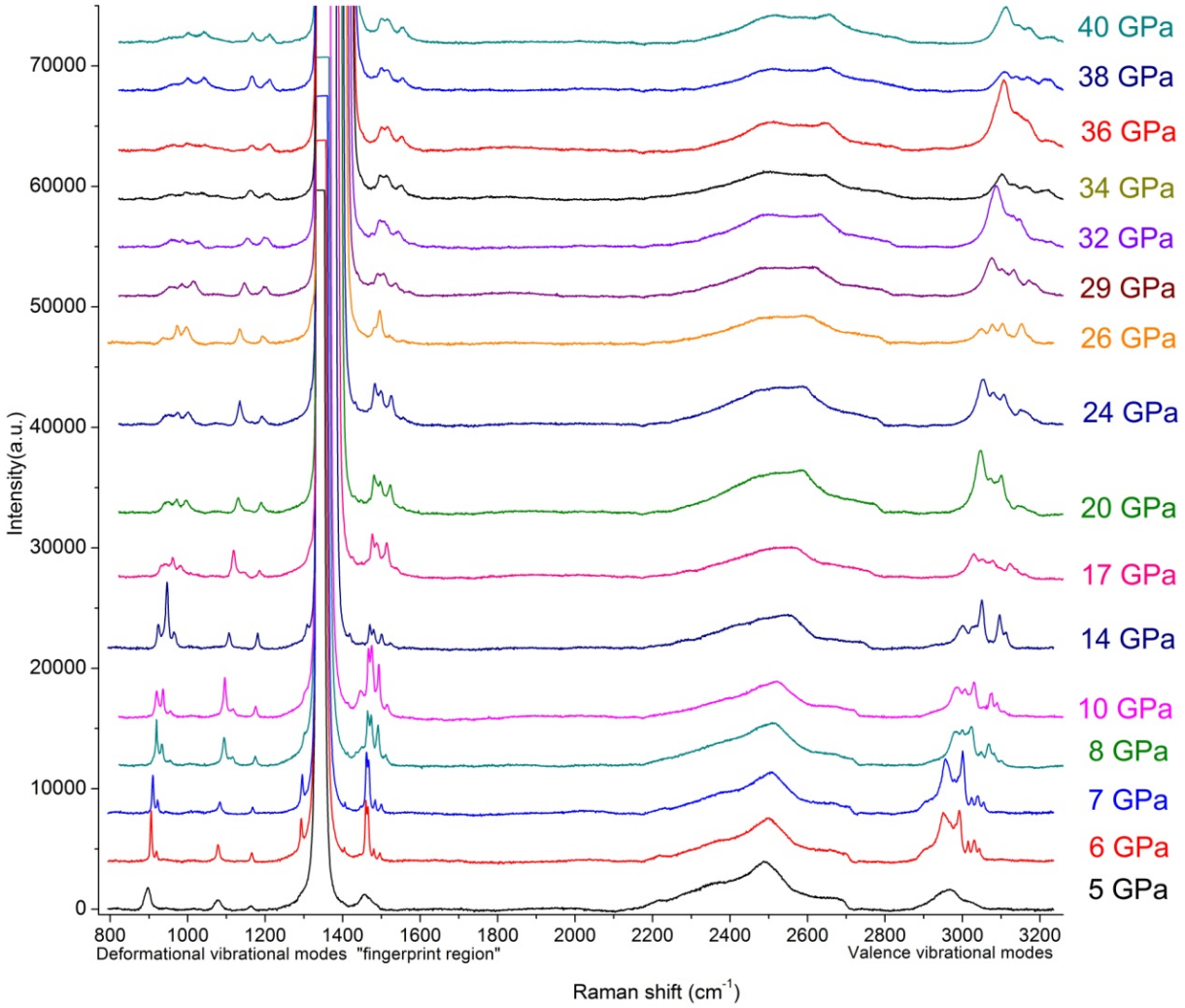

Fig. 3.7-5: Raman spectra of propane recorded at ambient temperature and at high pressures.

Directly after loading, pressure in the DAC was about 4 GPa. An analysis of the spectra suggests three phase transitions at about 6, 14, and 26 GPa. At 6 GPa, we can see a considerable change in the character of the spectra, especially among the symmetric skeletal C-C stretching mode (~ 860 cm^{-1}), CH_3 deformational modes (both symmetric and asymmetric ~ 1400-1450 cm^{-1}), and the modes of CH_2/CH_3-stretching (both symmetric and asymmetric) in the region of valence vibrations. The low-intensity bands of different vibrational modes become more distinct when comparing the Raman spectrum of propane at 5 and 6 GPa. At 14 GPa the doublet at ~ 860 cm^{-1} splits further, while other vibrational modes become less intense and less sharp, which can also be related to a phase transition. The last observed distinct mode change appears at 26 GPa, especially pronounced in the region of CH_3 deformational modes (~ 1400-1450 cm^{-1}).

e. *Structure-property relationships in multiferroic metal-organic frameworks at high pressure (I.E. Collings/Bayreuth, M. Bykov, E. Bykova, S. Petitgirard, D. Vasiukov/Bayreuth, C.A. McCammon, M. Hanfland/Grenoble, S. van Smaalen/Bayreuth, L.S. Dubrovinsky, N.A. Dubrovinskaia/Bayreuth)*

Dense metal–organic frameworks (MOFs) show promise for a new generation of multiferroic materials, which have technological importance in sophisticated multistate devices. MOFs present several advantages over already known multiferroic ceramic materials, such as increased framework flexibility, a vast chemical diversity, and numerous host–guest interactions. These characteristics could lead to increased ferroelectric responses and guest-tuned multiferroic properties. However, so far the study of multiferroic MOFs is in its infancy, and a much greater understanding of the structure–property relationships is needed in order to direct the design of functional multiferroic MOFs.

The dense MOF families of ammonium metal formates, $[NH_4][M(HCOO)_3]$, and di-methyl-ammonium metal formates, $[(CH_3)_2NH_2][M(HCOO)_3]$ (Fig. 3.7-6), have shown great potential for multiferroic behaviour at low temperatures. We perform high-pressure experiments on the MOFs in order to determine structure–property relationship for improving the ferroelectric and magnetic response in these materials.

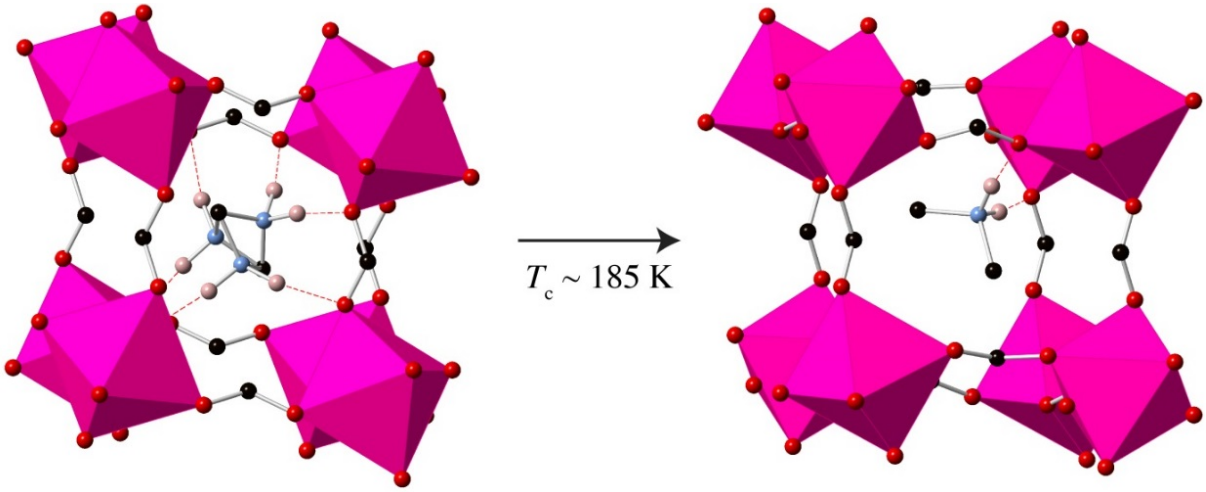

Fig. 3.7-6: Ferroelectric phase transition of $[(CH_3)_2NH_2][Mn(HCOO)_3]$ upon cooling, creating a uniaxial electric dipole. Hydrogen bonds are shown in dotted red lines, and Mn^{2+} octahedral coordination is represented by polyhedra.

High-pressure single-crystal X-ray diffraction (performed at ESRF), Raman and Mössbauer spectroscopy (both performed at BGI) were carried out on $[NH_4][M^{II}(HCOO)_3]$ and $[(CH_3)_2NH_2][M^{II}(HCOO)_3]$ (where M = Fe or Ni). For $[NH_4][M(HCOO)_3]$ we observe that the metal formate is susceptible to distort at very low pressures (below 1.5 GPa), creating a

polar high-pressure phase (Fig. 3.7-7). From the diffraction data, we observe that the ammonium cations in the pores are displaced because of the distortion of the framework, giving rise to polarity in the structure, but that with increasing pressure the polarity decreases due to greater packing efficiency achieved in a non-polar atomic arrangement. The transition pressure can be tuned by using different transition metal cations, where larger metal cations give lower transition pressures. Furthermore, we observe that the transition can be suppressed by using a pressure-transmitting medium that can enter into the pores of the metal-formate framework, such as neon.

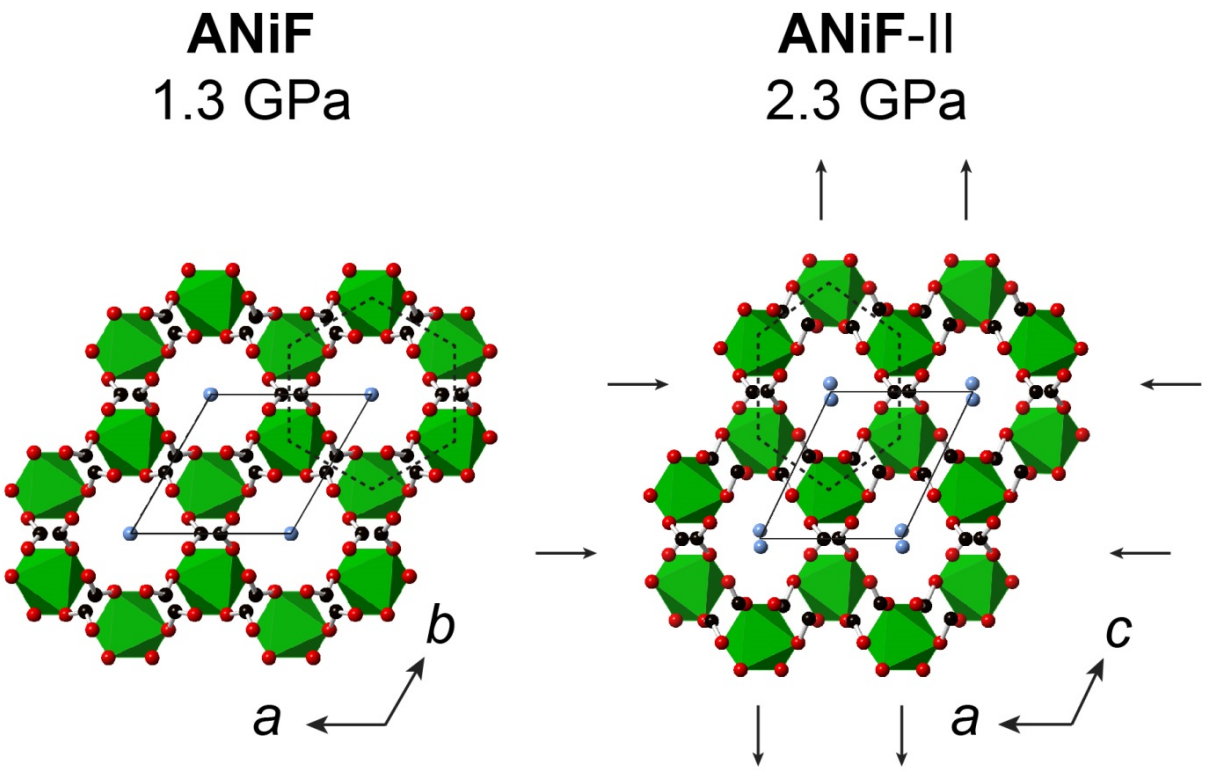

Fig. 3.7-7: Structural distortions that occur in the upon the high-pressure phase transition of $[NH_4][Ni(HCOO)_3]$.

The high-pressure measurements on the $[(CH_3)_2NH_2][Fe(HCOO)_3]$ compound showed that the compound exhibited much greater resistance to pressure, remaining in its ambient phase up to 7 GPa. The greater stiffness of $[(CH_3)_2NH_2][Fe(HCOO)_3]$ compared to $[NH_4][Fe(HCOO)_3]$ is due to the bulkier di-methyl-ammonium cation within the framework pores and the different structural topology it adopts. High-pressure Raman spectroscopy suggests that the high-pressure phase above 7 GPa involves both distortions to the iron formate framework and the di-methyl-ammonium cation. The Mössbauer spectroscopy experiments showed that a local iron environment in the high-pressure phase is similar to the low-temperature ferroelectric phase, suggesting that the dynamic disorder of the di-methyl-ammonium becomes frozen at high pressure.

f. *Adiabatic connection fluctuation-dissipation (ACFD) theory-based equation-of-state of hcp iron (G. Steinle-Neumann and V. Vlček)*

The large discrepancy in equation-of-state estimates for hcp iron between experiments and computations based on density functional theory (DFT) have been a source of concern for more than 20 years, putting the question of magnetism in hcp Fe at the center of attention. While computations within DFT using generalized gradient approximations (GGA) to exchange and correlation (xc) find a stable magnetic structure at P < 50 GPa, there is – at best – ambiguous indication of magnetism from experiments.

Typical functionals of representing xc are based on (semi-)local approximations and lead to systematic errors, such as the self-interaction error or the inaccurate description of negative ions, with the potential not showing an asymptotic 1/r Coulomb decay. Adiabatic connection fluctuation-dissipation (ACFD) theory provides – in principle – an exact evaluation of xc energy within DFT. In ACFD theory the Hartree xc energy E_{Hxc} is separated into E_H, and an exact evaluation of E_x, based on the KS wavefunctions, plus the ACFD formulation of E_c. For evaluation of E_c, the random phase approximation is used that ignores the xc kernel in evaluating the ACFD integral. Here we perform calculations on the equation-of-state of non-magnetic hcp iron to test whether within the ACFD theory the description of hcp Fe improves when compared to experiments. The importance of local correlation in the binding of hcp iron has been pointed out previously, and computations with dynamic mean field theory (DMFT) have been shown to significantly improve the description of physical properties of various Fe phases by parameterizing a local Coulomb interaction term to correctly describe the magnetic properties of bcc iron at ambient pressure.

In agreement with the DMFT results we find that the equilibrium volume of hcp Fe from the ACFD computations is expanded significantly when compared to non-spin-polarized results using GGA, at the same level as magnetism does within DFT-GGA (Fig. 3.7-8). However, the compressibility does not decrease appreciably to bring DFT-based computations in closer agreement with experiments, unlike the DMFT results. Our results imply that hcp iron (i) has to be considered a strongly-correlated material as suggested by the good agreement of the DMFT results using a local correlation correction with experiments or (ii) that magnetism plays an important role in its physical behaviour.

In agreement with the DMFT results we find that the equilibrium volume of hcp Fe from the ACFD computations is expanded significantly when compared to non-spin-polarized results using GGA, at the same level as magnetism does within DFT-GGA (Fig. 3.7-8). However, the compressibility does not decrease appreciably to bring DFT-based computations in closer agreement with experiments, unlike the DMFT results. Our results imply that hcp iron (i) has to be considered a strongly-correlated material as suggested by the good agreement of the DMFT results using a local correlation correction with experiments or (ii) that magnetism plays an important role in its physical behaviour.

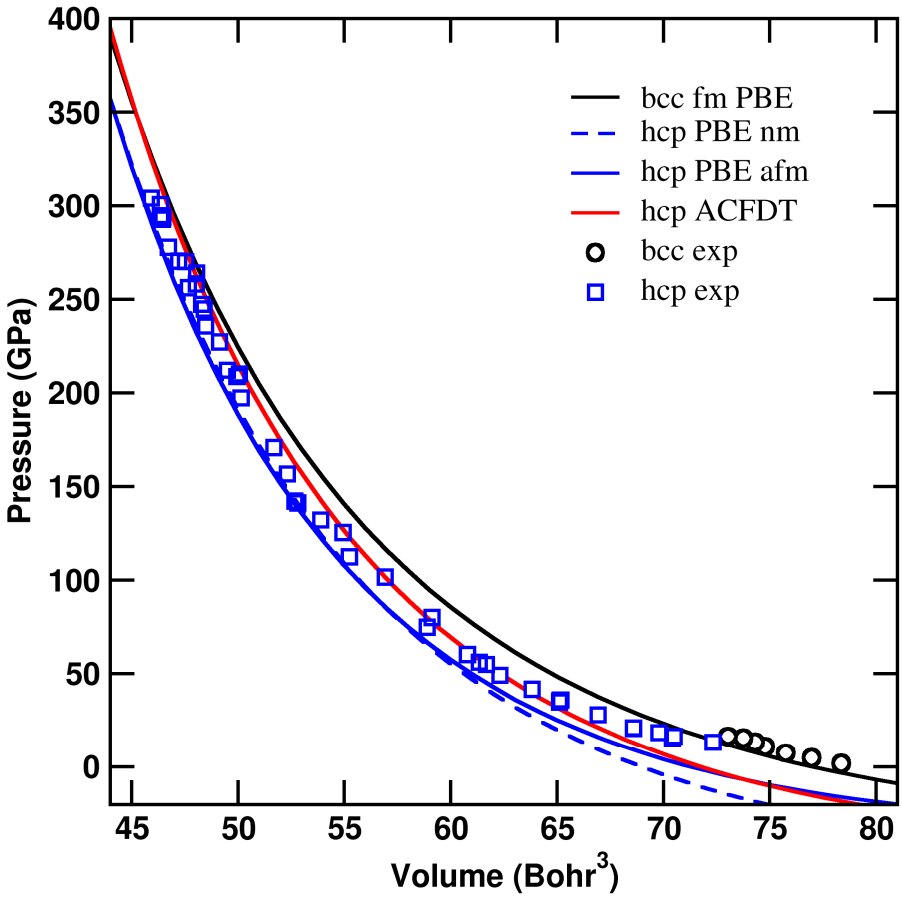

Fig. 3.7-8: P-V equation-of-state for hcp iron. Experiments (symbols) compare more favorably to GGA results using an antiferromagnetic structure than the newly obtained non-magnetic ACFDT results. Experiments and computational results for bcc iron are shown for comparison in black.

g. *Structure factor of liquid metals (F. Wagle and G. Steinle-Neumann)*

The static ion-ion structure factor $S(q)$ is an important quantity in condensed matter physics. It contains information on the spatial arrangement of atoms in ordered and disordered structures and thus on scattering properties and elasticity. In particular, in the long wavelength limit, the structure factor is related to the isothermal compressibility β_T by

$$\lim_{q\to 0} S(q) = nk_B T\beta_T,$$

where n is the density, k_B Boltzmann's constant and T the temperature.

Experimental structure factors of liquid metals from diffraction experiments are – at best – available at ambient pressure in a limited T-range and therefore unsuitable if one wants to understand liquids at higher densities in planetary interiors. Theoretically, a widely used model $S(q)$ is the one of a hard sphere liquid in the Percus-Yevick approximation. It has the

advantage of yielding a closed expression as a function of n and hard sphere radius only, and is capable of reproducing experimental structure factors surprisingly well in the small q region, *i.e.*, for long-range interactions. Although density enters the expression directly, one cannot expect the hard-sphere liquid to produce useful results at high P. At some point, the hard spheres will be close-packed, while in reality the system remains compressible. Moreover, T-effects are not easily included in the model, since the temperature exponent also depends on density in a non-trivial way.

Using first principles molecular dynamics (FPMD) simulations, we are able to compute $S(q)$ directly from the liquid configurations by averaging over a time-series of snapshots. Here we test a two parameter least square fit of the hard sphere model – using an effective density and hard sphere radius – that reproduces simulations results very well for all elements and *P-T* conditions considered (Fig. 3.7-9). In particular, the q-region over the first principal peak – that is responsible for a range of scattering properties – is reproduced well. That way we obtain a smooth, physical function for $S(q)$ of liquid metals, which describes FPMD results at arbitrary temperature and density.

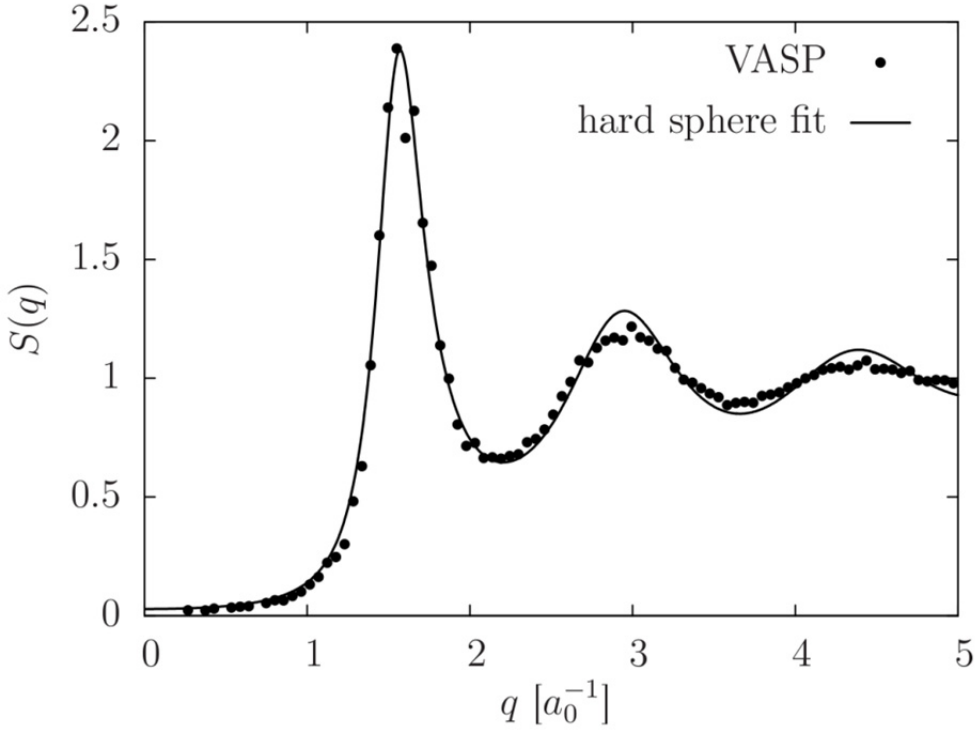

Fig. 3.7-9: Structure factor $S(q)$ of liquid iron at a density of 3,360 $\mathrm{kg \cdot m^{-3}}$ and a temperature of 4,000 K from FPMD simulations and a hard-sphere model fit.

However, FPMD is computationally demanding. In order to get sufficient statistics for the correlation functions and to avoid finite size effects, long runs of a few thousand time steps and large cells at the order of 100 atoms are required for each *P-T* point. Another problem

arises from the comparatively small size of FPMD cells: The resolution of the q-grid in reciprocal space is determined by $2\pi/L$, where L is the length of the simulation box, and $2\pi/L$ is also the shortest wave number for which $S(q)$ is determined. As a consequence, the thermodynamic limit $q \to 0$ cannot be sufficiently captured, which impairs the quality of the fit and the on-the-fly computation of β_T.

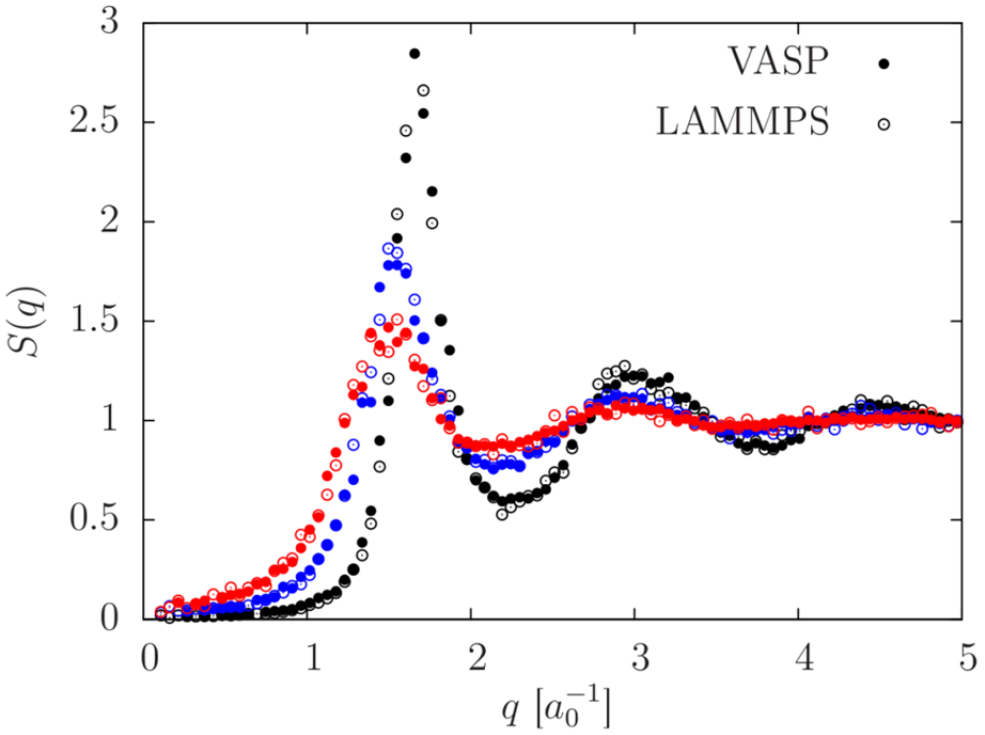

Fig. 3.7-10: Comparison of FMPD and force-field MD (LAMMPS) simulations of the liquid structure factor $S(q)$ of liquid iron at different densities and temperatures (black: 3,920 kg · m^{-3} and 4,000 K, blue: 2,940 kg · m^{-3}and 6,000 K, red: 2,350 kg · m^{-3} and 8,000 K). The LAMMPS simulations have been performed with a single "custom-made" potential.

We have solved this shortcoming by running larger-scale simulations with force-field molecular dynamics, using the code LAMMPS. Here, simulations of 10^5 atoms finish within a few minutes on a present-day desktop computer, while FPMD simulations with 10^2 atoms take a few days on a medium-scale parallel machine. At the same time, the LAMMPS simulation provide access to q-values one order of magnitude smaller than FPMD results. To keep FPMD and LAMMPS calculations as self-consistent as possible, we fit the forces of an FPMD snapshot at a reference P and T to match an embedded-atom-type potential. With this "custom-made" potential, we find that differences in $S(q)$ between FPMD and LAMMPS are marginal (Fig. 3.7-10). This opens the potential to explore large cells of liquid metals and alloys in terms of structure and compressibility.

3.8 Methodological Developments

An essential on-going goal in experimental studies in the Earth and material sciences is to improve existing techniques and to devise new ones. For example, such developments are applicable to (1) the extension of high pressure-temperature conditions and their better characterization, as required to obtain a better understanding of the Earth's deep interior, (2) making new measurements of physical and chemical properties of materials, and (3) characterizing the chemical composition and crystal defects of natural and experimental samples. The contributions in this section cover many of these aspects of methodological developments.

Methodological developments of multianvil experimental techniques are beneficial for the detailed analysis of recovered samples due to relatively large sample volumes and more stable heating with smaller temperature gradients across samples compared with those of a diamond anvil cell (DAC). The first contribution reports technical development using the multianvil apparatus with the newly-developed hardest tungsten carbide anvils, which enable experiments to be performed up to 63 GPa at room temperature and 45 GPa at 2000 K. The second contribution describes the rapid quenching of a sample at > 6000 K/s with a newly-designed cell assembly in the multianvil apparatus. This makes it possible to recover some unquenchable phases to ambient conditions and, in turn, to analyze the "unquenchable" phases by various analytical methods.

Four contributions present results of methodological developments for the DAC. The third contribution reports development of a portable CO_2 laser heating system, which overcomes problems of the present portable laser heating systems with fiber lasers. Moreover, heating with a pulsed laser, instead of a continuous one, may prevent chemical reaction between a sample and the diamond anvils in the DAC, which results in inaccurate measurements of the melting temperature of iron. The fourth contribution describes the chemical reaction between an iron sample and the diamond anvils when the sample was heated with a pulsed laser and a continuous wave laser in the same chamber of the DAC. The fifth contribution presents a developed setup for oxygen loading in a sample chamber of the DAC and reports its performance. Furthermore, the sixth contribution describes a resonating multi-turn micro-coil for nuclear magnetic resonance measurements in the DAC to study viscosity and the degree of polymerization of silicate glasses and the magnetic and electronic properties of solid materials at high pressure.

The last three contributions in this section describe advances in sample analysis. Observation and characterization of dislocations and stacking faults in crystals are essential in studies of rheological properties that are controlled by dislocation motion. The seventh and eighth contributions describe the use of electron channelling contrast imaging in the Earth sciences as a new method for observing dislocations and stacking faults, respectively, in minerals using a field-emission scanning electron microscope. The final contribution reports the reliability and performance of a dictionary indexing approach for indexing electron backscatter patterns of minerals.

a. *Pressure generation over 60 GPa using a large volume press with tungsten carbide anvils (T. Ishii, N. Tsujino/Misasa, T. Yamamoto/Hiroshima, Z.D. Liu, T. Kawazoe, L. Wang, D. Druzhbin, F. Maeda/Sendai, Y. Higo/Kouto, Y. Tange/Kouto and T. Katsura)*

High-pressure generation techniques with a Kawai-type multianvil press (KMAP) are important for understanding the mineral chemistry and physical properties under lower mantle conditions. Last year, we developed high-pressure generation techniques for reaching pressures in excess of 40 GPa using the new KMAP (IRIS-15) at BGI. Recently, the new extra-hard tungsten carbide (WC) has been developed, and pressures up to 50 GPa have been generated at room temperature. In this study, we attempted to generate higher pressures with the new extra-hard WC anvils by using our high-pressure generation techniques.

We performed high-pressure generation tests using the KMAP with DIA-type guide blocks, SPEED-Mk.II, at the synchrotron radiation facility, SPring-8, in Japan. We used second-stage anvils made of the extra-hard WC (TJS01, Fujilloy Co., Ltd) with a truncation of 1.5 mm and a taper of 1.0 degree. Figure 3.8-1 shows a cross section of the cell assembly. Semi-sintered MgO + 5 wt. % Cr_2O_3 octahedra were used as pressure the medium. Generated pressures were calibrated using an equation of state of Au by Tsuchiya (2003). A pressure calibrant of MgO + 10 wt. % Au was sintered at 1500 K and 15 GPa, and that was placed at the center of a Mo cylindrical heater in a $LaCrO_3$ thermal insulator. High temperatures were measured up to 2000 K with a W3%Re-W25%Re thermocouple.

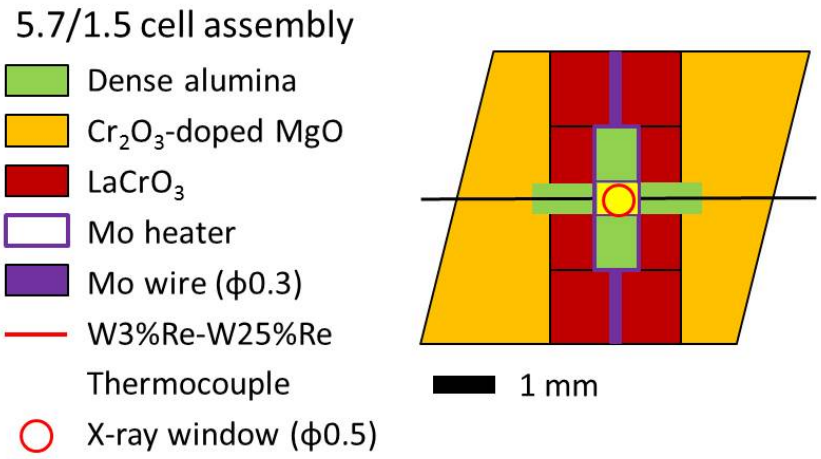

Fig. 3.8-1: Cross section of the cell assembly for high-pressure generation test.

Figure 3.8-2 shows a comparison of pressure generations with the new extra-hard anvils (TJS01) and conventional anvils which we have used (TF05) at room temperature. At the maximum load of 15 MN, pressures of 63 GPa were generated with TJS01, which is the highest pressure generated with WC anvils in the large volume press. The pressure efficiency with TJS01 was much higher than that of TF05 (max. P = 43 GPa). Pressures over 50 GPa

were generated up to 1400 K, and pressures over 45 GPa were obtained up to 2000 K. High-pressure generation using a KMAP with the TJS01 anvils will facilitate detailed studies of mineral chemistry and physical properties in the middle part of the lower mantle.

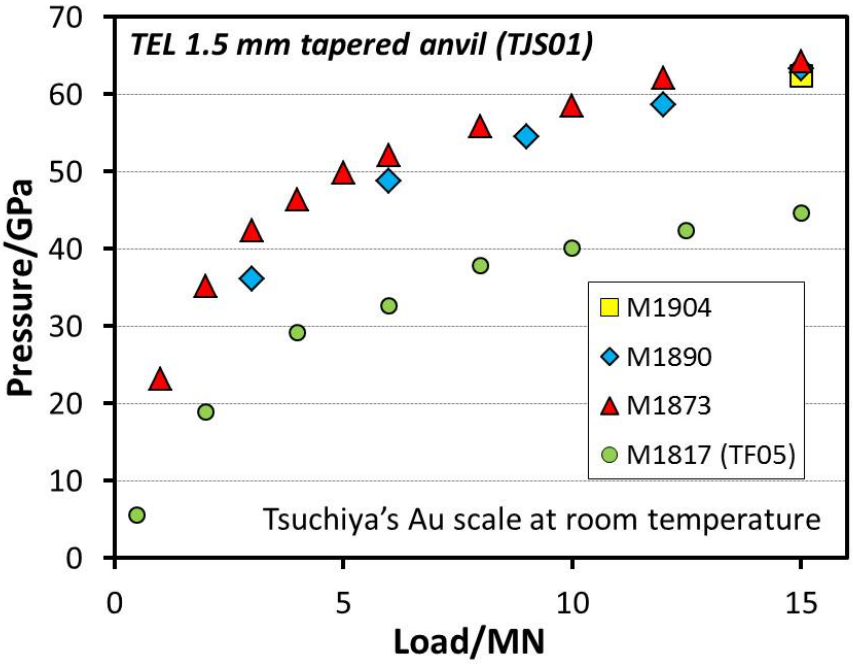

Fig. 3.8-2: Results of the pressure generation tests with the TJS01 second-stage anvils at room temperature. Results obtained using TF05 anvils are shown for comparison (run M1817).

b. *A design of a rapid quench cell (H. Fei, A. Zarei, L. Wang and T. Katsura)*

Multianvil experiments are widely used in high-pressure research. However, because of technical limitations, most analytical methods can only be applied to the samples after quenching, during which some physical and chemical properties might change if the quench rate is not fast enough, *e.g.*, water loss, crystallization of a melt phase, and transformation to a low-temperature phase. Although the quench rate in a normal multianvil experiment is as fast as 300-400 K/s, it is still difficult to preserve the original high-temperature phase for some materials (*e.g.*,olivine + basalt).

In this study, a rapid quench cell for multianvil experiments was developed. In this design, a sample capsule was placed in an MgO sleeve in a graphite heater. A tungsten cylinder with copper rods was used for thermal conduction in an octahedron. Liquid water was cycled to cool down the octahedron and the tungsten carbide cubes (Fig. 3.8-3). By using this design, a quench rate of > 6000 K/s as indicated by the thermocouple is achieved. The temperature decreased from 1600 °C to ~ 300 °C within 0.2 s. This quench rate is much faster than that in a normal multianvil experiment which requires several seconds (Fig. 3.8-4).

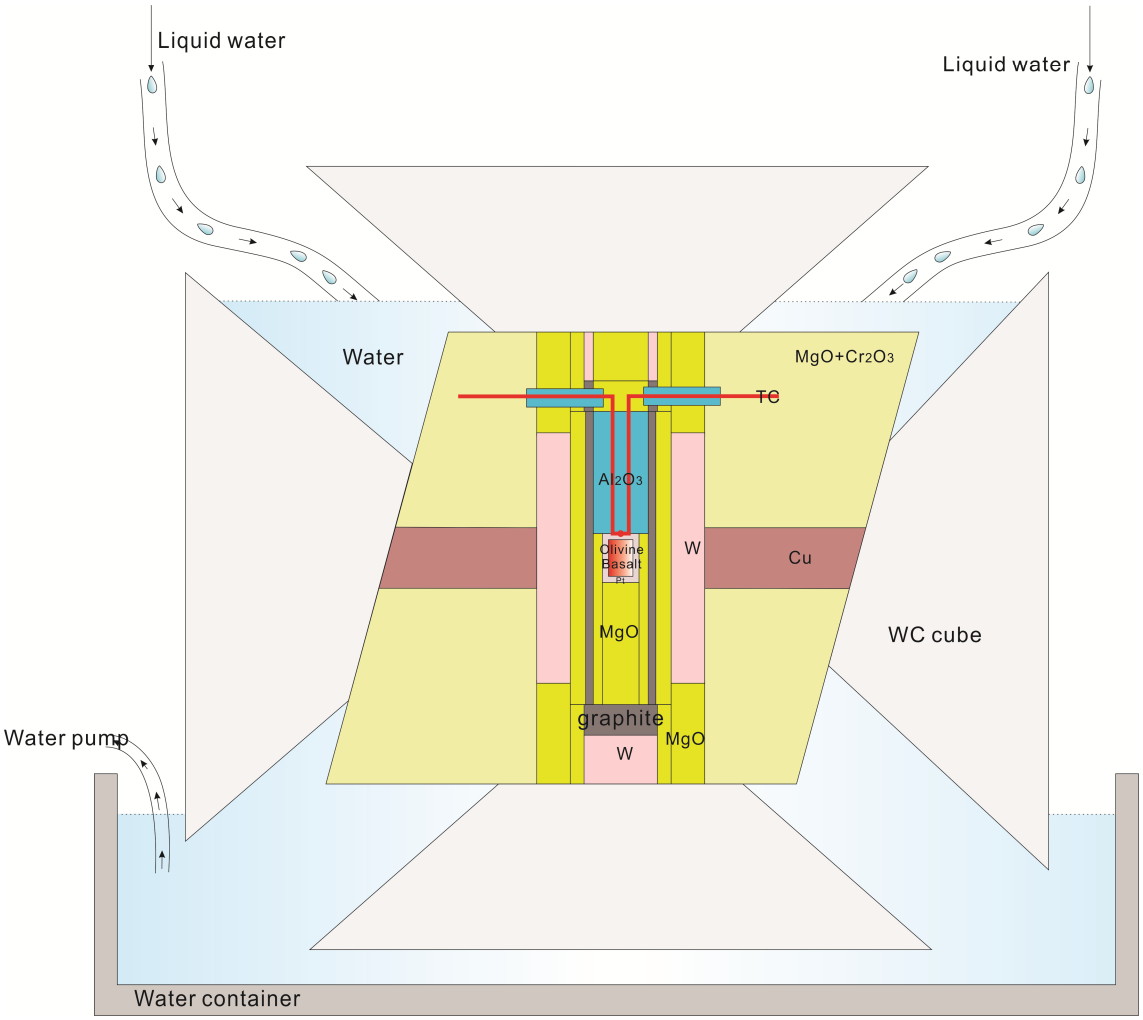

Fig. 3.8-3: The design of the rapid quench cell. The edge length of the octahedron is 18 mm.

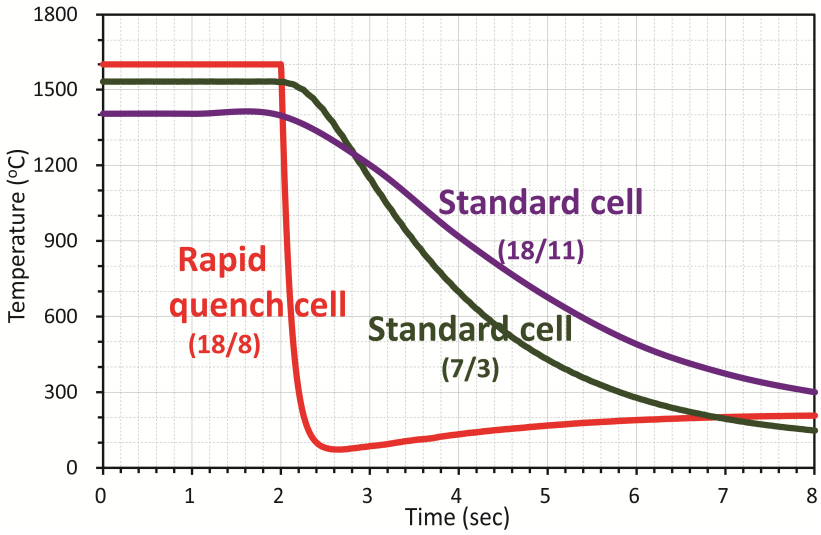

Fig. 3.8-4: A comparison of quench rate in the rapid quench cell and in standard multianvil cell assemblies indicated by the thermocouple.

Since thermocouple measurements might be questionable when the quench rate is relatively rapid, an olivine + basalt mixture (1:1 weight ratio) was used to test the performance of the new design. The mixture was contained in Pt capsules and was loaded into the rapid quench cell and standard multianvil cell assembly. Each cell assembly was compressed to 5 GPa, heated to 1400-1600 °C, which is above the liquidus, and then quenched. As shown in Fig. 3.8-5, when the standard cell assembly was used, the melt with the olivine + basalt composition completely crystallized during quenching. However, in the rapid quench cell, although a small fraction of quenched crystals appeared, most part of the sample remained as glass with the olivine + basalt composition. Therefore, the quench rate is successfully increased in the new design and can be used to obtain some phases which are "unquenchable" in the standard multianvil experiments.

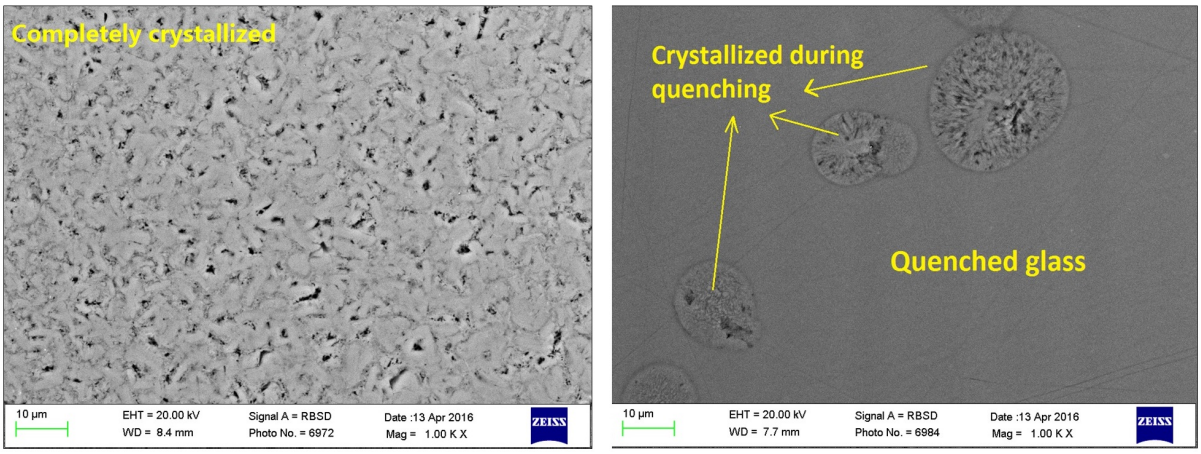

Fig. 3.8-5: A comparison of the recovered samples quenched from melt with an olivine + basalt composition. Left: standard multianvil cell assembly; right: rapid quench cell.

c. *Development and first test of a flexible waveguide-based CO_2 laser heating system (H. Marquardt, V. Potapkin, L.S. Dubrovinsky and A. Kurnosov)*

Knowledge of the physical properties and chemical behaviour of mantle minerals at the pressure and temperature conditions of the mantle is required to model processes in the deep inaccessible interior of our planet. The DAC allows simulation of the pressure conditions of the Earth's mantle and has been extensively used in conjunction with synchrotron-based methods (mostly diffraction) to make *in situ* measurements of physical properties of mantle materials. Only a few years ago, several high-pressure groups around the world developed compact "portable" laser heating systems that, for general users, drastically simplified the application of laser-heating to DACs and opened the perspective for new type of experiments, including single-crystal XRD in the laser-heated DAC. These developments were triggered by the increasing availability of compact high-power fibre lasers emitting radiation with a wavelength of about 1 µm. Fibre lasers are convenient to handle and are a prerequisite for developing "portable" laser-heating systems, where the optical part that needs to be close to the DAC is mechanically separated from the bulky laser and interferometer and only connected through thin fibres that can be several meters long. These developments led to a drastic increase of experiments where 1 µm wavelength radiation (as emitted by the available

fibre lasers) was used to heat mantle minerals in the DAC. However, several recent studies have shown that most mantle minerals are almost optically transparent and, as a consequence, only weakly (if at all) absorb laser radiation with 1 µm wavelength. In addition, inhomogeneous distribution of iron (clustering), that is mostly causing laser absorption, may lead to substantial spatial variations in sample temperature. Heating with a CO_2 laser that emits laser radiation with a wavelength of 10 µm overcomes these problems.

However, CO_2 lasers have been more complicated to handle and therefore their application has been restricted to (only a few) stationary heating setups. The recent availability of 10 µm wavelength transmitting waveguides opens the possibility to design flexible CO_2 laser heating systems that can be conveniently used in combination with a variety of experimental probes. In test experiments, a fan-cooled CO_2 laser was coupled to a commercially available Hollow Silica Core Waveguide (LaserComponents). The waveguides are characterized by a hollow core structure (Hollow Silica Waveguide HSW) that transmits the CO_2 laser radiation through internal reflections. In addition to the invisible laser radiation, visible laser light is transmitted in the cladding of the fibre and serves as a visible guide beam during laser alignment.

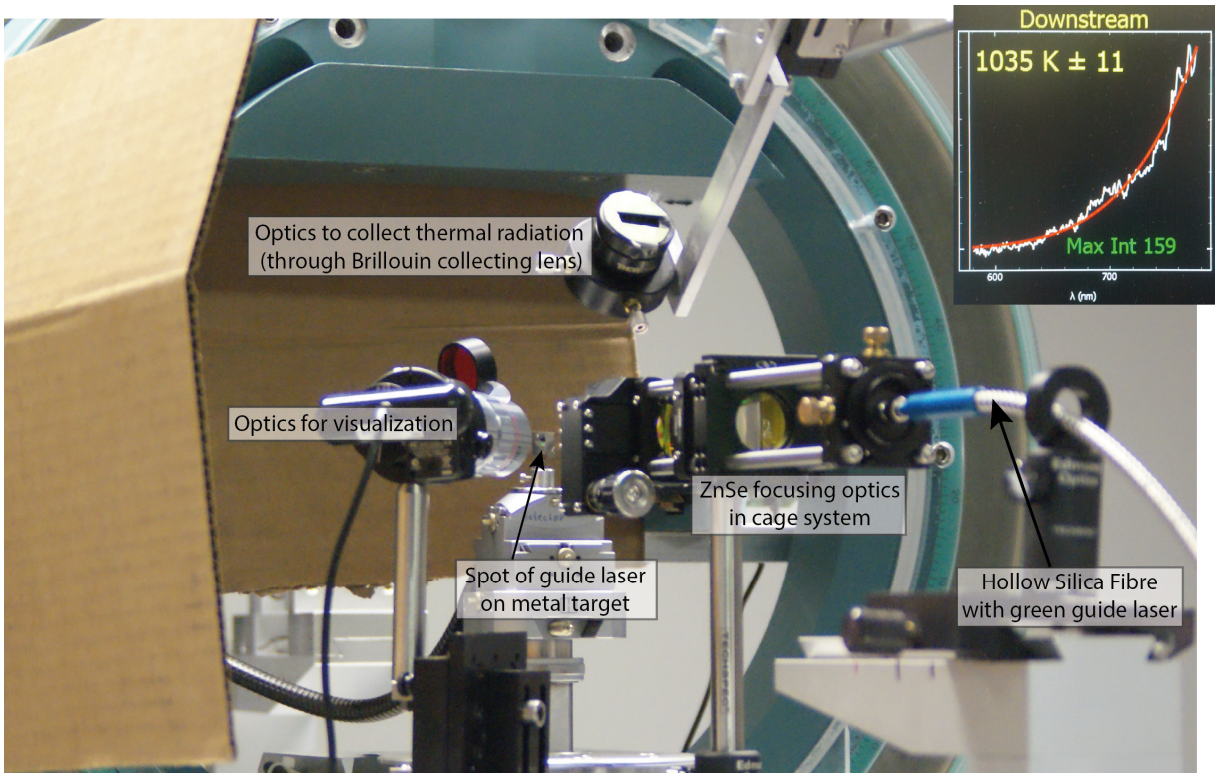

Fig. 3.8-6: A test version of the flexible waveguide-based CO_2 laser heating system mounted on the Brillouin/XRD system. The 3-m long Hollow Silica Waveguide is connected to the front of a 100W fan-cooled CO_2 laser. A visible guide laser beam is inserted into the fibre from the side and is transmitted through the waveguides cladding. The green spot of the guide beam is visible on the metal target. In a first proof-of-concept test, a metal foil was heated and thermal radiation was collected through the Brillouin collecting optics. The Signal was analysed using a Princeton Instruments Spectrometer with a PIXIS camera. The software "T-Rax" (by C. Prescher) was employed to derive the heating temperature (inset).

First tests at BGI indicate that the optical fibres sustain a sufficient power load of > 30 Watt. In these first tests, we coupled the waveguide to a cage system that contains ZnSe optics to focus the laser radiation to a sample. The system was installed on the Brillouin system at BGI, and temperature during heating of a metal foil was measured through the Brillouin collecting optics (Fig. 3.8-6). In the future, we plan to optimize the ZnSe optics to enable measurements in the DAC. In addition, we plan to integrate both the visualization and the temperature measurement optics into the cage-based system in order to construct a fully self-standing flexible CO_2 heating system. The further optimization of the waveguide-based CO_2 laser heating system offers unique perspectives for future experimental research using DACs both in laboratory environments and at synchrotron facilities.

d. *Chemical interaction of iron with diamond anvils in pulsed and continuous wave laser heated diamond anvil cells (G. Aprilis, I. Kantor/Copenhagen, I. Kupenko/Münster, C.A. McCammon, R. Torchio/Grenoble, L.S. Dubrovinsky and N.A Dubrovinskaia/Bayreuth)*

The determination of the melting curve of iron at high pressures, especially the melting point at the mantle-core boundary conditions, is very important for geosciences, providing constraints on the geothermal gradient, which in turn defines the conditions of the Earth's interior. Despite extensive research, the melting curve of iron remains uncertain, and the results so far are contradictory.

Laser heating inside the DAC is the main approach used to reach the necessary pressure and temperature conditions of iron melting. However, the measurement accuracy can be influenced by a number of factors. In contrast to resistive heating, laser heating inside the DAC is a surface heating technique, and the widely used spectroradiometry technique also estimates the surface temperature of the sample. In this sense, even a small amount of reacted material, when lying on the surface, is the main contributor of the measured temperature, and when melting is detected using methods that probe the whole body of the sample, it can cause errors on the estimation. Moreover, when the product of such a chemical interaction is a very small portion of the probed sample, it can fall under the limits of detection.

Pulsed laser heating is considered to be a technique that minimizes heating time of the sample and therefore improves the chemical stability of the system. However, there has not been so far direct comparison between pulsed laser heating and continuous wave heating under the same sample conditions.

In this study, we examined the effect of chemical interaction between the iron sample and the carbon of the diamond anvils during laser heating, which would lead to the formation of iron carbides or the dissolution of carbon into iron. Such a process is unwanted during melting experiments because it can significantly affect the estimated melting temperature. In order to investigate the influence of the sample's chemical environment, similar iron samples were loaded inside different DACs with different materials as pressure media; neon, argon and sodium chloride.

Using the Energy Dispersive X-ray Absorption setup of ID24 at ESRF, it was possible to detect the iron sample's reaction with the carbon environment, with possible iron carbide formation (Fig. 3.8-7). During a series of laser heating runs on each sample at nearby locations it was possible to keep track of the iron – carbon interaction by varying heating times and heating methods, using both pulsed and continuous wave laser heating (Fig. 3.8-8). It was observed that independent of the heating technique, there were cases that interaction occurred almost immediately, after only a few seconds of heating at moderate temperatures, depending mainly on the sample geometry and environment inside the DAC.

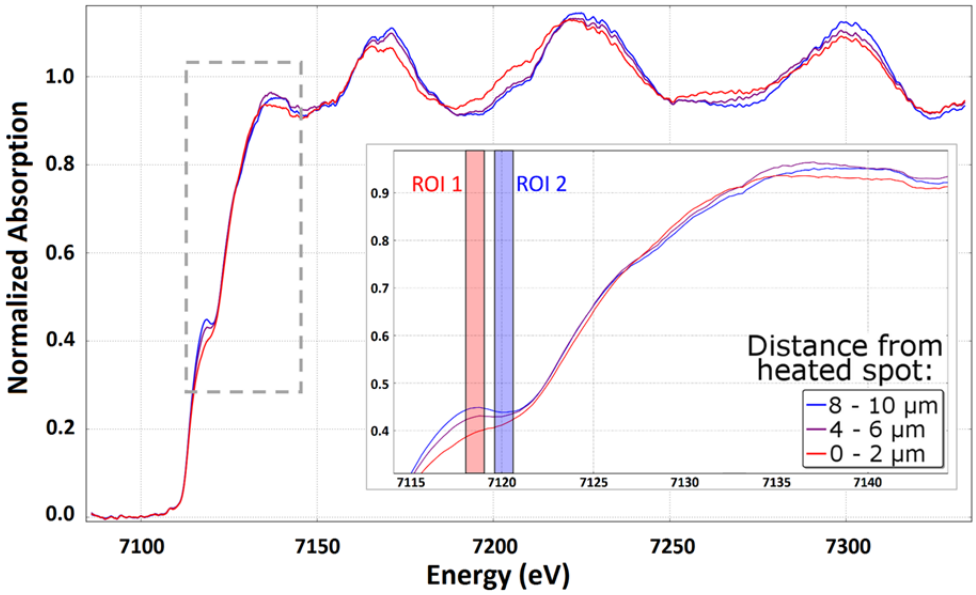

Fig. 3.8-7: X-ray absorption spectra of iron at 45 GPa at 3 different locations; at the center of the laser heated spot, on the edge, and a few µm away from it. The laser spot corresponds to the LH2 + LH3 laser heating runs shown in Fig. 3.8-8 (left). The highlighted energy regions ROI 1 and ROI 2 were used to generate the 'reaction map' of Fig. 3.8-8 (right).

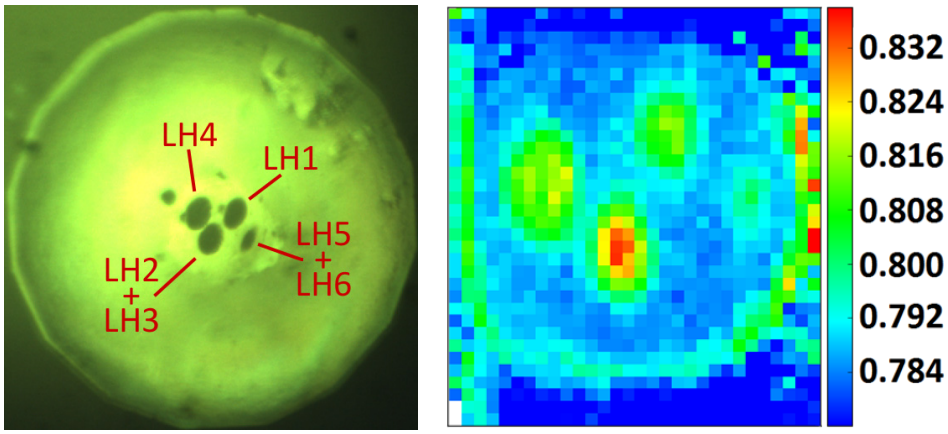

Fig. 3.8-8: Laser heated Fe foil inside a DAC at 45 GPa with neon as pressure medium. Left: View of the laser heating marks on the iron foil. The LH# indicate the different laser heating runs. Right: Iron reaction map of the same foil, represented by the X-ray absorption ratio of 7118.3 - 7119.3 eV and 7119.6 - 7120.6 eV energy windows.

e. *Cryogenic system for oxygen loading into diamond anvil cells (E. Koemets, L.S. Dubrovinsky, G. Aprilis and N.A. Dubrovinskaia/Bayreuth)*

As oxygen is one of the most abundant elements in the universe, its thermodynamic properties, structural stability, spin state, and chemical reactivity at high pressures and temperatures are of great interest for geochemistry, geophysics, and mineral physics. Presently there is a discrepancy between theoretical predictions and experimental data regarding the high-pressure high-temperature behaviour of oxygen so that further investigations are desirable. High *P-T* studies of oxygen are also important for further development of condensed matter theory, particularly concerning properties of highly compressed materials.

Oxygen was loaded cryogenically into a BX90 DAC with type Ia diamonds with a culet size of 250 µm. A rhenium gasket indented to the thickness of 35 µm with a hole of 120 µm was used as a sample chamber. The schematic presentation of the cryogenic loading system is provided in Fig. 3.8-9. The loading process was realized as follows: the DAC with the rhenium gasket was put into the loading chamber located in a styrofoam container. Then this container was filled in with liquid nitrogen. Gaseous oxygen from a gas bottle was supplied to the loading chamber, where it was cooled and liquefied. After that the cover of the loading chamber was opened, and the DAC was closed by tightening screws. Liquid oxygen was trapped in the sample chamber of the DAC, and the latter could be removed from the system. The balloon was used to support pressure of the loading gas in the closed chamber during the liquefaction process. Thus, the loading chamber could be isolated from the outer atmosphere and protected from the injection of drops of boiling liquid nitrogen.

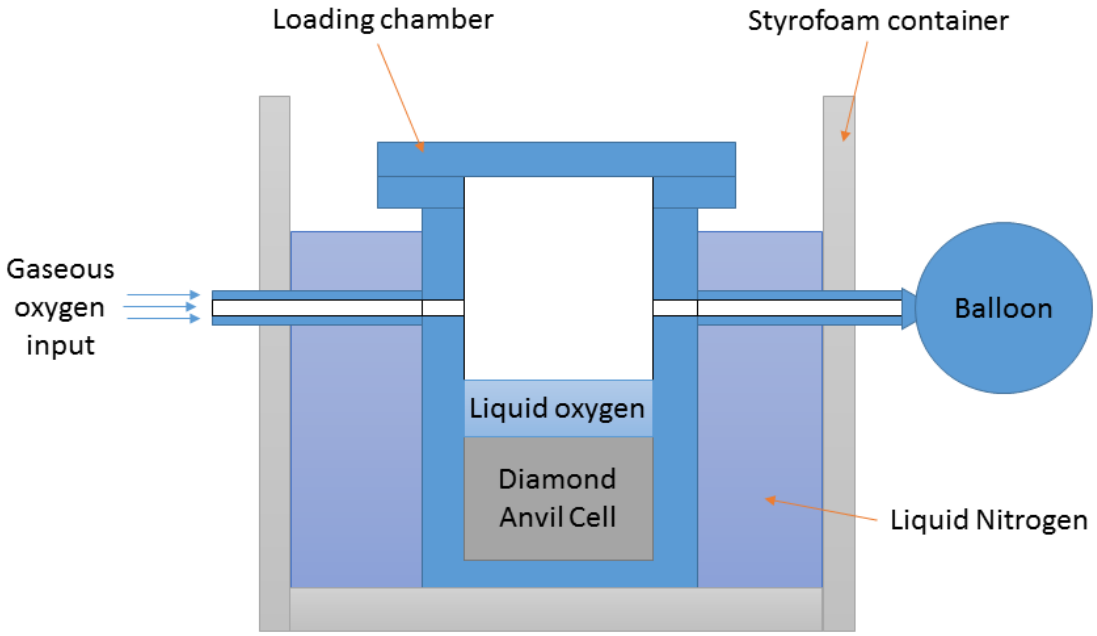

Fig. 3.8-9: The schematic illustration of the cryogenic system for loading DACs with gases.

Raman spectra of oxygen compressed to 37 GPa at room temperature corresponded to the ε–oxygen phase which is consistent with the literature (Fig. 3.8-10). After one-side and two-sided laser heating to 2500 K no signs of the presence of oxygen-nitrogen compounds were found.

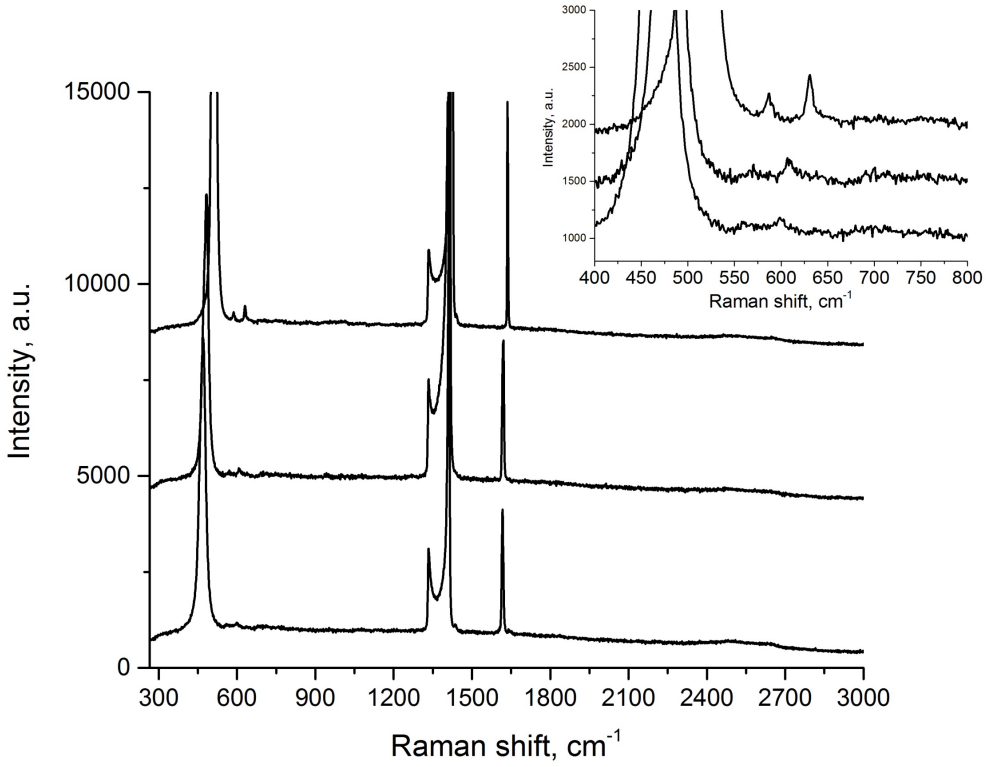

Fig. 3.8-10: Raman spectra of oxygen measured at 37 GPa in a DAC at room temperature (bottom curve) and after heating to 2500 K from one side (middle curve) and from two sides (upper curve).

f. *High-pressure nuclear magnetic resonance in the geosciences (T. Meier, L.S. Dubrovinsky and S. Petitgirard)*

Nuclear magnetic resonance (NMR) is nowadays a standard spectroscopic method in chemistry, physics and analytical biology, as it yields information about the structural and electronic properties of condensed matter systems which are not accessible with other methods. Nevertheless, in modern high-pressure geosciences it is still an exotic method and is often only rarely used. This partly originates from the difficulty to implement NMR measurements in DACs due to inherently low signal amplitudes and rather low spin sensitivities.

Here, we use a recent approach which uses a resonating multi-turn micro-coil of several micrometers in diameter which is placed directly in the sample volume of a typical DAC, see Fig. 3.8-11. Using this technique, the nuclear spin sensitivities could be improved by several orders of magnitude, and at the same time allows reliable NMR measurements at up to 30 GPa.

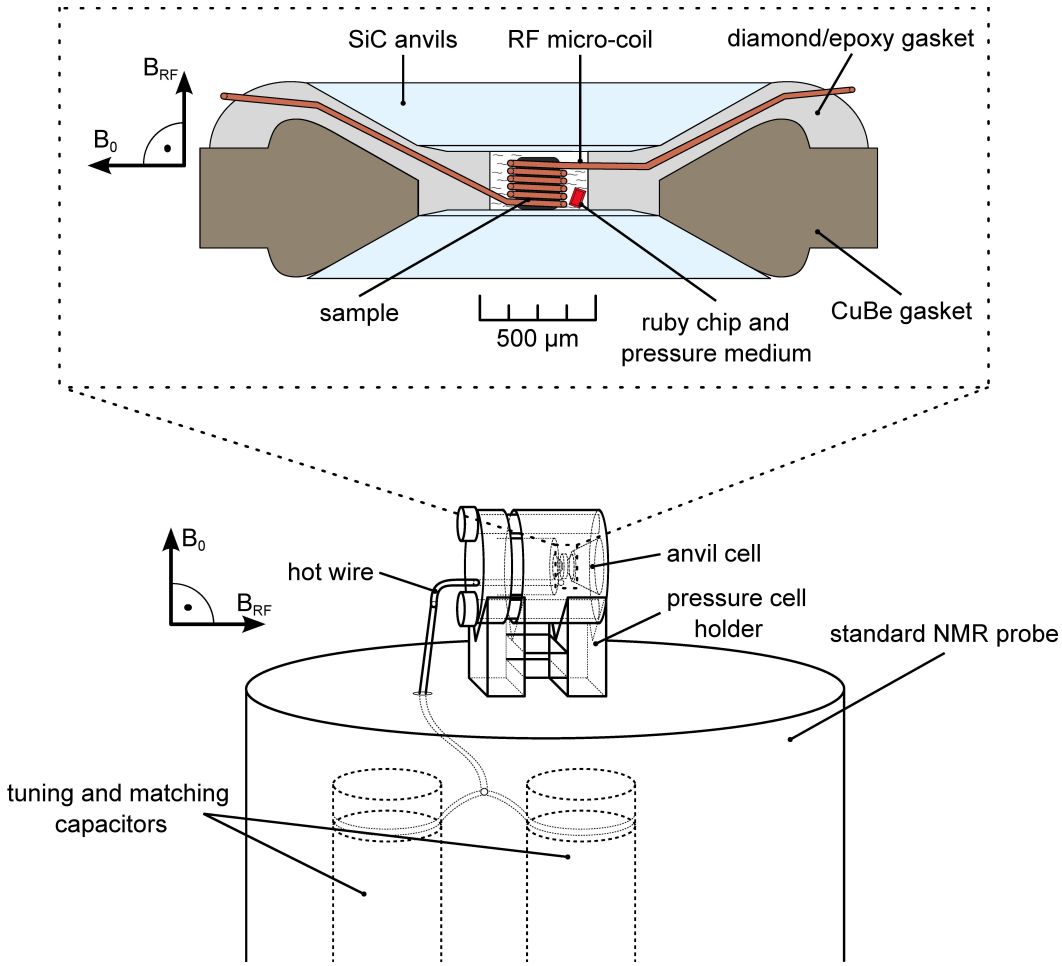

Fig. 3.8-11: Schematic drawing of the high-pressure anvil cells for NMR measurements.

The main goal of this new project is to close the gap between NMR and high-pressure geosciences in a variety of different experiments.

For example, using static ^{17}O NMR on silicate glasses will give crucial information about the abundance of network forming oxygens. At the same time, ^{29}Si NMR can be used to extract viscosities η, which, in combination with structural information, allows for an *in situ* high-pressure investigation of the relationship between the degree of polymerization and η.

Furthermore, as NMR measures to a first approximation the strength of the hyperfine interaction (HFI), *i.e.*, the interaction of conduction or core electrons with the nuclei, it will be used for identification of different magnetic orders in the recently found high-pressure phases of transition metal oxides.

In the same vein, NMR will be used for the detection of metallic phases, such as high-pressure boron, in a DAC. As the HFI changes significantly when going from an insulating material to a metal, this method will play a crucial role in identifying metallization conditions or even the onset for an electronic delocalization.

Finally, another important aspect of this project is the further development of high-pressure NMR set-ups. The main goal is to reach significantly higher pressures, possibly up to the mega-bar range at simultaneously high-temperature conditions. Furthermore, the development of *in situ* high-pressure magic angle spinning techniques will allow for high-resolution NMR experiments at moderate pressures.

g. *Potential new technique for imaging dislocations in a natural olivine by electron channelling contrast in a conventional field emission SEM. II. Comet-like contrasts in inclined dislocations in end-on view (N. Miyajima, Y. Li, S. Abeykoon and F. Heidelbach)*

Observation of individual dislocations in minerals is indispensable for the understanding of the deformation mechanisms in rocks at the sub-micrometer scale. Transmission electron microscopy (TEM) has been so far the main tool to observe individual dislocations in rock-forming minerals. On the other hand, chemical etching and oxidation decoration methods are often used for dislocation density measurements especially in Fe-bearing olivine, by using optical microscopy or scanning electron microscopy. Currently, electron channelling contrast imaging (ECCI) in a conventional field emission scanning electron microscope (FE-SEM) is developing into an alternative tool to observe crystal defects in metallic alloy and ceramics containing relatively heavier elements in the material science fields. We are developing the technique further for application on mantle minerals. Here we report ECCI of end-on dislocations in a naturally deformed olivine. Strong contrast in the form of bright or dark comet-like features is considered as end-on dislocations having different surface relaxation effects.

A natural olivine from the Finero lherzolite was examined in an FE-SEM equipped with an electron backscatter diffraction (EBSD) apparatus. The bulk rock specimen was polished using a 0.25-1 μm diamond paste followed by a 40 nm colloidal silica suspension. The polished surface was coated with amorphous carbon. The FE-SEM was operated at 20 kV acceleration voltage and ~ 9 nA probe current with a low convergent angle at 6.9 mm working distance. Back-scattered electron (BSE) images were obtained with a scintillator type BSE detector mounted below the pole piece and a line integration scanning mode. The crystal orientations of a target olivine grain were determined by EBSD.

The BSE image of a single crystal of olivine (Fig. 3.8-12) displays cross-hatched subgrain boundaries. The straight boundaries are nearly parallel to the (001) and (010) planes on the [100] projected image, which implies that the two slip systems were co-activated during the deformation. The ECCI of the olivine at a nearby (001) subgrain boundary is shown in Fig. 3.8-13. The right-side of the boundary in the image has a stronger channelling effect under the Bragg conditions of the (00l) planes. A few of the bright line features are the [001] screw dislocations in plan-view. Many bright or dark (bright/dark) spots with a tail can be characterized as having a “comet”-like feature. The comet-like contrast originates from dislocations that are inclined to the sample surface. The comet-like features likely correspond to end-on dislocations having different surface relaxation effects, although the character of

dislocations and the origin of the bright/dark contrast are still unknown. Especially, the bright/dark contrast might indicate different signs of the Burgers vector. Further ECCI studies are underway to determine the exact nature of the comet-like features in the inclined dislocations in end-on view.

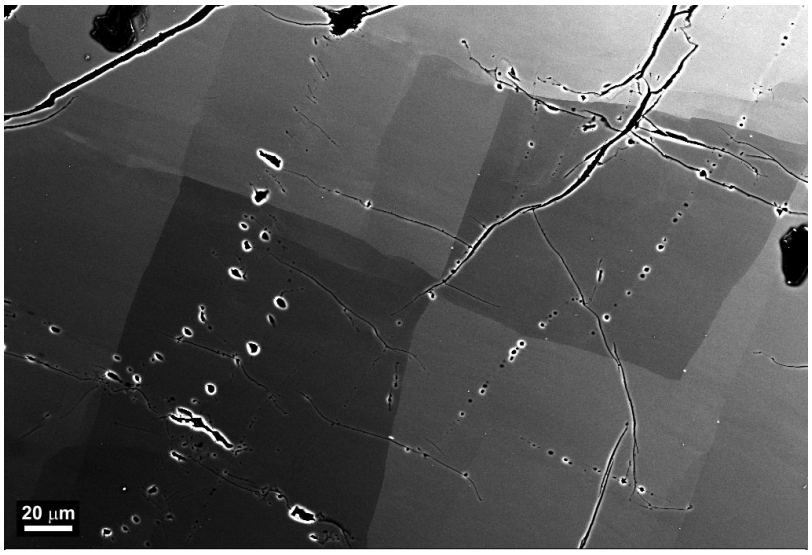

Fig. 3.8-12: BSE image of a naturally deformed olivine showing cross-hatched subgrain boundaries along the [010] and [001] directions.

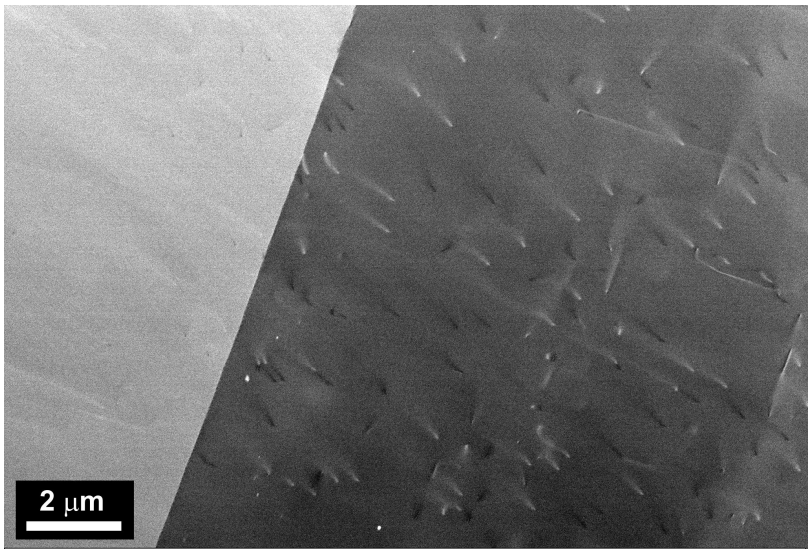

Fig. 3.8-13: ECCI of individual dislocations in a natural olivine. The comet-like features with bright/dark contrast correspond to inclined dislocations having different surface relaxation effects.

h. *Imaging of stacking faults in clinopyroxene using electron channelling contrast (S. Abeykoon and N. Miyajima)*

Direct observation of mineral lattice defects, such as dislocations, stacking faults, twins and grain boundaries, is important because the defects have direct influences on the physical and chemical properties of materials in geological processes from the micro scale to the global scale. Electron channelling contrast imaging (ECCI) using a conventional FE-SEM is becoming a low cost and less time consuming method to investigate microstructures in deformed materials. The orientation controlled ECCI provides a potential alternative method

to diffraction contrast imaging in the TEM. In this study we applied the ECCI technique for imaging stacking faults in geological materials. .

We studied a natural single crystal of an augite (clinopyroxene) (MC-CPX) sample from Moncaup, France. Conventional surface polishing by 40 nm silica colloidal suspension was done for BSE imaging in an FE-SEM. Prior to ECCI of the sample, EBSD measurements of the crystal were carried out in order to obtain the orientation information of the crystal. The ECCI in BSE geometry were performed at 20 kV acceleration voltage and ~ 9 nA probe current with a short working distance. The indexing of Kikuchi bands in EBSD patterns was done by using the SFC indexing software developed by Prof. T. Kogure's laboratory, University of Tokyo, Japan. We used a [001] oriented Si standard for the calibration of the sample normal and pattern center positions in the EBSD system.

The MC-CPX sample was oriented approximately to the [001] zone axis direction, *e.g.*, 20 degrees off from the [001] zone axis direction. Along the orientation, plenty of exsolution lamellae of orthopyroxene (OPX) are visible (Fig. 3.8-14). Distinguishing stacking faults

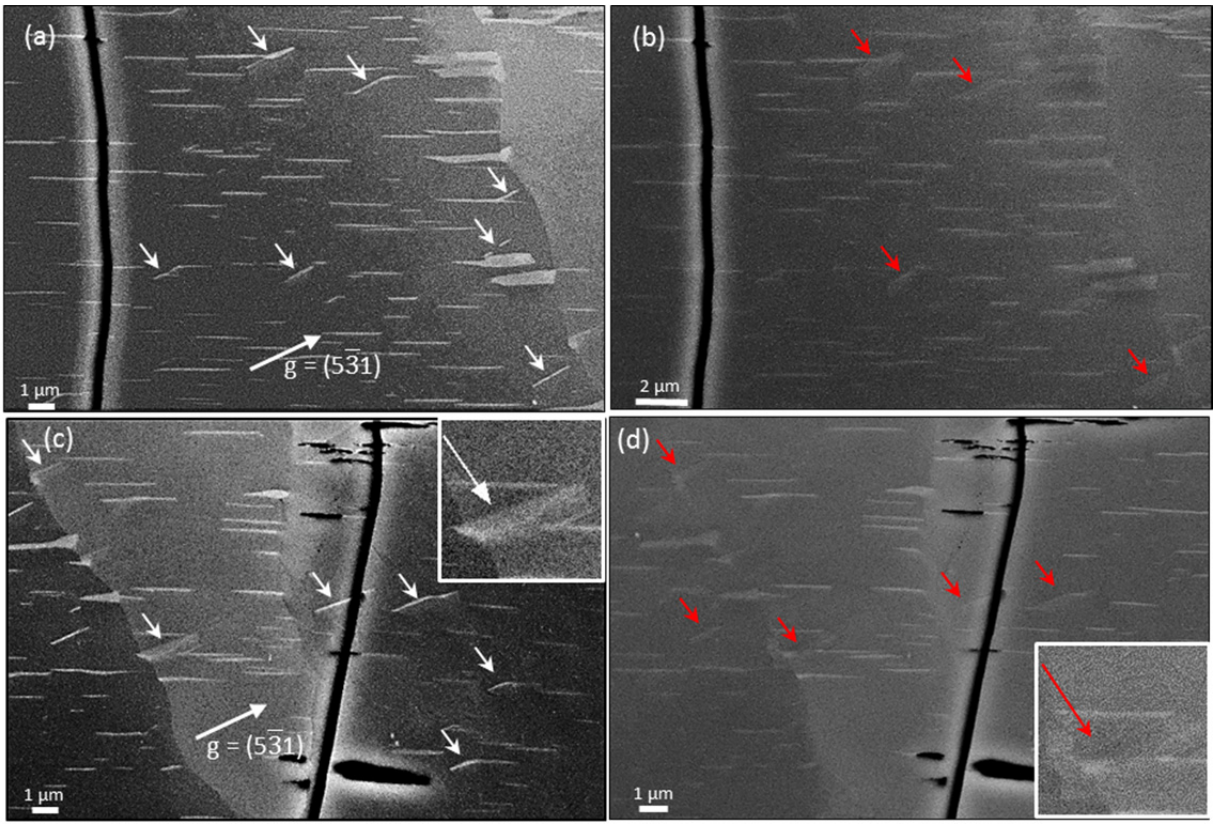

Fig. 3.8-14: ECC images of two different locations in the MC-CPX sample. (a) and (c) Tilting angle = 5.0°. (b) and (d) Tilting angle = 1.5°. Stacking faults with weak oscillation contrasts are shown with white arrows in (a), (c) and the inset. Residual contrasts of stacking faults are marked with red arrows in (b), (d) and the inset. The diffraction vector is $\boldsymbol{g} = (5\bar{3}1)$.

from the exsolution lamellae is sometimes difficult in the ECC images of the CPX sample because the dimensions of the OPX lamellae are comparable with that of the stacking faults, and the both of them are basically oriented on the (100) plane of the CPX. However, we identified stacking faults in orientation-optimized ECC images (Fig. 3.8-14 (a) and (c) and the inset). As shown in Fig. 3.8-14, white contrasts of stacking faults are invisible with changing the diffraction conditions by tilting the sample stage along the [010] axis, while the lamellae are still visible (Fig. 3.8-14 (b) and (d) and the inset). This could be a potential method to rule out the orientation contrast of stacking faults from the compositional contrast of lamellae in the BSE imaging. Moreover, we observed weak oscillation contrast on the stacking fault plane, *i.e.*, backscattering is stronger or weaker depending on the depth of the defect below the surface, when tilting the sample. The weak oscillation contrasts of the stacking faults can be detected under the Bragg condition g = $(5\bar{3}1)$ (white arrows in the inset of Fig. 3.8-14 (c)). The intensity oscillations are related to the depth sensitivity of electron channelling in the dynamical diffraction phenomena.

i. *Quantitative electron backscatter diffraction (EBSD) data analyses using the dictionary indexing (DI) approach: Overcoming indexing difficulties on geological materials (K. Marquardt, M. De Graef/Pittsburgh, S. Singh/Pittsburgh, H. Marquardt and A. Rosenthal/ Clermont-Ferrand)*

EBSD data are the source for plentiful information on microstructures and textures of geological samples. EBSD is used to study phase equilibria, and to characterize textures to understand the deformation history from deduced crystal preferred orientations that affect bulk rock properties - such as electrical conductivity and seismic anisotropy. Furthermore, EBSD is used to understand various phenomena such as seismic wave attenuation in the Earth's interior that might be caused by the presence of interfacial melt. In standard EBSD software solutions, however, the original EBSD patterns are rarely saved and indexing routines result in many artifacts such as pseudo symmetry or unindexed pixels at interfaces that may be misinterpreted as amorphous material such as a melt.

Here we introduce an alternative indexing routine, the dictionary indexing (DI), which is independent of the EBSD system and thus the used detector/software. The DI method calculates electron backscatter images for all possible crystal orientations taking the sample composition and experimental setups into account; the resulting image collection is called a dictionary. The experimental EBSP images are indexed by comparing them to the dictionary using a dot-product algorithm. We evaluate the new DI method in comparison to standard routines and highlight the advantages and disadvantages.

To test and compare the DI's reliability and performance we apply it to two scientific challenging samples: (1) An eclogite sample composed of garnet, clinopyroxene (monoclinic) and an amorphous melt phase, where the different hardnesses of the minerals cause surface

topology and (2) a pure forsterite (olivine) polycrystalline sample where the acquired EBSD patterns are of low quality as a result of fast data acquisition to reduce the on-line machine time.

We conclude that the new DI method is highly precise and surpasses the performance of previously available methods while being computer-time and -memory consuming. We find that the DI method is free of pseudo symmetry-related problems and, because all patterns are indexed, no datasets with unindexed pixels result. Interpolation of data becomes obsolete and high reproducibility is obtained, which minimizes the user impact on the final dataset. The latter is often caused by applying several cleaning steps on EBSD maps with low indexing fraction. Finally, the fact that all patterns have to be saved results in much higher scientific integrity and allows for subsequent re-analyses. The DI will help to obtain reliable information for the characterization of interface properties, including amorphous materials.

4. International Research and Training Group – "Deep Earth Volatile Cycles" (DFG GRK 2156/1)

The International Research and Training Group (IRTG) "Deep Earth Volatile Cycles" is funded by the *Deutsche Forschungsgemeinschaft* (DFG). This graduate school for doctoral studies started in April 2016 for a period of 4.5 years. It is a cooperation between the Bayerisches Geoinstitut (BGI) and the Department of Earth Sciences at Tohoku University, Sendai/Japan. The IRTG is chaired by Dan Frost/Bayreuth and Michihiko Nakamura/Sendai.

The objective of this collaborative research effort is to study the cycling of volatile elements through the deep interior of the Earth. Using mainly experimental and computational methods the group's goal is to quantify how volatile elements such as carbon, hydrogen and nitrogen are transported, stored and expelled from the interior as a result of plate tectonic processes. Doctoral researchers receive training in modern experimental and modelling techniques employed in solid Earth geosciences in a structured learning programme. At the same time they pursue independent research into geochemical and geophysical aspects of the internal volatile cycle. Doctoral researchers from the BGI spend between 6 to 12 months at Tohoku University as part of a complementary research exchange that sees scientists from Tohoku University spending time at the BGI.

In 2016 the following PhD students were enrolled in the IRTG at the BGI:

Greta Rustioni (M.Sc. 2016, Pavia) since 01.10.2016	*Effect of Cl on trace element mobility in subduction zones.* Supervisor: Prof. H. Keppler
Egor Koemets M.Sc. 2015, Novosibirsk) since 01.10.2016	*Oxygen behaviour at conditions of Earth's lower mantle and core.* Supervisor: Prof. L. Dubrovinsky
Philipp Eichheimer (M.Sc. 2016, Mainz) since 01.11.2016	*Numerical modelling of volatiles in the deep mantle and salt tectonics.* Supervisor: Prof. G. Golabek

IRTG Activities in 2016:

Joint International workshop "New Challenges in Volatile Cycling in the Deep Earth." Tohoku University 3-6th July:

The IRTG kick-off meeting was held at the beginning of July in Sendai directly after the Goldschmidt meeting in Yokohama. Seventeen scientists and seven PhD students from the BGI presented their research at the workshop. Keynote talks were presented by 10 invited speakers on topics central to the goals of the IRTG. Before the workshop a one day field trip was organised to visit areas affected by the 2011 Tohoku earthquake and tsunami.

International Workshop *New Challenges in Volatile Cycling in the Deep Earth*.
JGGE-IRTG meeting, Tohoku University, Sendai, 3-6 July, 2016

BGI 30th Anniversary Celebrations 28-30th September:

In September scientists from Tohoku University joined their BGI colleagues to celebrate the 30th anniversary of the foundation of the BGI. As part of these celebrations a series of lectures were presented with a strong volatiles theme, which included talks by nine international invited speakers with close links to the BGI. During the meeting Prof. Ohtani of Tohoku University received a certificate announcing his appointment as a *Distinguished Affiliated Professor* of Bayreuth University from the hands of Prof. Dr. Stefan Leible, President of the University of Bayreuth (Photo Right).

Women in Geosciences: Equal opportunities – careers, 29th September:

During the Anniversary meeting a breakout session was held in the form of a round table discussion on female scientific careers/equal professional opportunities attended by female scientist of the IRTG and BGI under the direction of Dr. Katharina Marquardt and in collaboration with the staff division for "Equal Opportunities" of the University of Bayreuth. As guest speaker Dr. Nathalie Bolfan Casanova/Clermont-Ferrand described her experiences and the challenges faced in balancing carreer and family commitments.

In 2016 several staff members and students of the two participating institutes made visits to the collaborating institutions for discussion of projects, presentations, experiments and internships:

Tohoku colleagues visiting BGI in 2016:

Name	Period	Name	Period
Ando, Junichi	29.02.-03.03.2016	Murakami, Motohiko, Prof.	09.05.-17.05.2016
Yamamoto, Takafumi	29.02.-03.03.2016	Mashino, Izumi	15.08.-26.08.2016
Nakahara, Hisashi, Dr.	07.03.2016	Ohira, Itaru	28.08.-01.10.2016
Nishimura, Takeshi, Prof.	07.03.2016	Maeda, Fumiya	03.09.-01.10.2016
Ichiki, Mashiro, Dr.	07.03.-08.03.2016	Nakatami, Takayuki, Dr.	22.09.-25.09.2016
Mujin, Mayumi	16.03.-20.03.2016	Ohtani, Eiji, Prof. emer.	28.09.-30.09.2016
Aruga, Takafumi	16.03.-20.03.2016	Tsujimori, Tatsuki, Prof.	28.09.-30.09.2016
Nakamura, Michihiko, Prof.	16.03.-20.03.2016	Nakatami, Takayuki, Dr.	02.10.-18.10.2016
Matsumoto, Keiko	16.03.-20.03.2016	Nakamura, Michihiko, Prof.	10.11.-24.11.2016
Ohtani, Mari	16.03.-23.03.2016	Yanagida, Yasuhiro	12.11.-24.11.2016
Yanagida, Yasuhiro	16.03.-23.03.2016	Matsumoto, Keiko	13.11.-22.11.2016
Okumra, Satoshi, Prof.	16.03.-23.03.2016	Nakamura, Tomoki, Prof.	13.12.-17.12.2016
Fujita, Wakana	16.03.-23.03.2016		

BGI colleagues visiting Tohoku in 2016:

Name	Period	Name	Period
Frost, Dan, Prof.	02.07.-29.07.2016	Miyajima, Nobuyoshi, Dr.	03.07.-06.07.2016
Katsura, Tomoo, Prof.	03.07.-06.07.2016	Petitgirard, Sylvain, Dr.	03.07.-06.07.2016
Rubie, David, Prof.	03.07.-06.07.2016	Shcheka, Svyatoslav, Dr.	03.07.-06.07.2016
Golabek, Gregor, Prof.	03.07.-06.07.2016	Steinle-Neumann, Gerd, Dr.	03.07.-06.07.2016
Boffa Ballaran, Tiziana, Dr.	03.07.-06.07.2016	Thielmann, Marcel, Dr.	03.07.-06.07.2016
Ishii, Takayuki, Dr.	03.07.-06.07.2016	Armstrong, Katherine	03.07.-06.07.2016
Jennings, Eleanor, Dr.	03.07.-06.07.2016	Arato, Robert	03.07.-06.07.2016
Kawazoe, Takaaki, Dr.	03.07.-06.07.2016	Buchen, Johannes	03.07.-06.07.2016
Mallik, Ananya, Dr.	03.07.-06.07.2016	Druzhbin, Dmitry	03.07.-15.07.2016
Marquardt, Hauke, Dr.	03.07.-06.07.2016	Schulze, Kirsten	03.07.-06.07.2016
Marquardt, Katharina, Dr.	03.07.-06.07.2016	Wang, Lin	03.07.-15.07.2016
McCammon, Catherine, Dr.	03.07.-06.07.2016	Yoshioka, Takahiro	03.07.-06.07.2016

5. Publications, Conference Presentations, Seminars

5.1 Publications (published)

a) Refereed international journals

BIANCHI, F.; THIELMANN, M.; MANI, R.; OR, D.; HERRMANN, H.J. (2016): Tensile stress relaxation in unsaturated granular materials. Granular Matter, 18(4) 75, doi: 10.1007/s10035-016-0673-6

BIEDERMANN, A.; HEIDELBACH, F.; JACKSON, M.; BILARDELLO, D.; MCENROE, S. (2016): Magnetic fabrics in the Bjerkreim Sokndal Layered Intrusion, Rogaland, Southern Norway. Tectonophysics 688, 101-118

BOLLINGER, C.; RATERRON, P.; CASTELNAU, O.; DETREZ, F.; MERKEL, S. (2016): Textures in deforming forsterite aggregates up to 8 GPa and 1673 K. Physics and Chemistry of Minerals 43, 409-417

BOSAK, A.; KRISCH, M.; CHUMAKOV, A.; ABRIKOSOV, I.A.; DUBROVINSKY, L. (2016): Possible artifacts in inferring seismic properties from X-ray data. Physics of the Earth and Planetary Interiors 260, 14-19

BUREAU, H.; FROST, D.J.; BOLFAN-CASANOVA, N.; LEROY, C.; ESTEVE, I.; CORDIER, P. (2016): Diamond growth in mantle fluids. Lithos 265, 4-15

BYKOV, M.; BYKOVA, E.; HANFLAND, M.; LIERMANN, H.-P.; KREMER, R.K.; GLAUM, R.; DUBROVINSKY, L.; VAN SMAALEN, S. (2016): High-pressure phase transformations in $TiPO_4$: A route to pentacoordinated phosphorus. Angewandte Chemie Int. Ed. 55, 15053-15057, doi: 10.1002/anie.201608530

BYKOVA, E.; DUBROVINSKY, L.; DUBROVINSKAIA, N.; BYKOV, M.; MCCAMMON, C.; OVSYANNIKOV, S.; LIERMANN, H.-P.; KUPENKO, I.; CHUMAKOV, A.; RUFFER, R.; HANFLAND, M.; PRAKAPENKA, V. (2016): Structural complexity of simple Fe_2O_3 oxide at high pressures and temperatures. Nature Communications 7, 10661, doi: 10.1038/ncomms10661

BYSTRICKY, M.; LAWLIS, J.; MACKWELL, S.; HEIDELBACH, F.; RATERRON, P. (2016): High-temperature deformation of enstatite aggregates. Journal of Geophysical Research: Solid Earth 121, doi: 10.1002/2016JB013011

BOFFA BALLARAN, T.; PAKHOMOVA, A.S.; KURNOSOV, A.V. (2016): Deformation of single crystals of water ice VI. Acta Crystallographica Section A: Foundations and Advances 72(a1), s280, doi: 10.1107/S2053273316095760

CHANTEL, J.; MANTHILAKE, G.M.; FROST, D.J.; BEYER, C.; BOFFA BALLARAN, T.; JING, Z.; WANG, Y. (2016): Elastic wave velocities in polycrystalline $Mg_3Al_2Si_3O_{12}$-pyrope garnet to 24 GPa and 1300 K. American Mineralogist 101, 991-997

COLLINGS, I.; BYKOVA, E.; BYKOV, M.; PETITGIRARD, S.; HANFLAND, M.; PALIWODA, D.; DUBROVINSKY, L.; DUBROVINSKAIA, N. (2016): Neon-bearing ammonium metal formates: formation and behavior under pressure. ChemPhysChem 17, 3369-3372, doi: 10.1002/cphc.201600854

COLLINGS, I.; BYKOV, M.; BYKOVA, E.; TUCKER, M.G.; PETITGIRARD, S.; HANFLAND, M.; GLAZYRIN, K.; VAN SMAALEN, S.; GOODWIN, A.; DUBROVINSKY, L.; DUBROVINSKAIA, N. (2016): Structural distortions in the high-pressure polar phases of ammonium metal formates. CrystEngComm 18, 8849-8857, doi: 10.1039/C6CE01891B

DE VRIES, J.; NIMMO, F.; MELOSH, H.J.; JACOBSON, S.A.; MORBIDELLI, A.; RUBIE, D.C. (2016): Impact-induced melting during accretion of the Earth. Progress in Earth and Planetary Science 3:7; doi: 10.1186/s40645-016-0083-8

DORFMAN, S.M.; DUTTON, S.E.; POTAPKIN, V.; CHUMAKOV, A.I.; RUEFF, J.-P.; CHOW, P.; XIAO, Y.; CAVA, R.J.; DUFFY, T.S.; MCCAMMON, C.A.; GILLET, P. (2016): Electronic transitions of iron in almandine-composition glass to 91 GPa. American Mineralogist 101, 1659-1667

DUBROVINSKAIA, N.; DUBROVINSKY, L.; SOLOPOVA, N.A.; ABAKUMOV, A.; TURNER, S.; HANFLAND, M.; BYKOVA, E.; BYKOV, M.; PRESCHER, C.; PRAKAPENKA, V.B.; PETITGIRARD, S.; CHUVASHOVA, I.; GASHAROVA, B.; MATHIS, Y.-L.; ERSHOV, P.; SNIGIREVA, I.; SNIGIREV, A. (2016): Terapascal static pressure generation with ultrahigh yield strength nanodiamond. Science Advances 2, e1600341, doi: 10.1126/sciadv.1600341

FEI, H.; KOIZUMI, S.; SAKAMOTO, N.; HASHIGUCHI, M.; YURIMOTO, H.; MARQUARDT, K.; MIYAJIMA, N.; YAMAZAKI, D.; KATSURA, T. (2016): New constraints on upper mantle creep mechanism inferred from silicon grain-boundary diffusion rates. Earth and Planetary Science Letters 433, 350-359

FEI, H.; KATSURA, T. (2016): Si and O self-diffusion in hydrous forsterite and iron-bearing olivine from the perspective of defect chemistry. Physics and Chemistry of Minerals 43, 119-126

FORBERG, D.; SCHWOB, T.; ZAHEER, M.; FRIEDRICH, M.; MIYAJIMA, N.; KEMPE, R. (2016): Single-catalyst high-weight% hydrogen storage in an N-heterocycle synthesized from lignin hydrogenolysis products and ammonia. Nature Communications 7, 13201, doi: 10.1038/ncomms13201

GENTILI, S.; BIAGIONI, C.; COMODI, P.; PASERO, M.; MCCAMMON, C.; BONADIMAN, C. (2016): Ferri-kaersutite, $NaCa_2(Mg_3TiFe^{3+})(Si_6Al_2)O_{22}O_2$, a new anhydrous amphibole from Harrow Peaks, Northern Victoria Land, Antarctica. American Mineralogist 101, 461-468

GILLMANN, C.; GOLABEK, G.J.; TACKLEY, P.J. (2016): Effect of a single large impact on the coupled atmosphere-interior evolution of Venus. Icarus 268, 295-312, doi: 10.1016/j.icarus.2015.12.024

GIRARD, J.; AMULELE, G.; FARLA, R.J.M.; MOHIUDDIN, A.; KARATO, S. (2016): Shear deformation of bridgmanite and magnesiowüstite aggregates at lower mantle conditions. Science 351, 144-147

GLAZYRIN, K.; MIYAJIMA, N.; SMITH, J.S.; LEE, K.K.M. (2016): Compression of a multiphase mantle assemblage: Effects of undesirable stress and stress annealing on the iron spin state crossover in ferropericlase. Journal of Geophysical Research-Solid Earth 121, 3377-3392

GOLOSOVA, N.O.; KOZLENKO, D.P.; KICHANOV, S.E.; LUKIN, E.V.; DUBROVINSKY, L.S.; MAMMADOV, A.I.; MEHDIYEVA, R.Z.; JABAROV, S.H.; LIERMANN, H.-P.; GLAZYRIN, K.V. (2016): Structural, magnetic and vibrational properties of multiferroic $GaFeO_3$ at high pressure. Journal of Alloys and Compounds 684, 352-358

GU, T.; LI, M.; MCCAMMON, C.; LEE, K.K.M. (2016): Redox-induced lower mantle density contrast and effect on mantle structure and primitive oxygen. Nature Geoscience 9, 723-727

GUTIERREZ, X.; SCHIAVI, F.; KEPPLER, H. (2016): The adsorption of HCl on volcanic ash. Earth and Planetary Science Letters 438, 66-74

IDRISSI, H.; BOLLINGER, C.; BOIOLI, F.; SCHRYVVERS, N.; CORDIER, P. (2016): Low-temperature plasticity of olivine revisited with *in situ* TEM nanomechanical testing. Science Advances 2, No. 3, e1501671

ISHII, T.; SHI, L.; HUANG, R.; TSUJINO, N.; DRUZHBIN, D.; MYHILL, R.; LI, Y.; WANG, L.; YAMAMOTO, T.; MIYAJIMA, N.; KAWAZOE, T.; NISHIYAMA, N.; HIGO, Y.; TANGE, Y.; KATSURA, T. (2016): Generation of pressures over 40 GPa using Kawai-type multi-anvil press with tungsten carbide anvils. Review of Scientific Instruments 87, 024501

ISMAILOVA, L.; BYKOVA, E.; BYKOV, M.; CERANTOLA, V.; MCCAMMON, C.; BOFFA BALLARAN, T.; BOBROV, A.; SINMYO, R.; DUBROVINSKAIA, N.; GLAZYRIN, K.; LIERMANN, H.-P.; KUPENKO, I.; HANFLAND, M.; PRESCHER, C.; PRAKAPENKA, V.; SVITLYK, V.; DUBROVINSKY, L. (2016): Stability of Fe, Al-bearing bridgmanite in the lower mantle and synthesis of pure Fe-bridgmanite. Science Advances 2, e1600247, doi: 10.1126/sciadv.1600427

JACOBSON, S.A. (2016): Multiple origins of asteroid pairs. Proceedings of the International Astronomical Union 318, 55-65

JACOBSON, S.A.; MARZARI, F.; ROSSI, A.; SCHEERES, D.J. (2016): Testing the YORP-induced rotational fission hypothesis. Icarus 277, 381-394

KARKIN, A.E.; VORONIN, V.I.; MOROZOVA, N.V.; OVSYANNIKOV, S.V.; TAKARABE, K.; MORI, Y.; NAKAMURA, S.; SHCHENNIKOV, V.V. (2016): Unconventional electronic properties of Mg_2Si thermoelectrics revealed by fast-neutron-irradiation doping. Journal of Physical Chemistry C 120, 9692-9701

KAWAZOE, T.; NISHIHARA, Y.; OHUCHI, T.; MIYAJIMA, N.; MARUYAMA, G.; HIGO, Y.; FUNAKOSHI, K.; IRIFUNE, T. (2016): Creep strength of ringwoodite measured at pressure-temperature conditions of the lower part of the mantle transition zone using a deformation-DIA apparatus. Earth and Planetary Science Letters 454, 10-19

KAWAZOE, T.; CHAUDHARI, A.; SMYTH, J.R.; MCCAMMON, C. (2016): Coupled substitution of Fe^{3+} and H^+ for Si in wadsleyite: a study by polarized infrared and Mössbauer spectroscopies and single-crystal X-ray diffraction. American Mineralogist (Letter) 101, 1236-1239

KEPPLER, R.; STIPP, M.; BEHRMANN, J.H.; ULLEMEYER, K.; HEIDELBACH, F. (2016): Deformation inside a subduction channel – Insights from microstructures and crystallographic preferred orientations of eclogites from the Tauern Window, Austria. Journal of Structural Geology 82, 60-79

KEMPL, J.; VROON, P.Z.; VAN DER WAGT, B.; ZINNGREBE, E.; FROST, D.J.; VAN WESTRENEN, W. (2016): Silicon stable isotope fractionation between metal and silicate at high-pressure, high-temperature conditions as a tracer of planetary core formation. Netherlands Journal of Geosciences 95, 113-129

KLIMM, O.; GÖBEL, Chr.; ROSENFELD, S.; PUCHTLER, F.; MIYAJIMA, N.; MARQUARDT, K.; DRECHSLER, M.; BREU, J.; FÖRSTER, St.; WEBER, B. (2016): Synthesis of $[Fe(L)(bipy)]_n$ spin crossover nanoparticles using blockcopolymer micelles. Nanoscale 8, 19058-19065, doi: 10.1039/C6NR06330F

KONYASHIN, I.; FROST, D.J.; CROSSLEY, A.; JURKSCHAT, K.; JOHNSTON, C.; ARMSTRONG, K. (2016): Nano-diamond obtained from adipic acid at ultra-high pressures. Materials Letters 183, 14-18

LAURENZ, V.; RUBIE, D.C.; FROST, D.J.; VOGEL, A.K. (2016): The importance of sulfur for the behavior of highly-siderophile elements during Earth's differentiation. Geochimica et Cosmochimica Acta 194, 123-138

LI, Y.; MARTY, B.; SHCHEKA, S.; ZIMMERMANN, L.; KEPPLER, H. (2016): Nitrogen isotope fractionation during terrestrial core-mantle separation. Geochemical Perspectives Letters 2, 138-147

LICHTENBERG, T.; GOLABEK, G.J.; GERYA, T.V.; MEYER, M.R. (2016): The effects of short-lived radionuclides and porosity on the early thermo-mechanical evolution of planetesimals. Icarus 274, 350-365, doi: 10.1016/j.icarus.2016.03.004

LIU, J.; LIN, J.-F.; ALATAS, A.; HU, M.Y.; ZHAO, J.; DUBROVINSKY, L. (2016): Seismic parameters of hcp-Fe alloyed with Ni and Si in the Earth's inner core. Journal of Geophysical Research B: Solid Earth 121, 610-623

LIU, X.; CHEN, X.; MA, H.A.; JIA, X.; WU, J.; YU, T.; WANG, Y.; GUO, J.; PETITGIRARD, S.; BINA, C.R.; JACOBSEN, S.D. (2016): Ultrahard stitching of nanotwinned diamond and cubic boron nitride in C_2-BN composite. Nature Scientific Reports, 6, 30518, doi: 10.1038/srep30518

LIU, Z.D.; DU, W.; SHINMEI, T.; GREAX, S.; ZHOU, C.; ARIMOTO, T.; KUNIMOTO, T.; IRIFUNE, T.: Garnets in the majorite-pyrope system: symmetry, lattice microstrain, and order-disorder of cations. Physics and Chemistry of Minerals, doi: 10.1007/s00269-016-0852-3

MALLIK, A.; DASGUPTA, R.; TSUNO, K.; NELSON, J. (2016): Effects of water, depth and temperature on partial melting of mantle-wedge fluxed by hydrous sediment-melt in subduction zones. Geochimica et Cosmochimica Acta 195, 226-243

MASOTTA, M.; KEPPLER, H.; CHAUDHARI, A. (2016): Fluid-melt partitioning of sulfur in differentiated arc magmas and the sulfur yield of explosive volcanic eruptions. Geochimica et Cosmochimica Acta 176, 26-43

MCCAMMON, C.; CARACAS, R.; GLAZYRIN, K.; POTAPKIN, V.; KANTOR, A.; SINMYO, R.; PRESCHER, C.; KUPENKO, I.; CHUMAKOV, A.; DUBROVINSKY, L. (2016): Sound velocities of bridgmanite from density of states determined by nuclear inelastic scattering and first principles calculations. Progress in Earth and Planetary Science 3, doi: 10.1186/s40645-016-0089-2

MCENROE, S.A.; ROBINSON, P.; MIYAJIMA, N.; FABIAN, K.; DYAR, D.; SKLUTE, E. (2016): Lamellar magnetism and exchange bias in billion-year-old titanohematite with nanoscale ilmenite exsolution lamellae: I. Mineral and magnetic characterization. Geophysical Journal International 206, 470-486

MONDAL, S.; BYKOVA, E.; DEY, S.; ALI, S.I.; DUBROVINSKAIA, N.; DUBROVINSKY, L.; PARAKHONSKIY, G.; VAN SMAALEN, S. (2016): Disorder and defects are not intrinsic to boron carbide. Nature Scientific Reports 6, 19330, doi: 10.1038/srep19330

MORBIDELLI, A.; BITSCH, B.; CRIDA, A.; GOUNELLE, M.; GUILLOT, T.; JACOBSON, S.A.; JOHANSEN, A.; LAMBRECHTS, M.; LEGA, E. (2016): Fossilized condensation lines in the solar system protoplanetary disk. Icarus 267, 368-376

MYHILL, R.; OJWANG, D.; ZIBERNA, L.; FROST, D.J.; BOFFA BALLARAN, T.; MIYAJIMA, N. (2016): On the P-T fO_2 stability of Fe_4O_5, Fe_5O_6 and Fe_4O_5-rich solid solutions. Contrib Mineral Petrol 171, 51, doi: 10.1007/s00410-016-1258-4

NAMUR, O.; CHARLIER, B.; HOLTZ, F.; CARTIER, C.; MCCAMMON, C. (2016): Sulfur solubility in reduced mafic silicate melts: Implications for the speciation and distribution of sulfur on Mercury. Earth and Planetary Science Letters 448, 102-114

NAMUR, O.; COLLINET, M.; CHARLIER, B.; GROVE, T.L.; HOLTZ, F.; MCCAMMON, C. (2016): Melting processes and mantle sources of lavas on Mercury. Earth and Planetary Science Letters 439, 117-128

NESTOLA, F.; CERANTOLA, V.; MILANI, S.; ANZOLINI, C.; MCCAMMON, C.; NOVELLA, D.; KUPENKO, I.; CHUMAKOV, A.; RÜFFER, R.; HARRIS, J.W. (2016): Synchrotron Mössbauer Source technique for *in situ* measurement of iron-bearing inclusions in natural diamonds. Lithos 265, 328-333

NIMIS, P.; ALVARO, M.; NESTOLA, F.; ANGEL, R.J.; MARQUARDT, K.; RUSTIONI, G.; HARRIS, J.W.; MARONE, F. (2016): First evidence of hydrous silicic fluid films around solid inclusions in gem-quality diamonds. Lithos 260, 384-389, doi: 10.1016/ j.lithos.2016.05.019

ORIOLO, S.; OYHANTÇABAL, P.; WEMMER, K.; HEIDELBACH, F.; PFÄNDER, J.; BASEI, M.A.S.; HUECK, M.; HANNICH, F.; SIEGESMUND, S. (2016): Structural and geochronological constraints on the tectonic evolution of the Neoproterozoic Dom Feliciano Belt, Uruguay: assessing the birth of Gondwana. Journal of Structural Geology 92, 59-78

OVSYANNIKOV, S.; BYKOV, M.; BYKOVA, E.; KOZLENKO, D.; TSIRLIN, A.; KARKIN, A.; SHCHENNIKOV, V.; KICHANOV, S.; GOU, H.; ABAKUMOV, A.; EGOAVIL, R.; VERBEECK, J.; MCCAMMON, C.; DYADKIN, V.; CHERNYSHOV, D.; VAN SMAALEN, S.; DUBROVINSKY, L. (2016): Incommensurate crystallographic transition with competing dimeric and trimeric orders in iron oxide Fe_4O_5. Nature Chemistry 8, 501-508, doi: 10.1038/nchem.2478

PALOT, M.; JACOBSEN, S.D.; TOWNSEND, J.P.; NESTOLA, F.; MARQUARDT, K.; HARRIS, J.W.; STACHEL, T.; MCCAMMON, C.A.; PEARSON, D.G. (2016): Evidence for H_2O-bearing fluids in the lower mantle from diamond unclusion. Lithos 265, 237-243, doi: 10.1016/j.lithos.2016.06.023

PAMATO, M.G.; KURNOSOV, A.; BOFFA BALLARAN, T.; FROST, D.J.; ZIBERNA, L.; GIANNINI, M.; SPEZIALE, S.; TKACHEV, S.N.; ZHURAVLEV, K.K.; PRAKAPENKA, V.B. (2016): Single crystal elasticity of majoritic garnets: Stagnant slabs and thermal anomalies at the base of the transition zone. Earth and Planetary Science Letters 451, 114-124

PARSHIN, P.P.; CHUMAKOV, A.I.; ALEKSEEV, P.A.; NEMKOVSKI, K.S.; PERßON, J.; DUBROVINSKY, L.; KANTOR, A.; RÜFFER, R. (2016): Experimental observation of phonons as spectators in FeSi electronic gap formation. Physical Review B – Condensed Matter and Materials Physics 93, 081102

POSNER, E.S.; GANGULY, J.; HERVIG, R. (2016): Diffusion kinetics of Cr in spinel: Experimental studies and implications for ^{53}Mn-^{53}Cr cosmochronology. Geochimica et Cosmochimica Acta 175, 20-35

POTAPKIN, V.; DUBROVINSKY, L.; SERGUEEV, I.; EKHOLM, M.; KANTOR, I.; BESSAS, D.; BYKOVA, E.; PRAKAPENKA, V.; HERMANN, R.P.; RÜFFER, R. (2016): Magnetic interactions in NiO at ultrahigh pressure. Physical Review B – Condensed Matter and Materials Physics 93, 201110

RAYMOND, S.N.; IZIDORO, A.; BITSCH, B.; JACOBSON, S.A. (2016): Did Jupiter's core form in the innermost parts of the Sun's protoplanetary disk? Monthly Notices of the Royal Astronomical Society 458, 2962-2972

ROBINSON, P.; MCENROE, S.A.; MIYAJIMA, N.; KARL, F.; NATHAN, C. (2016): Remanent magnetization, magnetic coupling and interface ionic configurations of intergrown rhombohedral and cubic Fe-Ti oxides: a short survey. American Mineralogist 101, 518-530

RUBIE, D.C.; LAURENZ, V.; JACOBSON, S.A.; MORBIDELLI, A.; PALME, H.; VOGEL, A.; FROST, D.J. (2016): Highly siderophile elements were stripped from Earth's mantle by iron sulfide segregation. Science 353, 1141-1144

RUBIE, D.C.; JACOBSON, S.A. (2016): Mechanisms and geochemical models of core formation. – In: TERASAKI, H.; FISCHER, R. (Eds): Deep Earth: Physics and Chemistry of the Lower Mantle and Core, AGU Geophysical Monograph Series 217, AGU/John Wiley & Sons, Inc., Washington, DC, USA, 181-190

RUDLOFF-GRUND, J.; BRENKER, F.E.; MARQUARDT, K.; HOWELL, D.; SCHREIBER, A.; O'REILLY, S.Y.; GRIFFIN, W.L.; KAMINSKY, F.V. (2016): Nitrogen nanoinclusions in milky diamonds from Juina area, Mato Grosso State, Brazil. Lithos 265, 57-67

RUDLOFF-GRUND, J.; BRENKER, F.E.; MARQUARDT, K.; KAMINSKY, F.V.; SCHREIBER, A. (2016): STEM EDX nitrogen mapping of nanoinclusions in milky diamonds from Juina, Brazil, using a windowless silicon drift detector system. Analytical Chemistry 88(11), 5804-5808, doi: 10.1021/acs.analchem.6b00373

SCHRENK, K.J.; HILÁRIO, M.R.; SIDORAVICIUS, V.; ARAÚJO, N.A.M.; HERRMANN, H.J.; THIELMANN, M.; TEIXEIRA, A. (2016): Critical fragmentation properties of random drilling: How many holes need to be drilled to collapse a wooden cube? Physical Review Letters 116(5), 055701, doi: 10.1103/PhysRevLett.116.055701

SINMYO, R.; BYKOVA, E.; OVSYANNIKOV, S.V.; MCCAMMON, C.; KUPENKO, I.; ISMAILOVA, L.; DUBROVINSKY, L. (2016): Discovery of Fe_7O_9: a new iron oxide with a complex monoclinic structure. Nature Scientific Reports 6, 32852, doi: 10.1038/srep32852

STECKLOFF, J.K.; JACOBSON, S.A. (2016): The formation of striae within cometary dust tails by a sublimation-driven YORP-like effect. Icarus 264, 160-170

TAL, A.A.; KATSNELSON, M.I.; EKHOLM, M.; JÖNSSON, H.J.M.; DUBROVINSKY, L.; DUBROVINSKAIA, N.; ABRIKOSOV, I.A. (2016): Pressure-induced crossing of the core levels in 5d metals. Physical Review B – Condensed Matter and Materials Physics, 93, 205150

VALKOVSKIY, G.A.; ALTYNBAEV, E.V.; KUCHUGURA, M.D.; YASHINA, E.G.; SUKHANOV, A.S.; DYADKIN, V.A.; TSVYASHCHENKO, A.V.; SIDOROV, V.A.; FOMICHEVA, L.N.; BYKOVA, E.; OVSYANNIKOV, S.V.; CHERNYSHOV, D.YU.; GRIGORIEV, S.V. (2016): Thermal expansion of monogermanides of *3d*-metals. Journal of Physics: Condensed Matter 28, 375401

VLČEK, V.; EISENBERG, H.R.; STEINLE-NEUMANN, G.; NEUHAUSER, D.; RABANI, E.; BAER, R. (2016): Spontaneous charge carrier localization in extended one-dimensional systems. Physical Review Letters 116, 186401

WAGNER, J.; ADJAOUD, O.; MARQUARDT, K.; JAHN, S. (2016): Anisotropy of self-diffusion in forsterite grain boundaries derived from molecular dynamics simulations. Contrib Mineral Petrol 171, 98, doi: 10.1007/s00410-016-1308-y

WANG, L.; BLAHA, S.; PINTÉR, Z.; FARLA, R.; KAWAZOE, T.; MIYAJIMA, N.; MICHIBAYASHI, K.; KATSURA, T. (2016): Temperature dependence of [100](010) and [001](010) dislocation mobility in natural olivine. Earth and Planetary Science Letters 441, 81-90, doi: 10.1016/j.epsl.2016.02.029

WANG, Z.; LAURENZ, V.; PETITGIRARD, S.; BECKER, H. (2016): Earth's moderately volatile element composition may not be chondritic: Evidence from In, Cd and Zn. Earth and Planetary Science Letters 435, 136-146

WU, Y.; WU, X.; LIN, J.-F.; MCCAMMON, C.A.; XIAO, Y.; CHOW, P.; PRAKAPENKA, V.B.; YOSHINO, T.; ZHAI, S.; QIN, S. (2016): Spin transition of ferric iron in the NAL phase: Implications for the seismic heterogeneities of subducted slabs in the lower mantle. Earth and Planetary Science Letters 434, 91-100

WU, X.; WU, Y.; LIN, J.-F.; LIU, J.; MAO, Z.; GUO, X.; YOSHINO, T.; MCCAMMON, C.; PRAKAPENKA, V.B.; XIAO, Y. (2016): Two-stage spin transition of iron in FeAl-bearing phase D at lower mantle. Journal of Geophysical Research – Solid Earth 121, doi: 10.1002/2016JB013209

XIE, L.; YONEDA, A.; YOSHINO, T.; FEI, H.; ITO, E. (2016): Graphite-boron composite heater in a Kawai-type apparatus: the inhibitory effect of boron oxide and countermeasures. High Pressure Research 36, 105-120

YANG, X.; KEPPLER, H.; LI, Y. (2016): Molecular hydrogen in mantle minerals. Geochemical Perspectives Letters 2, 160-168

YOUNG, E.D.; KOHL, I.E.; WARREN, P.H.; RUBIE, D.C.; JACOBSON, S.A.; MORBIDELLI, A. (2016): Oxygen isotopic evidence for vigorous mixing during the Moon-forming giant impact. Science 351, 493-496

ZAKHAROV, B.A.; SERYOTKIN, Y.V.; TUMANOV, N.A.; PALIWODA, D.; HANFLAND, M.; KURNOSOV, A.V.; BOLDYREVA, E.V. (2016): The role of fluids in high-pressure polymorphism of drugs: different behaviour of beta-chlorpropamide in different inert gas and liquid media. RSC Advances 6 (95), 92629-92637, doi: 10.1039/c6ra17750f

ZHANG, L.; SMYTH, J.R.; ALLAZ, J.; KAWAZOE, T.; JACOBSEN, S.D.; JIN, Z. (2016): Transition metals in the transition zone: crystal chemistry of minor element substitution in wadsleyite. American Mineralogist 101, 2322-2330

ZHANG, Q.; WU, X.; OVSYANNIKOV, S.V.; DONG, J.; QIN, S.; DUBROVINSKY, L.S.; CHEN, D. (2016): High-pressure, high-temperature synthesis and properties of the monoclinic phase of Y_2O_3. Chemical Research in Chinese Universities 32, 545-548

5.2 Publications (submitted, in press)

ARAKCHEEVA, A.; BYKOV, M.; BYKOVA, E.; DUBROVINSKY, L.; PATTISON, P.; DMITRIEV, V.: Incommensurate density waves in the high-pressure IV-B phase of barium. IUCRJ (submitted)

ARATÓ, R.; AUDÉTAT, A.: Experimental calibration of a new oxybarometer for silicic magmas based on vanadium partitioning between magnetite and silicate melt. Geochimica et Cosmochimica Acta (submitted)

BIANCHI, F.; THIELMANN, M.; HERRMANN, H.J.: Bursts in the permeability of particle-laden ows through porous media. Physical Review Letters (submitted)

BORCHARDT, S.; EBERT, T.; KONRAD-SCHMOLKE, M.; MCCAMMON, C.; NEVERMANN, H.; TRAUTH, M.H.: Correlating hyperspectral reflectance data with weathering induced chemico-mineralogical changes in a phonolite from the Suguta Valley, Kenya. Journal of Geophysical Research – Earth Surface (submitted)

BYKOVA, E.; KUPENKO, I.; MERLINI, M.; ISMAILOVA, L.; MCCAMMON, C.; BYKOV, M.; CHUMAKOV, A.; PETITGIRARD, S.; KANTOR, I.; SVITLYK, V.; JACOBS, J.; HANFLAND, M.; MEZOUAR, M.; PRESCHER, C.; RÜFFER, R.; DUBROVINSKY, L.: Stability of iron-bearing carbonates in the deep Earth's interior. Nature Communications (submitted)

CERANTOLA, V.; BYKOVA, E.; KUPENKO, I.; MERLINI, M.; ISMAILOVA, L.; MCCAMMON, C.; BYKOV, M.; CHUMAKOV, A.; PETITGIRARD, S.; KANTOR, I.; SVITLYK, V.; JACOBS, J.; PRESCHER, C.; RÜFFER, R.; DUBROVINSKY, L.: Stability of iron-bearing carbonates in the deep Earth's interior. Nature Communications (submitted)

ČERNOK, A.; MARQUARDT, K.; CARACAS, R.; BYKOVA, E.; HABLER, G.; LIERMANN, H.-P.; HANFLAND, M.; DUBROVINSKY, L.: High-pressure behaviour of cristobalite: bridging the gap towards the "seifertite enigma". Nature Scientific Reports (submitted)

CHARITON, S.; CERANTOLA, V.; ISMAILOVA, L.; BYKOVA, E.; BYKOV, M.; KUPENKO, I.; BOFFA BALLARAN, T.; MCCAMMON, C.; DUBROVINSKY, L.: The high-pressure behavior of spherocobaltite ($CoCO_3$): A Raman spectroscopy and XRD study. American Mineralogist (submitted)

CHUVASHOVA, I.; BYKOVA, E.; BYKOV, M.; SVITLYK, V.; GASHAROVA, B.; MATHIS, Y.-L.; CARACAS, R.; DUBROVINSKY, L.; DUBROVINSKAIA, N.: High-pressure behavior of α-boron studied on single crystals by X-ray diffraction, Raman and IR spectroscopy. Journal of Solid State Chemistry (in press) doi: 10.1016/j.jssc.2016.10.002

COLLINGS, I.E.; BYKOV, M.; BYKOVA, E.; TUCKER, M.G.; PETITGIRARD, S.; HANAND, M.; GLAZYRIN, K.; VAN SMAALEN, S.; GOODWIN, A.L.; DUBROVINSKY, L.; DUBROVINSKAIA, N.: Structural distortions in the high-pressure polar phases of ammonium metal formates. CrystEngComm (accepted), doi: 10.1039/C6CE01891B

COLLINGS, I.E.; BYKOVA, E.; BYKOV, M.; PETITGIRARD, S.; HANAND, M.; PALIWODA, D.; DUBROVINSKY, L.; DUBROVINSKAIA, N.: Neon-bearing ammonium metal formates: formation and behaviour under pressure. ChemPhysChem (accepted), doi: 10.1002/cphc.201600854

DANG, N.T.; ZAKHVALINSKII, V.S.; KOZLENKO, D.P.; PHAN, T.-L.; NEKRASOVA, YU.S.; TRANG, T.T.; KICHANOV, S.E.; SAVENKO, B.N.; THANH, T.D.; TARAN, S.V.; JABAROV, S.G.; OVSYANNIKOV, S.V.; KHIEM, L.H. (2016): Influence of Fe doping on the structural, magnetic and electrical transport properties of $La_{0.7}Ca_{0.3}Mn_{0.5}Fe_{0.5}O_3$. Journal of Electronic Materials (submitted)

DUCHOSLAV, M.; MARKS, M.A.W.; DROST, K.; MCCAMMON, C.; MARSCHALL, H.; WENZEL, T.; MARKL, G.: Changes in tourmaline composition during magmatic and hydrothermal processes leading to tin-ore deposition: The Cornubian Batholith, SW England. Ore Geology Reviews (in press)

FEI, H.; WIEDENBECK, M.; SAKAMOTO, N.; YURIMOTO, H.; YOSHINO, T.; YAMAZAKI, D.; KATSURA, T.: Negative activation volume of oxygen self-diffusion in forsterite. Physics of the Earth and Planetary Interiors (submitted)

GOLABEK, G.J.; BOURDON, B.; ROZEL, A.B.; GERYA, T.V.: Post-magma ocean mixing of reservoirs inside the angrite parent body. Earth and Planetary Science Letters (submitted)

GUO, H.; AUDÉTAT, A.: Solubility of gold in oxidized, sulfur-bearing fluids at 500-850 °C and 200-230 MPa: a synthetic fluid inclusion study. Geochimica et Cosmochimica Acta (submitted)

GUO, H.; AUDÉTAT, A.: Transfer of volatiles and metals from mafic to felsic magmas in composite magma chambers: an experimental study. Geochimica et Cosmochimica Acta (in press)

ISHII, T.; SINMYO, R.; KOMABAYASHI, T.; BOFFA BALLARAN, T.; KAWAZOE, T.; MIYAJIMA, N.; HIROSE, K.; KATSURA, T.: Synthesis and crystal structure of $LiNbO_3$-type $Mg_3Al_2Si_3O_{12}$. American Mineralogist (submitted)

ISMAILOVA, L.; BYKOV, M.; BYKOVA, E.; BOBROV, A.; KUPENKO, I.; CERANTOLA, V.; VASIUKOV, D.; DUBROVINSKAIA, N.; MCCAMMON, C.; HANFLAND, M.; GLAZYRIN, K.; LIERMANN, H.-P.; CHUMAKOV, A.; DUBROVINSKY, L.: Effect of composition on compressibility of skiagite-Fe-majorite garnet. American Mineralogist (in press), doi: 10.2138/am-2017-5856

JACOBSON, S.A.; HERNLUND, J.; RUBIE, D.C.; MORBIDELLI, A.: Formation, stratification, and mixing of Earth's core. Earth and Planetary Science Letters (submitted)

JACOBSON, S.A.: Asteroid geophysics from applying tidal theory to binary asteroids. Astronomy and Astrophysics (submitted)

JOURNAUX, B.; DANIEL, I.; PETITGIRARD, S.; CARDON, H.; PERRILLAT, J.P.; CARACAS, R.; MEZOUAR, M.: Salt partitioning between water and high-pressure ices. Implication for the dynamics and habitability of icy moons and water-rich planetary bodies. Earth and Planentary Science Letters (submitted)

KATSURA, T.; BABA, K.; YOSHINO, T.; KOGISO, T.: Electrical conductivity of the oceanic asthenosphere and its interpretation based on laboratory measurements. Lithos (submitted)

KATSURA, T.; FEI, H.: The effects of proton on Si and O self-diffusion coefficients in olivine and wadsleyite. – In: Water in the Earth – Origin and evolution of the blue planet. Book series: Advances in Geological Science, Elsevier (submitted)

KEPPLER, H.: Fluids and trace element transport in subduction zones. American Mineralogist (in press)

KRESSALL, R.D.; FEDORTCHOUK, Y.; MCCAMMON, C.; ELLIOT, B.: Stability of chromite and ilmenite in a silicate melt at various fO_2 at 0.1 MPa: new insights into use of oxides as diamond indicator minerals in kimberlites. Journal of Petrology (submitted)

KURNOSOV, A.; MARQUARDT, H.; FROST, D.J.; BOFFA BALLARAN, T.; ZIBERNA, L.: High-pressure single crystal elasticity measurements of Al-Fe-bridgmanite support a Fe^{3+}-rich pyrolitic lower mantle. Nature (submitted)

KUTZSCHBACH, M.; GUTTMANN, P.; MARQUARDT, K.; WERNER, S.; HENZLER, K.; WILKE, M.: Corrosion of silicate glasses at the nanometer scale: A TXM and XANES approach. Physics and Chemistry of Glasses – European Journal of Glass Science and Technology Part B (submitted)

LAUMONIER, M.; FARLA, R.; FROST, D.; KATSURA, T.; MARQUARDT, K.; BOUVIER, A.-S.: Experimental determination of melt interconnectivity and electrical conductivity in the upper mantle. Earth and Planetary Science Letters (submitted)

LAUMONIER, M.; GAILLARD, F.; MUIR, D.; BLUNDY, J.; UNSWORTH, M.: Giant magmatic water reservoirs at mid-crustal depth inferred from electrical conductivity and the growth of the continental crust. Earth and Planetary Science Letter (in press)

LICHTENBERG, T.; GOLABEK, G.J.; DULLEMOND, C.P.; SCHÖNBÄCHLER, M.; GERYA, T.V.; MEYER, M.R.: A thermo-mechanical 'Goldilocks' regime for impact splash chondrule formation. Science Advances (submitted)

LIN, F.; MERKEL, S.; HILAIRET, N.; MARQUARDT, H.; IMMOOR, J.; TOMÉ, C.; MIYAGI, L.: Application of the elasto-viscoplastic self-consistent (EVPSC) to modeling texture and lattice strain evolution in periclase. Journal of Applied Physics (submitted)

MAEDA, F.; KAMADA, S.; OHTANI, E.; HIRAO, N.; MITSUI, T.; MASUDA, R.; MIYAHARA, M.; MCCAMMON, C.: Spin state and electronic environment of iron in basaltic glass in the lower mantle. American Mineralogist (submitted)

MARQUARDT, H.; KURNOSOV, A.; FROST, D.J.; BOFFA BALLARAN, T.; ZIBERNA, L.: High-pressure single-crystal elasticity measurements of Al-Fe-bridgmanite support a Fe^{3+}-rich pyrolitic lower mantle. Nature (submitted)

MARQUARDT, K.; DE GRAEF, M.; SING, S.: Quantitative electron backscatter diffraction data (EBSD) analyses using the dictionary indexing (DI) approach: overcoming indexing difficulties on geological materials. American Mineralogist (submitted)

MARTIN, R.F.; ALARIE, É.; MINARIK, W.; WÁCZEK, Z.; MCCAMMON, C.A.: Titanian magnesio-hastingsite macrocrysts, Lafarge quarry, east-end Montreal: Disequilibrium crystallization in a pseudo-unary system. Canadian Mineralogist (in press)

MASOTTA, M.; KEPPLER H.: A new hydrothermal moissanite cell apparatus for optical *in situ* observations at high pressure and high temperature, with applications to bubble nucleation in silicate melts. American Mineralogist (submitted)

MIYAJIMA, N.; LI, Y.; ABEYKOON, S.; HEIDELBACH, F.: Electron channelling contrast imaging of individual dislocations in geological materials using a field emission scanning electron microscope. European Journal of Mineralogy (submitted)

MONTEUX, J.: GOLABEK, G.J.; RUBIE, D.C.; TOBIE, G.; YOUNG, E.D.: Water and the interior structure of terrestrial planets and icy bodies. – In: BLANC, M.; MORBIDELLI, A. (Eds.): The Delivery of Water to Proto-planets, Planets and Satellites. Space Science Series of ISSI 64 (submitted)

MORBIDELLI, A.; NESVORNY, D.; MARCHI, S.; RUBIE, D.; ELKINS-TANTON, L.; JACOBSON, S.A.; LAURENZ, V.: The lunar late heavy bombardment as the tail-end of accretion. Nature (submitted)

NISHIYAMA, N.; ISHIKAWA, R.; OHFUJI, H.; MARQUARDT, H.; KURNOSOV, A.; TANIGUCHI, T.; KIM, B.; YOSHIDA, H.; MASUNO, A.; BEDNARCIK, J.; KULIK, E.; IKUHARA, Y.; WAKAI, F.; IRIFUNE, T.: Transparent polycrystalline cubic silicon nitride. Nature Scientific Reports (submitted)

O'BRIEN, D.P.; RAYMOND, S.N.; RUBIE, D.C.; JACOBSON, S.A.; IZIDORO, A.: The delivery of water during terrestrial planet formation. – In: BLANC, M.; MORBIDELLI, A. (Eds.): The Delivery of Water to Proto-planets, Planets and Satellites. Space Science Series of ISSI 64 (submitted)

OVSYANNIKOV, S.V.; MOROZOVA, N.V.; KOROBEINIKOV, I.V.; HABORETS, V.; YEVYCH, R.; VYSOCHANSKII, Y.; SHCHENNIKOV, V.V. (2016): Tuning the electronic and vibrational properties of $Sn_2P_2Se_6$ and $Pb_2P_2S_6$ crystals and their metallization under high pressure. Dalton Transactions (in press)

PAKHOMOVA, A.; ISMAILOVA, L.; BYKOVA, E.; BYKOV, M.; BOFFA BALLARAN, T.; DUBROVINSKY, L.: A new high-pressure phase transition in clinoferrosilite: *in situ* single crystal X-ray diffraction study. American Mineralogist (accepted), doi: 10.2138/am-2017-5853

PETITGIRARD, S.: Density and structural changes of silicate glasses under high pressure. High Pressure Research (submitted)

PETITGIRARD, S.; SPIEKERMANN, G.; WEIS, C.; SAHLE, C.; STERNEMANN, C.; WILKE, M.: Miniature diamond anvils for X-ray Raman scattering spectroscopy high-pressure experiments. Journal of Synchrotron Radiation (submitted)

POMMIER, A.; KOHLSTEDT, D.L.; HANSEN, L.; MACKWELL, S.J.; TASAKA, M.; HEIDELBACH, F.; LEINENWEBER, K.: Experimental investigation of the effect of shear on the electrical properties of polycrystalline olivine. Earth and Planetary Science Letters (submitted)

POMMIER, A.; LAURENZ V.; DAVIES, C.J.; FROST, D.J.: Melting phase relations in the Fe-S and Fe-S-O systems at core conditions in small terrestrial bodies. Journal of Geophysical Research – Planets (submitted)

POSNER, E.; RUBIE, D.C.; FROST, D.J.; VLČEK, V.; STEINLE-NEUMANN, G.: High P-T experiments and first principles calculations of the diffusion of Si and Cr in liquid iron. Geochimica et Cosmochimica Acta (submitted)

ROZEL, A.B.; GOLABEK, G.J.; JAIN, C.; TACKLEY, P.J.; GERYA, T.V.: Pre-plate tectonics Earth: plutonic squishy lid or heat-pipe? Nature (submitted)

SAHLE, C.J.; ROSA, A.D.; ROSSI, M.; CERANTOLA, V.; SPIEKERMANN, G.; PETITGIRARD, S.; JACOBS, J.; HUOTARI, S.; MORETTI, M.; MIRONE, A.: Direct tomography imaging for inelastic X-ray scattering experiments at high pressure. Journal of Synchrotron Radiation (submitted)

SCHULZE, K.; BUCHEN, J.; KURNOSOV, A.; MARQUARDT, H.: Novel multi-sample approach for improved single-crystal elasticity measurements at high pressure and high temperature. High Pressure Research (submitted)

SHCHIPALKINA, N.; CHUKANOV, N.; PEKOV, I.; AKSENOV, S.; MCCAMMON, C.; BELAKOVSKY, D.; BRITVIN, S.; KOSHLYAKOVA, N.; SCHÄFER, C.; SCHOLZ, R.; RASTSVETAEVA, R.: Ferrorhodonite, $CaMn_3Fe[Si_5O_{15}]$, a new mineral species from Broken Hill, New South Wales, Australia. Physics and Chemistry of Minerals (in press)

SIERSCH, N.C.; BOFFA BALLARAN, T.; UENVER-THIELE, L.; WOODLAND, A.: Compressibility and high-pressure structural behavior of $Mg_2Fe_2O_5$. American Mineralogist (accepted)

SINMYO, R.; KEPPLER, H.: Electrical conductivity of NaCl-bearing aqueous fluids to 600 °C and 1 GPa. Contrib Mineral Petrol (submitted)

SINMYO, R.; MCCAMMON, C.; DUBROVINSKY, L.: The spin state of Fe^{3+} in lower mantle bridgmanite. American Mineralogist (submitted)

UENVER-THIELE, L.; WOODLAND, A.B.; BOFFA BALLARAN, T.; MIYAJIMA, N.; FROST, D.J.: Phase relations of $MgFe_2O_4$ at conditions of the deep upper mantle and transition zone. American Mineralogist (in press)

WANG, L.; BLAHA, S.; KAWAZOE, T.; MIYAJIMA, N.; KATSURA, T.: Identical activation volumes of dislocation mobility in the [100](010) and [001](010) slip systems in natural olivine. Geophysical Research Letters (submitted)

WU, Y.; QIN, F.; WU, X.; HUANG, H.; MCCAMMON, C.A.; YOSHINO, T.; ZHAI, S.; XIAO, Y.; PRAKAPENKA, V.B.: Spin transition of ferric iron in the CF phase in subducted MORB. Geophysical Research Letters (submitted)

XU, F.; YAMAZAKI, D.; SAKAMOTO, N.; SUN, W.; FEI, H.; YURIMOTO, H.; ITO, E.: Silicon and oxygen self-diffusion in stishovite: implications for stability of SiO_2-rich seismic reflectors in the mid-mantle. Earth and Planetary Science Letters (submitted)

YOSHINO, T.; ZHANG, B.; RHYMER, B.; ZHAO, C.; FEI, H.: Pressure dependence of electrical conductivity in forsterite. Journal of Geophysical Research (submitted)

YUSENKO, K.; BYKOVA, E.; BYKOV, M.; GROMILOV, S.A.; KURNOSOV, A.V.; PRESCHER, C.; PRAKAPENKA, V.B.; CRICHTON, W.A.; HANFLAND, M.; MARGADONNA, S.; DUBROVINSKY, L.S.: High-pressure high-temperature stability of hcp-IrxOs1-x (x = 0.50 and 0.55) alloys. Journal of Alloys and Compounds (submitted)

ZHANG, D.; AUDÉTAT, A.: Chemistry, mineralogy and crystallization conditions of porphyry Mo-forming magmas at Urad–Henderson and Silver Creek, Colorado, USA. Journal of Petrology (in press)

ZHANG, D.; AUDÉTAT, A.: What caused the formation of the giant Bingham Canyon porphyry Cu-Mo-Au deposit? Insights from melt inclusions and magmatic sulfides. Economic Geology (in press)

5.3 Presentations at scientific institutions and at congresses

ADAMS, A.; THIELMANN, M.; GOLABEK, G.: 11.-14.09.2016, German-Swiss Geodynamics Workshop 2016, Lichtenfels, Germany: "Viability of archean subduction initiation from gravitational spreading"

ADAMS, A.; THIELMANN, M.; GOLABEK, G.: 12.-16.12.2016, AGU Fall Meeting, San Francisco, USA[*D]: "Viability of archean subduction initiation from gravitational spreading", Abstract T31B-2894, 2016

ANZOLINI, C.; ANGEL, R.J.; NESTOLA, F.; BRENKER, F.E.; MILANI, S.; ALVARO, M.; CERANTOLA, V.; MCCAMMON, C.; HARRIS, J.W.: 23.-28.07.2016, Deep Carbon Observatory Summer School 2016, Yellowstone National Park, USA: "Inclusions in super-deep diamonds"

APRILIS, G.; STROHM, C.; KUPENKO, I.; MCCAMMON, C.; VASIUKOV, D.; LINHARDT, S.; DUBROVINSKY, L.; DUBROVINSKAIA, N.: 04.-09.09.2016, 54th EHPRG Meeting, Bayreuth, Germany[*C]: "Double-sided pulsed laser heating system for time resolved geoscience and materials science applications"

ARATÓ, R.; AUDÉTAT, A.: 17.-22.04.2016, European Geosciences Union General Assembly 2016, Vienna, Austria: "Experimental calibration of a new oxybarometer for silicic magmas based on the partitioning of vanadium between magnetite and silicate melt", Geophysical Research Abstracts 18, EGU2016-12829, 2016

ARATÓ, R.; AUDÉTAT, A.: 05.-08.06.2016, EMPG XV, Zurich, Switzerland[*A]: "Vanadium partitioning between magnetite and silicate melt – experimental calibration and first application of a new oxybarometer for silicic magmas"

ARATÓ, R.; AUDÉTAT, A.: 26.06.-01.07.2016, Goldschmidt 2016, Yokohama, Japan: "Experimental calibration of a new oxybarometer for silicic magmas based on the partitioning of vanadium between magnetite and silicate melt", Goldschmidt Abstracts, 2016, 96

ARATÓ, R.; AUDÉTAT, A.: 03.-06.07.2016, JSPS-DFG International Workshop, Tohoku University, Sendai, Japan[*B]: "Experimental calibration of a new oxybarometer for silicic magmas based on the partitioning of vanadium between magnetite and silicate melt"

ARMSTRONG, K.; FROST, D.J.; MCCAMMON, C.M.; RUBIE, D.; BOFFA BALLARAN, T.: 21.-25.03.2016, 47th Lunar and Planetary Science Conference, The Woodlands, Houston, USA: "Oxidation states of Fe in silicate melts as a function of pressure and implications for redox evolution of the early mantle", Abstract 2580

ARMSTRONG, K.; FROST, D.J.; MCCAMMON, C.M.; RUBIE, D.; BOFFA BALLARAN, T.: 05.-08.06.2016, EMPG XV, Zurich, Switzerland[*A]: "The oxidation state of Fe in silicate melts as a function of pressure"

ARMSTRONG, K.; FROST, D.J.; MCCAMMON, C.; RUBIE, D.; BOFFA BALLARAN, T.: 26.06.-01.07.2016, Goldschmidt 2016, Yokohama, Japan: "The oxidation state of iron in silicate melts as a function of pressure", Goldschmidt Abstracts, 2016, 105

ARMSTRONG, K.; FROST, D.; MCCAMMON, C.; RUBIE, D.; BOFFA BALLARAN, T.: 03.-06.07.2016, JSPS-DFG International Workshop, Tohoku University, Sendai, Japan[*B]: "Oxidation state of Fe as a function of pressure: implications for redox profile of a magma ocean"

ARMSTRONG, K.; FROST, D.; MCCAMMON, C.; RUBIE, D.; BOFFA BALLARAN, T.; MIYAJIMA, N.: 12.-16.12.2016, AGU Fall Meeting, San Francisco, USA[*D]: "Iron speciation in minerals and melts at high pressure: Implications for the redox evolution of the early mantle", Abstract DI41A-2603, 2016

AUDÉTAT, A.: 19.-24.06.2016, Gordon Research Conference on Geochemistry of Mineral Deposits, Les Diablerets, Switzerland (*invited*): "The metal content of magmatic-hydrothermal fluids and its relation to mineralization potential"

BOFFA BALLARAN, T.; KURNOSOV, A.; FROST, D.J.; MARQUARDT, H.: 05.-08.06.2016, EMPG XV, Zurich, Switzerland[*A] (*keynote lecture*): "Cation substitution in $MgSiO_3$ bridgmanite: implication for the mineralogy of the Earth's lower mantle"

BOFFA BALLARAN, T.: 07.-11.09.2016, AIC International Crystallography School 2016, 'Polymorphism, stability and phase transitions in crystals: theory, experiments and applications', Rimini, Italy: "Brillouin studies of polymorphs relevant in Earth sciences"

BOLLINGER, C.; FARLA R.; MARQUARDT, K.: 11.-15.09.2016, 2nd European Mineralogical Conference, Rimini, Italy: "Grain boundaries in forsterite: how do they move to produce shear?"

BOLLINGER, C.; FARLA R.; KNOEDLER, P.; MARQUARDT, K.: 12.-16.12.2016, AGU Fall Meeting, San Francisco, USA[*D]: "Grain boundaries in forsterite: how do they move to produce shear?", Abstract MR51A-2675, 2016

BREMNER, P.M.; FUQUA, H.; MALLIK, A.; DIAMOND, M.; LOCK, S.J.; PANOVSKA, S.; NISHIKAWA, Y.; JIMENEZ-PEREZ, H.; SHAHAR, A.; PANERO, W.; LOGNONNÉ, P.; FAUL, U.: 12.-16.12.2016, AGU Fall Meeting, San Francisco, USA[*D]: "Constraints on lunar structure from combined geochemical, mineralogical, and geophysical modeling", Abstract DI34A-07, 2016

BUCHEN, J.; MARQUARDT, H.; KURNOSOV, A.; BOFFA BALLARAN, T.; KAWAZOE, T.; SPEZIALE, S.: 22.-24.02.2016, Meeting of the Sections Chemistry, Physics & Crystallography of Minerals and Applied Mineralogy in Technology & Environment of the Deutsche Mineralogische Gesellschaft, Bad Windsheim, Germany: "Single-crystal elasticity of wadsleyite at high pressures and high temperatures: approaching the transition zone in Earth's mantle"

BUCHEN, J.; MARQUARDT, H.; BOFFA BALLARAN, T.; SPEZIALE, S.; KAWAZOE, T.; KURNOSOV, A.: 05.-08.06.2016, EMPG XV, Zurich, Switzerland[*A]: "Internally consistent high-pressure single-crystal elasticity of $(Mg,Fe)_2SiO_4$ wadsleyite"

BUCHEN, J.; MARQUARDT, H.; BOFFA BALLARAN, T.; SPEZIALE, S.; KAWAZOE, T.; KURNOSOV, A.: 03.-06.07.2016, JSPS-DFG International Workshop, Tohoku University, Sendai, Japan[*B]: "Internally consistent high-pressure single-crystal elasticity of $(Mg,Fe)_2SiO_4$ wadsleyite"

BUCHEN, J.; MARQUARDT, H.; KURNOSOV, A.; SPEZIALE, S.; KAWAZOE, T.; BOFFA BALLARAN, T.: 04.-09.09.2016, 54th EHPRG Meeting, Bayreuth, Germany[*C]: "Internally consistent single-crystal elasticity of $(Mg,Fe)_2SiO_4$ wadsleyite at high pressures and high temperatures"

BUCHEN, J.; MARQUARDT, H.; KURNOSOV, A.; SPEZIALE, S.; KAWAZOE, T.; BOFFA BALLARAN, T.: 11.-15.09.2016, 2nd European Mineralogical Conference, Rimini, Italy: "Internally consistent single-crystal elasticity of wadsleyite at high pressures and high temperatures"

BUCHEN, J.; KURNOSOV, A.; MARQUARDT, H.; BOFFA BALLARAN, T.; SPEZIALE, S.; KAWAZOE, T.: 12.-16.12.2016, AGU Fall Meeting, San Francisco, USA[*D]: "Internally consistent single-crystal elasticity of $(Mg_{0.89}Fe_{0.11})_2SiO_4$ wadsleyite at high pressures and high temperatures", Abstract MR23A-2665, 2016

BYKOV, M.; BYKOVA, E.; GLAZYRIN, K.; LIERMANN, H.-P.; HANFLAND, M.; DUBROVINSKY, L.; VAN SMAALEN, S.: 04.-09.09.2016, 54th EHPRG Meeting, Bayreuth, Germany[*C] (*invited*): "Incommensurate crystal structures of transition metal oxychlorides at high pressure"

BYKOVA, E.; BYKOV, M.; MCCAMMON C.A.; OVSYANNIKOV S.V.; LIERMANN H.-P.; KUPENKO, I.; CHUMAKOV, A.I.; RÜFFER, R.; HANFLAND, M.; PRAKAPENKA, V.; DUBROVINSKAIA, N.A.; DUBROVINSKY, L.S.: 30.05.-03.06.2016, 8th Russian Crystal Chemistry Conference, Suzdal, Russia: "Structural complexity of simple Fe_2O_3 oxide at high pressures and temperatures"

BYKOVA, E.; BYKOV, M.; MCCAMMON C.A.; OVSYANNIKOV, S.V.; LIERMANN, H.-P.; KUPENKO, I.; CHUMAKOV, A.I.; RÜFFER, R.; HANFLAND, M.; PRAKAPENKA, V.; DUBROVINSKAIA, N.A.; DUBROVINSKY, L.S: 04.-09.09.2016, 54th EHPRG Meeting, Bayreuth, Germany[*C]: "Structural complexity of simple Fe_2O_3 oxide at high pressures and temperatures"

BYKOVA, E.: 28.-29.10.2016, IUCr Workshop on High-Pressure Multigrain Crystallography, Argonne, USA: "High-pressure structural studies of iron oxides: progress and challenges"

CERANTOLA, V.; BYKOVA, E.; MERLINI, M.; KUPENKO, I.; ISMAILOVA, L.; MCCAMMON, C.; KANTOR, I.; BYKOV, M.; PETITGIRARD, S.; CHUMAKOV, A.; RÜFFER, R.; DUBROVINSKY, L.: 04.-09.09.2016, 54th EHPRG Meeting, Bayreuth, Germany*C: "From the crust to the core, $FeCO_3$ stability field in the deep Earth"

CHARITON, S.; CERANTOLA, V.; BYKOVA, E.; BYKOV, M.; ISMAILOVA, L.; KUPENKO, I.; APRILIS, G.; MCCAMMON, C.; DUBROVINSKY, L.: 04.-09.09.2016, 54th EHPRG Meeting, Bayreuth, Germany*C: "Transition metal carbonates ($MnCO_3$, $CoCO_3$) at extreme conditions"

CHARITON, S.; BYKOVA, E.; CERANTOLA, V.; BYKOV, M.; ISMAILOVA, L.; KUPENKO, I.; APRILIS, G.; MCCAMMON, C.A.; DUBROVINSKY, L.: 11.-15.09.2016, 2nd European Mineralogical Conference, Rimini, Italy: "The behavior of rhodochrosite ($MnCO_3$) at extreme conditions"

CHEN, J.; PAMATO, M.G.; INOUE, T.; KAKIZAWA, S.; YANG, B.; LIN, Y.; KATSURA, T.; KAWAZOE, T.; LIU, B.: 26.06.-01.07.2016, Goldschmidt 2016, Yokohama, Japan: "Water reservior in Earth's lower mantle", Goldschmidt Abstracts, 2016, 435

COLLINGS, I.E.; BYKOVA, E.; BYKOV, M.; PETITGIRARD, S.; HANFLAND, M.; PALIWODA, D.; DUBROVINSKAIA, N.; DUBROVINSKY, L.: 14.-17.03.2016, 24th Annual Meeting of the German Crystallographic Society (DGK) 2016, Stuttgart, Germany: "Neon-bearing ammonium metal formates: effect of inclusion at high pressure"

COLLINGS, I.E.; BYKOV, M.; BYKOVA, E.; DUBROVINSKAIA, N.; DUBROVINSKY, L.; PETITGIRARD, S.; VASIUKOV, D.; MCCAMMON, C.; HANFLAND, M.; PALIWODA, D.: 04.-09.09.2016, 54th EHPRG Meeting, Bayreuth, Germany*C: "Structure-property relationships in multiferroic metal-organic frameworks at high pressure"

CORDIER, P.; BOIOLI, F.; BOLLINGER, C.; IDRISSI, H.; MUSSI, A.; NZOGANG, B.C.; SCHRYVERS, D.: 17.-22.04.2016, European Geosciences Union General Assembly 2016, Vienna, Austria: "Dislocations: do you want them moving or in 3D?", Geophysical Research Abstracts 18, EGU2016-1761, 2016

DORFMAN, S.; POTAPKIN, V.; KUPENKO, I.; CHUMAKOV, A.; PRAKAPENKA, V.; MCCAMMON, C.; DUBROVINSKY, L.: 12.-16.12.2016, AGU Fall Meeting, San Francisco, USA*D: "Compressibility and spin state of iron-rich post-perovskite in ULVZs", Abstract MR21B-2647, 2016

DUBROVINSKY, L.S.: 26.-27.01.2016, Planetary Lecture, DESY Photon Science Users' Meeting 2016, Hamburg, Germany: "Studies at multimegabar pressures"

DUBROVINSKY, L.S.: 14.-17.03.2016, 24th Annual Meeting of the German Crystallographic Society (DGK) 2016, Stuttgart, Germany: "Iron-oxygen system at extreme conditions"

DUBROVINSKY, L.S.: 12.-15.06.2016, EPDIC15, The European Powder Diffraction Conference, Bari, Italy (*invited*): "Structural studies at high pressures"

DUNCAN, M.; GARBER, J.; HERNANDEZ, J.-A.; MARUYA, S.; ZENG, L.; FAUL, U.; MCCAMMON, C.; MONTAGNER, J.-P.; MORESI, L.; ROMANOWICZ, B.; STIXRUDE, L.: 11.12.2016, Pre-AGU 2016 CIDER Workshop, Berkeley, USA: "On the origin of high shear wave velocities in the deep roots of cratons"

FARLA, R.; HEIDELBACH, F.: 05.-08.06.2016, EMPG XV, Zurich, Switzerland[*A]: "Pure shear deformation of layered olivine – orthopyroxene aggregates"

FEI, H.; YAMAZAKI, D.; SAKURAI, M.; MIYAJIMA, M.; OHFUJI, H.; KATSURA, T.; YAMAMOTO, T.: 12.-16.12.2016, AGU Fall Meeting, San Francisco, USA[*D] (*invited*): "Dislocation mobility in ringwoodite and bridgmanite as functions of temperature and water content", Abstract MR14A-02, 2016

FEI, H.; WIEDENBECK, M.; SAKAMOTO, N.; YURIMOTO, H.; YOSHINO, T.; YAMAZAKI, D.; KATSURA, T.: 12.-16.12.2016, AGU Fall Meeting, San Francisco, USA[*D]: "Negative activation volume of oxygen self-diffusion in forsterite", Abstract MR42A-01, 2016

FROST, D.J.; KURNOSOV, A.; BOFFA BALLARAN, T.; MARQUARDT, H.; ARMSTRONG, K.; MYHILL, R.: 26.06.-01.07.2016, Goldschmidt 2016, Yokohama, Japan (*keynote*): "The redox state of the Earth's lower mantle", Goldschmidt Abstracts, 2016, 855

FROST, D.J.; BEYER, C.: 03.-06.07.2016, JSPS-DFG International Workshop, Tohoku University, Sendai, Japan[*B]: "The speciation of volatiles within the deep mantle and the formation of diamonds"

GAILLARD, F.; LAUMONIER, M.; SIFRÉ, D.: 05.-08.06.2016, EMPG XV, Zurich, Switzerland[*A]: "The electrical conductivity of hydrated silici, intermediate and carbonated melts"

GOLABEK, G.J.; LICHTENBERG, T.; GERYA, T.V.; MEYER, M.R.: 11.-15.01.2016, International Space Science Institute (ISSI) Workshop on 'The Delivery of Water to Proto-Planets, Planets and Satellites', Bern, Switzerland: "Early evolution of planetesimals"

GOLABEK, G.J.; JUTZI, M.; EMSENHUBER, A.; GERYA, T.V.; ASPHAUG, E.: 17.-22.04.2016, European Geosciences Union General Assembly 2016, Vienna, Austria: "Coupling giant impact and longer-term evolution models", Geophysical Research Abstracts 18, EGU2016-9599, 2016

GOLABEK, G.J.; GERYA, T.V.: 03.-06.07.2016, JSPS-DFG International Workshop, Tohoku University, Sendai, Japan[*B]: "Hydrated planetesimals as Earth's water source?"

GOLABEK, G.J.; ROZEL, A.B.; TACKLEY, P.J.; NÄF, R.: 08.07.2016, Tokyo Institute of Technology, Earth-Life Science Institute, Tokyo, Japan: "The ridge only tectonic regime"

GOLABEK, G.J.; ROZEL, A.B.; GERYA, T.V.; BOURDON, B.: 11.-14.09.2016, German-Swiss Geodynamics Workshop 2016, Lichtenfels, Germany: "Post-magma ocean mixing in the angrite parent body"

GOLABEK, G.J.; ROZEL, A.B.; GERYA, T.V.; BOURDON, B.: 28.09.2016, Université de Lausanne, Switzerland: "Early thermomechanical evolution of planetesimals"

GOLABEK, G.J.; ROZEL, A.B.; GERYA, T.V.; BOURDON, B.: 10.-11.10.2016, ACCRETE Group Meeting, Observatoire de la Cote d'Azur, Nice, France: "Post-magma ocean mixing in the angrite parent body"

GUO, H.; AUDÉTAT, A.: 05.-08.06.2016, EMPG XV, Zurich, Switzerland[*A]: "Transfer of volatiles and metals from mafic to felsic magmas in composite magma chambers: an experimental study"

HEIDELBACH, F. (2016): 19.-23.09.2016, EMU School on Mineral Reaction Kinetics, Vienna, Austria: "Experimental nucleation and growth of garnet under deviatoric stresses in the CMNAS system"

IDRISSI, H.; BOLLINGER, C.; CORDIER, P.; BOIOLI, F.: 11.-15.09.2016, 2nd European Mineralogical Conference, Rimini, Italy: "*In situ* deformation of olivine in the transmission electron microscope: from dislocation velocity measurements to stress-strain curves"

IMMOOR, J.; MARQUARDT, H.; SPEZIALE, S.; MIYAGI, L.; LIERMANN, H.P.: 17.-19.06.2016, DMG Section Meeting of Petrology, Petrophysics & Geochemistry, Bremen, Germany: "Experimental deformation of (Mg,Fe)O at conditions of the lower mantle"

IMMOOR, J.; MARQUARDT, H.; SPEZIALE, S.; MIYAGI, L.; LIERMANN, H.P.: 04.-09.09.2016, 54th EHPRG Meeting, Bayreuth, Germany*C: "Experimental deformation of (Mg,Fe)O at conditions of the lower mantle"

ISHII, T.; MIYAJIMA, N.; PETITGIRARD, S.; MCCAMMON, C.; KATSURA, T.: 26.06.-01.07.2016, Goldschmidt 2016, Yokohama, Japan: "Reductive decomposition of phase D by formation of Fe, Al-bearing bridgmanite", Goldschmidt Abstracts, 2016, 1274

ISHII, T.; MIYAJIMA, N.; PETITGIRARD, S.; MCCAMMON, C.; KATSURA, T.: 03.-06.07.2016, JSPS-DFG International Workshop, Tohoku University, Sendai, Japan*B: "Reductive decomposition of phase D by formation of Fe-bearing aluminous bridgmanite"

ISHII, T.; SHI, L.; HUANG, R.; TSUJINO, N.; DRUZHBIN, D.; MYHILL, R.; LI, Y.; WANG, L.; YAMAMOTO, T.; MIYAJIMA, N.; KAWAZOE, T.; HIGO, Y.; TANGE, Y.; KATSURA, T.: 04.-09.09.2016, 54th EHPRG Meeting, Bayreuth, Germany*C: "High-pressure generation over 40 GPa using Kawai-type multi-anvil press with tungsten carbide anvils"

ISMAILOVA, L.; BYKOVA, E.; BYKOV, M.; CERANTOLA, V.; MCCAMMON, C.; BOFFA BALLARAN, T.; BOBROV, A.; DUBROVINSKAIA, N.; DUBROVINSKY, L.: 26.06.-01.07.2016, Goldschmidt 2016, Yokohama, Japan: "Stability of Fe, Al-bearing bridgmanite in the lower mantle and synthesis of pure iron bridgmanite", Goldschmidt Abstracts, 2016, 1284

ISMAILOVA, L.; BYKOV, M.; BYKOVA, E.; BOBROV, A.; MCCAMMON, C.; DUBROVINSKAIA, N.; DUBROVINSKY, L.: 04.-09.09.2016, 54th EHPRG Meeting, Bayreuth, Germany*C: "Effect of composition on compressibility of skiagite-Fe-majorite garnet"

JACOBSON, S.A.: 11.-15.01.2016, International Space Science Institute (ISSI) Workshop on 'The Delivery of Water to Proto-Planets, Planets and Satellites', Bern, Switzerland: "Ice line fossilization"

JACOBSON, S.A.: 01.03.2016, Whole Earth Seminar, University of California, Department of Earth and Planetary Sciences, Santa Cruz, California, USA: "Growth of terrestrial planets"

JACOBSON, S.A.: 02.03.2016, Department of Earth and Planetary Sciences, Special Seminar, University of California, Santa Cruz, USA: "Differentiation of Earth"

JACOBSON, S.A.: 07.03.2016, Supérior École d'Aerospace, Advanced Dynamics Course, Toulouse, France: "Three body problem"

JACOBSON, S.A.: 14.03.2016, Northwestern University, Department of Earth and Planetary Sciences, Evanston, Illinois, USA: "Giant impacts and the formation of Earth's core"

JACOBSON, S.A.; DEMEO, F.; MORBIDELLI, A.; CARRRY, B.; FROST, D.J.; RUBIE, D.C.: 21.-25.03.2016, 47th Lunar and Planetary Science Conference, The Woodlands, Houston, USA: "There's too much mantle material in the asteroid belt", LPI Contribution 1903

JACOBSON, S.A.; MORBIDELLI, A.; CARRY, B.: 22.-26.05.2016, 47th DDA, Nashville, USA: "Establishing different size distributions in the asteroid belt"

JACOBSON, S.A.: 21.-23.06.2016, 4th Workshop on Binaries in the Solar System Conference, Prague, Czech Republic: "Asteroid geophysics from applying tidal theory to binary asteroids"

JACOBSON, S.A.; HERNLUND, J.; RUBIE, D.C.; MORBIDELLI, A.: 26.06.-01.07.2016, Goldschmidt 2016, Yokohama, Japan: "Terrestrial core stratification and subsequent mixing", Goldschmidt Abstracts, 2016, 1311

JACOBSON, S.A.; RUBIE, D.C.; MORBIDELLI, A.: 26.06.-01.07.2016, Goldschmidt 2016, Yokohama, Japan (*keynote*): "Beyond matching orbits and masses, terrestrial planet formation in the era of compositional constraints", Goldschmidt Abstracts, 2016, 1312

JACOBSON, S.A.: 24.-28.07.2016, University of Tokyo, APCosPA-Planet^2 RESCEU Summer School, Takayama, Japan: "From pebbles to planets: the story of the Solar System"

JACOBSON, S.A.: 13.-15.09.2016, ISSI-Europlanet Forum, Bern, Switzerland: "Formation and early evolution of the Solar System: the big picture"

JACOBSON, S.A.; MORBIDELLI, A.: 17.-21.09.2016, 48th DPS Meeting, Pasadena, USA: "Quantifying the lack of differentiated material amongst asteroid families", Talk 522.08

JACOBSON, S.A.; RUBIE, D.C.; MORBIDELLI, A.; YOUNG, E.D.: 12.-16.12.2016, AGU Fall Meeting, San Francisco, USA^{*D}: "Composition and origin of Theia – the Moon-forming impactor", Abstract V41A-3107, 2016

JENNINGS, E.S.; PETITGIRARD, S.; LORD, O.T.; WALTER, M.J.; FROST, D.J.; RUBIE, D.C.: 05.-08.06.2016, EMPG XV, Zurich, Switzerland^{*A}: "An experimental investigation of silicon and oxygen partitioning between silicate and iron liquids at core formation conditions"

JENNINGS, E.S.; PETITGIRARD, S.; LORD, O.T.; WALTER, M.J.; FROST, D.J.; RUBIE, D.C.: 26.06.-01.07.2016, Goldschmidt 2016, Yokohama, Japan: "Silicon and oxygen partitioning between silicate and iron at core formation conditions", Goldschmidt Abstracts, 2016, 1323

JENNINGS, E.S.; RUBIE, D.C.; FROST, D.J.; LAURENZ, V.; POSNER, E.; PETIGIRARD, S.; LORD, O.T.; MIYAJIMA, N.: 10.-11.10.2016, ACCRETE Group Meeting, Observatoire de la Cote d'Azur, Nice, France: "The partitioning of Si, Fe, Mg and O at core-formation conditions"

KATSURA, T.: 30.06.2016, JANET-Forum 2016, Freie Universität Berlin, Germany: "A joint international graduate school program between University of Bayreuth & Tohoku University"

KATSURA, T.; FEI, H.; WANG, L.; BLAHA, S.; MIYAJIMA, N.; MARQUARDT, K.; KOIZUMI, S.; WIEDENBECK, M.; SAKAMOTO, N.; YURIMOTO, H.: 03.-06.07.2016, JSPS-DFG International Workshop, Tohoku University, Sendai, Japan[*B] (*invited*): "Water-content dependence of olivine rheology inferred from quasi-hydrostatic experiments"

KATSURA, T.: 20.-24.09.2016: IUCr High-Pressure Workshop, Pohang, South Korea (*invited*): "Water-content dependence of olivine rheology inferred from quasi-hydrostatic experiments"

KATSURA, T.: 23.-25.09.2016, Award lecture, Japan Association of Mineralogical Science, Kanazawa, Japan: "High-pressure-temperature measurement of physical properties of mantle minerals and experimental geophysics"

KATSURA, T.; FEI, H.; KOIZUMI, S.; SAKAMOTO, N.; YURIMOTO, H.: 12.-16.12.2016, AGU Fall Meeting, San Francisco, USA[*D]: "Enhancement of the ionic conductivity of olivine by the water incorporation based on the Mg diffusivity", Abstract MR41E-08, 2016

KAWAZOE, T.; NISHIHARA, Y.; OHUCHI, T.; MIYAJIMA, N.; MARUYAMA, G.; HIGO, Y.; FUNAKOSHI, K.; IRIFUNE, T.: 26.06.-01.07.2016, Goldschmidt 2016, Yokohama, Japan: "Creep strength of ringwoodite measured up to 1700 K at 17-18 GPa using a deformation-DIA apparatus", Goldschmidt Abstracts, 2016, 1465

KAWAZOE, T.; CHAUDHARI, A.; SMYTH, J.R.; MCCAMMON, C.: 03.-06.07.2016, JSPS-DFG International Workshop, Tohoku University, Sendai, Japan[*B]: "Coupled substitution of Fe^{3+} and H^{+} for Si in wadsleyite"

KAWAZOE, T.; CHAUDHARI, A.; SMYTH, J.R.; MCCAMMON, C.: 04.-09.09.2016, 54th EHPRG Meeting, Bayreuth, Germany[*C]: "Coupled substitution of Fe^{3+} and H^{+} for Si in wadsleyite: a study by polarized infrared and Mössbauer spectroscopies and single-crystal X-ray diffraction"

KISEEVA, E.S.; VASIUKOV, D.M.; WOOD, B.; STACHEL, T.; MCCAMMON, C.A.; CHUMAKOV, A.; HARRIS, J.W.; DUBROVINSKY, L.: 11.-15.09.2016, 2nd European Mineralogical Conference, Rimini, Italy: "Highly oxidised majoritic inclusions in diamond"

KUPENKO, I.; APRILIS, G.; VASIUKOV, D.; MCCAMMON, C.; CHARITON, S.; CERANTOLA, V.; KANTOR, I.; CHUMAKOV, A.I.; RÜFFER, R.; DUBROVINSKY, L.: 04.-09.09.2016, 54th EHPRG Meeting, Bayreuth, Germany[*C]: "Critical temperatures of iron oxides at high pressures"

KURNOSOV, A.; MARQUARDT, H.; BOFFA BALLARAN, T.; FROST, D.J.: 04.-09.09.2016, 54th EHPRG Meeting, Bayreuth, Germany[*C]: "Study of the single-crystal elasticity of $Mg_{0.9}Fe_{0.1}Si_{0.9}Al_{0.1}O_3$ bridgmanite up to lower mantle pressures"

LAUMONIER, M.; FROST, D.; FARLA, R.; KATSURA, T.; MARQUARDT, K.: 17.-22.04.2016, European Geosciences Union General Assembly 2016, Vienna, Austria: "Electrical conductivity of partially-molten olivine aggregate and melt interconnectivity in the upper mantle", Geophysical Research Abstracts 18, EGU2016-4825-1, 2016

LAUMONIER, M.; GAILLARD, F.; MUIR, D.; BLUNDY, J.; UNSWORTH, M.: 17.-22.04.2016, European Geosciences Union General Assembly 2016, Vienna, Austria: "Giant magmatic water reservoir beneath Uturuncu volcano and Altiplano-Puna region (Central Andes)", Geophysical Research Abstracts 18, EGU2016-4801, 2016

LAURENZ, V.; RUBIE, D.C.; FROST, D.J.: 01.12.2016, Bonner Geowissenschaftliches Kolloquium, Rheinische Friedrich-Wilhelms-Universität Bonn, Steinmann Institut, Bonn, Germany: "Geo-LEGO or building the Earth – an experimental perspective"

LAURENZ, V.; RUBIE, D.C.; FROST, D.J.: 06.-08.04.2016, First General Meeting DFG SPP 1833 'Building a Habitable Earth', Köln, Germany: "Sulfide-silicate partitioning of Re and Os at high *P-T* conditions"

LAURENZ, V.; RUBIE, D.C.; FROST, D.J.: 05.-08.06.2016, EMPG XV, Zurich, Switzerland[*A]: "High *P-T* sulfide-silicate partitioning of Re and Os"

LAURENZ, V.; RUBIE, D.C.; FROST, D.J.: 11.-15.07.2016, 4th International Highly Siderophile Element Geochemistry Workshop, Durham, U.K.: "Sulfide-silicate partitioning of Re and Os at high *P-T* conditions"

LAURENZ, V.; RUBIE, D.C.; FROST, D.J.: 10.-11.10.2016, ACCRETE Group Meeting, Observatoire de la Cote d'Azur, Nice, France: "High P-T partitioning of Re and Os"

LI, Y.; SHCHEKA, S.; MARTY, B.; ZIMMERMANN, L.; KEPPLER, H.: 03.-06.07.2016, JSPS-DFG International Workshop, Tohoku University, Sendai, Japan[*B]: "Nitrogen isotope fractionation during terrestrial core-mantle separation"

LI, Y.; MARTY, B.; SHCHEKA, S.; ZIMMERMANN, L.; KEPPLER, H.: 26.06.-01.07.2016, Goldschmidt 2016, Yokohama, Japan: "Nitrogen isotope fractionation during terrestrial core-mantle separation", Goldschmidt Abstracts, 2016, 1970

LIN, F.; MERKEL, S.; HILAIRET, N.; MARQUARDT, H.; IMMOOR, J.; TOMÉ, C.; MIYAGI, L.: 12.-16.12.2016, AGU Fall Meeting, San Francisco, USA[*D]: "Application of the elasto-viscoplastic self consistent (EVPSC) code to modeling texture and lattice strain evolution in periclase", Abstract MR23A-2678, 2016

LIU, Z.D.; IRIFUNE, T.; NISHI, M.; TANGE, Y.; ARIMOTO, T.; SHINMEI, T.; KATSURA, T.; ISHII, T.; FEI, H.: 04.-09.09.2016, 54th EHPRG Meeting, Bayreuth, Germany[*C]: "Phase relations in the system $MgSiO_3$-Al_2O_3 in the lower mantle"

LIU, Z.D.; IRIFUNE, T.; NISHI, M.; TANGE, Y.; ARIMOTO, T.; SHINMEI, T.: 26.06.-01.07.2016, Goldschmidt 2016, Yokohama, Japan: "Phase relations in the system $MgSiO_3$-Al_2O_3 up to 52 GPa and 2000 K", Goldschmidt Abstracts, 2016, 1877

MAHENDRAN, S.; CARREZ, P.; BOLLINGER, C.; IDRISSI, H.; CORDIER, P.: 09.-14.10.2016, 8th International Conference on Multiscale Materials Modeling (MMM 2016), Dijon, France: "Plasticity of Olivine Mg_2SiO_4: Insights from nanomechanical experiments and atomistic calculations"

MALLIK, A.: 08.03.2016, Stanford University, Department of Geological Sciences, Stanford, USA: "Melting of Earth's heterogeneous upper mantle – what happens to crustal melt in the mantle milieu?"

MALLIK, A.: 18.04.2016, University of California at Davis, Department of Earth and Planetary Sciences, Davies, USA: "Crust-mantle interaction and melting of the Earth's heterogeneous upper mantle"

MALLIK, A.: 19.04.2016, University of California at Davis, Department of Earth and Planetary Sciences, Davies, USA: "Deep cycling of nitrogen through time and insight into evolution of the lunar interior"

MALLIK, A.: 05.-08.06.2016, EMPG XV, Zurich, Switzerland[*A]: "Experimental determination of nitrogen carrying capacity of slab melts"

MALLIK, A.; DASGUPTA, R.; TSUNO, K.; NELSON, J.M.: 05.-08.06.2016, EMPG XV, Zurich, Switzerland[*A]: "Partial melting of sediment melt fluxed peridotite with variable water content: Implications for the generation of subduction zone magmas"

MALLIK, A.: 26.06.-01.07.2016, Goldschmidt 2016, Yokohama, Japan: "Nitrogen carrying capacity of slab-derived melts: Implications for deep nitrogen cycling", Goldschmidt Abstracts, 2016, 1955

MALLIK, A.: 03.-06.07.2016, JSPS-DFG International Workshop, Tohoku University, Sendai, Japan[*B]: "Experimental determination of nitrogen carrying capacity of subducted slab-derived melt"

MARQUARDT, H.; KURNOSOV, A.; BOFFA BALLARAN T.; FROST, D.J.; ZIBERNA, L.; MIYAGI, L.; LIERMANN, H.-P.; SPEZIALE, S.; IMMOOR, J.: 17.-22.04.2016, European Geosciences Union General Assembly 2016, Vienna, Austria (*invited*): "Composition and structure of Earth's lower mantle from elasticity and rheology measurements", Geophysical Research Abstracts 18, EGU2016-14290, 2016

MARQUARDT, H.; KURNOSOV, A.; BOFFA BALLARAN, T; FROST, D.J.; KAWAZOE, T.; BUCHEN, J.; SCHULZE, K.: 03.-06.07.2016, JSPS-DFG International Workshop, Tohoku University, Sendai, Japan[*B] (*invited*): "Constraints on Earth's deep volatile cycles from elasticity measurements on mantle minerals"

MARQUARDT, H.; IMMOOR, J.; MIYAGI, L.; SPEZIALE, S.; LIERMANN, H.-P.: 05.-08.06.2016, EMPG XV, Zurich, Switzerland[*A]: "Experimental high-pressure/high-temperature deformation of lower mantle materials at DESY"

MARQUARDT, H.; KURNOSOV, A.; BOFFA BALLARAN, T.; MARQUARDT, K.; FROST, D.J.; LIERMANN, H.-P.; SPEZIALE, S.; MIYAGI, L.; MERKEL, S.; IMMOOR, J.; BUCHEN, J.; SCHULZE, K.: 11.-15.09.2016, 2nd European Mineralogical Conference, Rimini, Italy (*invited keynote*): "Insights into the nature of Earth's mantle from elasticity and rheology measurements at high pressure/high temperature"

MARQUARDT, K.; PALOT, M.; RUDLOFF, J.; PEARSON, G.; BRENKER, F.; NESTOLA, F.; JACOBSEN, S.; MIYAJIMA, N.; MCCAMMON, C.; HARRIS, J.; KAMINSKY, F.: 10.05.2016, Carnegie Mellon University Pittsburgh, USA: "Inclusions in diamond investigated by transmission electron microscopy: A Journey to the Earth's deep interior"

MARQUARDT, K.; MIYAJIMA, N.; PETITGIRARD, S.; ARMSTRONG, K.; FROST, D.J.: 26.06.-01.07.2016, Goldschmidt 2016, Yokohama, Japan: "Nano scale chemical analyses of ultra-high pressure melting experiments", Goldschmidt Abstracts, 2016, 1977

MARQUARDT, K.; MORALES, L.: 26.06.-01.07.2016, Goldschmidt 2016, Yokohama, Japan: "Partitioning of Al, Ca to olivine grain boundaries, the impact on crystal habit", Goldschmidt Abstracts, 2016, 1978

MARQUARDT, K.; PALOT, M.; RUDLOFF, J.; PEARSON, G.; BRENKER, F.; NESTOLA, F.; JACOBSEN, S.; MIYAJIMA, N.; MCCAMMON, C.; HARRIS, J.: 03.-06.07.2016, JSPS-DFG International Workshop, Tohoku University, Sendai, Japan[*B]: "Transmission electron microscopy on diamond inclusions of the deep Earth's interior"

MARQUARDT, K.; MORALES, L.F.G.; ROHRER, G.; DE GRAEF, M.; FARLA, R.: 12.-16.12.2016, AGU Fall Meeting, San Francisco, USA[*D]: "The habit of crystals in aggregates: five parameter grain boundary characterization of olivine", Abstract MR41E-02, 2016

MCCAMMON, C.; VAN DRIEL, J.; KAWAZOE, T.; MYHILL, R.; DUBROVINSKY, L.: 26.06.-01.07.2016, Goldschmidt 2016, Yokohama, Japan: "Strong affinity of Al-containing bridgmanite for ferric iron", Goldschmidt Abstracts, 2016, 2024

MCCAMMON, C.: 03.-06.07.2016, JSPS-DFG International Workshop, Tohoku University, Sendai, Japan[*B]: "The deep oxygen cycle"

MCCAMMON, C.A.; APRILIS, G.; STROHM, C.; KUPENKO, I.; CERANTOLA, V.; VASIUKOV, D.; CHUMAKOV, A.; RÜFFER, R.; DUBROVINSKY, L.S.: 03.-08.07.2016, International Conference on Hyperfine Interactions and Their Applications, Leuven, Belgium: "It's about time: a new parameter to probe hyperfine interactions under extreme conditions"

MCCAMMON, C.; CHARITON, S.; CERANTOLA, V.; KUPENKO, I.; VASIUKOV, D.; APRILIS, G.; CHUMAKOV, A.; DUBROVINSKY, L.: 04.-09.09.2016, 54th EHPRG Meeting, Bayreuth, Germany[*C]: "Elastic properties of iron-bearing carbonates and implications for the deep Earth"

MCCAMMON, C.A.; CHARITON, S.; CERANTOLA, V.; KUPENKO, I.; VASIUKOV, D.M.; APRILIS, G.; CHUMAKOV, A.; DUBROVINSKY, L.: 11.-15.09.2016, 2nd European Mineralogical Conference, Rimini, Italy: "A nuclear inelastic scattering window to the deep Earth"

MCCAMMON, C.: 12.-13.11.2016, 4th meeting of the FOR 2125, Wehrheim, Germany: "Elastic properties of carbonates at high pressures and temperatures & Chemical reactions between carbonates and pyrolite mantle and the origin of ultra-deep diamonds"

MCCAMMON, C.: 12.-16.12.2016, AGU Fall Meeting, San Francisco, USA[*D]: "Hot and pressed rocks inside our world can change what happens above", Abstract PA53B-15, 2016

MCCAMMON, C.; CARACAS, R.: 12.-16.12.2016, AGU Fall Meeting, San Francisco, USA[*D]: "Iron in post-perovskite with implications for the core-mantle boundary region", Abstract MR21C-07, 2016

MEIER, T.: 04.-09.09.2016, 54th EHPRG Meeting, Bayreuth, Germany[*C]: "High-sensitivity nuclear magnetic resonance up to 30 GPa"

MELAI, C.; MARQUARDT, K.; ARMSTRONG, K.; MCCAMMON, C.A.: 11.-15.09.2016, 2nd European Mineralogical Conference, Rimini, Italy: "Exploring a new geobarometer for ferropericlase inclusions in diamond from the lower mantle"

MILANI, S.; NESTOLA, F.; CERANTOLA, V.; ANZOLINI, C.; MCCAMMON, C.; NOVELLA, D.; KUPENKO, I.; CHUMAKOV, A.; RÜFFER, R.; HARRIS, J.W.: 11.-15.09.2016, 2nd European Mineralogical Conference, Rimini, Italy: "First *in situ* measurements of Fe^{3+}/Fe_{tot} for oxides and silicates included in natural diamonds with synchrotron Mössbauer source"

MISRA, S.; THIELMANN, M.; GOLABEK, G.: 11.-14.09.2016, German-Swiss Geodynamics Workshop 2016, Lichtenfels, Germany: "Heterogeneous layer folding"

MIYAJIMA, N.; LI, Y.; HEIDELBACH, F.: 05.-08.06.2016, EMPG XV, Zurich, Switzerland[*A]: "Imaging dislocations in a natural olivine by electron channeling contrast in a SEM"

MIYAJIMA, N.; FISCHER, R.A.; CAMPBELL, A.J.; FROST, D.J.; HARRIES, D.; LANGENHORST, F.; POLLOK, K.; PETITGIRARD, S.; RUBIE, D.C.: 03.-06.07.2016, JSPS-DFG International Workshop, Tohoku University, Sendai, Japan[*B]: "Quantitative chemical analysis of carbon and oxygen in molten Fe-rich alloy by electron energy-loss spectroscopy in TEM"

MUKHINA, E.; DUBROVINSKY, L.; SEROVAJSKII, A.; MCCAMMON, C.; KOLESNIKOV, A.; KUPENKO, I.; KUTCHEROV, V.: 26.06.-01.07.2016, Goldschmidt 2016, Yokohama, Japan: "Transformations of hydrocarbons during hot subduction", Goldschmidt Abstracts, 2016, 2175

NAKAJIMA, M.; RUBIE, D.C.; MELOSH, H.J.; JACOBSON, S.A.; GOLABEK, G.; NIMMO, F.; MORBIDELLI, A.: 12.-16.12.2016, AGU Fall Meeting, San Francisco, USA[*D]: "A scaling relationship for impact-induced melt volume", Abstract P51A-2118, 2016

NISHIHARA, Y.; OHUCHI, T.; KAWAZOE, T.; MARUYAMA, G.; SETO, Y.; HIGO, Y.; FUNAKOSHI, K.; TANGE, Y.: 26.06.-01.07.2016, Goldschmidt 2016, Yokohama, Japan: "Lattice-preferred-orientation of hcp metals studied by high-pressure deformation", Goldschmidt Abstracts, 2016, 2290

OVSYANNIKOV, S.; BYKOV, M.; BYKOVA, E.; KOZLENKO, D.; TSIRLIN, A.; KARKIN, A.; SHCHENNIKOV, V.; KICHANOV, S.; GOU, H.; ABAKUMOV, A.; EGOAVIL, R.; VERBEECK, J.; MCCAMMON, C.; DYADKIN, V.; CHERNYSHOV, D.; SMAALEN, S.V.; DUBROVINSKY, L.: 04.-09.09.2016, 54th EHPRG Meeting, Bayreuth, Germany[*C]: "Metal-insulator-type transition in a high-pressure iron oxide polymorph Fe_4O_5 involving dimer and trimer formation"

OVSYANNIKOV, S.V.; BYKOVA, E.; BYKOV, M.; WENZ, M.D.; PAKHOMOVA, A.S.; GLAZYRIN, K.; LIERMANN, H.-P.; DUBROVINSKY, L.: 04.-09.09.2016, 54th EHPRG Meeting, Bayreuth, Germany[*C]: "Structural and vibrational properties of single crystals of Scandia, Sc_2O_3 under high pressure"

PAKHOMOVA, A.S.; BOFFA BALLARAN, T.; KURNOSOV, A.: 03.-06.07.2016, JSPS-DFG International Workshop, Tohoku University, Sendai, Japan[*B]: "Plastic response of single-crystals of water ice V"

PAKHOMOVA, A.S.; BOFFA BALLARAN, T.; KURNOSOV, A.: 28.08.-01.09.2016, 30th Meeting of the European Crystallographic Association, Basel, Switzerland: "Deformation of single-crystals of water ice VI"

PALOT, M.; JACOBSEN, S.D.; TOWNSEND, J.P.; NESTOLA, F.; MARQUARDT, K.; HARRIS, J.W.; STACHEL, T.; MCCAMMON, C.A.; PEARSON, D.G.: 11.-15.09.2016, 2nd European Mineralogical Conference, Rimini, Italy: "Evidence for H_2O-bearing fluids in the lower mantle from diamond inclusion"

PALOT, M.; JACOBSEN, S.; TOWNSEND, J.; NESTOLA, F.; MARQUARDT, K.; HARRIS, J.; STACHEL, T.; MCCAMMON, C.; PEARSON, D.: 26.06.-01.07.2016, Goldschmidt 2016, Yokohama, Japan: "Evidence for water in the lower mantle from ferropericlase included in diamond", Goldschmidt Abstracts, 2016, 2423

PAMATO, M.G.; VOČADLO, L.; DOBSON, D.P.; WOOD, I.G.; KURNOSOV, A.; PAKHOMOVA, A.; BOFFA BALLARAN, T.: 26.06.-01.07.2016, Goldschmidt 2016, Yokohama, Japan: "Pre melting in rare gases", Goldschmidt Abstracts, 2016, 2424

PETITGIRARD, S.; MALFAIT, W.; SINMYO, R.; KUPENKO, I.; JOURNAUX, B.; COLLINGS, I.; KANTOR, I.; HENNET, L.; HARRIES, D.; DANE, T.; BURGHAMER, M.; RUBIE, D.: 26.06.-01.07.2016, Goldschmidt 2016, Yokohama, Japan: "Amorphous $MgSiO_3$ and SiO_2 densities at core-mantle boundary conditions", Goldschmidt Abstracts, 2016, 2484

PETITGIRARD, S.: 04.-09.09.2016, 54th EHPRG Meeting, Bayreuth, Germany^{*C}: " Density of silicate glasses and melts to extreme conditions of pressure"

POLEDNIA, J.; MARQUARDT, K.; DOHMEN, R.: 17.-19.06.2016, DMG Section Meeting of Petrology, Petrophysics & Geochemistry, Bremen, Germany: "Grain boundary diffusion experiments using the bicrystal setup to test the effect of ionic size"

POLEDNIA, J.; MARQUARDT, K.; DOHMEN, R.: 11.-14.09.2016, German-Swiss Geodynamics Workshop 2016, Lichtenfels, Germany: "Grain boundary diffusion experiments using the bicrystal setup to test the effect of ionic size"

POMMIER, A.; LAURENZ, V.; DAVIES, C.J.; FROST, D.J.: 12.-16.12.2016, AGU Fall Meeting, San Francisco, USA^{*D}: "The effect of oxygen on the structure and dynamics of planetary cores: Insights from melting phase relations in the Fe-S and Fe-S-O systems", Abstract MR23B-06, 2016

POSNER, E.S.; RUBIE, D.C.; FROST, D.J.; VLČEK, V.; STEINLE-NEUMANN, G.: 17.-22.04.2016, European Geosciences Union General Assembly 2016, Vienna, Austria: "High P-T experiments and first principles calculations of Si, O, Cr diffusion in liquid iron"

POSNER, E.S.; RUBIE, D.C.; FROST, D.J.; VLČEK, V.; STEINLE-NEUMANN, G.: 05.-08.06.2016, EMPG XV, Zurich, Switzerland^{*A}: "High P-T diffusive transport properties of liquid iron alloys and peridotite melt"

POSNER, E.S.; RUBIE, D.C.; FROST, D.J.; STEINLE-NEUMANN, G.: 04.-05.10.2016, Final Meeting of the DFG SPP 1385, Universität Heidelberg, Institut für Geowissenschaften, Heidelberg, Germany: "Chemical evolution of planetesimal cores during the early history of the solar system"

RITTER, X.; SANCHEZ-VALLE, C.; KING, A.; PERILLAT, J.P.; GUIGNOT, N.; LAUMONIER, M.; MORIZET, Y.; SIFRÉ, D.; GAILLARD, F.: 05.-08.06.2016, EMPG XV, Zurich, Switzerland^{*A}: "Density of carbonated melts along the $CaCO_3$-$MgCO_3$ join determined by synchrotron X-ray radiography"

ROZEL, A.; GOLABEK, G.; THIELMANN, M.; SCHIERJOTT, J.; TACKLEY, P.: 17.-22.04.2016, European Geosciences Union General Assembly 2016, Vienna, Austria: "Evolutionary models of the Earth with a grain size-dependent rheology: diffusion versus dislocation creep"

RUBIE, D.C.; JACOBSON, S.A.; MORBIDELLI, A.; NIMMO, F.; O'BRIEN, D.; PALME, H.; YOUNG, E.; FROST, D.J.: 11.-15.01.2016, International Space Science Institute (ISSI) Workshop on 'The Delivery of Water to Proto-Planets, Planets and Satellites', Bern, Switzerland: "Origin of Earth's volatiles: Constraints from core formation"

RUBIE, D.C.; LAURENZ, V.; JACOBSON, S.A.; MORBIDELLI, A.; PALME, H.; VOGEL, A.K.: 21.-25.03.2016, 47th Lunar and Planetary Science Conference, The Woodlands, Houston, USA: "High concentrations of highly siderophile elements were stripped from Earth's mantle by the segregation of exsolved iron sulfide melt", Abstract 1112

RUBIE, D.C.: 05.04.-06.04.2016, Initial Training Workshop DFG SPP 1833 'Building a Habitable Earth', Köln, Germany: "Core formation and magma oceans on the early Earth"

RUBIE, D.C.; DE VRIES, J.; NAKAJIMA, M.; NIMMO, F.; MELOSH, H.J.; JACOBSON, S.A.; MORBIDELLI, A.; GOLABEK, G.: 06.-08.04.2016, First General Meeting DFG SPP 1833 'Building a Habitable Earth', Köln, Germany: "Impact-induced melting during Earth's accretion"

RUBIE, D.C.; LAURENZ, V.; JACOBSON, S.A.; MORBIDELLI, A.; PALME, H.; VOGEL, A.-K.; FROST, D.J.: 26.06.-01.07.2016, Goldschmidt 2016, Yokohama, Japan: "Evolution of sulfur concentrations in magma oceans during Earth's accretion", Goldschmidt Abstracts, 2016, 2667

RUBIE, D.C.; JACOBSON, S.A.; MORBIDELLI, A.; NIMMO, F.; O'BRIEN, D.; PALME, H.; YOUNG, E.; FROST, D.J.: 03.-06.07.2016, JSPS-DFG International Workshop, Tohoku University, Sendai, Japan[*B]: "The origin of Earth's water"

RUBIE, D.C.; LAURENZ, V.; JACOBSON, S.A.; MORBIDELLI, A.; PALME, H.; VOGEL, A.; FROST, D.J.; VOGEL, A.; 04.-05.10.2016, Final Meeting of the DFG SPP 1385, Universität Heidelberg, Institut für Geowissenschaften, Heidelberg, Germany: "Conditions, timescales and Cosmochemical evolution during the early accretion of terrestrial planets"

RUBIE, D.C.: 10.-11.10.2016, ACCRETE Group Meeting, Observatoire de la Cote d'Azur, Nice, France: "Combining accretion and core formation – current progress and future prospects"

RUBIE, D.C.: 21.-23.11.2016, TRR 170 Winter School 'Planetary Geodynamics' and Annual Retreat, Hodenhagen, Germany: "Geochemical aspects of core formation"

RUBIE, D.C.; LAURENZ, V.; FROST, D.J.; JACOBSON, S.A.; MORBIDELLI, A.; PALME, H.; VOGEL, A.: 21.-23.11.2016, TRR 170 Winter School 'Planetary Geodynamics' and Annual Retreat, Hodenhagen, Germany: "Addition of sulfur to the Earth and its partitioning between core and mantle during accretion and core formation"

SCHULZE, K.; MARQUARDT, H.; KAWAZOE, T.; KOCH-MÜLLER, M.; KURNOSOV, A.; BOFFA BALLARAN, T.: 26.02.2016, DMG-Sektionstreffen 'Angewandte Mineralogie in Umwelt & Technik' und 'Chemie, Physik und Kristallographie der Minerale', Bad Windsheim, Germany: "The effect of iron content and hydration state on the elastic constants of single-crystal ringwoodite under HP/HT conditions"

SCHULZE, K.; MARQUARDT, H.; KAWAZOE, T.; KOCH-MÜLLER, M.; KURNOSOV, A.; BOFFA BALLARAN, T.: 27.05.-05.06.2016, International School of Crystallography, 49th Course 'High-pressure crystallography: *status artis* and emerging opportunities', Erice, Italy: "Comparative HP/HT elasticity measurements on single-crystals of hydrous/iron-bearing ringwoodite"

SCHULZE, K.; MARQUARDT, H.; KAWAZOE, A.; KURNOSOV, A.; KOCH-MÜLLER, M.; SPEZIALE, S.; BOFFA BALLARAN, T.: 05.-08.06.2016, EMPG XV, Zurich, Switzerland[*A]: "Direct quantification of the effect of Fe and OH on the HP/HT single-crystal elasticity of ringwoodite"

SCHULZE, K.; MARQUARDT, H.; KAWAZOE, T.; KURNOSOV, A.; KOCH-MÜLLER, M.; KURNOSOV, A.; BOFFA BALLARAN, T.: 04.-09.09.2016, 54th EHPRG Meeting, Bayreuth, Germany*C: "The effect of iron content and hydration state on the elastic moduli of single-crystal ringwoodite at high pressure"

SIFRÉ, D.; LAUMONIER, M.; MEZOUAR, M.; PERILLAT, J-P.; CHAMPALLIER, R.; MORIZET, Y.; RITTER, X.; MOUSSALLAM, Y.; GAILLARD, F.: 05.-08.06.2016, EMPG XV, Zurich, Switzerland*A: "The viscosity of carbonated silicate melts"

SINMYO, R.; KEPPLER, H.: 05.-08.06.2016, EMPG XV, Zurich, Switzerland*A: "Electrical conductivity of H_2O-NaCl fluids to 10 kbar"

SINMYO, R.; MCCAMMON, C.; DUBROVINSKY, L.: 26.06.-01.07.2016, Goldschmidt 2016, Yokohama, Japan: "The spin state of Fe^{3+} in lower mantle bridgmanite", Goldschmidt Abstracts, 2016, 2879

SMYTH, J.R.; ZHANG, L.; KAWAZOE, T.: 12.-16.12.2016, AGU Fall Meeting, San Francisco, USA*D: "Stability, composition, and crystal structure of DHMS phase E in the transition zone", Abstract MR11A-2364, 2016

STEINLE-NEUMANN, G.: 06.-08.04.2016, First General Meeting DFG SPP 1833 'Building a Habitable Earth', Köln, Germany: "Crystallizing the Martian magma ocean"

STEINLE-NEUMANN, G.; CHEMIA, Z.; DOLEJŠ, D.: 03.-06.07.2016, JSPS-DFG International Workshop, Tohoku University, Sendai, Japan*B: "Thermal effects of variable properties and metamorphic reactions in a three-component subducting slab"

STEINLE-NEUMANN, G.; CHUST, T.: 14.-16.09.2016, IUCr 5th Joint Workshop on High Pressure, Planetary and Plasma Physics (HP4), Hamburg, Germany: "A computational framework of mantle thermodynamics"

STEINLE-NEUMANN, G.: 14.-16.09.2016, IUCr 5th Joint Workshop on High Pressure, Planetary and Plasma Physics (HP4), Hamburg, Germany: "Adiabatic connection fluctuation-dissipation (ACFD) theory-based equation-of-state of hcp iron"

STEKIEL, M.; THANH, T.N.; CHARITON, S.; MCCAMMON, C.; BOSSAK, A.; REFSON, K.; WINKLER, B.: 04.-09.09.2016, 54th EHPRG Meeting, Bayreuth, Germany*C: "High-pressure elastic properties of $FeCO_3$"

THIELMANN, M.; ROZEL, A.: 17.-22.04.2016, European Geosciences Union General Assembly 2016, Vienna, Austria: "Grain size reduction and shear heating: a recipe for intermediate-depth earthquake generation?"

THIELMANN, M.: 11.-14.09.2016, German-Swiss Geodynamics Workshop 2016, Lichtenfels, Germany: "Shear localization due to grain size evolution and shear heating: an energy perspective"

THIELMANN, M.: 12.10.2016, GFD seminar, Zürich, Switzerland: "Shear localization due to grain size evolution and shear heating: an energy perspective"

THIELMANN, M.: 17.10.2016, Structural Geology Seminar, Tübingen, Germany: "Grain size assisted thermal runaway: A mechanism for plate boundary creation and intermediate-depth earthquake generation?"

UENVER-THIELE, L.; WOODLAND, A.; BOFFA BALLARAN, T.; MIYAJIMA, N.; FROST, D.J.: 05.-08.06.2016, EMPG XV, Zurich, Switzerland*A: "New Fe-Mg oxides at conditions of the deep upper mantle and transition zone?"

VASIUKOV, D.; BYKOVA, E.; KUPENKO, I.; ISMAILOVA, L.; CERANTOLA, V.; APRILIS, G.; MCCAMMON, C.; CHUMAKOV, A.I.; GREENBERG, E.; PRESCHER, C.; PRAKAPENKA, V.B.; DUBROVINSKY, L.; DUBROVINSKAIA, N.: 04.-09.09.2016, 54th EHPRG Meeting, Bayreuth, Germany[*C]: "Pressure-induced spin pairing transition in trivalent iron octahedrally coordinated by oxygen"

WAGLE, F.; VLČEK, V.; STEINLE-NEUMANN, G.: 14.-16.09.2016, IUCr 5th Joint Workshop on High Pressure, Planetary and Plasma Physics (HP4), Hamburg, Germany: "Electronic transport properties of metals at extreme conditions"

WANG, Z.; LAURENZ, V.; PETITGIRARD, S.; BECKER, H.: 21.-25.03.2016, 47th Lunar and Planetary Science Conference, The Woodlands, Houston, USA: "Earth's moderately volatile element composition may not be chondritic: Evidence from In, Cd and Zn", Abstract 1219

WANG, L.; BLAHA, S.; KAWAZOE, T.; MIYAJIMA, N.; KATSURA, T.: 12.-16.12.2016, AGU Fall Meeting, San Francisco, USA[*D]: "Negative water-content dependence of the dislocation mobility in the olivine [001](100) slip system", Abstract MR23A-2675, 2016

WOODLAND. A.B.; UENVER-THIELE, L.; BOFFA BALLARAN, T.: 11.-15.09.2016, 2nd European Mineralogical Conference, Rimini, Italy: "High P-T stability of Fe_5O_6 and its coexistence with other Fe-oxides"

WOODLAND, A.B.; UENVER-THIELE, L.; BOFFA BALLARAN, T.: 26.06.-01.07.2016, Goldschmidt 2016, Yokohama, Japan (*invited*): "Stability of of Fe_5O_6 and other Fe^{2+}-Fe^{3+}-oxides at transition zone conditions", Goldschmidt Abstracts, 2016, 3434

YOSHIOKA, T.; WIEDENBECK, M.; SHCHEKA, S.; KEPPLER, H.: 26.06.-01.07.2016, Goldschmidt 2016, Yokohama, Japan: "Nitrogen solubility in transition zone and lower mantle minerals", Goldschmidt Abstracts, 2016, 3619

YOSHIOKA, T.; WIEDENBECK, M.; SHCHEKA, S.; KEPPLER, H.: 03.-06.07.2016, JSPS-DFG International Workshop, Tohoku University, Sendai, Japan[*B]: "Nitrogen solubility in transition zone and lower mantle minerals"

ZHANG, L.; AUDÉTAT, A.: 05.-08.06.2016, EMPG XV, Zurich, Switzerland[*A]: "Diffusional modification of Cu concentrations in melt inclusions"

ZENG, L.; DUNCAN, M.; GARBER, J.; HERNANDEZ, J.-A.; MARUYA, S.; ZHANG, H.; FAUL, U.; MCCAMMON, C.; MONTAGNER, J.-P.; MORESI, L.; ROMANOWICZ, B.; RUDNICK, R.; STIXRUDE, L.: 12.-16.12.2016, AGU Fall Meeting, San Francisco, USA[*D]: "On the origin of high shear wave velocities in the deep roots of cratons", Abstract DI31A-2611, 2016

[*A] **Fifteenth International Symposium on Experimental Mineralogy, Petrology and Geochemistry, 05.-08.06.2016, Zurich, Switzerland**

[*B] **International Workshop: 'New Challenges in Volatile Cycling in the Deep Earth', JSPS-DFG Japanese German Graduate Externship Kick Off Symposium, 03.-06.07.2016, Tohoku University, Sendai, Japan**

[*C] **The 54th European High Pressure Research Group (EHPRG) International Meeting on High Pressure Science and Technology, 04.-09.09.2016, Bayreuth, Germany**

[*D] **AGU: American Geophysical Union Fall Meeting, 12.-16.12.2016, San Francisco, USA**

5.4 Lectures and seminars at Bayerisches Geoinstitut

ADAMS, Donat, Swiss Federal Laboratory for Materials Science and Technology, Dübendorf, Switzerland: "Non-perturbative treatment of anharmonic effects in materials at temperature: The decoupled anharmonic mode approximation, DAMA", 06.10.2016

ARATÓ, Robert, Bayerisches Geoinstitut, Bayreuth, Germany: "Vanadium partitioning between magnetite and silicate melt – calibration of a new oxybarometer for silicic magmas", 19.05.2016

BARON, Marzena, University of Oslo, Centre for Earth Evolution and Dynamics (SEED), Oslo, Norway – University of Bristol, School of Earth Sciences, Bristol, U.K.: "Melting in the Earth's lower mantle captured by the refined LH-DAC experiments on simplified and natural peridotite and basalt compositions", 18.04.2016

BELL, Aaron, University of New Mexico, Institut of Meteoritics, Albuquerque, USA: "What can Cr valance in olivine tell us about the oxidation state of Martian basalts and their mantle sources?", 27.10.2016

BLANCHARD, Ingrid, Institut de Physique du Globe de Paris, France: "High-pressure and high-temperature metal-silicate partitioning of gallium. Implications for terrestrial accretion and differentiation", 21.06.2016

BONS, Paul, Universität Tübingen, Strukturgeologie, Tübingen, Germany: "Numerical modelling of ductile deformation microstructures", 23.06.2016

BOULTON, Carolyn, University of Liverpool, School of Environmental Sciences, Rock Deformation Lab, Liverpool, U.K.: "Towards understanding observations of repeated slip in Alpine Fault gouges", 16.06.2016

CHAUDHARI, Alok, Bayerisches Geoinstitut, Bayreuth, Germany: "Hydrogen (H2) solubility in silicate melts", 06.05.2016

COLTICE, Nicolas, Université Claude Bernard Lyon 1, Laboratoire de Géologie, Lyon, France: "On a path to reconstruct past tectonics and convection on Earth", 03.11.2016

CONDAMINE, Pierre, Université Blaise Pascal, Laboratoire Magmas et Volcans, Clermont-Ferrand, France: "Role of phlogopite on potassium-rich magma genesis: An experimental approach", 18.02.2016

CONSOLMAGNO, Guy, Vatikan Observatorium, Vatican City State: "Is Vesta a Protoplanet?", 12.05.2016

DOHMEN, Ralf, Ruhr-Universität Bochum, Institut für Geologie, Mineralogie und Geophysik, Bochum, Germany: "Effect of doping on defects and trace element diffusion in minerals", 03.03.2016

DORN, Caroline, Universität Bern, Space Research and Planetary Sciences, Bern, Switzerland: "Interior diversity of low-mass exoplanets", 01.12.2016

EMILIEN, Joanna, Bayerisches Geoinstitut, Bayreuth, Germany: "The behaviour of sulfur in a magma ocean under reducing conditions: HP-HT phase relations in the Fe-S-Si system and the solubility of FeS in silicate melts", 20.09.2016

FERREIRA, Filippe, Universidade de Brasília, Instituto de Geociências, Brasília, Brazil: "Texture development during progressive deformation of hematite aggregates: Constraints from VPSC models and naturally deformed iron oxides from Minas Gerais, Brasil", 14.11.2016

GILLMANN, Cédric, Royal Observatory of Belgium, Brussels, Belgium: "Modeling the evolution of Earth's hot sister Venus", 10.11.2016

GORYAEVA, Alexandra, Université Lille 1, Unité Matériaux et Transformations, Villeneuve d'Ascq, France: "Anisotropic plasticity of $MgSiO_3$ post-perovskite: An atomic-scale study", 20.07.2016

ICHIKI, Masahiro, Tohoku University, Graduate School of Science, Research Center for Prediction of Earthquakes and Volcanic Eruptions, Sendai, Japan: "A mantle wedge flow model as imaged by three-dimensional electrical resistivity model beneath Northeastern Japan", 08.03.2016

ISMAILOVA, Leyla, Universität Bayreuth, Materialphysik – Kristallographie, Bayreuth, Germany: "Stability of Fe,Al-bearing bridgmanite in Earth's lower mantle and synthesis of pure Fe-bridgmanite", 17.03.2016

JOACHIM, Bastian, Universität Innsbruck, Institut für Mineralogie und Petrographie, Innsbruck, Austria: "Distribution and recycling of halogens in the Earth's mantle", 21.07.2016

JOURNAUX, Baptiste, Université Joseph Fourier, Laboratoire de Glaciologie et Géophysique de l'Environnement, Grenoble, France: "Incorporation of solutes in high-pressure ice: Influence on physical properties and implication for the structure and habitability of icy moons and ocean exoplanets", 04.08.2016

KRAYCH, Antoine, Université Lille 1, Unité Matériaux et Transformations, Villeneuve d'Ascq, France: "The role of dislocations in bridgmanite deformation: An atomic scale study", 21.09.2016

LABROSSE, Stephane, École Normale Supérieure de Lyon, France: "The thermal evolution of the mantle and the core as a window to the early Earth", 14.04.2016

LI, Yang, Bayerisches Geoinstitut, Bayreuth, Germany: "Development of single crystal synthesis of orthoenstatite at high pressure and high temperature: Selection of flux and control of temperature field", 25.10.2016

LIN, Yangting, Chinese Academy of Sciences, Beijing, P.R. China: "Volcanic history of the Imbrium basin illuminated by NanoSIMS 50L", 04.08.2016

MAINPRICE, David, Université Montpellier, CNRS, Montpellier, France: "The phase transformation of olivine to antigorite in geological conditions", 25.05.2016

MASSUYEAU, Malcolm, Institut des Sciences de la Terre d'Orléans, France: "Thermodynamics of melting in the Earth's mantle in presence of CO_2-H_2O", 02.06.2016

MATSUMOTO, Keiko, Tohoku University, Graduate School of Science, Department of Earth Science, Sendai, Japan: "Syn-eruptive oxidation of pyrrhotite as an indicator of air entrainment into eruption columns and lava flows", 18.03.2016

MEIER, Thomas, Universität Leipzig, Fakultät für Physik und Geowissenschaften, Leipzig, Germany: "High-sensitivity nuclear magnetic resonance at extreme conditions", 04.02.2016

MUJIN, Mayumi, Tohoku University, Graduate School of Science, Department of Earth Science, Sendai, Japan: "A nanolite record of eruption style transition", 17.03.2016

NEAVE, David, Leibniz Universität Hannover, Institut für Mineralogie, Hannover, Germany: "Estimating Icelandic magma reservoir depths: Challenges and possible solutions", 20.10.2016

NISHIMURA, Takeshi, Tohoku University, Department of Geophysics, Sendai, Japan: "Introduction of the Department of Geophysics, Tohoku University", 07.03.2016

OHTANI, Mari, Tohoku University, Graduate School of Science, Department of Earth Science, Sendai, Japan: "Inter-granular fluid compositions in mantle xenoliths inferred from direct observation of crystal surfaces", 22.03.2016

POTAPKIN, Vasily, Bayerisches Geoinstitut, Bayreuth, Germany: "Study of strongly correlated systems by application of high pressure: new horizons for solid state physics", 21.01.2016

RAUER, Heike, Deutsches Zentrum für Luft- und Raumfahrt (DLR), Institut für Planetenforschung, Berlin, Germany: "The population of extrasolar planets", 09.06.2016

RAYMOND, Sean, Laboratoire d'Astrophysique de Bordeaux, France: "Solar system mysteries", 16.11.2016

REUBER, Georg, Johannes Gutenberg-Universität, Institut für Geowissenschaften, Mainz, Germany: "Non-lithostatic pressure during subduction and collision", 15.09.2016

SCHMINCKE, Hans-Ulrich, GEOMAR, Helmholtz-Zentrum für Ozeanforschung Kiel, Germany: "Explosive eruptions, their products and their causes", 16.11.2016

SHIM, Sang-Heon, Arizona State University, School of Earth and Space Exploration, Tempe, USA: "Possible changes in the crystal chemistry of bridgmanite", 02.05.2016

SPERLING, Philipp, European XFEL, Hamburg, Germany: "Transport properties of matter under extreme conditions", 19.12.2016

STEINLE-NEUMANN, Gerd, Bayerisches Geoinstitut, Bayreuth, Germany: "Structure of the Earth's interior based on thermodynamic models of mantle mineralogy", 14.01.2016

TOMMASI, Andréa, Université de Montpellier, Géosciences Montpellier, France: "Memory in plate tectonics: the role of deformation-induced anisotropy of physical properties in the upper mantle", 22.09.2016

VASIUKOV, Denis, Universität Bayreuth, Materialphysik – Kristallographie, Bayreuth, Germany: "Spin transition of Fe(III) in oxygen octahedra", 21.04.2016

YANAGIDA, Yasuhiro, Tohoku University, Graduate School of Science, Department of Earth Science, Sendai, Japan: "Petrological study of mafic xenoliths from arc deep crust beneath Ichinomegata crater, NE Japan", 21.03.2016

ZHANG, Zhou, University of Minnesota, Department of Earth Sciences, Minneapolis, USA: "Fe-Ni-S-C system under high pressure, with implications to Earth's mantle", 13.04.2016

5.5 Conference organization

26.06.-01.07.2016, Goldschmidt 2016, Yokohama, Japan: Co-chair – Session: "Mantle melting in Earth and planetary interiors" (S. LAMBART, S. PETITGIRARD)

26.06.-01.07.2016, Goldschmidt 2016, Yokohama, Japan: Session 18c: "Mineral Physics of the Earth's Interior: Constraints on the Chemistry and Physics of our Planet from Experimental and Computational Studies" (R. SINMYO; V. STAGNO; C. MCCAMMON; T. KOMABAYASHI; J. TSUCHIYA; R. CARACAS; X. WANG)

18.-20.07.2016, PhD Short Course "Seismology and Mineral Physics of Earth's Mantle", Westfälische Wilhelms-Universität Münster, Germany (H. MARQUARDT, C. THOMAS)

28.08.-01.09.2016, 30th Meeting of the European Crystallographic Association, Basel, Switzerland: Micro-symposium 18: "Structures of minerals, planetary and carbon materials at Earth and planetary conditions" (T. BOFFA BALLARAN)

04.-09.09.2016, The 54th European High Pressure Research Group (EHPRG) International Meeting on High Pressure Science and Technology, Bayreuth, Germany: Conference Chair (L.S. DUBROVINSKY)

11.-14.09.2016, German-Swiss Geodynamics Workshop 2016, Lichtenfels, Germany (G. GOLABEK, M. THIELMANN)

11.-15.09.2016, 2nd European Mineralogical Conference, Rimini, Italy: "Diffusion and Deformation at High Temperature in Minerals" (K. MARQUARDT, session convener)

11.-15.09.2016, 2nd European Mineralogical Conference, Rimini, Italy: Session S14: "Advances in Computational and Experimental Mineralogy: A Journey from the Surface to the Deep Earth and Beyond" (A. ZUCCHINI; C. MCCAMMON; P. COMODI; M. MOOKHERJEE)

14.-16.09.2016, 5th Joint Workshop on High Pressure, Planetary and Plasma Physics (HP4), DESY, Hamburg, Germany (H. MARQUARDT, member of organizing committee)

29.09.2016, EINBLICKE - Women | Geoscience | Careers, an offer for young female scientist to discuss with senior female scientists, jointly organized with the Equal Opportunities Department of the University of Bayreuth for the International Research Training Group "Deep Earth Volatile Cycles" (K. MARQUARDT)

6. Visiting scientists

6.1 Visiting scientists funded by the Bayerisches Geoinstitut

ADAMS, Donat, Swiss Federal Laboratory for Materials Science and Technology, Dübendorf, Switzerland: 05.-07.10.2016

BONS, Paul, Universität Tübingen, Strukturgeologie, Tübingen, Germany: 23.-24.06.2016

BROMBACHER, Lisa, TU Bergadademie Freiberg, Germany: 29.-30.03.2016

COLTICE, Nicolas, Université Claude Bernard Lyon 1, Laboratoire de Géologie, Lyon, France: 01.-04.11.2016

CONDAMINE, Pierre, Université Blaise Pascal, Laboratoire Magmas et Volcans, Clermont-Ferrand, France: 16.-19.02.2016

CONSOLMAGNO, Guy, Vatikan Observatorium, Vatican City State: 11.-13.05.2016

DAVIS, William, University College London, Department of Earth Sciences, London, U.K.: 01.06.-28.07.2016, 13.-20.10.2016

DOHMEN, Ralf, Ruhr-Universität Bochum, Institut für Geologie, Mineralogie und Geophysik, Bochum, Germany: 02.-04.03.2016

DOLEJŠ, David, Universität Freiberg, Institut für Geo- und Umweltnaturwissenschaften, Freiberg, Germany: 22.-24.02.2016

EICHHEIMER, Philipp, Johannes Gutenberg-Universität, Institut für Geowissenschaften, Mainz, Germany: 19.-31.03.2016

EJAZ, Tariq, Indian Institute of Technology, Kharagpur, India: 20.07.-16.10.2016

FLANIGAN, Michaela, Australian National University, Research School of Earth Sciences, Canberra, Australia: 27.03.-03.04.2016

GILLMANN, Cédric, Royal Observatory of Belgium, Brussels, Belgium: 08.-11.11.2016

HUANG, Dongyang, Center for High Pressure Science and Technology Advanced Research (HPSTAR), Shanghai, P.R. China: 13.-16.06.2016

JOACHIM, Bastian, Universität Innsbruck, Institut für Mineralogie und Petrographie, Innsbruck, Austria: 21.-23.07.2016

JOURNAUX, Baptiste, Université Joseph Fourier, Laboratoire de Glaciologie et Géophysique de l'Environnement, Grenoble, France: 01.-05.08.2016

JUN, He, Guangzhou Institute of Geochemistry, Chinese Academy of Sciences, Guangzuhou, P.R. China: 20.10.-31.12.2016

KEMPERLE, Marina, Universität zu Köln, Germany: 30.-31.03.2016

KOEMETS, Egor, Novosibirsk State University, Novosibirsk, Russia: 14.-18.06.2016

LABROSSE, Stephane, École Normale Supérieure de Lyon, France: 13.-15.04.2016

LICHTENBERG, Tim, ETH Zurich, Institute of Geophysics, Zurich, Switzerland: 14.-16.09.2016

MAINPRICE, David, Université Montpellier, CNRS, Montpellier, France: 23.-27.05.2016

MASOTTA, Matteo, Istituto Nazionale di Geofisica e Vulcanologia, Roma, Italy: 21.-27.02.2016, 01.-31.08.2016

MASSUYEAU, Malcolm, CNRS Orleans, France: 01.-05.06.2016

MEIER, Thomas, Universität Leipzig, Fakultät für Physik und Geowissenschaften, Leipzig, Germany: 03.-05.02.2016

NI, Huaiwei, China University of Geosciences, Wuhan, P.R. China: 27.09.-01.10.2016

RAUER, Heike, Deutsches Zentrum für Luft- und Raumfahrt (DLR), Institut für Planetenforschung, Berlin, Germany: 09.-10.06.2016

RAYMOND, Sean, Laboratoire d'Astrophysique de Bordeaux, France: 15.-17.11.2016

REICHMANN, Hans-Josef, GeoForschungsZentrum Potsdam, Germany: 03.-04.11.2016

REUBER, Georg, Johannes Gutenberg-Universität, Institut für Geowissenschaften, Mainz, Germany: 14.-15.09.2016

ROZEL, Antoine, ETH Zurich, Institute of Geophysics, Zurich, Switzerland: 14.-16.09.2016

SCHIERJOTT, Jana, ETH Zurich, Institute of Geophysics, Zurich, Switzerland: 19.-21.09.2016

SCHWARZ, Marcus, TU Bergakademie Freiberg, Institut für Anorganische Chemie, Freiberg, Germany: 21.-24.02.2016

SHIM, Sang-Heon, Arizona State University, School of Earth and Space Exploration, Tempe, USA: 01.-02.05.2016

TOMMASI, Andréa, Université de Montpellier, Géosciences Montpellier, France: 21.-24.09.2016

YAMAMOTO, Takafumi, Hiroshima University, Graduate School of Science, Department of Earth and Planetary Systems Science, Hiroshima, Japan: 29.02.-03.03.2016

ZHANG, Zhou, University of Minnesota, Department of Earth Sciences, Minneapolis, USA: 11.-16.04.2016

6.2 Visiting scientists supported by other externally funded BGI projects

ANGEL, Ross, Università degli Studi di Padova, Dipartimento di Geoscienze, Padova, Italy: 28.09.-01.10.2016 (DFG [*B])

BAER, Roi, The Hebrew University, Fritz Haber Research Center for Molecular Dynamics, Jerusalem, Israel: 20.-22.06.2016 (DFG [*B])

BLANCHARD, Ingrid, Institut de Physique du Globe de Paris, France: 19.-22.06.2016 (ERC [*C])

BOLFAN-CASANOVA, Natalie, Université Blaise Pascal, Laboratoire Magmas et Volcans, Clermont-Ferrand, France: 28.09.-01.10.2016 (DFG [*B])

BRETSCHNEIDER, Judith, Westfälische Wilhelms-Universität Münster, Germany: 15.-16.08.2016 (DFG [*B])

DOLEJŠ, David, Universität Freiberg, Institut für Geo- und Umweltnaturwissenschaften, Freiberg, Germany: 28.09.-01.10.2016 (DFG [*B])

DORN, Caroline, Universität Bern, Space Research and Planetary Sciences, Bern, Switzerland: 30.11.-02.12.2016 (DFG [*B])

FAUL, Ulrich, Massachusetts Institute of Technology, Earth, Atmospheric and Planetary Sciences, Cambridge, USA: 31.10.-29.11.2016 (DFG [*B])

FERREIRA, Filippe, Universidade de Brasília, Instituto de Geociências, Brasília, Brazil: 13.-15.11.2016 (DFG [*B])

GAILLARD, Fabrice, Université d'Orléans, Institut des Sciences de la Terre d'Orléans, France: 27.09.-01.10.2016 (DFG [*B])

GALLORINI, Andrea, Università degli Studi di Firenze, Dipartimento di Scienze della Terra, Firenze, Italy: 31.05.-02.06.2016 (DFG [*B])

GORYAEVA, Alexandra, Université Lille 1, Unité Matériaux et Transformations, Villeneuve d'Ascq, France: 19.-21.07.2016 (DFG [*B])

GROSS, Eberhard K.U., Max-Planck-Institut für Mikrostrukturphysik, Halle/Saale, Germany: 21.-22.06.2016 (DFG [*B])

HOFFMANN, Marie, Museum für Naturkunde, Berlin, Germany: 15.11.2016 (DFG [*B])

JOURNAUX, Baptiste, Université Joseph Fourier, Laboratoire de Glaciologie et Géophysique de l'Environnement, Grenoble, France: 08.-17.09.2016 (DFG [*B])

KOSLOFF, Ronnie, The Hebrew University, Institute of Chemistry, Jerusalem, Israel: 21.-22.06.2016 (DFG [*B])

KRAYCH, Antoine, Université Lille 1, Unité Matériaux et Transformations, Villeneuve d'Ascq, France: 20.-23.09.2016 (DFG [*B])

MUKHINA, Elena, KTH Royal Institute of Technology, Stockholm, Sweden: 01.01.-29.02.2016 (DFG [*B])

NEAVE, David, Leibniz Universität Hannover, Institut für Mineralogie, Hannover, Germany: 20.-21.10.2016 (DFG [*B])

RUSTIONI, Greta, Università degli Studi di Pavia, Dipartimento di Scienze della Terra e dell'Ambiente, Pavia, Italy: 31.05.-02.06.2016 (DFG [*B])

SCHMINCKE, Hans-Ulrich, GEOMAR, Helmholtz-Zentrum für Ozeanforschung Kiel, Germany: 15.-17.11.2016 (DFG [*B])

STAGNO, Vincenzo, Università degli Studi di Roma "La Sapienza", Dipartimento di Scienze della Terra, Roma, Italy: 28.09.-01.10.2016 (DFG [*B])

WALTE, Nico, TU München, Forschungs-Neutronenquelle Heinz Maier-Leibnitz (FRM II), Garching, Germany: 28.-30.09.2016 (BMBF [*A])

WILLE, Ephraim, Ruhr-Universität Bochum, Institut für Geologie, Mineralogie und Geophysik, Bochum, Germany: 15.11.2016 (DFG [*B])

[*A)] BMBF: Bundesministerium für Bildung und Forschung

[*B)] DFG: Deutsche Forschungsgemeinschaft

[*C)] ERC: European Research Council

6.3 Visiting scientists supported by the DFG Core Facility programme

BORISOVA, Anastassia, Géosciences Environnement Toulouse, France: 10.-25.03.2016

AUZENDE, Anne-Line, Institut des Sciences de la Terre, Grenoble, France: 24.01.-01.02.2016

KLUMBACH, Steffen, Karlsruher Institut für Technologie, Institut für Angewandte Geowissenschaften, Karlsruhe, Germany: 03.03.2016

MEZZADRI, Francesco, Università degli Studi di Parma, Dipartimento di Chimica, Parma, Italy: 12.-18.06.2016

MORIZET, Yann, Université de Nantes, Laboratoire de Planétologie et Géodynamique, Nantes, France: 03.-08.04.2016

PAMATO, Martha, University College London, Department of Earth Sciences, London, U.K.: 25.01.-04.02.2016, 29.02.-11.03.2016, 03.-11.05.2016

SOFER, Zdenek, University of Chemistry and Technology, Prague, Czech Republic: 28.-31.03.2016

SOLFERINO, Giulio, University College Cork, School of Biological, Earth and Environmental Sciences, Cork, Ireland: 23.01.-07.02.2016

UENVER-THIELE, Laura, Johann Wolfgang Goethe-Universität, Physikalisch-Chemische Mineralogie, Frankfurt/M., Germany: 12.-15.04.2016

VERSEILS, Marine, Pierre and Marie Curie University – Paris 6, Institut de Minéralogie, de Physique des Matériaux et de Cosmochimie (IMPMC), Paris, France: 22.-27.05.2016

ZAGRTDENOV, Nail, Géosciences Environnement Toulouse, France: 10.-24.03.2016

6.4 Visitors (externally funded)

ANDO, Jinichi, Hiroshima University, Graduate School of Science, Department of Earth and Planetary Systems Science, Hiroshima, Japan: 29.02.-03.03.2016

ARUGA, Takafumi, Tohoku University, Graduate School of Science, Department of Earth Science, Sendai, Japan: 16.-20.03.2016

BARON, Marzena, University of Oslo, Centre for Earth Evolution and Dynamics (SEED), Oslo, Norway – University of Bristol, School of Earth Sciences, Bristol, U.K.: 10.04.-06.05.2016

BELL, Aaron, University of New Mexico, Institut of Meteoritics, Albuquerque, USA: 18.-29.10.2016

BIEDERMANN, Nicole, European XFEL GmbH, Schenefeld, Germany: 18.-20.07.2016

BOULTON, Carolyn, University of Liverpool, School of Environmental Sciences, Rock Deformation Lab, Liverpool, U.K.: 12.-18.06.2016

BUREAU, Hélène, Institut de minéralogie, de physique des matériaux et de cosmochimie (IMPMC), Paris, France: 26.09.-07.10.2016

CARACAS, Razvan, École Normale Supérieure de Lyon, Laboratoire de Géologie, Lyon, France: 26.-29.01.2016

FUJITA, Wakana, Tohoku University, Graduate School of Science, Department of Earth Science, Sendai, Japan: 16.-23.03.2016

FUNAMORI, Nobumasa, High Energy Accelerator Research Organization (KEK), Tsukuba, Japan: 13.-14.05.2016

GORELOVA, Liudmila, Saint-Petersburg State University, Institute of Earth Sciences, Department of Crystallography, Saint-Petersburg, Russia: 23.-29.07.2016

GOU, Huiyang, Center for High Pressure Science & Technology Advanced Research (HPSTAR), Beijing, P.R. China: 15.-30.09.2016

HÜBNER, Manuel, Universität Bonn, Steinmann Institut, Bonn, Germany: 26.-29.04.2016

ICHIKI, Masahiro, Tohoku University, Graduate School of Science, Research Center for Prediction of Earthquakes and Volcanic Eruptions, Sendai, Japan: 07.-08.03.2016

KULIK, Eleanora, DESY Hamburg, PETRA III Extension, Hamburg, Germany: 23.-24.08.2016, 09.-14.09.2016

KUTCHEROV, Vladimir, Royal Institute of Technology, Department of Energy Technology, Stockholm, Sweden: 14.-21.01.2016

LI, Yuan, Guangzhou Institute of Geochemistry, Chinese Academy of Sciences, Guangzuhou, P.R. China: 20.10.-31.12.2016

LIN, Yangting, Chinese Academy of Sciences, Beijing, P.R. China: 03.-05.08.2016

LUKIN, Evgenii, Frank Laboratory of Neutron Physics, Joint Institute for Nuclear Research, Dubna, Russia: 04.-23.09.2016

MAEDA, Fumiya, Tohoku University, Division of Earth and Planetary Materials Science, Sendai, Japan: 03.09.-01.10.2016

MASHINO, Izumi, Tohoku University, Division of Earth and Planetary Materials Science, Sendai, Japan: 15.-26.08.2016

MATSUMOTO, Keiko, Tohoku University, Graduate School of Science, Department of Earth Science, Sendai, Japan: 16.-20.03.2016, 13.-22.11.2016

MUJIN, Mayumi, Tohoku University, Graduate School of Science, Department of Earth Science, Sendai, Japan: 16.-20.03.2016

MURAKAMI, Motohiko, Tohoku University, Division of Earth and Planetary Materials Science, Sendai, Japan: 09.-17.05.2016

NAKAHARA, Hisashi, Tohoku University, Department of Geophysics, Sendai, Japan: 07.03.2016

NAKAMURA, Michihiko, Tohoku University, Graduate School of Science, Department of Earth Science, Sendai, Japan: 16.-20.03.2016, 10.-24.11.2016

NAKAMURA, Tomoki, Tohoku University, Division of Earth and Planetary Materials Science, Sendai, Japan: 13.-17.12.2016

NAKATANI, Takayuki, Tohoku University, Division of Earth and Planetary Materials Science, Sendai, Japan: 20.-25.09.2016, 02.-18.10.2016

NISHIMURA, Takeshi, Tohoku University, Department of Geophysics, Sendai, Japan: 07.03.2016

OHIRA, Itaru, Tohoku University, Division of Earth and Planetary Materials Science, Sendai, Japan: 28.08.-01.10.2016

OHTANI, Mari, Tohoku University, Graduate School of Science, Department of Earth Science, Sendai, Japan: 16.-23.03.2016

OKUMRA, Satoshi, Tohoku University, Graduate School of Science, Department of Earth Science, Sendai, Japan: 16.-23.03.2016

ORIOLO, Sebastian, Georg-August-Universität Göttingen, Abteilung Strukturgeologie und Geodynamik, Göttingen, Germany: 27.-29.01.2016

PATOČKA, Vojtěch, Charles University Prague, Department of Geophysics, Prague, Czech Republic: 08.-09.09.2016

PESCE, Giacomo, The University of Edinburgh, School of Geosciences, Edinburgh, U.K.: 07.-13.11.2016

RAEPSAET, Caroline, Institut de minéralogie, de physique des matériaux et de cosmochimie (IMPMC), Paris, France: 03.-07.10.2016

SATTA, Niccolò, GeoForschungsZentrum Potsdam, Germany: 08.12.2016

SCHREIBER, Anja, GeoForschungsZentrum Potsdam, Germany: 21.-23.02.2016

SMYTH, Joseph R., University of Colorado at Boulder, Department of Geological Sciences, Boulder, USA: 05.-20.05.2016, 26.-27.05.2016, 06.-09.06.2016

SPERLING, Philipp, European XFEL, Schenefeld, Germany: 19.-21.12.2017

UENVER-THIELE, Laura, Johann Wolfgang Goethe-Universität, Physikalisch-Chemische Mineralogie, Frankfurt/M., Germany: 29.02.-05.03.2016, 18.-23.07.2016,

VOLKOVA, Yana, Ural State University, Yekaterinburg, Russia: 10.01.-10.02.2016

VOGEL, Sebastian, Ludwig-Maximilians-Universität, Inorganic Solid State Chemistry Department, München, Germany: 17.-31.10.2016

WEI, Qingguo, Ludwig-Maximilians-Universität, Department für Geo- und Umwelt-wissenschaften, München, Germany: 18.-25.04.2016, 04.05.-17.06.2016

WOODLAND, Alan, Johann Wolfgang Goethe-Universität, Physikalisch-Chemische Mineralogie, Frankfurt/M., Germany: 29.02.-05.03.2016

YANAGIDA, Yasuhiro, Tohoku University, Graduate School of Science, Department of Earth Science, Sendai, Japan: 16.-23.03.2016, 12.-24.11.2016

7. Additional scientific activities

7.1 Theses

Ph.D. theses

ISMAILOVA, Leyla: An experimental study of the system FeO-Fe_2O_3-SiO_2 at high pressures and temperatures: Garnet, perovskite and post-perovskite phases.

VLČEK, Vojtech: Electronic structure of extended systems, within density functional theory and beyond.

M.Sc. theses

CHAUDHARI, Alok: Hydrogen (H_2) solubility in silicate melts.

EMILIEN, Joanna: The behaviour of sulfur in a magma ocean under reducing conditions: HP-HT phase relations in the Fe-S-Si system and the solubility of FeS in silicate melts.

LI, Yang: Development of single crystal synthesis of orthoenstatite at high pressure and high temperature: selection of flux and control of temperature field.

7.2 Honours and awards

FROST, Dan	received the Gottfried Wilhelm Leibniz Preis 2016 of the German Research Association (DFG)
KATSURA, Tomoo	Japan Association of Mineralogical Science Award 2016 Mineralogical Society of America, Fellow
MARQUARDT, Hauke	was appointed member of the “Junges Kolleg” of the Bavarian Academy of Sciences
PETITGIRARD, Sylvain	was one of the two winners of the EHPRG research prize in September 2016
POLEDNIA, Joana	Best Student's Poster at the German Mineralogical Society (DMG) Section Meeting of Petrology, Petrophysics & Geochemistry, Bremen, Germany, June 2016
SEIFERT, Fritz	became an honorary member of the German Mineralogical Society (DMG)

SCHULZE, KIRSTEN	Best Student Poster Prize, 54th European High Pressure Research Group (EHPRG) International Meeting on High Pressure Science and Technology, Bayreuth, Germany, September 2016

7.3 Editorship of scientific journals

DUBROVINSKY, Leonid	Member, Editorial Board of the Journal of High Pressure Research
KATSURA, Tomoo	Associate Editor "Reviews of Geophysics"
KEPPLER, Hans	Editorial Board "Contributions to Mineralogy and Petrology"
MCCAMMON, Catherine	Chief Editor and Managing Editor "Physics and Chemistry of Minerals" Advisory Editor "Springer Briefs in Earth Sciences"
MIYAJIMA, Nobuyoshi	Associate Editor "European Journal of Mineralogy"

7.4 Membership of scientific advisory bodies

BOFFA BALLARAN, Tiziana	Member of the Review Panel for allocation of beam-time at the Advanced Light Source, Berkeley
DUBROVINSKY, Leonid	Member, Review Panel for allocation of beam-time at ESRF Member, Review Panel of Canadian Light Source Chair, Subcomission on Spectroscopy, Diffraction, and new Instrumentations in Mineral Physics of the International Mineralogical Association Member, Deep Carbon Observatory Scientific Steering Committee Member, Review Panel of PETRA III
FROST, Dan	Chair of the Executive Committee for Elements Magazine
JACOBSON, Seth	Member, Division Committee, Division on Dynamical Astronomy, American Astronomical Society

KEPPLER, Hans	Member, Abraham Gottlob Werner Medal Committee, German Mineralogical Society (DMG) Member, Commission for Research of Bayreuth University (Präsidialkommission für Forschung und wissenschaftlichen Nachwuchs) Member, German National Academy of Sciences (Leopoldina) Member, Bavarian Academy of Sciences Member, Deep Carbon Observatory Scientific Steering Committee Member, Alexander von Humboldt Foundation Selection Panel for Humboldt Awardees
MARQUARDT, Hauke	Member, Bavarian Academy of Sciences (Young Scholars' Programme)
MCCAMMON, Catherine	Member, Starting Grant Panel PE10, European Research Council Member, Council, International Mineralogical Association Chair, Mineralogy and Mineral Physics Theme, Goldschmidt 2016 Past-President, Volcanology, Geochemistry & Petrology Section of the American Geophysical Union Chair, Nominations Committee, Volcanology, Geochemistry & Petrology Section of the American Geophysical Union Member, Affiliation and Engagement Task Force of the American Geophysical Union Member, Centennial Task Force of the American Geophysical Union Member, Governance Committee of the American Geophysical Union Chair, Bunsen Medal Committee, European Geosciences Union Chair, Sub-committee "Earth's Deep Interior" of the Commission of the Physics of Minerals, International Mineralogical Association Member, IASPEI/IAVCEI/IAGA Commission on Physics and Chemistry of Earth Materials

8. Scientific and Technical Personnel

Name		Position	Duration in 2016	Funding source
ABEYKOON, Sumith	B.Sc.	Student. Hilfskraft	from 11.05.	DFG
ADAMS, Andrea	B.Sc.	Student. Hilfskraft		DFG
APRILIS, Georgios	Dipl.-Ing.	Wiss. Mitarbeiter	15.05.-14.11.	DFG
ARATO, Robert	M.Sc.	Wiss. Mitarbeiter		DFG
ARMSTRONG, Katherine	M.Sc.	Wiss. Mitarbeiterin		DFG
AUDÉTAT, Andreas	Dr.	Akad. Rat		BGI
BEYER, Christopher	M.Sc.	Wiss. Mitarbeiter	to 29.02.	DFG
BÖHM, Ulrich		Mechaniker		BGI
BOFFA BALLARAN, Tiziana	Dr.	Akad. Oberrätin		BGI
BOLLINGER, Caroline	Dr.	Forschungsstipendiatin		AvH
BUCHEN, Johannes	Dipl.-Min.	Wiss. Mitarbeiter		DFG
BUCHERT, Petra		Fremdsprachen-sekretärin		BGI
BYKOV, Maxim	Dr.	Wiss. Mitarbeiter		DFG
BYKOVA, Elena	Dr.	Wiss. Mitarbeiterin	to 30.04. from 01.05.	BMBF DFG
CHANG, Jia	M.Sc.	Stipendiat	from 20.10.	CSC
CHARITON, Stella	M.Sc.	Wiss. Mitarbeiterin		DFG
CHAUDHARI, Alok	B.Sc.	Student. Hilfskraft	to 14.05. 01.07.-31.08.	DFG GIF
CHUVASHOVA, Irina	Dipl.-Chem.	Wiss. Mitarbeiterin	from 01.04.	DFG
CONDAMINE, Pierre	Dr.	Wiss. Mitarbeiter	from 01.08.	Leibniz
DRUZHBIN, Dmitry	M.Sc.	Wiss. Mitarbeiter		DFG
DUBROVINSKY, Leonid	Apl. Prof. Dr.	Akad. Direktor		BGI
EICHHEIMER, Philipp	M.Sc.	Wiss. Mitarbeiter	from 01.11.	IRTG
EL GORESY, Ahmed	Prof. Dr.			BGI/VP[1]
EMILIEN, Joanna	M.Sc.	Nebenberufliche Wiss. Hilfskraft	to 29.02. 01.03.-05.09. 20.10.-19.12.	UBT[2] HiWi IRTG
FARLA, Robert	Dr.	Forschungsstipendiat		AvH
FEI, Hongzhan	Dr.	Wiss. Mitarbeiter		DFG
FISCHER, Heinz		Mechaniker		BGI
FISCHER, Nicole	RAmtfr	Verwalt. Beamtin		BGI
FROST, Daniel	Prof. Dr.	Leiter		BGI
GOLABEK, Gregor	Prof. Dr.	Professor		BGI
GUO, Haihao	M.Sc.	Stipendiat		CSC

HEIDELBACH, Florian	Dr.	Wiss. Mitarbeiter	to 30.06.	DFG
			01.07.-30.11.	UBT[2]
			from 01.12.	UBT[3]
HUANG, Rong	M.Sc.	Wiss. Mitarbeiterin	to 28.02.	DFG
			from 01.03.	AvH
IMMOOR, Julia	Dipl.-Geol.	Wiss. Mitarbeiterin		DFG
ISHII, Takayuki	Dr.	Stipendiat		JSPS
JACOBSON, Seth	Dr.	Wiss. Mitarbeiter		EU
JENNINGS, Eleanor	Dr.	Wiss. Mitarbeiterin		EU
KATSURA, Tomoo	Prof. Dr.	Stellvertr. Leiter		BGI
KAWAZOE, Takaaki	Dr.	Akad. Rat		BGI
KEPPLER, Hans	Prof. Dr.	Professor		BGI
KEYSSNER, Stefan	Dr.	Akad. Oberrat		BGI
KISON-HERZING, Lydia		Sekretärin		BGI
KLASINSKI, Kurt	Dipl.-Ing. (FH)	Techn. Angestellter		BGI
KLUMBACH, Steffen	Dr.	Wiss. Mitarbeiter	from 01.06.	DFG
KOEMETS, Egor	M.Sc.	Wiss. Mitarbeiter	from 01.10.	IRTG
KOEMETS, Iuliia	B.Sc.	Student. Hilfskraft	from 01.11.	HiWi u. UBT[4]
KRAUßE, Detlef	Dipl.-Inform. (FH)	Techn. Angestellter		BGI
KRIEGL, Holger		Haustechniker		BGI
KUDRYAVTSEV, Daniil	M.Sc.	Stipendiat	29.09.-13.11.	DAAD
KURNOSOV, Alexander	Dr.	Wiss. Mitarbeiter	to 30.06.	DFG
			from 01.07.	Leibniz
LAURENZ-HEUSER, Vera	Dr.	Wiss. Mitarbeiterin		EU
LI, Yang	B.Sc.	Student. Hilfskraft		DFG
LINHARDT, Sven		Elektrotechniker		BGI
LIU, Zhaodong	Dr.	Wiss. Mitarbeiter		BGI/VP
MAKOWSKA, Malgorzata	Dr.	Wiss. Mitarbeiterin	from 01.09.	BMBF
MALLIK, Ananya	Dr.	Wiss. Mitarbeiterin	to 31.01.	BGI/VP
		Stipendiatin	from 01.02.	AvH
MANDOLINI, Tommaso	B.Sc.	Student. Hilfskraft	from 15.10.	IRTG
MARQUARDT, Hauke	Dr.	Nachwuchs-gruppenleiter		DFG
MARQUARDT, Katharina	Dr.	Akad. Rätin		BGI
MCCAMMON, Catherine	Dr.	Akad. Direktorin		BGI
MEIER, Thomas	Dr.	Wiss. Mitarbeiter	from 01.06.	BGI/VP
MELAI, Caterina	B.Sc.	Student. Hilfskraft	to 30.06.	DFG
			from 01.07.	GIF
METZ, Rouven	B.Sc.	Student. Hilfskraft	from 01.11.	IRTG

MISRA, Sourav	B.Sc.	Student. Hilfskraft	from 04.05.	DFG
MIYAJIMA, Nobuyoshi	Dr.	Akad. Rat		BGI
MUKHINA, Elena	M.Sc.	Stipendiatin	to 29.02.	DAAD
NJUL, Raphael		Präparator		BGI
OVSYANNIKOV, Sergey	Dr.	Wiss. Mitarbeiter		DFG
PAKHOMOVA, Anna	Dr.	Wiss. Mitarbeiterin	to 12.06.	DFG
PETIGIRARD, Sylvain	Dr.	Wiss. Mitarbeiter		DFG
POLEDNIA, Joana	M.Sc.	Wiss. Mitarbeiterin		DFG
POSNER, Esther	M.Sc.	Wiss. Mitarbeiterin	to 31.08.	DFG
			from 01.09.	EU
POTAPKIN, Vasily	Dr.	Wiss. Mitarbeiter	to 07.07.	DFG
POTZEL, Anke		Chem.-Techn. Assistentin		BGI
RAMMING, Gerd		Elektroniker		BGI
RAUSCH, Oliver		Mechaniker		BGI
ROSENTHAL, Anja	Dr.	Wiss. Mitarbeiterin	to 29.02.	DFG
RUBIE, David C.	Prof. Dr.	Professor		EU
RUSTIONI, Greta	M.Sc.	Wiss. Mitarbeiterin	from 01.10.	IRTG
SCHARFENBERG, Romina	B.Sc.	Sekretärin		BGI
SCHULZE, Hubert		Präparator		BGI
SCHULZE, Kirsten	M.Sc.	Wiss. Mitarbeiterin		DFG
SEROVAISKII, Aleksandr	M.Sc.	Stipendiat	from 01.09.	DAAD
SHCHEKA, Svyatoslav	Dr.	Wiss. Mitarbeiter		DFG
SIERSCH, Nicki	M.Sc.	Wiss. Mitarbeiterin	to 31.10.	DFG
			from 01.11.	Leibniz
SIMONOVA, Dariia	M.Sc.	Wiss. Mitarbeiterin	from 15.07.	DFG
STEINLE-NEUMANN, Gerd	Dr.	Akad. Oberrat		BGI
THIELMANN, Marcel	Dr.	Wiss. Mitarbeiter		BGI/VP
TRENZ, Ulrike		Biol.-Techn. Assistentin		BGI
ÜBELHACK, Stefan		Mechaniker		BGI
URGESE, Matteo	B.Sc.	Student. Hilfskraft	from 15.10.	IRTG
WAGLE, Fabian	M.Sc.	Wiss. Mitarbeiter		DFG
WALTE, Nicolas	Dr.	Wiss. Mitarbeiter	to 30.06.	BMBF
WANG, Lin	M.Sc.	Wiss. Mitarbeiter		DFG
WIESNER, Dorothea		Techn. Assistentin		BGI
YAO, Jie	M.Sc.	Wiss. Mitarbeiter	from 01.11.	DFG
YOSHIOKA, Takahiro	M.Sc.	Wiss. Mitarbeiter		DFG
ZAREI, Alireza	B.Sc.	Student. Hilfskraft	to 19.10.	DFG
			from 20.10.	IRTG
ZHANG, Daohan	M.Sc.	Stipendiat		CSC

Abbreviations/explanations:

AvH	Alexander von Humboldt Foundation
BGI	Staff Position of Bayerisches Geoinstitut
BGI/VP	Visiting Scientists' Program of Bayerisches Geoinstitut
BMBF	Federal Ministry of Education and Research
CSC	Chinese Science Council
DAAD	German Academic Exchange Service
DFG	German Science Foundation
EU	European Union
GIF	German-Israeli Foundation for Scientific Research and Development
HiWi	Hilfskraftmittel BGI
IRTG	International Research Training Group "Deep Earth Volatile Cycles"
JSPS	Japanese Society for the Promotion of Science
Leibniz	Leibniz-Preis der Deutschen Forschungsgemeinschaft Prof. Frost
UBT	Universität Bayreuth

[1] partially funded by the Visiting Scientists' Program of Bayerisches Geoinstitut

[2] Profilfeld Hochdruckforschung

[3] freie Stellenmittel

[4] Mittel zur Erfüllung des Gleichstellungsauftrages

Index